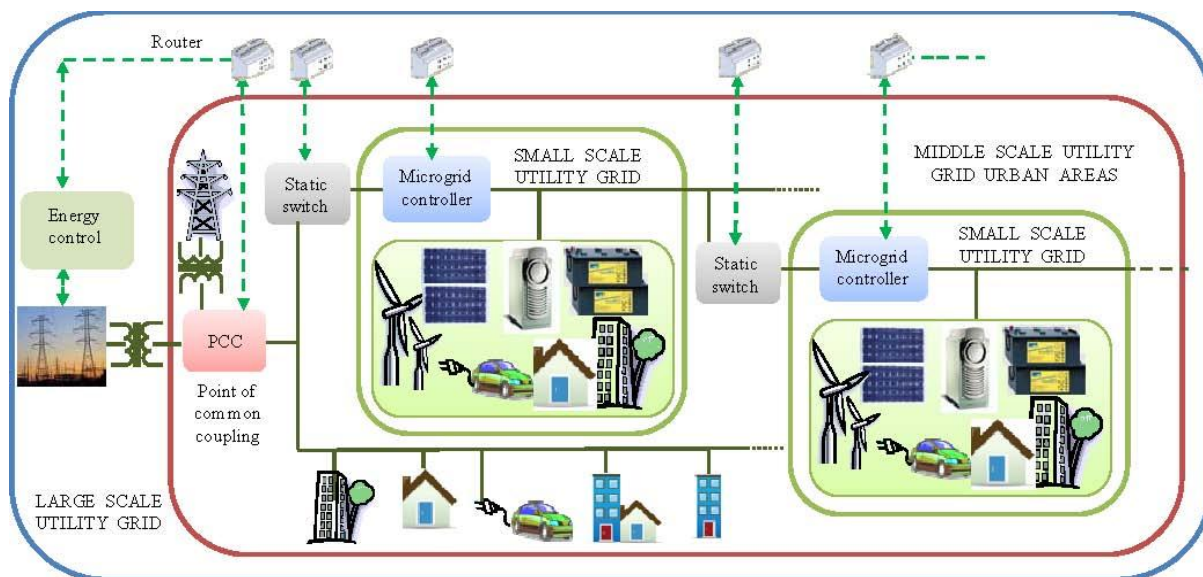


Par **Baochao WANG**

Intelligent control and power flow optimization of microgrid : energy management strategies

Thèse présentée
pour l'obtention du grade
de Docteur de l'UTC



Soutenu le 12 décembre 2013
Spécialité : Énergies renouvelables

D2122

UNIVERSITE DE TECHNOLOGIE DE COMPIEGNE

THESE

pour obtenir le grade de

DOCTEUR

Spécialité : Energies Renouvelables

par

Baochao WANG

Intelligent control and power flow optimization of
microgrid. Energy management strategies

Laboratoire AVENUES-GSU, EA 7284

Soutenue le 12 décembre 2013 devant le jury composé de :

Rapporteurs :

Daniel HISSEL

PR 63^e section CNU, FEMTO-ST, Belfort

Xavier GUILLAUD

PR 63^e section CNU, L2EP, Lille

Examineurs :

Maurice FADEL

PR 63^e section CNU, LAPLACE, Toulouse

Franck BETIN

PR 63^e section CNU, LTI, Amiens

Christine PRELLE

PR 61^e section CNU, ROBERVAL, Compiègne

Directeurs de thèse :

Manuela SECHILARIU

MCF, HDR 63^e section CNU, AVENUES-GSU, Compiègne

Fabrice LOCMONT

MCF, 63^e section CNU, AVENUES-GSU, Compiègne

Abstract

The intermittent and random production of renewable sources, such as photovoltaic and wind turbine, is always a problem for their large-scale integration in the utility grid. One of the solutions is to group renewable sources, traditional sources, storage and local consumption and treat it as a single unit in the utility grid. This is the concept of microgrid. A microgrid has the potentials of better responding both grid and end-user requirement, it facilitate the implementation of future smart grid.

Based on a representative microgrid in urban area and integrated in buildings, this thesis proposes a multi-layer supervision, in order to realise a systemic study while particularly attempting to cover the research gap of implementing optimisation in real-time operation.

The supervision handles together power balancing, energetic cost optimisation, metadata using, and information exchanges from both end-users and the smart grid. The supervision has been validated by experimental tests. The feasibility of implementing optimisation in real-time operation is validated even with uncertainties. The supervision is able to manage efficiently the power flow while maintaining power balancing in any case. Nevertheless, optimization effect relies on prediction precision. This problem can be improved in future works by updating optimization in real-time.

Keywords: Microgrid, photovoltaic, hierarchical control, supervision, prediction, optimization, control.

Résumé

La production intermittente et aléatoire des énergies renouvelables, sources photovoltaïques et éoliennes, est toujours un problème pour leur intégration massive dans le réseau public. L'une des solutions est de grouper des sources renouvelables, des sources traditionnelles, des dispositifs de stockage et des charges locales, et les traiter comme une seule unité dans le réseau public. Il s'agit du concept "micro-réseau". Un micro-réseau a des potentiels pour mieux répondre aux besoins de l'utilisateur final et du réseau public, et il facilite la mise en œuvre de futur smart grid, soit le réseau intelligent.

Basé sur un micro-réseau représentatif en zone urbaine et intégré aux bâtiments, cette thèse propose une supervision multicouche, afin d'effectuer une étude systémique en mettant en exergue un verrou scientifique concernant l'implémentation d'une optimisation dans l'exploitation en temps réel.

La supervision traite un ensemble d'opérations telles que : l'équilibré des puissances, l'optimisation des coûts énergétiques, utilisation de métadonnées, et échange d'informations avec le réseau intelligent et avec l'utilisateur final. Cette supervision a été validée par des tests expérimentaux. Malgré les incertitudes concernant les prévisions météorologiques, la faisabilité d'implémentation de l'optimisation dans l'exploitation réelle est vérifiée. La supervision proposée est en mesure de gérer efficacement les flux en assurant l'équilibre des puissances dans tous les cas. Néanmoins, la performance d'optimisation est liée aux précisions de prédiction. Ce problème peut être amélioré dans les travaux futurs par la mise à jour des résultats d'optimisation en temps réel.

Mots-clés : Micro-réseau, photovoltaïque, contrôle hiérarchique, supervision, prédiction, optimisation, commande.

Acknowledgements

First of all, I would like to express my sincere gratitude to my supervisors, Dr. Manuela SECHILARIU and Dr. Fabrice LOCMONT, for the good guidance and great efforts throughout the research and the writing of the thesis. Thanks to this teamwork and their well-organized working style, this thesis has advanced well according planning, which has permitted the thesis work can be published in each phase of progressing. Particular thanks goes to Dr. Manuela SECHILARIU for the great advice and efforts in writing and revising of this thesis, as well as other publications.

I also express my very gratitude to Professor Daniel HISSEL and Professor Xavier GUILLAUD, who have made detailed reports and remarks on my thesis, which helps a lot in improving the quality of my thesis for both research content and presentation. Thanks also to Professor Maurice FADEL, chairman of the thesis committee, Professor Franck BETIN and Professor Christine PRELLE for their interest in my work.

In addition, I would like to thank all colleagues of the laboratory AVENUES-GSU: Nassima MOUHOUS-VOYNEAU, Nathalie MOLINES, Jean-louis BATOZ, Josiane GILLES, Christian LEMAITRE, Eduard ANTALUCA, Sylvie LEFEBVRE, Bruno RAMOND, Janine FAIRWETHER, Jean-Pascal FOUCAULT, Gilles MOREL, Hipolito MARTELL-FLORES, Philippe DEHAN and Benoit BECKERS, for the good ambiance during my PhD studies in France.

I also thank my friends from the different countries in AVENUS-GSU: Issam HOUSSAMO, Hossam AL-GHOSSINI, Leonardo TRIGUEIRO DOS SANTOS, Hongliang LIU, Louis MERINO, Toha SALEH, Aurélie PREVOST, Lita SARI BARUS, Diana RODRIGUEZ, Walid BOUCHENAFI, Thibaut VERMEULEN and Nadia BEN ABDALLAH for sharing the PhD and life experience, for discussions on culture and customs, as well as on the study.

I would like to thank my friends Weidong DANG, Yang SONG, Lili WANG, Yang XIA, Xingxing Liu, Jun LIN, Zhenzhou ZHU for their help during the PhD studies.

I would like to thank the China Scholarship Council (CSC) for offering the opportunity to support my PhD study in France. I will treasure the experiences both academic and personal in my life.

Finally, a special bunch of thanks goes to my wife Xiaojuan, my daughter Nairan and my parents for all their love and encouragement to support me in finishing the PhD studies.

Table of contents

Table of contents	1
List of figures	4
List of tables	8
Abbreviations	9
Nomenclature	10
General introduction.....	15
Chapter I. From connecting to integrating renewable energy in utility grid	19
I.1. Traditional grid issues and smart grid	20
I.2. Microgrid.....	23
I.2.1. AC and DC microgrid	24
I.2.2. Research issues on microgrid.....	25
I.2.2.1. Control	25
I.2.2.2. Protection.....	27
I.2.2.3. Energy management.	28
I.2.3. Droop control	28
I.3. Objective of the thesis	31
I.4. Conclusion.....	32
Chapter II. Power system modeling and control for grid-connected operation	35
II.1. Electrical scheme and experimental platform	36
II.2. Functions of the power system control	38
II.2.1. Power balancing.....	38
II.2.2. Smart grid interaction	39
II.3. Power system modeling considering constraints.....	41
II.3.1. Introduction to Petri Nets modeling.....	41
II.3.2. Smart grid interaction modeling	43
II.3.3. Grid-operating mode modeling.....	44
II.3.4. Storage-operating mode modeling.....	45
II.3.5. PVA-operating mode modeling	47
II.3.6. Load-operating mode modeling.....	49
II.3.7. Power system global behavior by interpreted PN modeling.....	50
II.4. Power system control strategy.....	52
II.4.1. Control algorithm.....	52
II.4.2. PVA operating algorithm.....	55
II.4.2.1. PVA characteristics	55

II.4.2.2. PVA control strategy	55
II.4.2.2.1. Perturb and observe MPPT algorithm	56
II.4.2.2.2. MPPT and power limiting control strategy	56
II.5. Simulation results	58
II.5.1. Power system discrete behavior simulation	59
II.5.2. Power system continuous behavior simulation	61
II.6. Experimental test	66
II.7. Conclusion	68
Chapter III. Supervision system design	69
III.1. Supervision design overview	70
III.2. Human-machine interface	71
III.3. Prediction layer	72
III.3.1. PVA power prediction	72
III.3.1.1. Raw data processing considering sun position	73
III.3.1.2. PVA model	75
III.3.1.2.1. Linear model	75
III.3.1.2.2. Single diode PV model	76
III.3.1.2.3. Simple experimental prediction model	78
III.3.1.2.4. Experimental validation of PV power prediction model	82
III.3.2. Load power prediction	85
III.4. Energy management layer	86
III.4.1. Optimization problem formulation	87
III.4.1.1. Grid-connected mode	87
III.4.1.2. Off-grid mode	92
III.4.2. Solving the problem	94
III.4.3. Interface for operation layer	96
III.5. Operation layer	97
III.5.1. Grid-connected mode	98
III.5.2. Off-grid mode	99
III.6. Simulation results of supervision control	101
III.6.1. Grid-connected mode	101
III.6.2. Off-grid mode	107
III.7. Conclusion	110
Chapter IV. Experimental validation of supervision control	111
IV.1. Validation for grid-connected mode	113
IV.1.1. Improvement for experimental platform: simple phase compensation grid-connected inverter control with LCL filter	113

IV.1.1.1. Grid connection control	115
IV.1.1.2. Current feedback selection and grid voltage influence	117
IV.1.1.2.1. Grid-side current feedback	117
IV.1.1.2.2. Inverter-side current feedback	119
IV.1.1.3. Phase error compensation	121
IV.1.1.4. Improvements for simplified phase error compensation.....	122
IV.1.1.4.1. Fundamental compensation using PLL	123
IV.1.1.4.2. Passive damping	123
IV.1.1.5. Experimental results.....	124
IV.1.1.6. Conclusion	127
IV.1.2. Experimental tests of grid-connected supervision control	128
IV.1.2.1. Test 1.....	129
IV.1.2.2. Test 2.....	134
IV.1.2.3. Test 3.....	139
IV.1.3. Conclusion.....	143
IV.2. Experimental validation of off-grid supervision control	143
IV.2.1. Experimental tests of off-grid supervision control.....	144
IV.2.1.1. Test 1.....	144
IV.2.1.2. Test 2.....	148
IV.2.1.3. Test 3.....	152
IV.2.2. Conclusion.....	156
IV.3. Conclusion.....	156
General conclusions and perspectives.....	159
References	165
Annex 1: PV panel technical notice	173
Annex 2: Storage unit technical notice	176
Annex 3: C++ program that formulates the optimization problem in CPLEX form and interfaces with CPLEX.....	179

List of figures

Figure 1. Possible smart grid topology.....	22
Figure 2. Microgrid general scheme.	23
Figure 3. Multi-inverter power sharing scheme.	29
Figure 4. DC microgrid system overview.	31
Figure 5. Power system electric scheme.	36
Figure 6. Experimental platform.	37
Figure 7. Simplified effect of DSM on electricity market prices [74].	39
Figure 8. PN example: (a) marking before firing the enabled transition T1; (b) marking after firing T1.	42
Figure 9. Smart grid interaction modeling by PN.	43
Figure 10. Grid discrete state modeling by interpreted PN.	45
Figure 11. Grid behavior Stateflow model.	45
Figure 12. Storage discrete state modeling by interpreted PN.	47
Figure 13. Storage behavior Stateflow model.	47
Figure 14. PVA discrete state modeling by interpreted PN.	48
Figure 15. PVA source behavior Stateflow model.	49
Figure 16. Load discrete state modeling by interpreted PN.	50
Figure 17. Load behavior Stateflow model.	50
Figure 18. Energy management communication modeling by interpreted PN.	51
Figure 19. Flowchart of power system control algorithm.	53
Figure 20. Overview of control strategy.	54
Figure 21. $p_{PV} - v_{PV}$ characteristics at different solar irradiance and constant PV cell temperature.	55
Figure 22. Proposed PVA constrained production control strategy.....	57
Figure 23. PI controller with anti-windup.....	58
Figure 24. Screen-printing during simulation of Stateflow model in MATLAB.....	60
Figure 25. Powers (a) and voltages (b) evolution for $K_D = 1$ in normal grid mode.....	62
Figure 26. Powers (a) and voltages (b) evolution for $K_D = 0.8$ in normal grid mode.	63
Figure 27. Powers (a) and voltages (b) evolution for $K_D = 1$ in constrained grid mode.....	64
Figure 28. Powers (a) and voltages (b) evolution for $K_D = 0.8$ in constrained grid mode.	65
Figure 29. Powers evolution.....	67
Figure 30. DC bus voltage and storage <i>soc</i> evolution.....	67
Figure 31. Coefficients evolution.....	67
Figure 32. Supervision design overview.....	70

Figure 33. HMI design.....	71
Figure 34. Prediction layer design.....	72
Figure 35. Principle of solar irradiance calculation on the panel from ground data.	73
Figure 36. Solar position evolution during a day.(http://www.sunearthtools.com)	74
Figure 37. Calculation of shadow area.....	74
Figure 38. PV modeling generic schemes.....	75
Figure 39. Single-diode PV cell model.....	77
Figure 40. Experimental prediction model generic scheme.....	79
Figure 41. Images of the experimental devices.....	80
Figure 42. Process measurements electrical scheme.....	80
Figure 43. A typical example of current-voltage characteristics by proposed experimental test...	81
Figure 44. A typical example of power-voltage characteristics by proposed experimental test. ...	81
Figure 45. Experimental data of voltage model, measured function to g and θ	82
Figure 46. Experimental data of current model, measured function to g and θ	82
Figure 47. Operating conditions of the experimental tests.....	83
Figure 48. Comparison of PVA output power measured and predicted.....	84
Figure 49. Energy management layer design.....	86
Figure 50. Power flow in grid-connected mode.....	88
Figure 51. Power flow in off-grid mode.....	92
Figure 52. Operation layer design.....	97
Figure 53. Operating algorithm for grid-connected operation.....	100
Figure 54. Operating algorithm for off-grid operation.....	101
Figure 55. PVA MPPT power evolution for 23 rd of April 2011.....	102
Figure 56. Hourly PVA power measurement and PVA power prediction.....	102
Figure 57. Load power measurement and day-ahead prediction.....	103
Figure 58. Flowchart of optimization solving.....	103
Figure 59. Optimized power flow by energy management layer for grid-connected mode.....	104
Figure 60. Optimized K_D and soC evolution by energy management layer for grid-connected mode.....	104
Figure 61. Simulated power flow with optimum K_D for grid-connected mode.....	105
Figure 62. Simulated soC evolution with optimum K_D for grid-connected mode.....	105
Figure 63. Simulated power flow with constant $K_D = 0.5885$ for grid-connected mode.....	106
Figure 64. Simulated soC evolution with constant $K_D = 0.5885$ for grid-connected mode.....	106
Figure 65. Optimized power flow by energy management layer for off-grid mode.....	108
Figure 66. Optimized K_D and soC evolution by energy management layer for off-grid mode..	108

Figure 67. Simulated power evolution with optimum K_D for off-grid mode.	109
Figure 68. Simulated soC evolution with optimum K_D for off-grid mode.....	109
Figure 69. Load power prediction and load power demand for experiment.	112
Figure 70. Microgrid grid-connected inverter by LCL filter.....	115
Figure 71. Block diagram of LCL filter.	116
Figure 72. Current control by grid-side current feedback.	117
Figure 73. Stability margin of grid-side current feedback: (a) without damping resistor, (b) with damping resistor.	118
Figure 74. Current control by inverter-side current feedback.	119
Figure 75. Stability margin of inverter-side current feedback: (a) without damping resistor, (b) with damping resistor.	120
Figure 76. Differences of full compensation and simplified compensation in frequency domain.	122
Figure 77. Compensation structure using passive damping by PI controller: (a) compensation control structure, (b) equivalent derived structure.	123
Figure 78. Passive damping power loss relationship with capacitor <i>versus</i> resistor values.....	124
Figure 79. Experimental waveforms with peak current reference 1A following different compensation strategies: (a) no compensation, (b) fundamental compensation, (c) simplified compensation, (d) simplified compensation with passive damping.	126
Figure 80. Current distortion in frequency domain with peak current reference 1A following different compensation strategies: (a) no compensation, (b) fundamental compensation, (c) simplified compensation, (d) simplified compensation with passive damping.	127
Figure 81. PVA power prediction and measure for grid-connected test 1.	130
Figure 82. Power flow given by optimization for grid-connected test 1.....	131
Figure 83. K_D and soC evolution given by optimization for grid-connected test 1.....	131
Figure 84. PVA cell temperature and solar irradiance on the 21 st August 2013.	132
Figure 85. Experimental power flow for grid-connected test 1.....	133
Figure 86. Experimental soC evolution and DC bus voltage for grid-connected test 1.	133
Figure 87. Actual power sharing ratio between storage and grid for grid-connected test 1.....	133
Figure 88. PVA power prediction and measure for grid-connected test 2.	135
Figure 89. Power flow given by optimization for grid-connected test 2.....	135
Figure 90. K_D and soC evolution given by optimization for grid-connected test 2.....	136
Figure 91. PVA cell temperature and solar irradiance on the 9 th August 2013.....	136
Figure 92. Experimental power flow for grid-connected test 2.....	137
Figure 93. Experimental soC evolution and DC bus voltage for grid-connected test 2.....	137
Figure 94. Actual power sharing ratio between storage and grid for grid-connected test 2.....	137

Figure 95. PVA power prediction and measure for grid-connected test 3.....	139
Figure 96. Power flow given by optimization for grid-connected test 3.....	140
Figure 97. K_D and SOC evolution given by optimization for grid-connected test 3.....	140
Figure 98. PVA cell temperature and solar irradiance on the 30 th July 2013.....	141
Figure 99. Experimental power flow for grid-connected test 3.....	141
Figure 100. Experimental SOC evolution and DC bus voltage for grid-connected test 3.....	142
Figure 101. Actual power sharing ratio between storage and grid for grid-connected test 3.....	142
Figure 102. PVA power prediction and measure for off-grid test 1.....	145
Figure 103. Power flow given by optimization for off-grid test 1.....	145
Figure 104. K_D and SOC evolution given by optimization for off-grid test 1.....	145
Figure 105. PVA cell temperature and solar irradiance on the 4 th September 2013.....	147
Figure 106. Experimental power flow for off-grid test 1.....	147
Figure 107. Experimental SOC evolution and DC bus voltage for off-grid test 1.....	147
Figure 108. Actual MT on off signal for off-grid test 1.....	148
Figure 109. PVA power prediction and measure for off-grid test 2.....	149
Figure 110. Power flow given by optimization for off-grid test 2.....	149
Figure 111. K_D and SOC evolution given by optimization for off-grid test 2.....	150
Figure 112. PVA cell temperature and solar irradiance on the 27 th August 2013.....	150
Figure 113. Experimental power flow for off-grid test 2.....	151
Figure 114. Experimental SOC evolution and DC bus voltage for off-grid test 2.....	151
Figure 115. Actual MT on off signal for off-grid test 2.....	151
Figure 116. PVA power prediction and measure for off-grid test 3.....	153
Figure 117. Power flow given by optimization for off-grid test 3.....	153
Figure 118. K_D and SOC evolution given by optimization for off-grid test 3.....	154
Figure 119. PVA cell temperature and solar irradiance on 6 th September 2013.....	154
Figure 120. Experimental power flow for off-grid test 3.....	155
Figure 121. Experimental SOC evolution and DC bus voltage for off-grid test 3.....	155
Figure 122. Actual MT on off signal for off-grid test 3.....	155

List of tables

Table 1. Principal element detail of power system for experimental test.	38
Table 2. P&O algorithm by voltage control.	56
Table 3. Arbitrary values for experimental test.	66
Table 4. STC specifications of PV panel.	76
Table 5. Mean absolute error given by the experimental prediction model.	85
Table 6. Comparison of different cases for grid-connected simulation test.	107
Table 7. Comparison of different cases for off-grid mode simulation test.	109
Table 8. Converter efficiencies for optimization.	112
Table 9. System parameters	116
Table 10. Parameters for grid-connected operation.	129
Table 11. Comparison between optimization and experiment for grid-connected test 1.	134
Table 12. Comparison between optimization and experiment for grid-connected test 2.	139
Table 13. Comparison between optimization and experiment for grid-connected test 3.	143
Table 14. Parameters for off-grid operation.	144
Table 15. Comparison between optimization and experiment for off-grid test 1.	148
Table 16. Comparison between optimization and experiment for off-grid test 2.	152
Table 17. Comparison between optimization and experiment for off-grid test 3.	156

Abbreviations

AC	Alternative Current
ACR	Automatic Current Regulator
AVR	Automatic Voltage Regulator
BMS	Building Management System
DC	Direct Current
DR	Demand Response
DSM	Demand Side Management
HMI	Human-Machine Interface
HVDC	High Voltage DC
INC	Incremental Conductance
LUT	Look Up Table
MPP	Maximum Power Point
MPPT	Maximum Power Point Tracking
MT	Microturbine
P&O	Perturb and Observe
PCC	Point of Common Coupling
PI	Proportional-Integral
PLL	Phase Lock Loop
PN	Petri Net
PR	Proportional-Resonant
PV	Photovoltaic(s)
PVA	Photovoltaic Array
PWM	Pulse Width Modulation
RMS	Root Mean Square
STC	Standard Test Conditions
TOU	Time of Use

Nomenclature

C	DC bus capacitor (μF)
C_{C_G}	Capacitor in grid-connected LCL filter (μF)
C_G	Grid energy cost(€)
c_G	Grid energy tariff (€/kWh)
C_I	Controller integral gain
C_{LS}	Load shedding cost(€)
c_{LS}	Load shedding energy tariff (€/kWh)
c_{NH}	Grid normal hours energy tariff (€/kWh)
C_P	Controller proportional gain
c_{PH}	Grid peak hours energy tariff (€/kWh)
C_{PV}	Capacitor connected in parallel with PVA (μF)
C_{PVS}	PVA shedding cost(€)
c_{PVS}	PVA shedding energy tariff (€/kWh)
C_{REF}	Storage capacity (Ah)
C_S	Storage energy cost(€)
c_S	Storage energy tariff (€/kWh)
C_{total}	Total energy cost (€)
DPF	Displacement power factor
Δp_{PV}	Mean absolute error between PVA output power and the proposed mode (W)
Δt	Time increment (s)
dt_{MT}	MT working duty cycle (s)
E_G	The band gap energy of semi-conductor (<i>constant 1.12eV for silicon</i>)
g	Solar irradiance (W/m^2)
γ	PV power temperature coefficient at the MPP (1/K)
G^*	Solar irradiance reference of STC (<i>constant 1000W/m²</i>)
g_1	Solar irradiance on PV panel (W/m^2)
g_2	Solar irradiance on the ground (W/m^2)
G_{MIN}	Solar irradiance threshold (W/m^2)
G_x	Transfer function for object x
η_G	Grid converter efficiency (%)
η_{MT}	MT converter efficiency (%)
η_{PV}	PV converter efficiency (%)
η_S	Storage converter efficiency (%)
I	AC current RMS value
i_G^*	Grid current control reference (A)
i_{PV}^*	PVA current control reference (A)
i_S^*	Storage current control reference (A)
i_c	PV cell output current (A)
i_{C_G}	Current of capacitor branch of grid-connected LCL filter (V)
i_D	Diode current in single-diode PV cell model (A)
i_G	Grid current (A)
I_H	Total harmonic current RMS value (A)
i_I	Grid inverter output current (A)
i_L	Load current (A)
I_{MPP}	PV panel maximum power current at STC (A)

I_N	N^{th} harmonic RMS values of the current (A)
i_p	Current through parallel resistance in single-diode PV cell model (A)
i_{ph}	Current of photo-current source (A)
i_{PV}	PVA current (A)
i_{PV_MPP}	PV source MPP current (A)
i_S	Storage current (A)
i_{sat}	Diode saturation current (A)
I_{SC}	PV panel short circuit current at STC (A)
φ_I	Phase error between fundamental AC voltage and AC current
K	Boltzmann's constant ($constant\ 1.3806488 \times 10^{-23}\ \text{m}^2\ \text{kg}\ \text{s}^{-2}\ \text{K}^{-1}$)
K_C	PI controller anti-windup branch gain
K_D	Distribution coefficient for power balancing operation
K_I	Temperature coefficient for PV current (A/K)
K_i	PI controller integral gain
K_L	Load shedding coefficient
K_p	PI controller proportional gain
L_G	Grid side inductor of LCL filter connected grid inverter (mH)
L_I	Inverter side inductor of LCL filter connected grid inverter (mH)
Limit	Grid power changing rate limits (W/s)
L_{PV}	Inductor connected with PV converter (mH)
L_S	Inductor connected with storage converter (mH)
n	Diode ideality factor
N	Total number of cells in PVA
N_{PV}	The number of serial PV panels that compose the PVA
N_S	Number of cells in series in a PV panel
nvi	Network variable input
nvo	Network variable output
P	AC active power
p^*	Power control reference for microgrid power balancing (W)
p_G^*	Grid power control reference (W)
p_{MT}^*	MT power control reference (W)
p_{PV}^*	PVA power control reference (W)
p_{PVA}^*	PVA power limiting control reference(W)
p_S^*	Storage power control reference (W)
PF	Power factor
p_G	Grid power (W)
p_{G_I}	Grid injection power (W)
$p_{G_I_LIM}$	Grid injection power limit (W)
$p_{G_I_PRED}$	Grid injection power prediction (W)
p_{G_S}	Grid supply power (W)
$p_{G_S_LIM}$	Grid supply power limit (W)
$p_{G_S_PRED}$	Grid supply power prediction (W)
p_L	Load power (W)
p_{L_C}	Constrained load power via load shedding (W)
p_{L_D}	Load power demand (W)
p_{L_LIM}	Load power limit (W)
P_{L_MAX}	Contracted power (W)
p_{L_PRED}	Predicted load power (W)

p_{L_S}	Shed load power (W)
P_{MPP}	PV panel maximum power at STC (W)
P_{MT_P}	MT rated power (W)
p_{PV}	PVA power (W)
p_{PV_LIM}	PVA power controlled by power limiting algorithm (W)
p_{PV_MPPT}	PVA power by MPPT algorithm(W)
P_{PV_P}	PVA peak power (W)
p_{PV_PRED}	Predicted PVA power (W)
p_{PV_S}	Shed PVA power (W)
p_{PV_MPP}	PV source MPP power (W)
$p_{PV_m}^y$	Measured PV power for each measurement point y
p_{PV}^y	Predicted PV power for each point y
p_S	Storage power (W)
p_{S_C}	Storage charging power (W)
p_{S_D}	Storage discharging power (W)
P_{S_MAX}	Maximum storage power (W)
θ	PV cell temperature (K or °C)
q	Electron charge (<i>constant</i> $1.60217657 \times 10^{-19}$ C)
θ^*	PV cell temperature reference of STC (<i>constant</i> 298K)
R	Resister in capacitor branch of grid-connected LCL filter (Ω)
r_P	Parallel resistance in single-diode PV cell model (Ω)
r_S	Serial resistance in single-diode PV cell model (Ω)
s	Laplace operator
S	AC apparent power
S_I	PV panel area (m^2)
S_2	Area of PV panel shadow on the ground (m^2)
soc	Storage state of charge (%)
SOC_{MAX}	soc upper limit (%)
SOC_{MIN}	soc lower limit (%)
t	Continuous time (s)
t_0	Initial time instant (s)
t_F	Final time instant (s)
THD	Total harmonic distortion
t_i	The i^{th} time instant (s)
U	AC voltage RMS value
v	DC bus voltage (V)
v^*	DC bus voltage control reference (V)
v_{PV}^*	PVA voltage control reference (V)
$v_{PV_LIM}^*$	PVA voltage control reference given by power limiting algorithm (V)
$v_{PV_MPPT}^*$	PVA voltage control reference given by MPPT algorithm(V)
v_c	PV cell output voltage (V)
v_{C_G}	Voltage of capacitor branch of grid-connected LCL filter (V)
v_D	Diode voltage in single-diode PV cell model (V)
v_G	Grid voltage (V)
v_I	Grid inverter output voltage (V)
V_{MPP}	PV panel maximum power voltage at STC (V)
V_{OC}	PV panel open circuit voltage at STC (V)
v_{PV}	PVA voltage (V)

v_{PV_MPP}	PV source MPP voltage (V)
v_S	Storage voltage (V)
V_{S_MIN}	Storage minimum voltage (V)
V_{S_MAX}	Storage maximum voltage(V)
V_T	Thermal voltage (V)
X	Overall RMS value of AC measurement
X_N	N^{th} harmonic RMS values of AC measurement
z	Total number of measurement points

General introduction

In order to improve greenhouse gas of power generation, the existing utility grid incorporates already renewable energy resources that are the necessary complement to the traditional electricity generation. The distributed power generation is based on systems that may be classified as:

- grid-connected system, with a total and permanent power injection;
- stand-alone system, seen as a substitute of utility grid connection, mostly for remote sites;
- off-grid / grid-connected and safety network system.

In urban area, there is a significant development of small plants of decentralized photovoltaic (PV) power production, therefore associated or integrated to buildings. Due to the PV energy purchase conditions, the grid-connected system for permanent energy injection is proposed in most applications. However, this increased development leads to grid-connection incidents, which became true technical constraints. The fluctuations in both energy demand and renewable power generation, even for few minutes, induce an effort to supplementary setting on conventional production units. The number of conventional production units in operation must grow to ensure the balance between power generation and power demand. This is due to the fact that the renewable power generation, hardly predictable and very unsettled, is not participating in technical regulations for grid connection (setting voltage and frequency, islanding detection ...) and behaves as passive electric generators. In response to these technical constraints, research works are being carried out on grid integration of renewable

decentralized generation or developing new supervision strategies as high level energy management control.

Concerning grid-connected systems, many studies have been carried out and propose solutions on power electronic converters or complex systems approach. However, having regard to the absence of the grid integrated energy management, the development of renewable energy grid-connected systems could be restrained especially by the power back grid capacity in real time.

Given the intermittent nature of renewable sources, the major problem associated with the stand-alone systems is the service continuity, from whence the energy storage and conventional sources are required. The studies in this axis concentrate more on techno-economic feasibility conditions, optimized storage sizing, and load management.

In this context, in urban areas and for buildings equipped with renewable resources, an alternative solution could be the off-grid / grid-connected system seen as building-integrated microgrid: low voltage distribution system with distributed energy sources, storage devices and controllable loads. This microgrid represents a form of power local generation, often multi-source, and can operate both in grid-connected and in off-grid operating mode. The off-grid aspect is given by the fact that the energy produced is intended for self-feeding. Thanks to the grid connection, the microgrid can receive power from the utility grid. Moreover, excess power can be traded back to the utility grid or directed toward other urban microgrid.

On the other hand, the increased power consumption involves more quality and reliability to regulate electricity flows, less mismatching between electricity generation and consumption, and more integrated renewable energies. Thus, the concept of smart grid is born in recent years. Smart grid could be easily defined as the electricity delivery system, which transports, converts and distributes the power efficiently (from producers to consumers), integrated with communication and information technology. The main goal of smart grid communication is to assist in balancing the power generation and the power consumption. As renewable and distributed electricity increase, their grid integration associated with an energy management system is more necessary than ever. Hence, in order to improve PV grid penetration, it is necessary to combine power balancing control and high level energy management together, and providing ability to adjust grid power level at the point of common coupling (PCC).

According to this context, this thesis intends to make a further contribution toward the conceptualization of a decentralized multi-source power hierarchical control where the smart grid communication is integrated. The goal is to design an advanced local energy management by a hierarchical control which allows a decentralized and cooperative architecture for power flow balance. Specifically, for buildings equipped with PV array, this study presents a DC microgrid with multi-layer supervision control which handles instantaneous power balancing following the power flow optimization while providing interface for smart grid communication. The optimization takes into account forecast of PV power production and load power demand, while satisfying constraints such as

storage capability, grid power limitations, grid time-of-use pricing and grid peak hour. Optimization, whose efficiency is related to the prediction accuracy, is carried out by mixed integer linear programming. Experimental results show that the proposed microgrid structure is able to implement optimization in real power control and ensures self-correcting capability. The power flow can be controlled near optimum cost when the prediction error is within certain limits. Even the prediction is imprecise, the power balancing can be maintained with respect of rigid constraints. The proposed supervision control can respond to issues of performing peak shaving, avoiding undesired injection, and making full use of locally produced energy with respect to rigid element constraints.

The thesis is organized in four chapters. After the general introduction, Chapter I gives firstly a review of issues in grid and places microgrid concept in the context of renewable energy integration. Then, this chapter outlines the objective of the thesis. Aiming at improving penetration level of PV installation associated with buildings, this study focuses on DC microgrid composed of a power system and its control called "supervision system". The power system consists of PV sources, storage, grid-connection, microturbine (MT) and DC load. The supervision system, designed as a multi-layer control structure, combines power balancing, energy management and smart grid interaction. The proposed microgrid can work in both grid-connected mode and off-grid mode.

In Chapter II, the power system modeling and power balancing control for grid-connected mode are studied and presented. The interaction between the smart grid messages and the DC microgrid is taken into account. To identify constraints and how to coordinate different sources to establish overall power balancing control strategy, the power system modeling by interpreted Petri Nets (PN) formalism and Stateflow is presented firstly. Based on power system behavior modeling, the power system control strategy is designed with consideration of each element constraints and their behavior. Algorithms for PV power limiting and load shedding management are developed. The proposed power system control is associated with our laboratory scale experimental platform, whose detailed presentation is given at the beginning of this chapter. Simulation and experimental results of day tests validate the basic control strategy design, which ensures power balancing while respecting all element constraints. It should be noted that, considered as a simplified grid-connected case, the off-grid power balancing control is developed based on grid-connected power balancing control in Chapter III.

Based on the study of power system operation in grid-connected mode, Chapter III further develops the supervision system in power balancing for both grid-connected and off-grid operation, power flow optimization, prediction data processing and human-machine interface (HMI). The supervision is proposed as a multi-layer structure with local energy management based on end-user's request, estimated operating building appliances, weather forecasts, conditions concerning utility grid availability, possibilities of shedding building facilities... An operational layer is developed to maintain the power balancing, taking into account multiple constraints. The aim of supervision control is to provide a continuous supply to the building with an optimized energy cost under constraints. The whole supervision control is fully developed for both grid-connected mode and off-grid mode, which

includes power balancing, optimization, prediction and interaction with smart grid and end-user. Simulations for different cases are carried out for validation of the supervision control. The obtained results show that the supervision control can maintain power balancing while performing optimized control, even with uncertainties of prediction and arbitrary energy tariffs.

In Chapter IV, the proposed supervision control is validated through experimental test in order to identify the merits and shortages in real operating conditions. The experimental tests, for both grid-connected mode and off-grid mode, are carried out with our experimental platform. For grid-connected mode, firstly an improvement of experimental platform is proposed; it is related to grid-connected LCL filter. In low power operation, which is often the case with PV generation according to weather conditions, grid power factor degradation is induced by LCL filter. The degradation causes are studied and a phase error compensation structure is proposed. Experimental results conclude that the proposed compensation structure improves the grid power quality in case of low PV production, in both power factor and harmonics. Concerning the DC microgrid, the experimental results are strongly influenced by the solar irradiance evolution and induced prediction errors. To analyze DC microgrid validation and its technical feasibility, three case studies, corresponding to three types of solar irradiance evolution, are proposed and discussed following the two operating mode: grid-connected and off-grid. Given the obtained experimental results, the feasibility of DC microgrid control with energy management and smart grid interaction, in real operation with respect to rigid constraints, is validated. In addition, the proposed supervision control which parameterizes power balancing strategy and provides interface for optimization is also technically verified.

General conclusion and perspectives of the proposed DC microgrid research study are given in the end.

Chapter I. From connecting to integrating renewable energy in utility grid

The developing technology of power electronics enables to connect distributed renewable and non-renewable sources to the utility grid. However, simply "connecting" does not enhance overall grid performance. Scaling from waveform of power electronic device output to grid regulation and grid stability, extra problems emerge. To achieve high level renewable energy penetration into grid, control strategies and means of power management should be developed to build a more robust utility grid. To sum up, efforts need to be done to overcome integration barriers, from control to energy management and protection, to form a more flexible and robust grid. Information and communication are indispensable for such a heterogeneous grid that should adapt to the future high penetration of renewable energy and plug-in electric vehicle. Thus, the concept of smart grid was born in recent years. Towards the smart grid, microgrid that combines distributed energy sources and loads is believed as an effective and promising approach to address the renewable energy source integration issues as well as traditional grid issues. With communication technology, microgrid can interact with smart grid in order to assist grid power balancing by an advanced energy management and so to reduce the cost and to improve power quality. This chapter gives a review of issues in grid and places microgrid concept in the context of renewable energy integration.

1.1. Traditional grid issues and smart grid

Traditional utility grid is under challenge of balancing ever-growing heavy load, performing load demand management, improving asset efficiency and incorporating renewable energy.

Nowadays, electric power is mostly generated in a "centralized" way. The overall electric power is generated by several giant power plants. It is then supplied to end-users through transmission and distribution lines, substations and transformers. As grid operation and protection mechanisms are based on unidirectional power flow, it is difficult to integrate and manage unpredictable bi-directional power flow induced by the renewable sources introduction. Moreover, electricity travels long distance to reach the end-users, which cause certain amount of power loss. The distributed generation, which means generating local power by large number of dispersed power sources, can improve the overall efficiency, decrease impact on grid by local consumption and ameliorate supply reliability. However, facing high penetration level of renewable energies, communication and new control strategies are required to coordinate distributed generation within the existing utility grid.

With the ever-growing load, the utility grid scale is growing significantly. One blackout affects much larger range than ever, so self-healing enhanced by distributed generation is demanded for future. The utility grid must be able to balance heavy load, match nearly instantly the production with the load demand. Unbalanced power would cause fluctuations in grid voltage amplitude and frequency, or even blackout. This power balancing requires certain amount of fast responding spinning reserves, such as natural gas and petroleum fired power plants working in stand-by mode. Maintaining these reserves online represents the most expensive economical and environmental part in utility grid. The load demand in utility grid varies according to seasons, days, hours, minutes and seconds. The grid capacity is built to satisfy the peak load consumption. Most of the time, the assets in the grid are not fully used. During a day, if the peak consumption can be shifted to other time, referred to as "power peak shaving", the grid capacity and energy cost could be largely reduced.

Demand side management (DSM) is proposed as a solution for reducing peak consumption and total energy cost [1]. DSM refers to all the means to affect the load aiming to reduce power demand during peak hours, through load shedding program for scheduling of appliances. The utility already provide indirect DSM, referred to as "power demand response"; for example, time-of-use (TOU) tariff to encourage users to shift uncritical load consumption to off-peak hours. It is not yet possible for the grid to automatically manage the load demand and shift uncritical load to off-peak hours. The utility direct load control requires communication support and specific devices.

On the other hand, facing increasing energy demand, environmental problems and decreasing fossil resources, renewable energies have been being connected with the utility grid. Due to the energy purchase conditions and policies encouragement, renewable energy plants as PV sources and wind turbine, both large-scale and small-scale or individual local plants, are developing significantly. Most

of these systems are grid-connected with a total and permanent power injection. However, renewable power generation is very intermittent and random. If this continuously growing production is injected into the grid without control, it will increase the power mismatching in the utility grid and cause fluctuations in voltage and frequency [2-3], or even blackout. Thus, the vulnerability of the utility grid could increase.

The traditional utility grid regulation time varies from 30 seconds to more than 72 hours. In contrast, the renewable generation fluctuation is 1-2 seconds, which means one PV plant output power can change to zero from rated power within seconds. It is thus difficult and costly for the grid to compensate this kind of sudden change. Considering relative low renewable energy penetration level, the grid is able to absorb the fluctuations without causing severe problem. However, considering future high renewable energy penetration level, large regional power fluctuations cause problems. The uncontrolled renewable power injection must be improved, and fluctuations of renewable energy should be reduced or managed.

Energy storage seems to be a perfect solution to handle the intermittent nature of renewable energy, but it has limitations based on available technologies, life cycle cost and environmental impact [4]. For large-scale renewable energy plant, as wind farm or PV park, the pumped-storage hydroelectricity station is a promising technology to deal with the random production of renewable sources [5]. This technique is the most cost-effective form of current available grid energy storage. However, capital costs and requirement of appropriate terrain cannot generalize this solution. Recent progress in grid energy storage makes hydrogen technologies (combined fuel cells and electrolyzers with hydrogen tanks) an alternative to pumped-storage [6]. Nevertheless, especially for future high penetration of distributed small plant, as building-integrated renewable generators, there is no much innovation on storage technology; lead-acid batteries are still commonly used as storage because of low cost with regards to their performance. Hence, with limited storage capacity, local energy management strategy needs to be developed to optimize the use of renewable energy.

Facing the challenges of power balancing, load side management and integrating renewable generations, the concept of smart grid is born in recent years [7]. Smart grid could be easily defined as the electricity delivery system, which transports, converts and distributes the power efficiently (from producers to consumers), integrated with communication and information technology. The main goal of smart grid communication is to assist in balancing the power generation and the power consumption, while providing energy optimization and improving the robustness of the utility grid.

Smart grid ideas dates from 2001 in USA; Electric Power Research Institute (EPRI) started the study on "Intelligrid". The Department of Energy (DOE) published "Grid 2030" in 2003 [8], then, in 2004, DOE initiated "Grid Wise" project. In 2005 DOE and National Energy Technology Laboratory (NETL) initiated research named "Modern Grid Initiative", and published "The Modern Grid Initiative: a vision for the modern grid" in 2007. Ever since, institutions, universities and companies cooperate with power companies to propose their own pilot project development and practice on "Smart Grid".

Thus, developing smart grid is announced as main strategy in North America as well in Europe and Asia. Researches on smart grid have been boosting ever since, on communication, measurement, advanced components and devices, advanced control, modeling and market strategies. Several industry products already exist, such as smart meters. Standards on smart grid communication hardware have been carried out as well [9-11].

Because the smart grid is a very complex network with nonlinearity, randomness, bidirectional power flow, and bidirectional communication [12-13], despite of the technologies of smart devices and communication protocol, supervising the status of the whole system, and dealing with the large-scale real time data, remain an open problem.

Microgrid is believed as one promising approach to facilitate smart grid. A microgrid consists of distributed energy sources, traditional and renewable, storage devices and controllable loads. The microgrid combines local power generation and local consumption, and can operate in grid-connected and in islanded operation mode, as well in off-grid mode. A microgrid could refer to different power scales from few kW to MW.

By organizing a set of microgrids [14-18] with several grid connections, through an adequate interface controller, power balancing becomes more a local issue rather than a region-wide issue [13]. The possible smart grid topology evolution facilitated by microgrid is shown in Figure 1 [19].

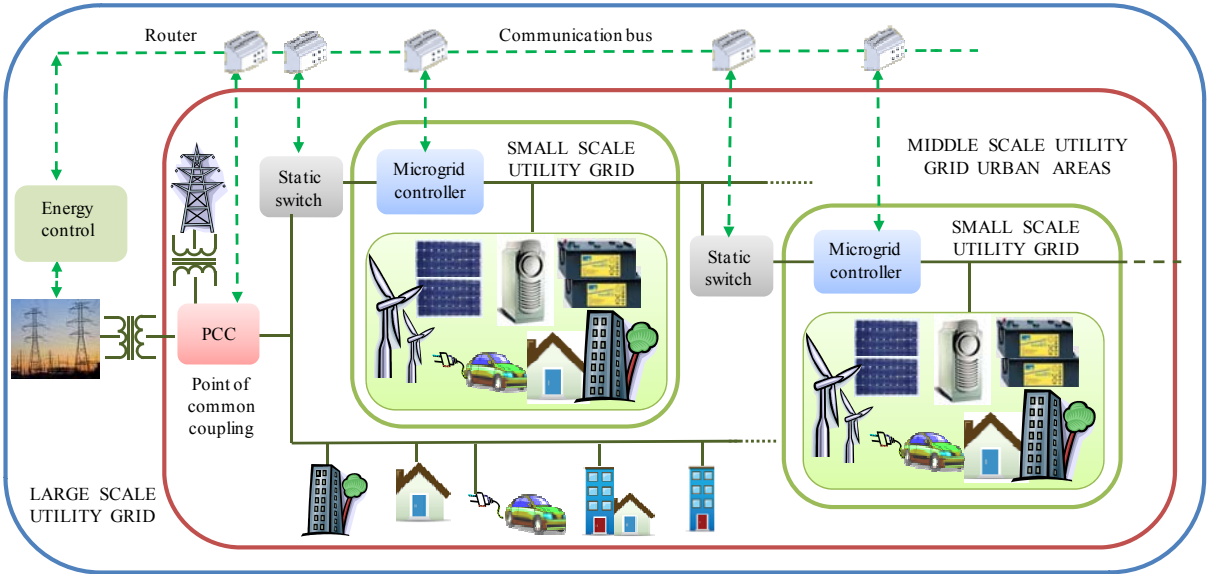


Figure 1. Possible smart grid topology.

Thus, the smart grid topology could be seen at:

- small-scale: microgrid, able to maintain a basic power balancing, to exchange power between each other and with the traditional utility grid through a specific interface controller, able to exchange data;
- middle-scale: a set of microgrids combined with the traditional utility grid as a single system able to exchange power and data through a specific interface at PCC;

- large-scale: numerous microgrids with energy management seamlessly integrated with utility control to transform the traditional power grid into smart grid.

Data can be exchanged via a bidirectional bus communication which is based on appropriate routers and protocols.

1.2. Microgrid

As mentioned above, microgrid aggregates local power production, consumption and storage together. According to different applications and projects, the microgrid structure varies. It is generally considered that microgrid controls on-site generation and power demand to meet the objectives of providing local power, ancillary services and injecting power into the utility grid if required. The general topology of microgrid is shown in Figure 2.

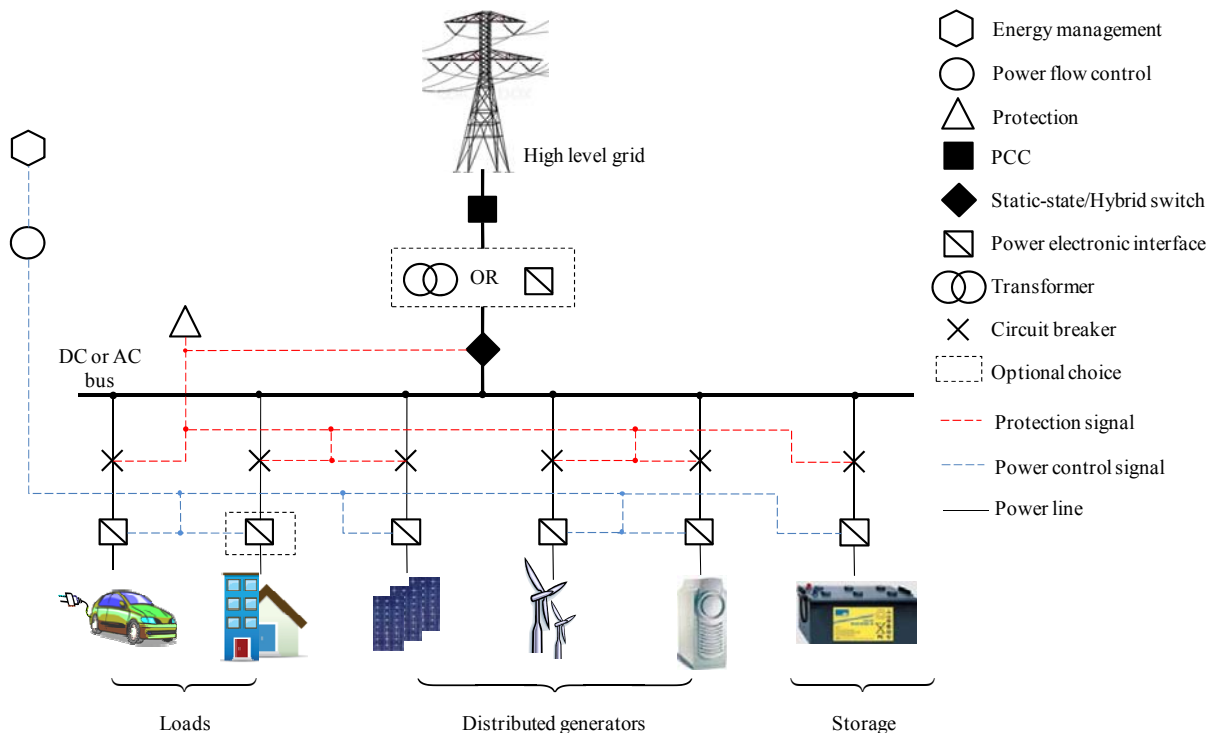


Figure 2. Microgrid general scheme.

Concerning microgrid approach, several main advantages can be given: improving renewable energy penetration level, facilitating the smart grid implementation, better energy supply for remote areas, power balancing at local level with self-supplying possibility, and maintaining load supply during islanding operation or off-grid mode. Thus, the microgrid controller becomes essential for balancing power and load management, and facilitates the sources pooling during islanding.

This chapter describes the general concept of microgrid, its configurations, main research issues on microgrid, and gives a review on droop control.

1.2.1. AC and DC microgrid

Depending on the usage of AC or DC bus for coupling different elements within microgrid, AC microgrid, DC microgrid and hybrid AC/DC microgrid structures exist.

AC microgrid refers to the configuration of coupling microgrid elements with AC bus, and connecting to AC local grid. DC microgrid refers to DC bus coupling and connection to DC local grid. Hybrid AC/DC microgrid refers to the presence of both DC and AC coupling. At present, the DC grid is not ubiquitous, but more HVDC transmission lines are being built in MW level, while low voltage DC grid is being adopted, starting with data centers, for the reason of more efficiency, less cost, less occupied space, lower lifetime cost and more reliability [20]. DC grid is seen, by some authors, as the future trend in both transmission and distribution lines [21]. At present, the main technical obstacle to bring DC grid into reality lies in the aspect of protection, for example high power rating DC circuit breakers.

Comparing AC and DC configuration of microgrid, AC systems have advantages over DC systems in the following aspects:

- *Voltage transformation.*

AC voltage can be easily and economically transformed to another level (increasing or decreasing) by electromagnetic transformers without control strategy. While DC transformation requires power electronic devices with complex measuring and control.

- *Circuit protection for AC system is more mature than for DC systems.*

Firstly, for AC systems line impedance is much higher than DC systems. Meanwhile, an AC element, such as transformer, can withstand more overloading (for example, a 30/40MVA, 138/13.8kV transformer can withstand 160% overload for 30 minutes and 170% during 15 minutes according to transformer factory test [22]) than DC system for which a slight overloading for milliseconds over power electronic device rating could permanently damage the power converter. In case of fault such as short circuit, the AC current can be limited and also it rises slowly because of relatively high AC impedance; thus, the overloading ability provide enough time for protection devices to operate. While in DC system, the low DC "impedance" induces high rising rate in the fault current, resulting in more challenges for the design of a fast response DC circuit breaker.

Secondly, AC circuit breaker is much mature than DC. Forced by AC voltage, AC current has nature zero-crossing features, while DC current is always persisting. Breaking the DC circuit is much more difficult, especially in high current rating, than breaking AC current.

Nevertheless, DC systems offer several advantages over AC systems:

- *Incorporation of DC native generators which are often renewable energy sources.*

Fuel cells and PV sources, but also storage means as batteries, can be more easily and efficiently integrated with DC grid without needing inversion stage.

- *Synchronization is not required.*

Coupling AC microgrid element with AC bus and AC grid requires all conversion stages work at the same frequency, while amplitude and harmonic must also be as consistent as possible to avoid undesired loop current. Concerning DC microgrid, as zero frequency system, only the voltage amplitude should be regulated and there is no need for synchronization when connecting DC bus or DC local grid. Coupling DC bus to AC local grid needs only one inversion stage.

- *No need of reactive power supply for AC sources.*

In DC microgrid, AC sources, such as wind turbine, diesel generators, and MT are connected to the DC bus through converters. As no reactive power is present in the DC bus, connected AC sources could run with only active power, which increases the power efficiency and power transfer ability.

- *Higher efficiency.*

With technical development, semiconductor application can be found everywhere, from industrial variable speed motor drive to building lighting, not to mention ubiquitous information technology devices. Appliances based on semiconductors require always the use of DC power. Conversion from AC to DC generally loses 10-25% of energy, depending on various devices and/or their rated power [21]. On the other hand, DC systems do not suffer from skin effect, so thinner cable can be used with improved material efficiency.

To sum up, AC systems may have more advantages in certain high voltage and high power applications, while DC systems would provide advantage for the end-users in low voltage levels.

1.2.2. Research issues on microgrid

As microgrid is initiated using AC voltage, many studies concern the AC microgrid; DC microgrid has not been explored as much as AC microgrid. Despite the studies, microgrid varies from application to application; researches on microgrid can be roughly divided into three groups: control, protection system and devices, and energy management.

1.2.2.1. Control

Microgrid control issues relate different scales from single device to multi-inverter, and may be summarized as follows:

1. *Applying new power components in microgrid.*

With the development of materials, the recent emerged components are proposed for application in microgrids, such as silicon carbide (SiC) based power electronic devices [23] and high frequency transformer [24], with aim of improving conversion efficiency and reducing size of bulky converters.

2. *New topologies of converter or inverter.*

High step-up DC/DC converter are proposed for embracing low DC voltage sources, such as fuel cell and PV panel, to high DC voltage bus without multiple conversion stages [25-27]. In [28], a novel topology integrating DC and AC converter together and economizing 25% of semiconductors is proposed. Quasi Z-source inverter can also be found for microgrid application [29]. These new topologies provide advantages of improving efficiency, reducing cost and increase reliability to fault.

3. *Single inverter control to improve performance and power quality.*

3.1. *Improving power quality.*

Microgrid power quality issues mainly result from grid connection and nonlinear load, both of which introduces harmonic current. Hence, various controllers and control strategies are proposed. Resonant or proportional-resonant (PR) current controller could offer higher harmonic rejection ability at selected frequency, and is widely used for eliminating selective harmonics [30]. Methodology which assesses and optimizes PR current controller is also studied [31]. Sliding mode control is used for low harmonic and high power factor in grid-connected operation [32]. Feed-forward control are also proved effective in improving the waveform quality under nonlinear critical load [33]. Grid voltage unbalance compensation [34] and reactive power compensation [35-36] are often addressed as power quality issues. In [37], the authors proposed H_∞ cascade current-voltage controller to inject balanced clean current to the grid while keeping the nonlinear harmonic currents and unbalanced local load currents locally.

3.2. *Power quality issues due to other application-based configuration.*

In case of supplying both three-phase and single-phase load, a three-phase four-wire configuration must be applied, H_∞ current controller to stabilize neutral point voltage for connecting unbalanced load and/or utility grid [38] is proposed. Voltage fluctuations resulting from variable output power of renewable energy sources are also addressed by D-STATCOM [39].

3.3. *Efforts for improving dynamic control response with classical control techniques.*

Except for control strategy based on complex parameters proposed by most authors, the classic control theory are also used to avoid complex parameter tuning in microgrid control, such as the proportional-integral (PI) controller used in [40].

4. *Multi-inverter power sharing.*

In off-grid operation mode of a microgrid, several sources supply the load at the same time; one important issue is to distribute load power evenly/proportionally with respect of rated power capacity to multi-source. Research proposals on multi-inverter power sharing can be identified into two groups: with communication and without communication. One typical example when communication is required is "master-slave" control; for example, in [41], the master fixes the voltage and frequency in microgrid, while the slaves are current sources. Concerning the second group, without communication, research works have drawn much more attentions because of the low cost and especially "plug-and-play" feature, which means in a microgrid, no need of reconfiguring the system when adding or removing a single energy source. In this case, the control method proposed is called droop control, which is detailed in the next section.

Despite droop control can achieve automatic active and reactive power sharing in microgrid, it is not efficient in harmonic sharing due to grid connection and non-linear load. Recently, harmonic sharing in islanded operation is often addressed [42-43].

On the other hand, droop control algorithm is also affected by grid impedance, it is also necessary to accommodate impedance variation or decouple active and reactive power. Thus, [44] proposed an improved droop controller to achieve accurate proportional load sharing without meeting two rigid requirements of classic droop controller: same per-unit impedance and generating same voltage set-point. Decoupling active and reactive power taking into consideration of both inductive and resistive component of the equivalent output impedance, the current control for active and reactive current sharing is proposed by [45].

5. *Other control issues.*

Other control issues are also involved, such as phase lock loop (PLL) for fast detection of selective individual harmonic [46], PV maximum power point tracking (MPPT) control algorithm for operation in partial shedding condition [47], new topology of parallel converters for reducing capacity of full power converter in wind application [48], controlling power transfer at PCC by tap control of a smart transformer [49], and smoothing renewable production fluctuations by fuzzy logic controller and storage [50].

1.2.2.2. *Protection*

For microgrid it is still necessary to research and develop new fault detection and protection control. Microgrid introduces bidirectional current and the flexible "plug and play" feature makes the

fault current values varies, conventional relays, breakers and other protection devices may not work anymore, new protection algorithm should respond to the issues [51]. Microgrid also, by definition, works in both off-grid and grid-connected mode, so microgrid protection devices are to develop effective protection algorithm to handle the complex working environment [52]. Microprocessor [53] and communication [54-55] are implemented for protection devices to reinforce the complex protection algorithm. Other requirements concern remote measuring [56], protection for small generators [57], or ability of supporting voltage under grid faults [58].

1.2.2.3. Energy management.

Energy management is supposed to manage the power flow in microgrid and power flow exchanged with the utility grid during the grid-connected mode, with the objective of making full use of each source while respecting their constraints on capacity and power; thus, that operation can be optimized and the cost can be reduced, nevertheless, data communication by smart grid is required for overall grid performance enhancement.

The energy management can be classified into rule-based and optimization-based approaches. Rule-based approach manages the system according to prefixed rules, such as simple rule base, multi-agent system [17] and fuzzy logic approaches [18, 59]. Optimization based approach manages the system by mathematical optimization, carried out with objective function and constraints. The optimization methods include the artificial intelligence joint with linear programming [18], linear programming [59] or dynamic programming [60-61], and genetic algorithms [62].

The rule based system is simple and robust, but not guarantee the optimal performance with given operating conditions. Moreover, rules become complex when facing different scenarios. The optimization gives an optimal solution within given constraints and operation condition. Nevertheless, optimization is usually treated as separate problem from the power balancing strategy, and optimization usually requires *priori* information on energy production and energy consumption. Error between the forecast and real condition could result in degradation of optimization performance or even undesired operation that may violate certain constraints, then the system would no longer be able to operate. Hence, requirement is to develop the power balancing and optimization together, and taking into account that, when errors of *priori* information occur, the power balancing strategy should be affected as less as possible.

1.2.3. Droop control

In microgrid studies, droop control has drawn a lot of attentions; its principle and its shortcomings are discussed in this section. Droop control is initially applied to AC systems, but it is also compatible with DC control.

In microgrid, inverters are coupled on the common bus through impedance; as shown in Figure 3.

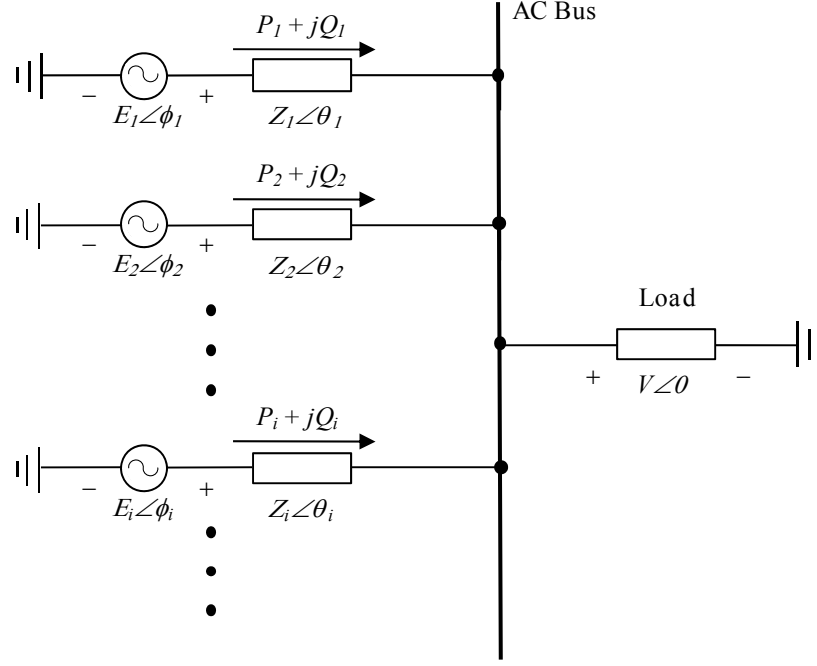


Figure 3. Multi-inverter power sharing scheme.

E_1, E_2, E_i are output root mean square (RMS) voltages of the each inverter, while ϕ_1, ϕ_2, ϕ_i the inverter output voltage phases. Z_1, Z_2, Z_i are inverter output impedance magnitudes while $\theta_1, \theta_2, \theta_i$ are the output impedances phases. The AC bus voltage V is chosen as voltage reference with phase angle at 0. As V is supplied by several converters, it is considered as constant and independent with inverter output. P_i and Q_i are the active and reactive power outputs for each inverter. P_i and Q_i can be calculated as:

$$\begin{cases} P_i = \frac{E_i V}{Z_i} \cos(\theta_i - \phi_i) - \frac{V^2}{Z_i} \cos(\theta_i) \\ Q_i = \frac{E_i V}{Z_i} \sin(\theta_i - \phi_i) + \frac{V^2}{Z_i} \sin(\theta_i) \end{cases} \quad (1.1)$$

$i = \{1, 2, \dots\}$

Considering that output impedance is usually considered inductive predominating, so $Z_i \angle \theta_i = X_i \angle 90^\circ$, where X_i is the predominating inductive impedances magnitude. Equation (1.1) can be simplified as:

$$\begin{cases} P_i = \frac{E_i V}{X_i} \sin(\phi_i) \\ Q_i = \frac{E_i V \cos(\phi_i) - V^2}{X_i} \end{cases} \quad (1.2)$$

$i = \{1, 2, \dots\}$

In steady state operation, ϕ_i is relatively small, and V is considered constant. So (1.2) can be roughly approximated as proportional function [43]:

$$\begin{cases} P_i \sim \phi_i \\ Q_i \sim E_i \end{cases} \quad (1.3) \\ i = \{1, 2, \dots\}$$

Equation (1.3) indicates that inverter output active power and reactive power can be controlled separately by means of adjusting the output phase angle and voltage amplitude respectively.

Then an additional characteristic, described by (1.4), is added to each inverter control so that the load power can be evenly/proportionally shared in an automatic way.

$$\begin{cases} \omega_i^* = \omega_0 - mP_i \\ E_i^* = E_0 - nQ_i \end{cases} \quad (1.4) \\ i = \{1, 2\}$$

where ω_0 and E_0 , are constants representing inverter angular frequency and voltage output at no-load operation, m and n are droop control parameters, ω_i^* , E_i^* are the references of output voltage angular frequency and amplitude respectively to generate the voltage reference signal $\sqrt{2}E_i^* \sin(\omega_i^* t)$.

Thanks to (1.4), each inverter measures its own output active power and reactive power for generating its own voltage reference. According to different load power, every inverter output, *i.e.* voltage and frequency, varies until reaching a steady state that the load power is evenly shared by different sources. The whole process does not need communication between inverters, but droop parameters must be tuned.

Although studies have improved the droop control performance in harmonic sharing and tolerance of impedance variation, limitations still exist.

Firstly, the droop control assumes that every energy source in microgrid has sufficient capacity to output desired power following the load demand. Nevertheless, it is not the case for some sources as PV panel and wind turbine whose output powers change according to environmental conditions, such as the solar irradiance, temperature and wind speed respectively. These output powers cannot change according to load demand. It is difficult for such renewable energy sources to operate in droop mode.

Secondly, the droop control is not suitable for the grid-connected mode. In grid-connected mode, voltage amplitude and frequency are fixed by the grid, so that the droop control that shares power by varying voltage amplitude and frequency no longer works. The multi-inverter power sharing of grid-connected mode still needs communication. As microgrid works in both off-grid and grid-connected mode, the main advantage of droop control of load power sharing among multi-inverter without communication disappears [63]. In grid-connected mode, inverters working as current source mode with communication are preferred [64-66].

Thirdly, constant power devices, such as rectifiers and voltage regulators, can result in dynamic instability of droop-controllers of the inverter [67].

1.3. Objective of the thesis

As an element of future smart grid, microgrid should be developed in both control and energy management considering interactions with smart grid. In literature, the aspects of control and energy management of microgrid are treated separately, and smart grid interaction is merely proposed. In this thesis, a further attempt on systemic study of microgrid control combined with energy management and smart grid messages is provided, aiming mainly at improving penetration level of distributed small PV plant with less impact in grid while optimizing local power.

The studied microgrid is dedicated to tertiary building. As many small PV plant are associated or integrated to buildings that represent a large sector of energy consumption, it is essential to restructure their use and to improve their performance by microgrid[68]. For distributed PV energy, on-site generation through the microgrid can be better scaled to match the power needs of end-users who require specified power services and may more easily accept some load shedding.

The proposed DC microgrid, consisting of power system and control system called “supervision”, is proposed in Figure 4.

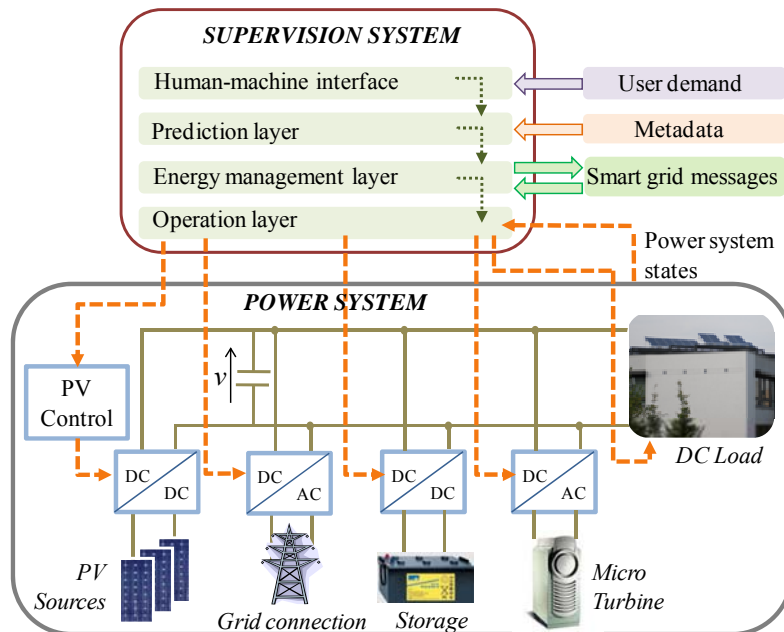


Figure 4. DC microgrid system overview.

The multi-source power system of the proposed DC microgrid is composed of a DC load and four sources: PV array (PVA), utility grid, electrolytic storage and MT. The storage and the utility grid are two reversible sources concerned by power supply and power injection. The utility grid and MT operate in complementary cycle: grid connection is used only in grid-connected mode and MT works only in off-grid mode.

In most of the cases, PVA is controlled by MPPT algorithm, but it can be cut off or controlled to output a constrained power to protect storage from overcharging or to maintain control of grid power injection. Storage and grid connection are used as buffer to cover the gap between the intermittent renewable production and the load demand. Grid connection also ensures continuous and safe supply for critical load, as well as provides the possibility of trading back excess production to grid. Taking into account the aforementioned DC microgrid advantages, the proposed DC microgrid uses DC bus because of following additional reasons: DC feeding is more efficient for low voltage systems for the demand side. Furthermore, mostly 90% of a tertiary building's electrical load is possible to be DC fed in efficiency manner [69] while for the grid side the power factor can be controlled at 1. DC load power is demanded by the end-user, but the supervision system can intervene by load shedding.

To integrate control, optimization and grid interaction together with flexible structure, the supervision system is designed in multi-layer structure, which consists of operation layer, energy management layer, prediction layer and HMI. The basic layer of the supervision is the operation layer. It operates the power system with the primary objectives of power balancing with load shedding, PV constrained control and with respect to power limits imposed by the utility grid in the form of smart grid messages. Energy management layer controls the operation layer with an aim of improving energy efficiency and reducing energy cost, while responding to grid issues, such as peak shaving. Prediction layer predicts load consumption and renewable energy production, which are necessary information (metadata) for optimization in energy management layer. HMI permits interaction with end-users, for whom some energy management criteria could be defined.

The multi-layer structure design provides more flexibility in both software and hardware. Firstly, each layer can be designed to run independently, they are coupled by some variables. By modifying coupled variable values, the upper layer affects the lower layer operation to perform advanced energy management. Secondly, without changing the control structure, the strategy can be put in one or several microcontrollers in order to execute complex algorithm for a large-scale application, which could help form autonomous microgrid groups and facilitate integration with the future smart grid.

Moreover, the supervision subsystem facilitates information exchange with the smart grid; only low speed communication is required. Based on this information, grid adjustment such as direct load management, or peak shaving, can be more easily performed. Following grid adjustment, an optimal local power flow can be achieved.

1.4. Conclusion

The state of the art highlights the complexity of the overall problem of the smart grid, which, in turn, requires the realization of microgrids. The difficulty to define the control of a microgrid for

several strategies leads to deeply analyze the control of specific components the power system and its supervision.

To build a global energy model, adapted to the microgrid operation integrated with the smart grid communication, it is necessary to study and propose appropriate models for each component. For PV sources, a power prediction model is needed that quickly adapts to all weather conditions (solar irradiance and PV cell temperature). Thus, based on the weather forecast, the PVA production can be reliably forecasted. As for the means of electrolytic storage, it turns out that the existing models are more related to aging, health status, and rarely developed for a reliable calculation of their voltage and state of charge for a given current to better control their use over a long period of time (a few hours).

On the other hand, the control of these components is also important to get the best energy performance at a reasonable cost. PV sources are often controlled using tracking methods of the maximum power point (MPP). Several MPPT algorithms are available in the literature, but often having as criterion the maximum power extracted and not the energy of a sufficiently long period of time, such as day. In addition, control of the PV power extracted in a given limit is not yet widespread, probably due to the absence of bidirectional communication with the smart grid. Finally, the supervision, as interface between the microgrid and the utility grid, is not always designed and built to address constraints imposed by the utility grid and act on the load of the microgrid simultaneously.

Therefore, compared to the research studies mentioned above, this thesis on microgrid, is distinguished by integration of the smart grid messages and by adopting the approach of multi-physics and multi-scale system in order to obtain a global response. Limited to DC microgrid applied in urban areas, this systemic approach leads to study the interaction between the microgrid and the utility grid at different time scales involving different types of physical parameters and with different operating modes of operation that meet specific needs.

Another important aspect concerns the optimization of energy costs, taking into account constraints. The requirements are: on one hand, to meet the requirements of the utility grid for limited injection or absorption power, and to meet the DC load ensuring the stability of the DC bus, on the other hand. Another aspect taken into account is to act as a partial load shedding; however, the study of intelligent management of building loads is not done.

The proposed models and related commands on the power system are validated by experimental tests. The coupling between the power system and its supervision is validated by numerical simulation and by experimental tests based on experimental platform whose description is given in the next section.

Chapter II. Power system modeling and control for grid-connected operation

Microgrid operates both in grid-connected mode and off-grid mode. The power balancing control with smart grid interaction in grid-connected operation requires the most consideration in this study. In off-grid mode, MT can be considered as grid connection with reduced transient performance and with only unidirectional power flow. So, the off-grid operation can be seen as a simplified grid-connected case. Hence, in this chapter, the grid-connected operation is studied and analyzed through the behavior of each element in power system to establish an overall strategy adapting to supervision functions.

Firstly, power system control must keep power balancing. It extracts maximum power from PVA and manages the power transfer in order to feed directly the DC load (building), respecting to available storage level and regarding the utility grid connection.

Moreover, required by the DC microgrid integration in the future smart grid, despite power balancing, the power system control must incorporate complex operations such as interacting with the smart grid to respond grid issues such as peak shaving, as well as optimizing local power. The complex operating context demands robust yet simple control strategy, which is able to ensure power balancing, to respond smart grid demand and to embrace local power optimization. To obtain the adequate control algorithm, behaviors of each element are studied based on PN modeling through

identifying possible physical states of the system. Based on the modeling, a power balancing control strategy is established. The PN modeling is then simulated in MATLAB-Simulink with the help of Stateflow toolbox. Simulation and experiment results validate the proposed control strategy.

II.1. Electrical scheme and experimental platform

In the power system of proposed DC microgrid, the PVA, storage and grid are connected to a common DC bus through their dedicated power electronic interface to provide fast power response for power system control. The power electronic interface is composed of a four-leg power converter (B_1 , B_2 , B_3 and B_4) and a set of inductors and capacitors. DC load is connected to the DC bus, as shown in Figure 5, where \mathcal{G} and θ are respectively solar irradiance and PV cell temperature.

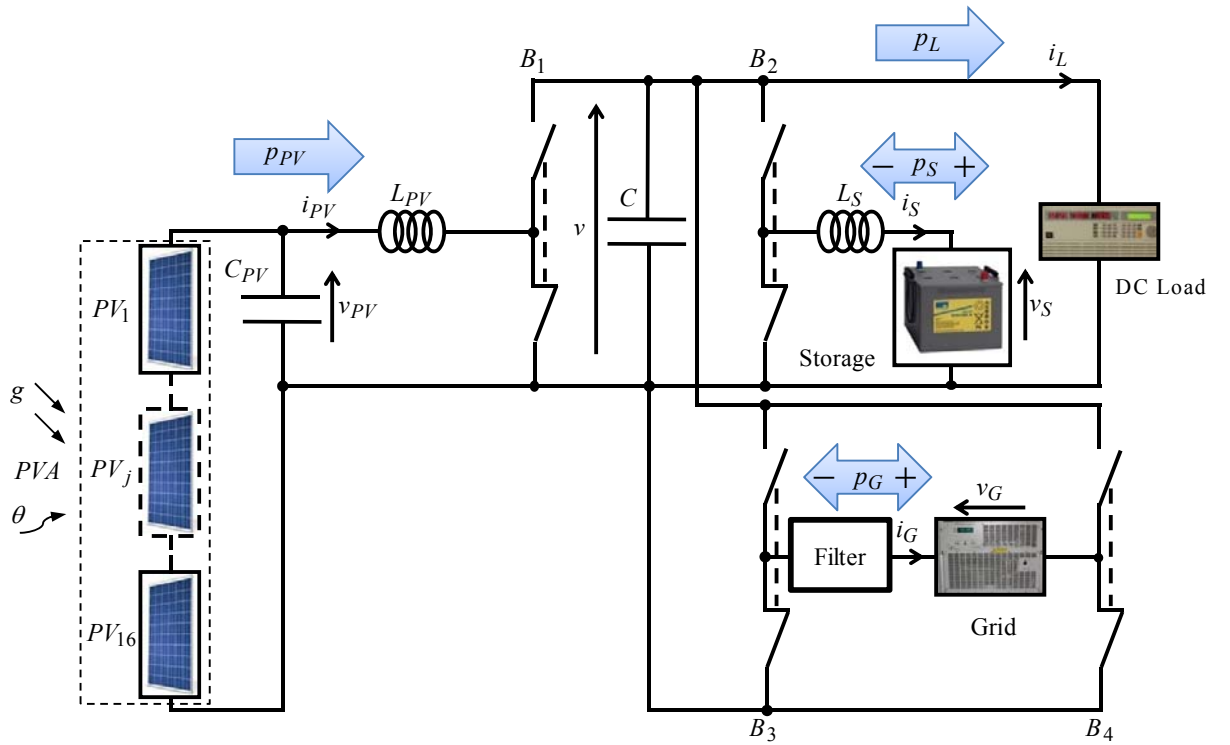


Figure 5. Power system electric scheme.

The DC bus consists of a capacitor C , coupling electrically the DC bus voltage v , the DC load demands power directly from the DC bus. To extract the maximum power from PVA, a boost converter is implemented, consisting of C_{PV} capacitor, L_{PV} inductor and B_1 power converter leg. The storage consists of a set of electrolytic storage cells as a voltage source v_S , and is coupled with DC bus through an inductor L_S and B_2 power converter leg. The utility grid emulator is connected to the DC bus through the B_3 and B_4 power converter legs and a filter. v_{PV} and i_{PV} are PVA output voltage and current. i_S is the storage current and i_L is the load current.

The power flow is shown in Figure 5 with blue flashes. The following sign conventions for power flow are assumed:

- for the two reversible sources (grid and storage), grid power p_G and storage power p_S , the positive value means to receive power and negative value means to supply power;
- for load power p_L and the PVA power p_{PV} , they are always considered positive.

Regarding the grid control, no reactive power control is involved: grid current i_G is always controlled in phase or in opposite-phase with grid voltage v_G . The synchronization between i_G and v_G is achieved by PLL [70]. The powers are calculated by multiplying corresponding voltage with current, *i.e.* $p_{PV} = v_{PV} \cdot i_{PV}$, $p_S = v_S \cdot i_S$, $p_G = v_G \cdot i_G$ and $p_L = v \cdot i_L$.

The proposed power system control is associated with our laboratory scale experimental platform, which has been installed in Centre Pierre Guillaumat 2 of our university. PVA consists of 16 PV panels. Storage uses a set of lead acid battery. Grid connection is emulated by reversible AC voltage sources and the DC load is emulated with programmable DC electronic load. The proposed 4-leg power converter is based on IGBTs (Insulated Gate Bipolar Transistor) with commutation frequency at 10kHz. The controller is dSPACE 1006. The picture of the experimental platform is given in Figure 6.



Figure 6. Experimental platform.

The platform specifications are given in Table 1. Concerning the PVA, current and voltage are given for the maximum power point (MPP) at the standard test conditions (STC). The technical specifications of used PV panel and storage unit are given respectively in Annex 1 and in Annex 2.

Table 1. Principal element detail of power system for experimental test.

Element	Parameter	Device
Storage (serial 8 battery units)	96V/130Ah	Battery unit: Sonnenschein Solar S12/130 A
PVA (16 PV panel in series)	$I_{MPP} = 7.14A$ $V_{MPP} = 280V$	PV panel: Solar-Fabrik SF-130/2-125
	}STC	
Grid emulator	3kVA	Bidirectional linear amplifier (Puissance+)
Programmable DC electronic load	2.6kW	Chroma 63202
Controller board		dSPACE 1006
Power electronic converter	600V-100A	SEMIKRON SKM100GB063D

II.2. Functions of the power system control

As aforementioned, the DC microgrid requires the following functions: power balancing, interacting with the smart grid, and optimizing power flow. The three aspects must be considered and integrated in the control strategy.

II.2.1. Power balancing

Neglecting the power loss in the conversion, the power must be balanced as:

$$p_{PV} = p_G + p_S + p_L \quad (2.1)$$

PVA power p_{PV} changes with solar irradiance and temperature. Load power p_L changes according to building's power demand. Powers p_G and p_S can be controlled by giving corresponding current control reference, i_G^* and i_S^* . Grid and storage should balance the power error between production and consumption by means of stabilizing DC bus voltage v . To stabilize v , the required power p^* is defined by (2.2):

$$\begin{cases} p^* = p_{PV} - p_L - C_p(v^* - v) - C_i \int (v^* - v) dt \\ p^* = p_G^* + p_S^* \end{cases} \quad (2.2)$$

with v^* the DC bus voltage reference, C_p proportional gain and C_i the integral gain. The power reference p^* is the output of the controller for stabilizing the DC bus voltage. The power reference p^* must be distributed to grid and storage. Thus, storage power reference p_S^* is calculated mainly according to a distribution coefficient K_D as in (2.3),

$$p_S^* = K_D \cdot p^* \quad (2.3)$$

The distribution coefficient K_D is constrained between 0 and 1, although other values still work. The reason is as follows: PV feed-in tariffs are still incentives, nowadays, grid charged storage and

grid power injection by storage are forbidden by almost all power providers. In this study, it is assumed that the energy storage does not inject power into the grid. So, constraining K_D between 0 and 1 makes sure that power grid injection is only from PVA production. Grid power reference is obtained as in (2.4),

$$p_G^* = p^* - p_s^* \quad (2.4)$$

The distribution coefficient K_D describes the power distribution between grid and storage for a general case; however, special situations must be taken into consideration. In those cases, powers p_G^* and p_s^* must be modified according to their corresponding limits, either physical or imposed, resulting in extra power balancing considerations, which are detailed in the subsequent PN modeling study.

II.2.2. Smart grid interaction

DSM exists already and is expected as one important feature of future smart grid. The term demand side management is used in a loose way by different people across the world. It is either a narrow definition concerning only energy efficiency [71], such as retrofit of building by more efficient appliances, or a broad range concerning energy efficiency, TOU tariff, market demand response, physical demand response and spinning reserve [72]. However, the main goal is the same: using the load as an additional degree of freedom to improve the overall efficiency in the grid.

Despite energy efficiency, DSM refers to modifying end-users' energy demand through various ways, either explicit orders or financial incentives, such as demand response (DR) and TOU tariff. Since the grid supply capability is built not only to satisfy the peak consumption but also to provide supplementary security margin for unforeseen events, by simply reducing peak consumption, DSM can significantly reduce the need for expensive new generation, transmission and distribution to satisfy peak demand. It has been reported that a small reduction of demand by 5% could have been resulted in a 50% price reduction during California electricity crisis in 2000-2001 [73]. As well, it greatly reduces peak energy price and volatility of price in the electric market. Figure 7 shows how the load decrease ability can reduce electric market price in peak supply.

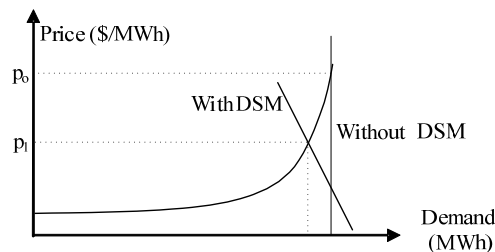


Figure 7. Simplified effect of DSM on electricity market prices [74].

This phenomenon is due to the fact that generation cost increases exponentially near maximum generation capacity. A small reduction in demand will result in a big reduction in generation cost and

in turn a reduction in price of electricity. In this example, original demand curve is represented by a vertical line because it is assumed that the system is without DSM. DSM programs induce a negative slope on the original demand curve leading to small deduction in demand and a huge reduction in price. To sum up DSM advantages, simply reducing or shifting peak consumption is much less expensive than building new power plants and introducing energy storage.

DR is referred to affecting the load using an explicit signal, broadcasted by transmission or distribution system operators. Most of the time, the signal is not necessarily instantaneous, which may refer to a situation for next day [72]. It is performed for three reasons: emergency, economic and ancillary services. Currently, it mainly refers to mechanisms used to encourage consumers to reduce demand. Nevertheless, DR can be used to increase load demand in case of high production and low demand as well. Arbitrage between periods of low and high demand (or low and high prices) for energy storage is also encouraged by some systems.

Current DR schemes are implemented with large and small commercial as well as residential end-users by different means as direct grid operator control, special contract, voluntary response to signals or bidding for curtailing power supply access at attractive prices. Dedicated control systems handle the signal to shed loads (lighting appliances, machines, air conditioning) according to a preplanned load prioritization scheme.

TOU tariff is also a useful mean to perform peak shaving. It can also be found with most power suppliers at present. It refers to the energy tariff variations *versus* time: energy price is more expensive in peak hours than in off-peak hours. So, the end-users are encouraged to shift uncritical load in the off-peak hours. Energy consumption for both peak hours and off-peak hours is recorded separately to calculate the energy invoice. It requires a meter able to respond to grid switching signals between peak and off-peak. In the case of energy dynamic pricing, expected in the coming years, a smart meter should be designed and implemented; its main ability is linked to the smart grid communication that is supposed to transmit messages concerning energy tariffs.

Another issue of the current utility grid is linked to the power injection from distributed renewable sources. Thus, due to intermittency and fluctuation characteristics of renewable production, considerations must be taken to handle injection problems facing future high-level penetration of renewable sources. Volatile renewable productions can result in new challenges in the grid for power balancing and stability problems [75-79]. Hence, it is also essential for DSM to regulate the injected power.

To perform DSM, different technologies, especially communication, are necessary. Hence, the future smart grid communication is considered and involved in the proposed microgrid to provide capability for grid regulation in both supply and injection cases. The dynamic mechanism is proposed in forms of smart grid message, which are both proposed as explicit orders, in forms of grid power limits, for both supply and injection. TOU tariff is also included. Hence, the microgrid should use grid power following the limits transmitted by the message, as well as optimize power flow to reduce

energy cost. In addition, the proposed microgrid should be able to inform the utility grid of power demand and injection forecasts.

II.3. Power system modeling considering constraints

In order to analyze the system with a goal of establishing the overall control strategy, the modeling and simulation are necessary. The described global system can be seen as a hybrid dynamical system defined as system with continuous-time dynamics interacting with discrete-event dynamics. The hybrid behavior consists of continuous-time power system behavior controlled by discrete logic/event like circuits switching and supervision system outputs. Therefore, the behavioral modeling of global system is proposed by means of interpreted PN formalism [80-81] which is a powerful graphical and mathematical tool for describing and analyzing different hybrid dynamical systems. Thus, interpreted PN modeling is used to split continuous element behavior into discrete states, permitting a bottom up modeling to facilitate the design of overall control strategy by studying each detailed discrete state. Control functions are then studied and integrated into each discrete state.

The simulation of power system control has a hybrid aspect. The continuous and discrete aspects coexist and interact with each other. The power system components behave with continuous dynamics while the control strategy by PN modeling behaves in a discrete way. In order to perform numerical hybrid simulation tests, Simulink and Stateflow development in MATLAB environment are proposed.

Simulink helps to model the continuous dynamics of the system and Stateflow is used to specify the discrete control logic and the modal behavior of the system. Stateflow design language is based on the concept of hierarchical automata from Statecharts [82] and allows developing PN model through the approximation made between states/places and switching/firing transitions conditions.

Thus, in this section, at the same time of PN modeling, Stateflow modeling is given, which permits simulating the PN model in MATLAB-Simulink environment.

II.3.1. Introduction to Petri Nets modeling

Carl A. Petri proposed for the first time in 1962 a net-like mathematical tool, called Petri Net, for the study of communication with automata. Wide PN application areas are found in performance evaluation, communication protocols, discrete-event systems, flexible manufacturing/industrial control systems, digital filters, asynchronous circuits and structures.

PN are a powerful graphical and mathematic tool providing a uniform environment for modeling, formal analysis, and design of discrete event systems. With the same PN model, behavioral analysis, discrete event simulator and controller design as well as performance evaluation can be accomplish [83]. Moreover, unlike other tools, PN have an exact mathematical definition of their execution

semantics, with a well-developed mathematical theory for process analysis. It is possible to set up state equations, algebraic equations, and other mathematical models governing the behavior of systems [84].

To quickly summarize, a PN is defined as a five-tuple: $PN = \langle P, T, F, W, M_0 \rangle$ where:

$P = \{p_1, p_2, \dots, p_m\}$ is a finite set of places,

$T = \{t_1, t_2, \dots, t_n\}$ is a finite set of transitions,

$F \in (P \times T) \cup (T \times P)$ is a set of arcs (flow relation),

$W : F \rightarrow \{1, 2, 3, \dots\}$ is weight function that assigns a weight to each arc,

$M_0 : F \rightarrow \{1, 2, 3, \dots\}$ is the initial marking,

$P \cap T = \emptyset$ and $P \cup T \neq \emptyset$.

Hence, a PN graphic contains four kinds of objects: place (state variable), transition (state transformer), token (indicator for active state) and arc. The directed arcs connect places and transitions and arc weight indicate the token flow when transition is fired. A transition can be enabled if its upstream or input places have enough tokens according to corresponding arc weights. An enabled transition may fire at any time. As interpreted PN, each transition could have conditions related to it, and transition is fired only if the transition is enabled and its conditions are satisfied. When fired, the tokens in the input places are moved to output places, according to arc weights and place capacities. Starting with an initial marking, given by initial tokens in places, the graph-based structure simulates the dynamic behavior of a system by continuously firing enabled transitions. Many static and dynamic properties of a PN may be mathematically proven.

The basic concepts of PN is illustrated by a simple PN example for the case of the following well known chemical reaction $2H_2 + O_2 \rightarrow 2H_2O$, given in Figure 8.

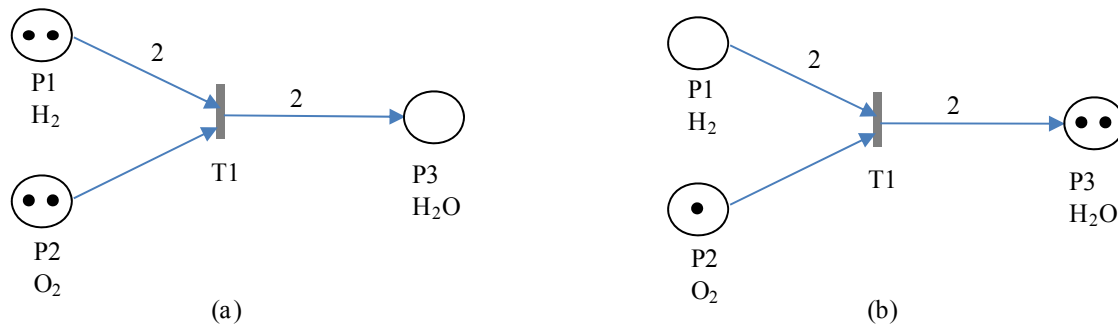


Figure 8. PN example: (a) marking before firing the enabled transition T1; (b) marking after firing T1.

The PN model includes the following elements:

- places: graphically presented by circles, corresponding P1, P2 and P3,
- transitions: graphically bars, T1,
- directing arcs: graphically flashes,
- arc weights: numbers over flashes,
- marking: graphically token within places.

Places occupied by tokens are interpreted as indicating state of the system or available resources in the system. As aforementioned, an enabled transition may or may not be fired, depending on the additional firing condition related to the transition. For example, firing condition relating to T1 may be a high temperature. The transition is enabled with enough token presented in input places in Figure 8 (a), but cannot be fired while the transition condition is not satisfied. Firing transition T1 means removing tokens in input places, whose number depends on the arc weight, and adds tokens to output places whose number also depends on the corresponding arc weight, as shown in the Figure 8 (b). After firing, the system status change.

Concerning the microgrid modeling study, the directed arcs weight is considered to be one. Furthermore, the basic analysis of PN models is not necessary to be detailed and presented in this modeling study. However, regarding the PN models presented below, based on place-invariants and transition-invariants, we note that the structural verification proves that each model is live (there exists an initial marking for which the PN is live), bounded (tokens limitation for all initial marking), and without deadlocks or conflicts.

II.3.2. Smart grid interaction modeling

As aforementioned, on one hand the microgrid should respond to smart grid issues, such as performing peak shaving and avoid unwanted injection. On the other hand, the microgrid must optimize energy cost. Hence, it is assumed that the smart grid informs microgrid at different times about the grid operating parameters: peak hours, energy price, grid usage limitations, *i.e.* limits for grid power supply $P_{G_S_LIM}$ and grid power injection $P_{G_I_LIM}$. This communication is modeled with a timed interpreted PN represented by two places (P0, P1) and two transitions (T1, T2), as illustrated in Figure 9.

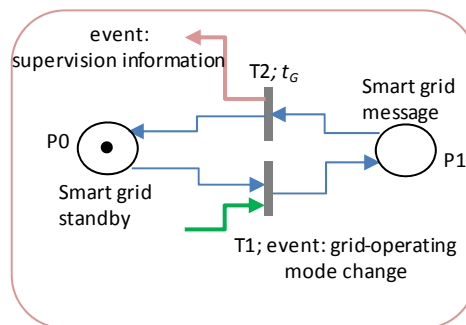


Figure 9. Smart grid interaction modeling by PN.

In different grid-operating mode, the powers that users can demand from or inject to the grid are different, resulting in different operating strategy design considerations.

Thus, the place P0 represents the smart grid in a standby mode and the place P1 is reached when the smart grid message is sent out to inform end-users of grid-operating mode change. This event is

the firing condition associated with the transition T1. After the t_G time, which could be measured in minutes or hours, from the arrival of the token in place P1, the transition T2 can be fired and the supervision system is informed of the switching operating mode instant. Once the supervision system is advised about the grid-operating mode, it controls the multi-source power system according to the transmitted grid-operating mode and with respect to other elements behavior.

II.3.3. Grid-operating mode modeling

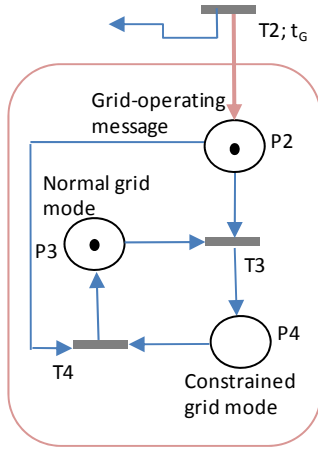
In order to illustrate the differences between grid-operating modes, it is firstly assumed that the load has P_{L_MAX} as contractual subscribed power, and PVA has P_{PV_P} as maximum or "peak" power at STC. Both of them are positive constant values.

The values of $p_{G_S_LIM}$ and $p_{G_I_LIM}$ are imposed by the smart grid message and determine the grid-operating mode. Grid power p_G is separated for supply power p_{G_S} and injection power p_{G_I} . Hence, it is defined $0 \leq p_{G_S} \leq p_{G_S_LIM}$, with $p_{G_S_LIM} \leq P_{L_MAX}$ and $0 \leq p_{G_I} \leq p_{G_I_LIM}$, with $p_{G_I_LIM} \leq P_{PV_P}$.

As renewable energy benefits incentive feed in tariff, power injection into the utility by storage is forbidden for abusive benefits. So, it is assumed that the storage energy is not used for injection into the grid. Two grid-operating modes are considered:

- *normal grid mode*: the load may demand maximum power P_{L_MAX} from grid, and the microgrid may inject maximum power into the grid, $p_{G_S_LIM} \geq P_{L_MAX}$ and $p_{G_I_LIM} \geq P_{PV_P}$. So, during this mode, both grid supply and injection powers are not limited. The grid is always able to supply the load, and it is controlled to cooperate with storage supply. On the other hand, the grid power injection can absorb total PVA power.
- *constrained grid mode*: the smart grid message constrains the grid usage as $p_{G_S_LIM} < P_{L_MAX}$ and $p_{G_I_LIM} < P_{PV_P}$. During grid constrained mode, the grid power should respect both supply and injection limits. Once the calculated reference power p_G^* exceeds supply or injection limits, p_G^* is constrained to the corresponding limit. If grid power is constrained, the load power demand may suffer a shortage of power supply and should be constrained to ensure power balance in the system.

The discrete states of the grid connection given as interpreted PN model is shown in Figure 10.



Name	Description
P2	grid-operating message after t_G
P3	$p_{G_S_LIM} \geq P_{L_MAX} \ \& \ p_{G_I_LIM} \geq P_{PV_P}$
P4	$p_{G_S_LIM} < P_{L_MAX} \ \text{or} \ p_{G_I_LIM} < P_{PV_P}$

Figure 10. Grid discrete state modeling by interpreted PN.

As the smart grid gives information about the grid-operating mode, this message is an event associated with the T2 transition as described earlier. Moreover, the switching operating mode event will occur after the time t_G . In this model, the T3 and T4 firing conditions are given only by the token presence in upstream places.

The Stateflow model of the grid operation modes and the transition conditions are illustrated in Figure 11.

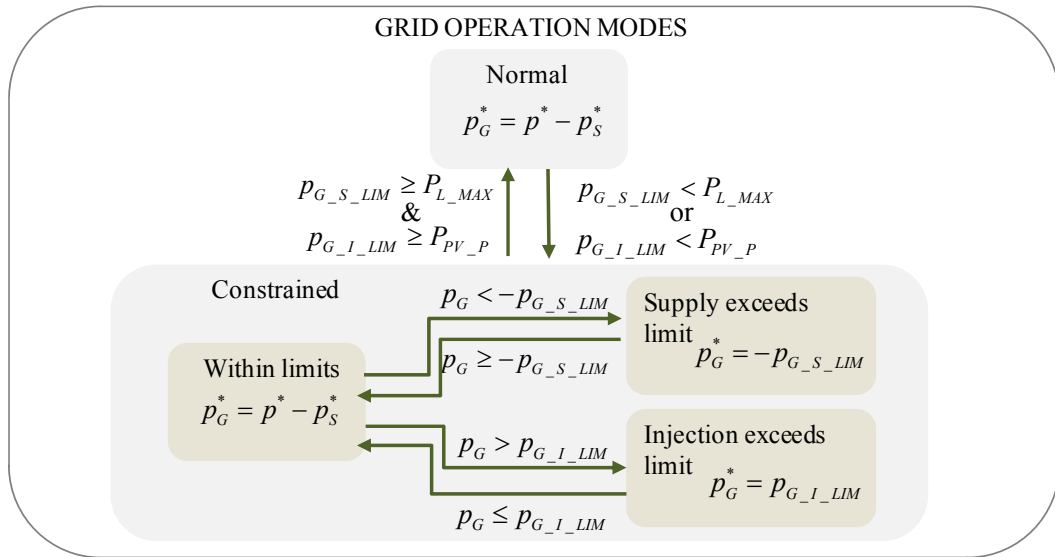


Figure 11. Grid behavior Stateflow model.

II.3.4. Storage-operating mode modeling

As storage capacity is limited, storage state of charge soc , indicating the storage charging level ranging from 0%-100%, is an important parameter to avoid storage damage by overcharging and overdischarging. The storage is able to charge/discharge when the soc is in normal range $SOC_{MIN} \leq soc \leq SOC_{MAX}$, with SOC_{MIN} and SOC_{MAX} representing respectively the minimum and maximum soc limits for batteries operation. Many complex soc calculation algorithms proposed

using Extended Kalman Filter, H_∞ observer and neural network [85-88], however, these methods depend on parameters that are difficult to tune. A simplified soc calculation [89] is implemented by (2.5), which is robust yet satisfies the requirement of the supervision control:

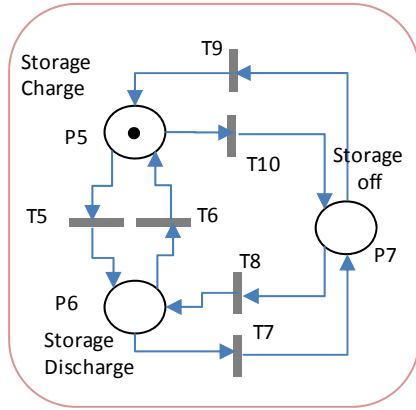
$$soc = SOC_0 + \frac{1}{3600 \cdot v_s \cdot C_{REF}} \int p_s \cdot dt \quad (2.5)$$

with C_{REF} as storage nominal capacity (Ah), v_s as storage voltage and SOC_0 as initial soc .

The storage charging is done only by PVA production. There are three storage-operating modes: charge, discharge and turn off.

- *Charge mode.* During charge, before the SOC_{MAX} is reached, the storage power should be controlled following K_D , which is supposed to be determined and transmitted by energy management layer, to balance power in the system, as $p_s^* = K_D \cdot p^*$.
- *Discharge mode.* During discharge, before the SOC_{MIN} is reached, the storage power should be controlled following K_D given by energy management layer, to balance power in the system, as $p_s^* = K_D \cdot p^*$.
- *Turn off mode.* This mode is activated when reaching SOC_{MIN} in discharge case or SOC_{MAX} in charge case. If necessary, it is also possible to send an order “turn off” by supervision system. When SOC_{MAX} is reached, the storage should be protected from overcharge. So, in case of positive power reference p^* , the storage power reference p_s^* should not be calculated according to K_D , but to be modified as $p_s^* = 0$. In case of discharge when SOC_{MIN} is reached, $p_s^* = 0$ as well. In case of $p^* = 0$, the grid is supposed to supply or absorb the necessary power, without respecting K_D value. This is why in grid operation, grid power is calculated by $p_G^* = p^* - p_s^*$ instead of $p_G^* = (1 - K_D) p^*$.

The interpreted PN model of discrete states of storage and definitions of places and transitions firing conditions are shown in Figure 12.



Name	Description
P5	Charge mode
P6	Discharge mode
P7	Turn off mode
T5	$soc > SOC_{MIN} \ \& \ p_{PV} < p_L$
T6	$soc < SOC_{MAX} \ \& \ p_{PV} > p_L$
T7	$soc \leq SOC_{MIN}$ or “turn off” order
T8	$soc > SOC_{MIN} \ \& \ p_{PV} < p_L$
T9	$soc < SOC_{MAX} \ \& \ p_{PV} > p_L$
T10	$soc \geq SOC_{MAX}$ or “turn off” order

Figure 12. Storage discrete state modeling by interpreted PN.

The Stateflow model of the storage operation modes and the transition conditions are illustrated in Figure 13.

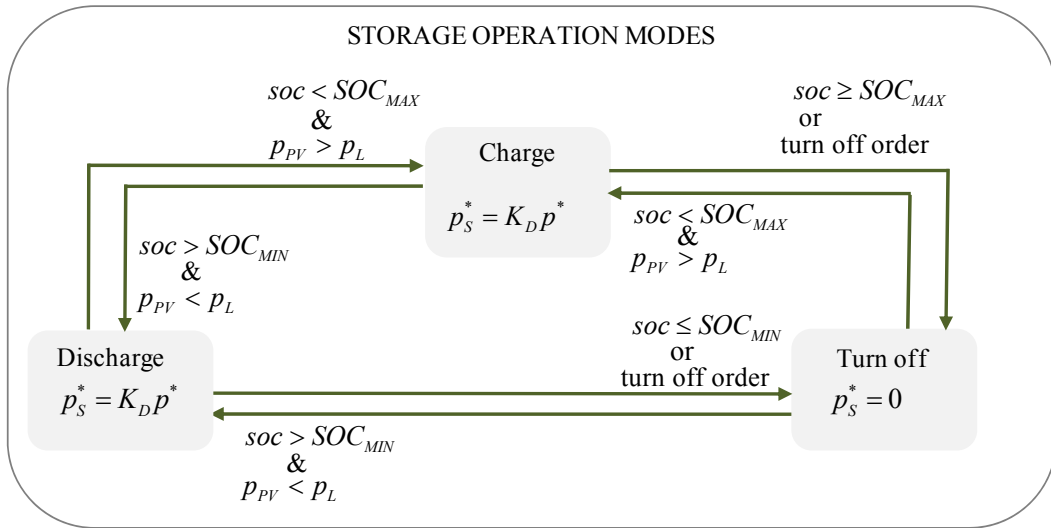


Figure 13. Storage behavior Stateflow model.

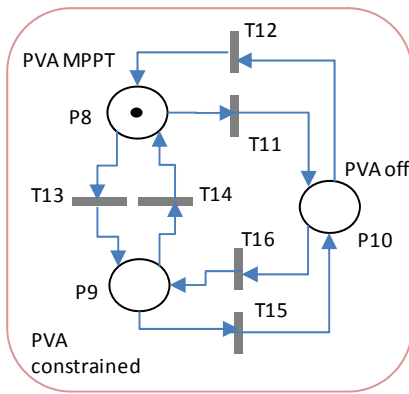
II.3.5. PVA-operating mode modeling

In order to operate a PVA at its MPP, however the solar irradiance and PV cell temperature varies, a MPPT method is needed to find and maintain the maximum power. Many MPPT methods have been proposed and reported in literature [90-93]. Two direct algorithms are commonly used to track the MPP: Perturb & Observe (P&O) and INcremental Conductance (INC). They act in real time either on the voltage reference or on the current reference, corresponding to the maximum power provided by the PV system. In [94], these two algorithms, are experimentally compared, for strictly the same given set of conditions, and it is shown that both MPPT energy efficiency of the proposed algorithms are very similar. In this study, we are interested in P&O MPPT strategy.

Three PVA-operating modes are considered:

- *Off mode.* When there is no enough solar irradiance, $g < G_{MIN}$, or no power demanded by the other elements, PVA is turned off, so $p_{PV} = 0$. The minimum of solar irradiance, G_{MIN} (W/m²), represents the least level for which the $p_{PV} \neq 0$.
- *MPPT mode.* With solar irradiance and power demand, the PVA is supposed to operate with MPPT algorithm to produce MPPT power as $p_{PV} = p_{PV_MPPT}$.
- *Constrained mode.* In case of grid injection limitation $p_{G_I_LIM} < P_{PV_P}$, the PVA constrained mode may occur and must be considered. It happens when storage is full and the PVA produces more power than the load demand plus grid injection limit. PVA must be able to limit output power to the just needed power represented by PVA limiting power p_{PV_LIM} , instead of outputting the MPPT power p_{PV_MPPT} . PVA limiting power p_{PV_LIM} is constrained by the supervision control by giving $p_{PV_LIM} = p_L + p_{G_I_LIM}$. Hence, it involves an adequate PVA power limiting algorithm.

Thus, the interpreted PN model of discrete states of PVA and definitions of places and transitions firing conditions are shown in Figure 14.



Name	Description
P8	$p_{PV} = p_{PV_MPPT}$
P9	$p_{PV} = p_{PV_LIM}$
P10	$p_{PV} = 0$
T11	$g < G_{MIN}$ or $(p_L = 0 \ \& \ soc = SOC_{MAX} \ \& \ p_{G_I_LIM} = 0)$
T12	$g \geq G_{MIN} \ \& \ p_{PV} < p_L + p_S + p_{G_I_LIM}$
T13	$g \geq G_{MIN} \ \& \ p_{PV} > p_L + p_{G_I_LIM} \ \& \ soc \geq SOC_{MAX}$
T14	$g \geq G_{MIN} \ \& \ p_{PV} < p_L + p_S + p_{G_I_LIM}$
T15	$g < G_{MIN}$ or $(p_L = 0 \ \& \ soc = SOC_{MAX} \ \& \ p_{G_I_LIM} = 0)$
T16	$g \geq G_{MIN} \ \& \ p_{PV} > p_L + p_{G_I_LIM} \ \& \ soc \geq SOC_{MAX}$

Figure 14. PVA discrete state modeling by interpreted PN.

The Stateflow model of the PVA operation modes and the transition conditions are illustrated in Figure 15.

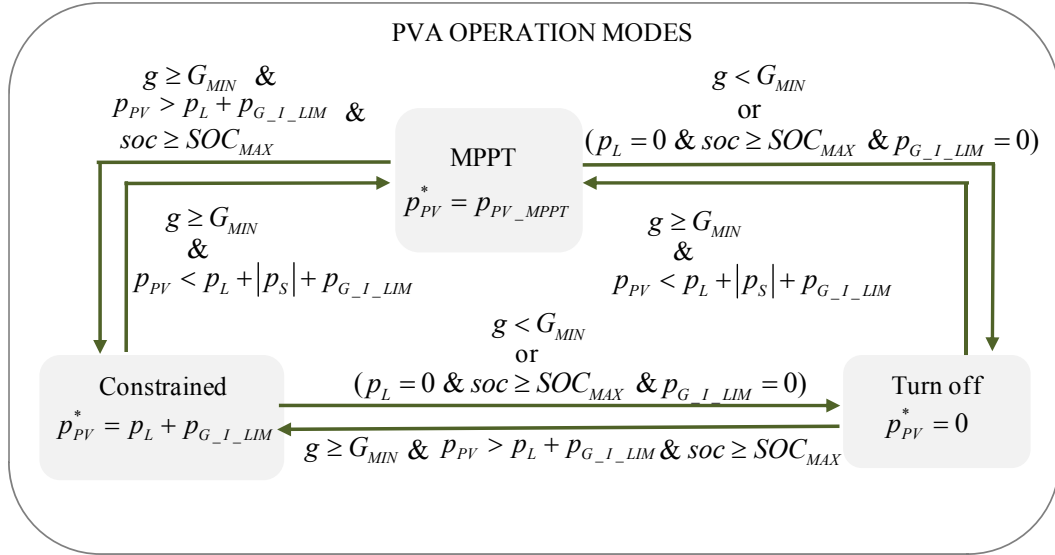


Figure 15. PVA source behavior Stateflow model.

II.3.6. Load-operating mode modeling

The DC load consists of critical load and interruptible load. The critical load requires a continuous power supply, such as computers. The interruptible load can be shed temporarily, such as cooling and heating appliances. Some lighting can also be partially shed. As the load is mainly demanded by the end-user, the power system can only control the load by load shedding. To keep safe supply for the critical load, the power system control can send load shedding signal to disconnect some appliances; therefore, load power demand can only reach a limited power level p_{L_LIM} . In order to describe the limit imposed to the load, despite system scale for different building applications, the load shedding coefficient $K_L = p_{L_LIM} / p_{L_MAX}$ is defined. Many values of K_L could be physically possible, with $K_L \in [0,1]$.

Two load-operating modes are considered.

- *Normal load mode.* The load can demand the maximum power p_{L_MAX} , $0 \leq p_L \leq p_{L_MAX}$; so, load shedding is not needed, so $K_L = 1$.
- *Constrained load mode.* According to smart grid messages, in the case when storage is empty and grid supply is constrained, the demanded load power cannot reach p_{L_MAX} ; its evolution is only within a limited power as $0 \leq p_L \leq p_{L_LIM}$. Therefore, if $p_L > p_{L_LIM}$, the microgrid control must turn off part of the DC load, resulting in load shedding. The power limit p_{L_LIM} refers to the case that when the storage is empty, the capacity of supplying the load by PVA production and grid maximum supply. Therefore, $p_{L_LIM} = p_{PV} + p_{G_S_LIM}$.

Then, the power system compares the current load demand with p_{L_LIM} , if the load demand is greater than the limit, the load should be shed. Therefore, K_L changes according to the available energy for supplying the load as $K_L = (p_{PV} + p_{G_S_LIM})/P_{L_MAX}$.

The interpreted PN model of discrete states of storage and definitions of places and transitions firing conditions are shown in Figure 16.

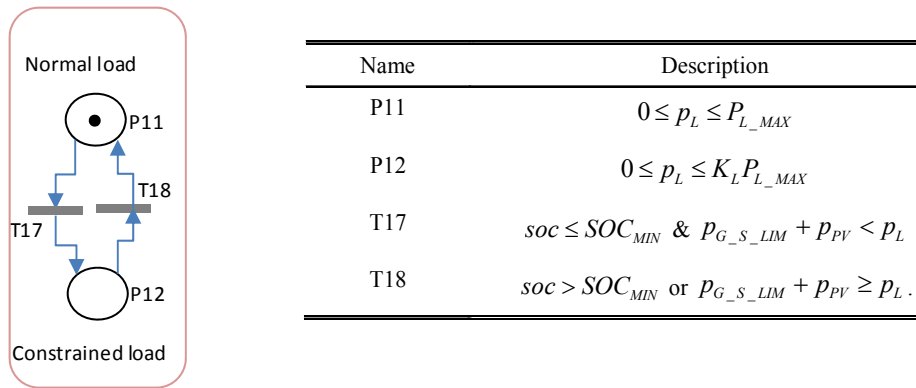


Figure 16. Load discrete state modeling by interpreted PN.

The Stateflow model of the load operation modes and the transition conditions are illustrated in Figure 17.

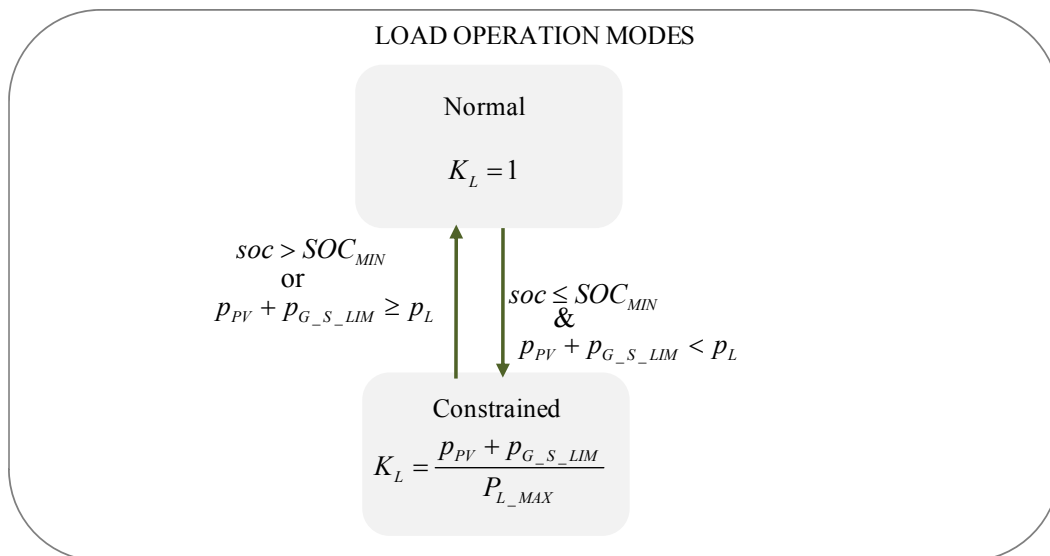


Figure 17. Load behavior Stateflow model.

II.3.7. Power system global behavior by interpreted PN modeling

The power system global behavior obtained by interpreted PN modeling with smart grid communication is presented in Figure 18.

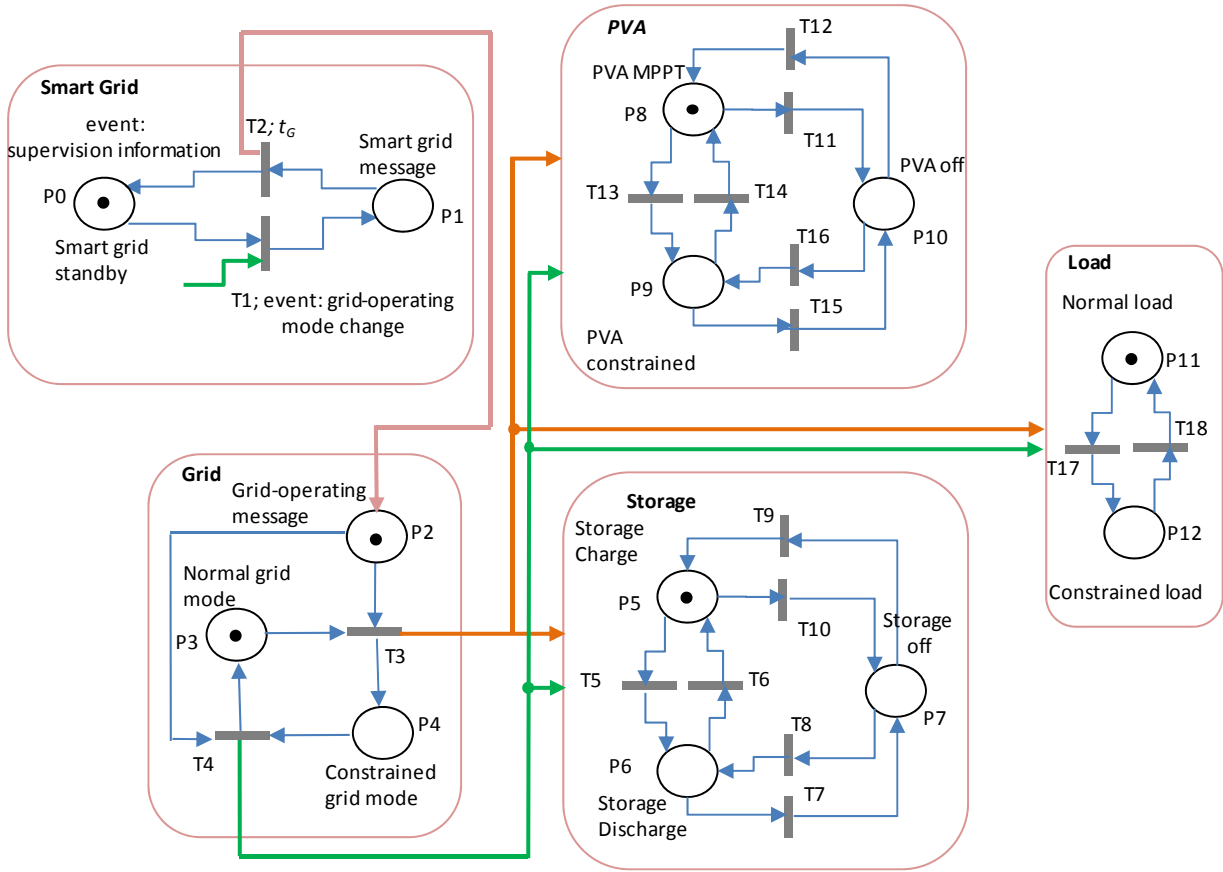


Figure 18. Energy management communication modeling by interpreted PN.

Supposing that PVA is in MPPT operating mode, the storage is in charge mode, and the power provider is sending message to announce the grid-operating mode. Therefore, T1 transition is fired and a token arrives in place P1. After t_G time, the T2 is fired and P2 wins a token and validates T3. This is exactly the grid-operating mode switching instant.

Thus, the place P4 is occupied by a token and grid power limits $p_{G_S_LIM}$ and $p_{G_I_LIM}$ are given. The algorithm in charge of power balancing control considers these values. Concerning the load, that could be possible, but not immediately required, to switch in constrained mode. This happens only if the T17 firing conditions, $soc \leq soc_{MIN} \& p_{G_S_LIM} + p_{PV} < p_L$, are true. In this case, the operation layer transmits the coefficient K_L to main circuit breaker or to demand controller device to shed loads.

The interpreted PN modeling helps better analyze and understand the phenomena and modes of operation that have to be considered in the design of the supervision, and to validate a comprehensive approach that permits analyzing relations between different discrete states by numerical simulation.

Therefore, a set of minimum requirements can define the supervision's design:

- Limits imposed by the utility grid, $p_{G_S_LIM}$ and $p_{G_I_LIM}$, have to be taken into account.
- Distribution coefficient K_D has to be an optimization results whose objective function is the global energy cost minimization. This optimization is under constraints that are related to:

energy tariff, TOU, grid power limits, real SoC of storage, power required by the load in real time, load shedding level accepted by the customer.

- Grid power and storage power references, p_G^* and p_S^* , have to be calculated.
- PVA has to be controlled following a MPPT method but also with a constrained algorithm with respect to a limited output power; so, the PVA power limiting reference $p_{PV_LIM}^*$ has to be calculated.
- Load shedding coefficient K_L has to be calculated and transmitted to the shedding device.

As already mentioned, thanks to the interpreted PN modeling transferred to the Stateflow tool of MATLAB-Simulink, power system behavior simulation, that allows validation before experimental tests, can be obtained. For this, an algorithm that allows control powers balancing, as modeled above, is needed.

II.4. Power system control strategy

The power system behavior modeling leads to the whole control strategy design, which concerns the power balancing, load shedding, PVA power limiting and imposed limits by the utility grid. To obtain a real time control, power system elements must be ranged in specified sequence and an algorithm could be obtained. Hence, the continuous dynamics of the system are operated through an implemented algorithm that calculates power system references with respect to imposed limitations and gives the load shedding level. This algorithm focuses on the power system control strategy.

II.4.1. Control algorithm

In order to describe the overall vision of the power system operation, Figure 19 presents the power system control algorithm flowchart and the load shedding management.

According to this algorithm, taking into account the electric status of the power system, the power flow in the power system can be affected by three external variables:

- K_D , distribution coefficient for distributing power between the grid and the storage,
- $P_{G_S_LIM}$, grid power supply limit from the smart grid message,
- $P_{G_I_LIM}$, grid power injection limit from the smart grid message,

With respect of the priorities of load shedding, the final value of K_L is fixed following the algorithm shown in Figure 19.

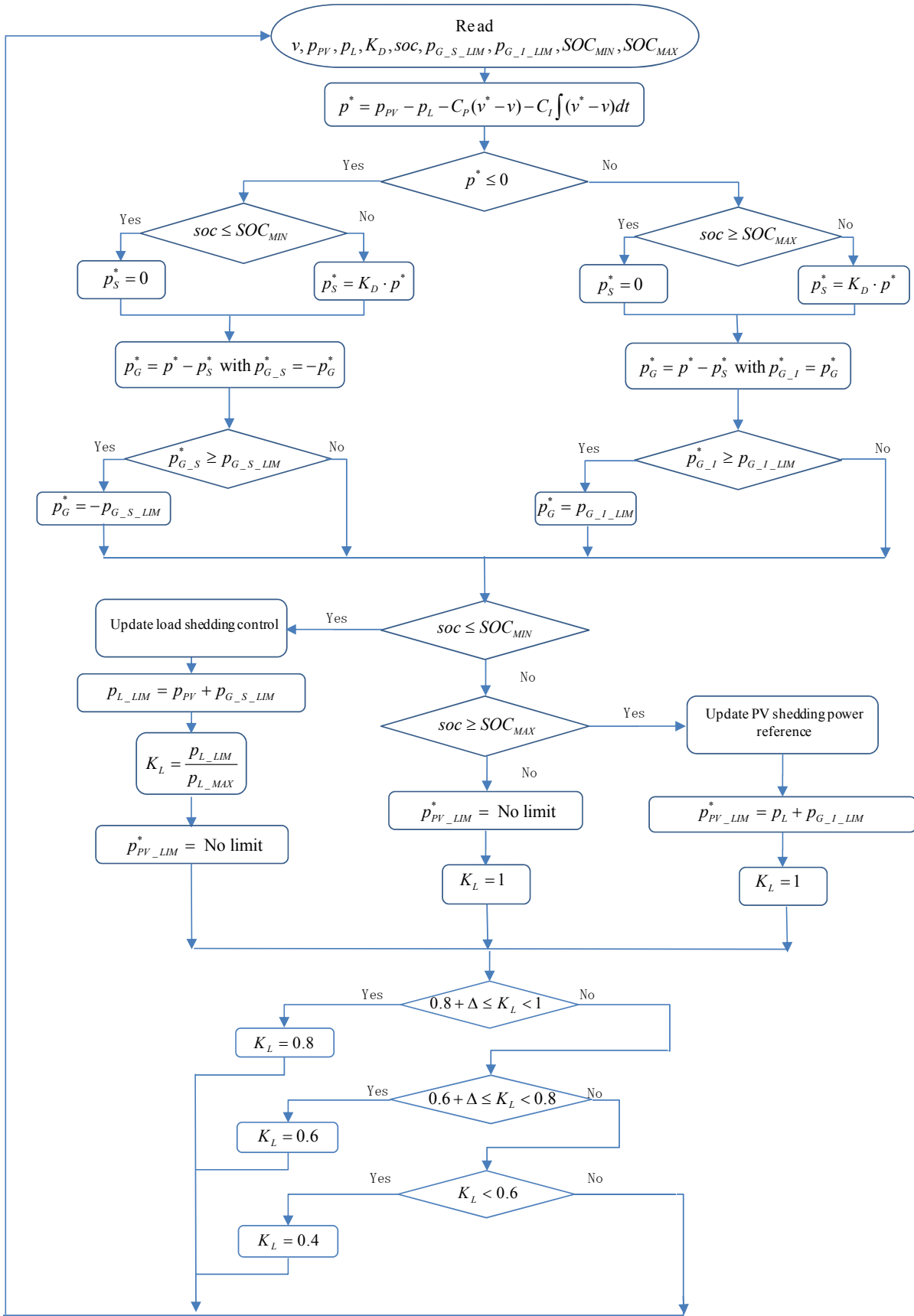


Figure 19. Flowchart of power system control algorithm.

To avoid load shedding switching oscillations, one possible load shedding program is added to transform continuous load shedding parameter K_L into different levels. K_L indicates the level of load being cut off from the DC bus, *i.e.* the lower K_L means the highest load shedding. In this study, arbitrary discrete levels and intervals of K_L were chosen, which may vary according to load conditions. Calculated K_L is transmitted to the load shedding device to disconnect appliances of the load. In addition, aiming to obtain a constant load power value with noise rejection from the measure, the hysteresis mode (Δ) is used to avoid load shedding fluctuations near the critical values (for example, 0.8 or other chosen values).

The algorithm calculates power references p_G^* , p_S^* , $p_{PV_LIM}^*$ with respect of their limitations, and gives the value of K_L .

To sum up the above described power system control algorithm and the PVA power limiting control, considering external control interface, corresponding controllers and smart grid message, the overall algorithm is shown in Figure 20. The control strategy receives an interface value of K_D to control local power flow. The calculation of K_D requires further development of power flow optimization.

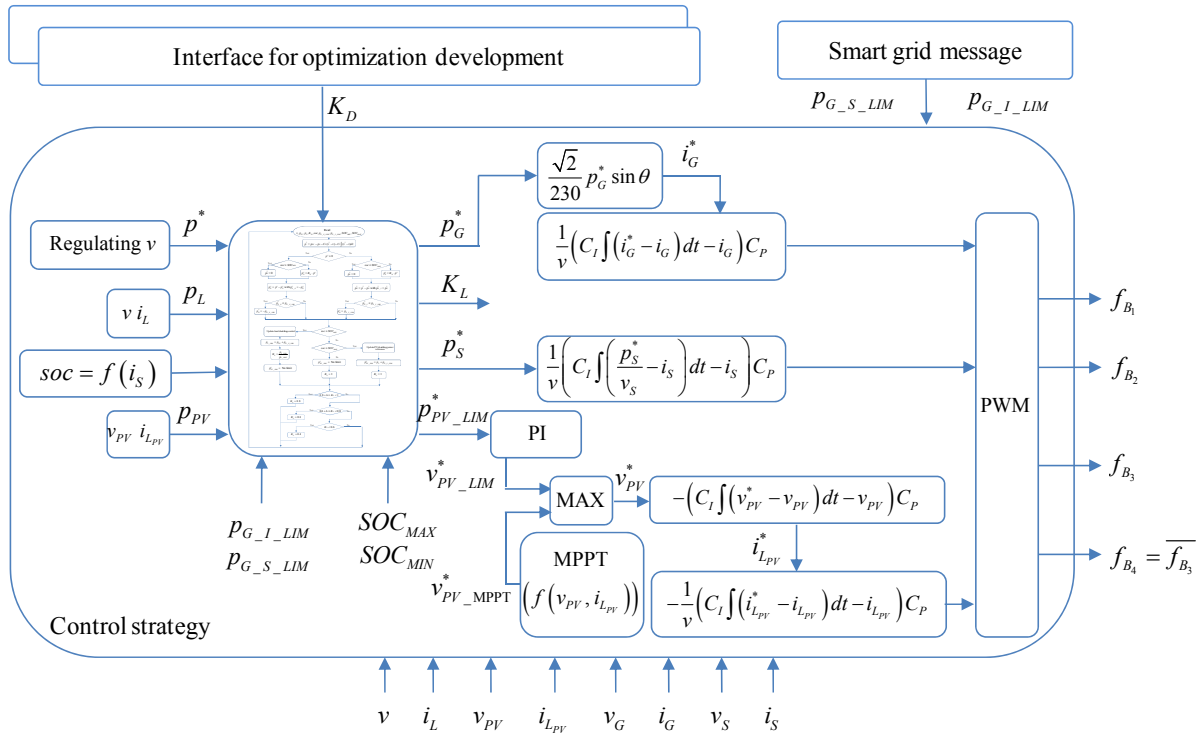


Figure 20. Overview of control strategy.

All controller coefficients are referred as C_I and C_P , the integral gain and the proportional gain. For different controllers, C_I and C_P are not the same value; they are calculated so that each controller can work properly. Finally, the controllers output duty cycle to corresponding converters for pulse

width modulation (PWM) control, which is a classic technique for power electronic control. For PVA control, in the following section a control strategy is developed to keep PV power within limit.

II.4.2. PVA operating algorithm

The simulation test as well the experimental test require adequate PVA control algorithm, which combines MPPT operation and power limiting operation, corresponding PVA MPPT mode and PVA constrained mode as presented in the PVA modeling section. Moreover, in the PVA operation, the MPPT production and constrained production must be switched seamlessly.

To achieve such a control strategy, the non-linear PVA characteristics are firstly studied. Based on the characteristic study, the PVA control strategy, combining MPPT production and constrained production, is proposed for simulation and experimental tests of power balancing strategy.

II.4.2.1. PVA characteristics

According to single diode PV model used in [94], the studied PVA $p_{PV} - v_{PV}$ characteristics at different solar irradiance conditions for a constant PV cell temperature are obtained in Figure 21.

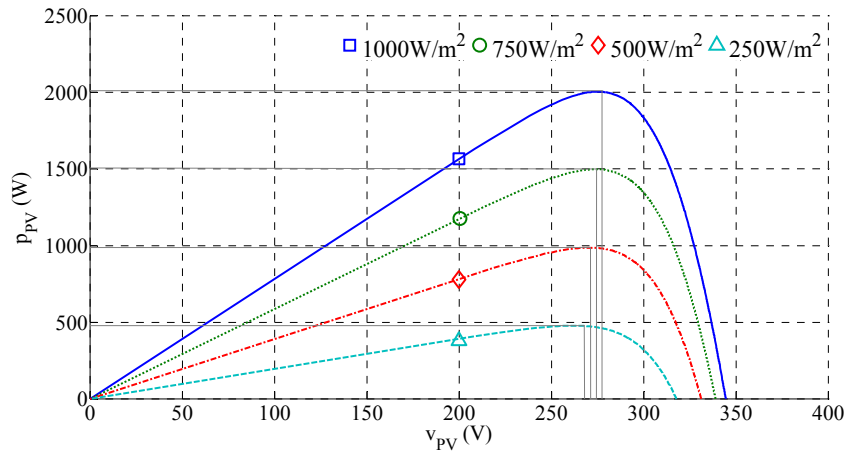


Figure 21. $p_{PV} - v_{PV}$ characteristics at different solar irradiance and constant PV cell temperature.

This characteristic is non-linear. With given solar irradiance, the MPP is unique. An MPPT algorithm is needed to reach this maximum production and maintain it. The constrained power control should control PVA operating point under the MPP.

II.4.2.2. PVA control strategy

Based on the PVA characteristics, an adequate algorithm for a PVA production control is developed. Following the power system operating requirement, this control should be able to output maximum PVA power production as well as constrained PVA power.

II.4.2.2.1. Perturb and observe MPPT algorithm

P&O method is one of the most commonly used MPPT algorithms [94]. Following the typical $p_{PV} - v_{PV}$ characteristic curve shown in Figure 21, as the voltage increases, PVA power increases on the left side of the MPP, and PVA power decreases on the right-side of MPP. In order to maintain the output power at MPP, it is important to know exactly on which side the current operation point is.

During operation, the power converter will continuously change the voltage or current reference, or directly change the duty cycle, whence the perturbation is. Then, the PVA power is affected and changed. By observing the power change, the operation point can be identified locating on which side of MPP, and next perturbation would move the operation point towards MPP to maintain a MPPT production.

By PVA voltage control, which is implemented in this thesis, the P&O process can be summarized as in Table 2.

Table 2. P&O algorithm by voltage control.

Last perturbation	Change in power	Next perturbation
$v_{PV}^* \uparrow$	$p_{PV} \uparrow$	$v_{PV}^* \uparrow$
$v_{PV}^* \uparrow$	$p_{PV} \downarrow$	$v_{PV}^* \downarrow$
$v_{PV}^* \downarrow$	$p_{PV} \uparrow$	$v_{PV}^* \downarrow$
$v_{PV}^* \downarrow$	$p_{PV} \downarrow$	$v_{PV}^* \uparrow$

The P&O MPPT algorithm keeps perturbing the PVA operation so that the output power moves around MPP. In application, two sensors are needed for measuring voltage and current of PVA. PVA power is calculated by multiplying measured PVA voltage and current.

II.4.2.2.2. MPPT and power limiting control strategy

Figure 21 shows PVA $p_{PV} - v_{PV}$ characteristics at different solar irradiance levels. It is observed that as the solar irradiance increases, the MPP gets higher and the corresponding voltage also goes higher. The MPP power-voltage relationship is monotonous. On the other hand, with a given solar irradiance, it can be seen each curve $p_{PV} - v_{PV}$ is nonlinear at the whole voltage range.

However, if splitting a curve by MPP, each part of the curve, either on the left side or on the right side of MPP, is monotonous and can have an approximate linearization, which provide the possibility of power closed-loop control by voltage to constrain PVA power.

Based on the system monotonicity, by choosing the $p_{PV} - v_{PV}$ curve on the right side of MPP for a constrained power closed-loop control, a PVA power limiting algorithm is proposed, as shown in Figure 22.

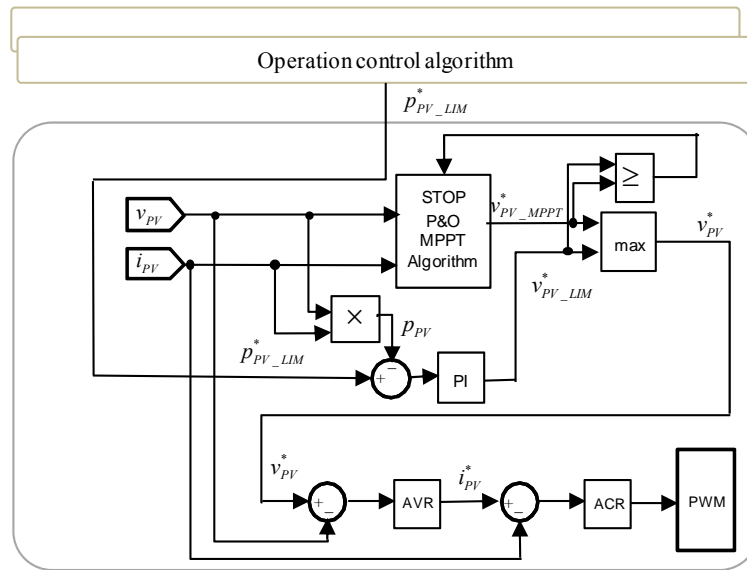


Figure 22. Proposed PVA constrained production control strategy.

In the proposed control strategy, the P&O MPPT algorithm and the power limiting algorithm, which follows power limiting reference $P_{PV_LIM}^*$ given by the control algorithm, give at the same time corresponding voltage reference $v_{PV_MPPT}^*$ and $v_{PV_LIM}^*$ to operate PVA, the MPPT voltage reference and voltage reference of power limiting control, respectively. The maximum of these two voltage references is taken as the PVA voltage control reference v_{PV}^* , which represents the minimum power. Following v_{PV}^* , the PVA system is operated by voltage and current double closed-loop control via automatic voltage regulator (AVR) and automatic current regulator (ACR).

During the MPPT operation, if a limiting power reference within the MPPT ability is given, the PI controller would increase the $v_{PV_LIM}^*$. When $v_{PV_LIM}^*$ is greater than $v_{PV_MPPT}^*$, $v_{PV_LIM}^*$ is taken and the MPPT algorithm is stopped. By constrained power closed loop control, the PI controller could control the PVA power at the constrained level. In case of low solar irradiance, the PVA output power ability is less than the constrained power reference, so the PI controller will decrease $v_{PV_LIM}^*$ until the lower limit, and $v_{PV_MPPT}^*$ is taken to control the PVA. So, the power limiting control does not affect MPPT algorithm and MPPT power is produced. Experimental results of the PVA control is provided in [95].

To avoid continuous decreasing of PI controller output towards infinite in this case, an anti-windup PI controller is used as the PI controller for power limiting algorithm to avoid the integrator output saturation, as in Figure 23.

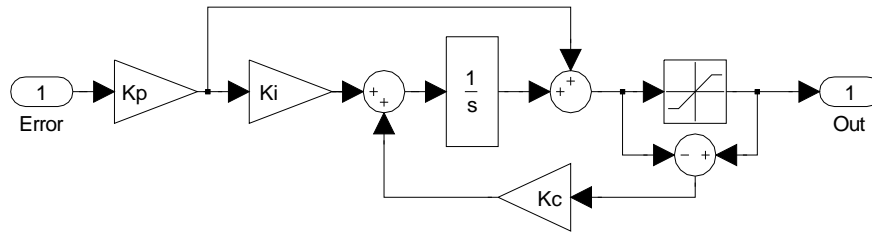


Figure 23. PI controller with anti-windup.

An anti-windup PI controller is a typical PI controller with an extra feedback with the gain K_C in order to deal with the integrator saturation. K_p and K_i are proportional and integral gain. The block $1/s$ is the integrator.

The saturation block limits is assigned as the range PV working voltage. When the output is within the saturation limits, the extra K_C branch does not work. If the integrator saturates, the extra K_C branch interacts to keep the integrator output at the saturation lower or upper limit instead of integrating towards infinite, which could eliminate the control dead-time caused by the delay for integrator output returning to normal control range.

Concerning the PI controller, the main goal is not to develop synthesis of controller, but to perform a control in a simple and robust manner. Experimental tuning of controller parameters is obtained from few tests. In this application, K_p is given as negative value in order to decrease the voltage reference when the controller input error is positive and vice versa. For experimental validation: $K_p = -0.2$, $K_i = 100$, and $K_C = 200$.

II.5. Simulation results

The described power system has a hybrid aspect from the higher level, which is supervision, to the lower one, which is local control. The continuous and discrete aspects coexist and interact with each other. As method for validating such models, the hybrid simulation is proposed. It is based on the connection and interaction of two submodels that continuous and discrete simulation progress in alternation. Continuous simulation takes care of the continuous dynamic and is executed while no event has been detected. The main problem of the hybrid simulation is the synchronization between the two submodels.

Due to the hybrid nature of the power system behavior, the simulation is carried out under the MATLAB-Simulink and Stateflow environment. MATLAB-Simulink helps to simulate the continuous dynamics of the system and Stateflow is used to specify the discrete control logic and the modal behavior of the system.

II.5.1. Power system discrete behavior simulation

The Stateflow simulation permits observing element behavior during the whole process of simulation. Thus, the proposed control strategy modeled by interpreted PN is translated into Stateflow charts model. Figure 24 shows discrete state system simulation by Stateflow in the MATLAB environment during its interaction with Simulink, which is a screen-printing of the Stateflow model taken during simulation. In this figure the overall behavior of the power system is shown in the way that activated states or transitions are highlighted. This figure shows the instant when load is in normal mode, the storage is fully charged, grid power injection reaches the injection limit and PV is thus constrained. Hence, with the help of Stateflow, it is possible to verify the proposed control strategy with visualization of detailed element behavior at each time instant.

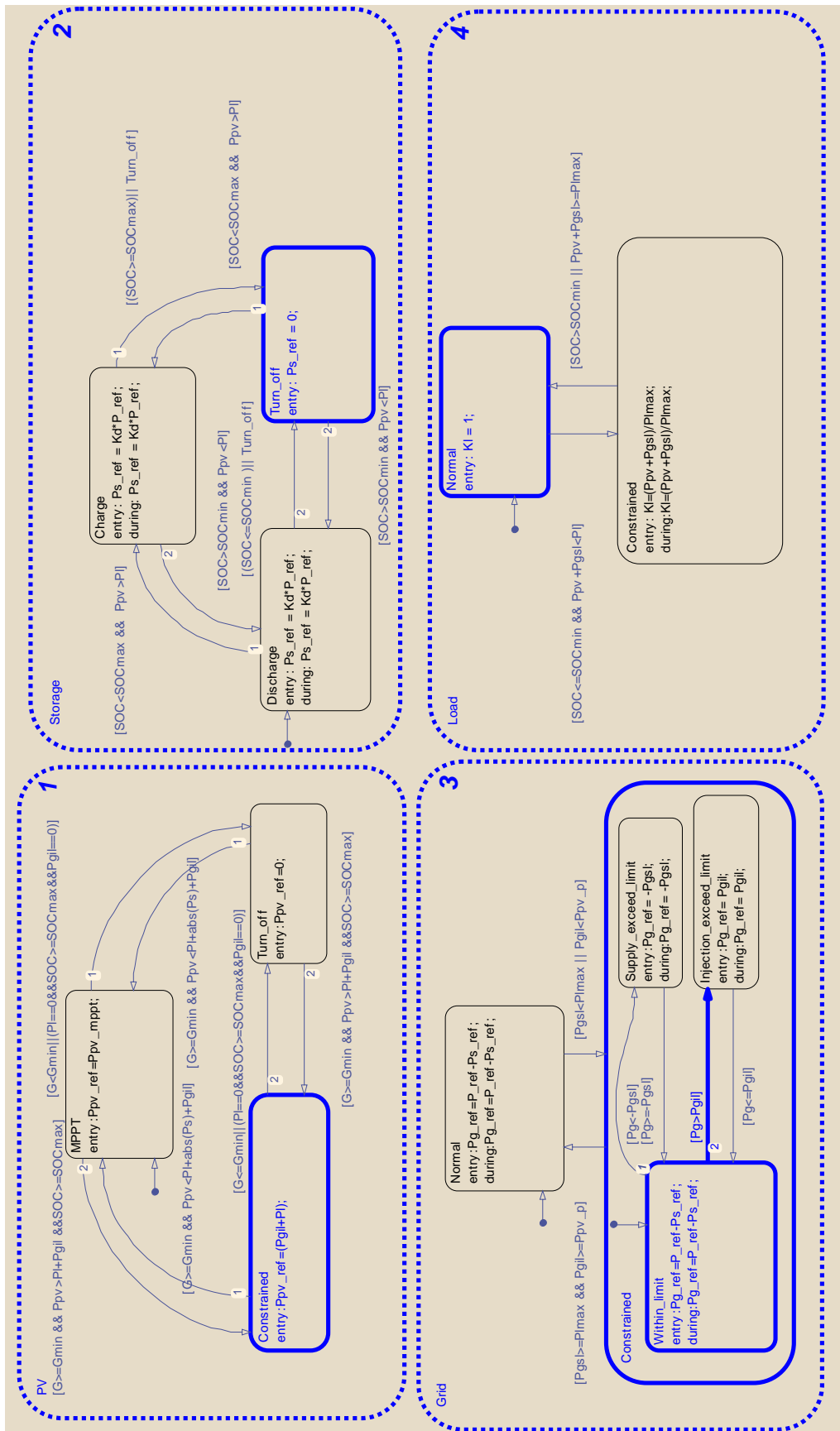


Figure 24. Screen-printing during simulation of Stateflow model in MATLAB.

II.5.2. Power system continuous behavior simulation

Following the Stateflow model, Simulink features a Stateflow library with which it is possible to encode graphically the behavior of each power system component. The MATLAB-Simulink model concerns the physical model of the power system components and is relatively simple.

For preliminary test simulation a simplified version of the proposed control strategy is used. PVA model is given in [94] and batteries are modeled as capacitor corresponding 88Ah in its voltage operating range.

In order to be economically profitable, an optimal DC bus voltage value to adopt may be 325V [80, 96], therefore, the DC bus voltage is fixed at 325V.

To further simplify this first simulation test, the storage control is operated with respect to its voltage limits, *i.e.* $soc = SOC_{MIN}$ for $v_s = V_{S_MIN}$ and $soc = SOC_{MAX}$ for $v_s = V_{S_MAX}$, in the normal voltage range $V_{S_MIN} = 24V$, $V_{S_MAX} = 26V$.

Load is an arbitrary power profile which can be shed, that could represent house lighting which demands DC current from the DC bus.

Grid power supply limit $P_{G_S_LIM}$ is given following two values, for normal and constrained grid-operating mode, $P_{G_S_LIM} = P_{L_MAX}$ and $P_{G_S_LIM} = 0.8P_{L_MAX}$, grid injection limit $P_{G_I_LIM}$ is not imposed, and the corresponding load shedding control parameter K_L is assigned as $K_L \in \{0.8, 1\}$.

The simulation implemented two arbitrary K_D values, $K_D = 1$ and $K_D = 0.8$, respectively for normal and constrained grid-operating mode. Simulation results are shown in Figure 25, Figure 26, Figure 27 and Figure 28.

Figure 25 (a) and Figure 26 (a) concern normal grid-operating mode with $P_{G_S_LIM} = P_{L_MAX}$, thus, the load does not need to switch in constrained mode and the load power demand P_{L_D} is identical to the power constrained P_{L_C} by the system.

In Figure 27 (a) and Figure 28 (a) the constrained grid mode imposes $P_{G_S_LIM} = 0.8P_{L_MAX}$, hence, when PVA does not provide sufficient power and the storage is empty (near 16:00), the system constraints the load power to predefined load shedding level as $P_{L_C} = 0.8P_{L_MAX}$.

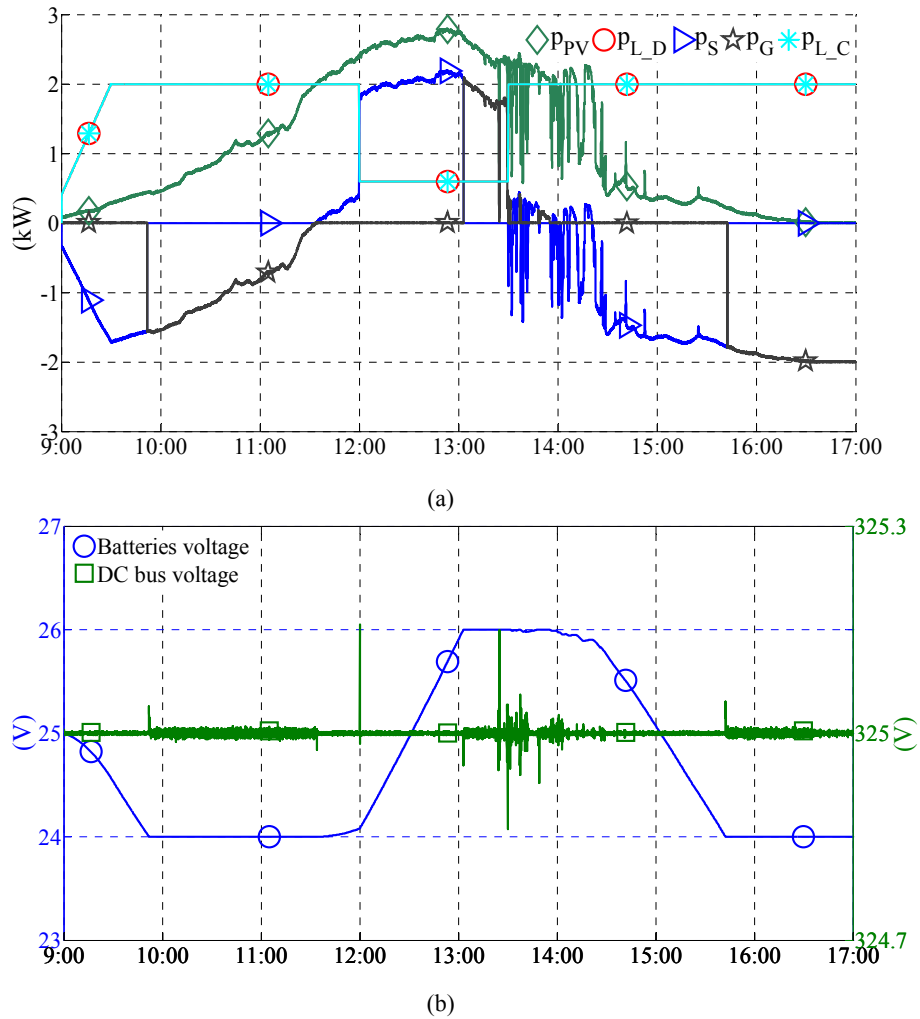


Figure 25. Powers (a) and voltages (b) evolution for $K_D = 1$ in normal grid mode.

The implemented automatic control described earlier works satisfactorily. For the period taken into account, from Figure 25 to Figure 28, it is observed that the strategy outlined earlier is well respected at all times.

When $p_{PV} > p_L$, the storage system receives power, in contrast it provides. The storage charge or discharge has priority over the utility grid. The relatively large K_D indicates the storage is more used than the grid to fill the power gap between PVA production and load demand. Once the storage has reached its high or low voltage/capacity limits, the utility grid takes over.

For $K_D = 1$, the storage works alone, never cooperate with the grid at same time if storage does not reach *soc* limits. In contrast, they share power supply for $K_D = 0.8$.

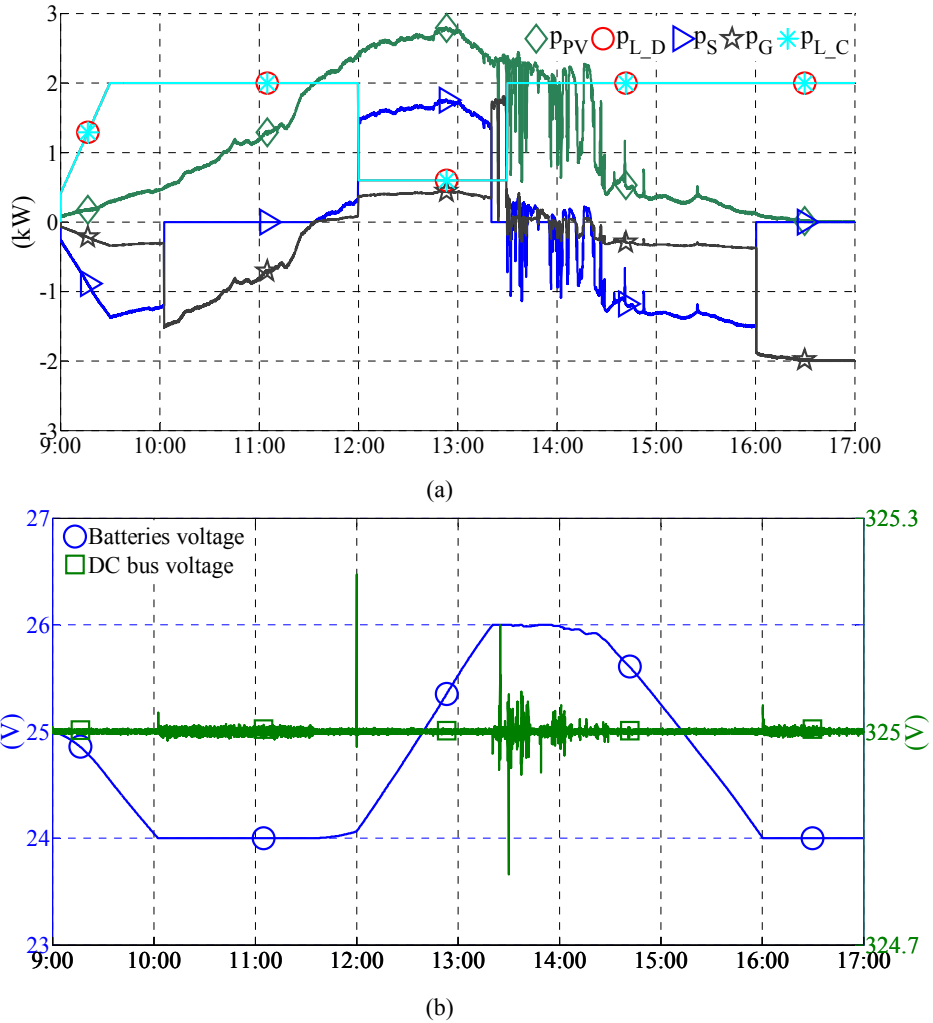


Figure 26. Powers (a) and voltages (b) evolution for $K_D = 0.8$ in normal grid mode.

For each operation, it is observed that the power is well balanced, signified by steady DC bus voltage, meanwhile element constraints are well respected by the control strategy all the time. However, some fluctuations are observed from time to time corresponding to state changes of the coefficient K_D . These voltage's fluctuations are less than 0.50% of the rated DC bus voltage and can be considered negligible. The fluctuations are also related to the simulation step.

The most significant fluctuation during the dynamic process can be observed in Figure 27 (b) and Figure 28 (b), around 15:40 and respectively 16:00. In this case, the storage reaches the lower voltage limit 24V and the grid takes over. However, the control is able to make the DC bus voltage steady with a very light fluctuation which could be improved by means of a better controller tuning, if required by the experiment test.

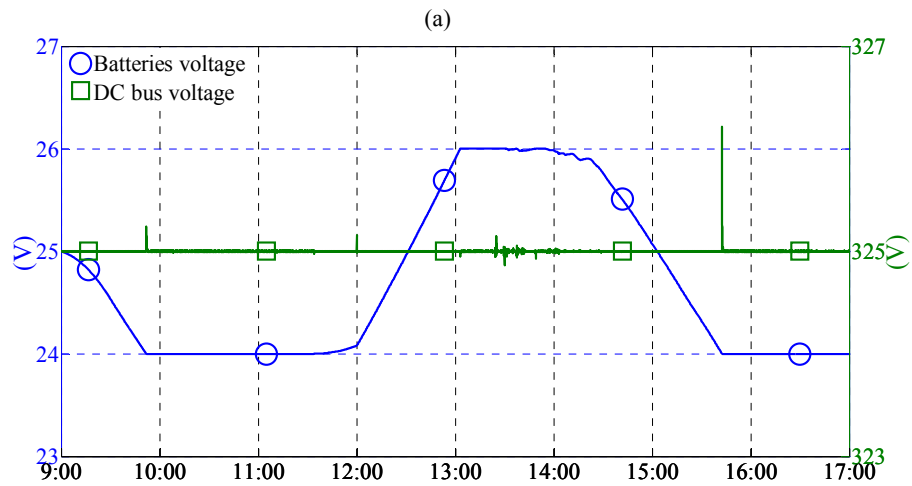
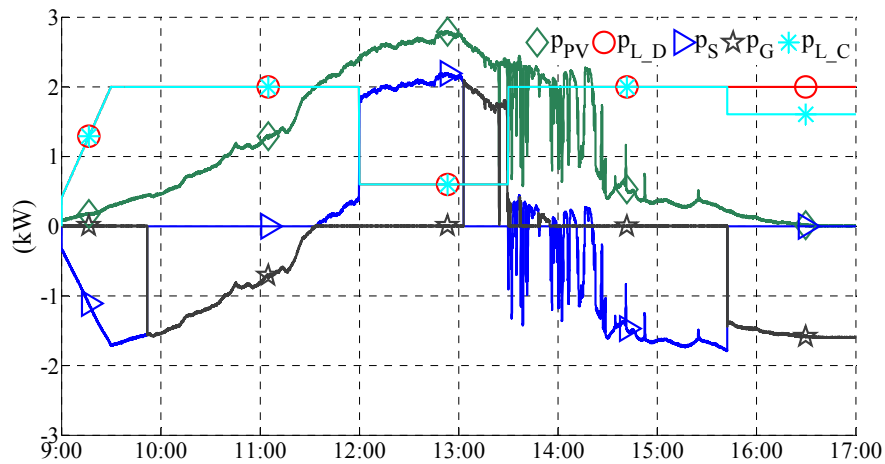
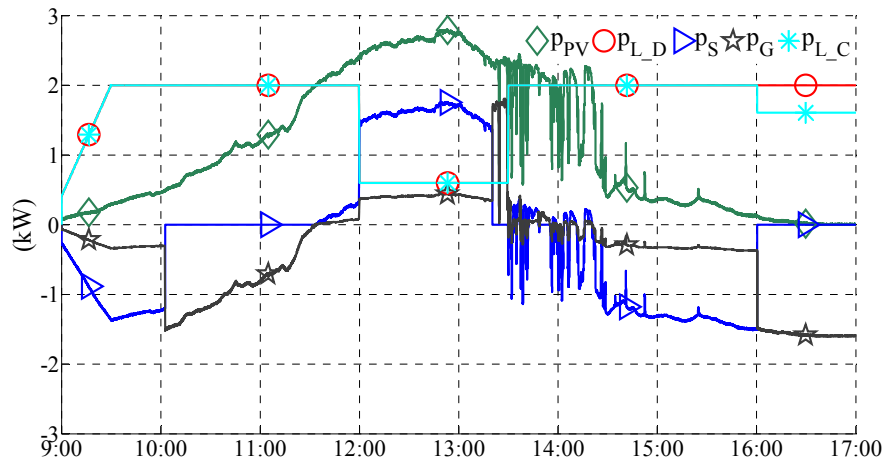


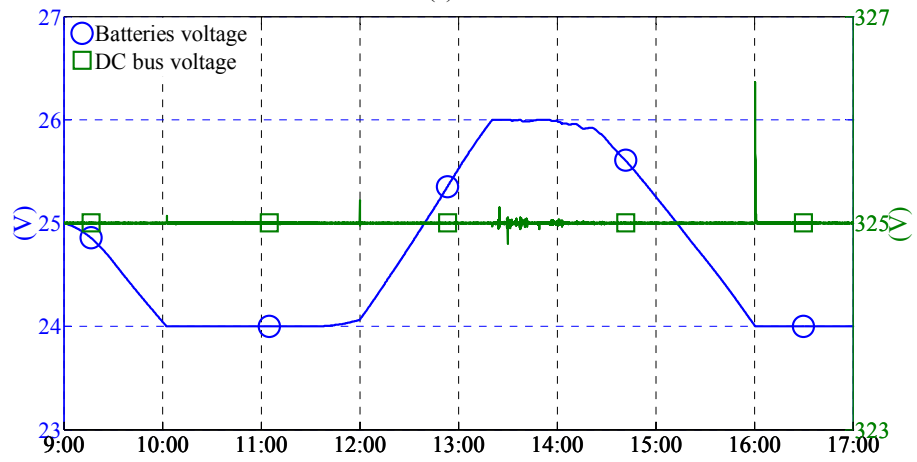
Figure 27. Powers (a) and voltages (b) evolution for $K_D = 1$ in constrained grid mode.

The simulation results, with calculation step of 0.05s, have shown that the designed control strategy works well in power balancing, and that the system power flow is affected by both grid power limits and control parameter K_D . As the grid power limits are given by smart grid message, the control strategy can offer possibility for grid to manage grid usage. The K_D value is given by supervision energy management layer, which leads to the development interface with local power flow optimization.

According to the message received from the smart grid, the supervision system should respect the power grid limitations, calculates the power reference of storage and grid, and constraints the load and PVA. Simulation results validate the design of the power balancing strategy, which lead further to experimental test and optimization design.



(a)



(b)

Figure 28. Powers (a) and voltages (b) evolution for $K_D = 0.8$ in constrained grid mode.

II.6. Experimental test

Based on experimental platform described in section II.1, the whole power system control is tested in a short time period (9 hours), utility grid constraints values and *soc* limits are chosen, as well as an arbitrary value of K_D , as in Table 3. Considering the storage capacity installed on the platform, the *soc* limits are selected to show the system behavior with relevant storage events, as full and empty, in a day run, although the values indicated by the manufacturer are far larger.

Table 3. Arbitrary values for experimental test.

Variable	Value
K_D	0.8
$P_{G_S_LIM}$	800W
$P_{G_I_LIM}$	700W
P_{L_MAX}	1500W
K_L	{0.2, 0.4, 0.6, 0.8, 1}
P_{PV_P}	2000W
SOC_{MIN}	49%
SOC_{MAX}	51%
v^*	400V

Figure 29 shows the powers evolution during September 3rd, 2011, recorded at Compiègne. When the storage is available, it works together with the grid. The storage offers 80% of the demanded power reference p^* , as indicated by $K_D = 0.8$. When the storage reaches the *soc* lower limit, the grid supplies the load with respect of its own limits $P_{G_S_LIM}$ and $P_{G_I_LIM}$.

When the storage is empty, if the load requests more power than the system can supply, which is the grid power supply limit $P_{G_S_LIM}$ plus PVA power (15:40, 16:20-18:00), the load is shed to maintain the power balance, so the load demand power (P_{L_D}) is constrained (P_{L_C}). The load shedding level depends on the real-time PVA production and $P_{G_S_LIM}$.

When the load power is less than PVA production, as $K_D = 0.8$, 20% of excess energy is injected into the grid and 80% is used to charge the storage until the *soc* upper limit is reached (10:40-11:55). If the injection power exceeds $P_{G_I_LIM}$, the PVA production is constrained by the PVA power limiting control (11:55-14:00).

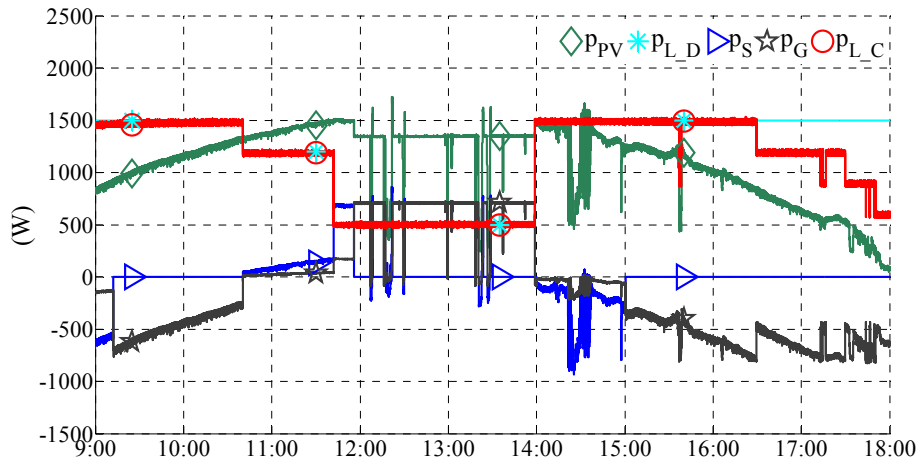


Figure 29. Powers evolution.

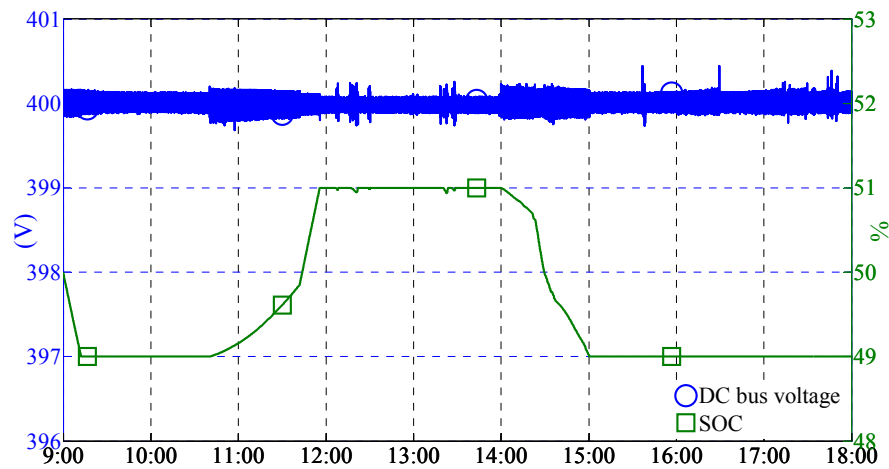


Figure 30. DC bus voltage and storage *soc* evolution.

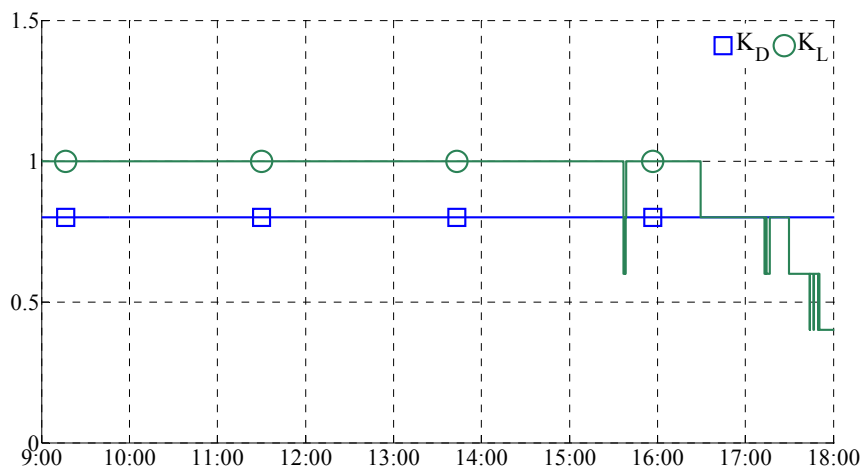


Figure 31. Coefficients evolution.

During PVA power limiting periods, due to the sudden transition of clouds, the PVA power limit becomes higher than the ability of PVA production, thus, the PVA control returns to MPPT production (12:20, for example). A thick cloud makes the PVA power less than the load; the storage and grid supply the load, and the *soc* decrease. After the cloud passing, the storage is recharged until the upper

limit SOC_{MAX} with the PVA MPPT production, and then PVA power is limited again, which forms the pulses in PVA power curve. With more load power demands, PVA returns to MPPT production (after 14:00). During strong PVA production fluctuations around 14:30, the grid is less fluctuated because of the relatively high value of K_D . The grid injection limits also helps downscale grid power fluctuations during the period of PVA surplus production (12:00-14:00). Grid power is kept within limits during the whole period of operation, which is ensured by PVA constrained control and load shedding.

The steady DC bus voltage illustrated in Figure 30 proves that the strategy works well to balance the powers. The K_D value and the evolution of K_L are given in Figure 31. The load shedding works satisfactory, but fluctuations can be observed. To overcome these load control fluctuations, additional storage or reserved soc would be a solution, or the negative impact can be reduced by a special designed load shedding program, for example, imposing minimum load shedding duration.

The goal of this experimental test was to verify the feasibility of the designed microgrid power control under proposed operating conditions. The experimental results have validated that the control strategy design, which is able to keep power balancing while respecting grid power limits and storage capacity constraints. The grid power injection limit helps avoid undesired injection and downscale power fluctuation. Grid supply limit helps adjust peak consumption.

II.7. Conclusion

Based on power system behavior modeling by interpreted PN and Stateflow, the power system control strategy is designed with consideration of each element constraints and their behavior. Algorithms for PVA power limiting and load shedding management are developed. Simulation and experimental results of day tests validate the basic layer design, which ensures power balancing while respecting all element constraints. According to the strategy, power flow is mainly affected by both grid power limits and control parameter K_D . The grid power limits are given by smart grid message, so the control strategy can offer possibility for smart grid to manage grid usage, acting for DR to help make better use of grid assets and improve overall grid performance. The control strategy can maintain power balancing with any K_D value. However, by giving different distribution coefficient K_D values, the power flow in the power system can be different. A large K_D value during peak hour can reduce the power demand from the grid, as load shedding. The K_D value should be calculated by supervision energy management layer, which leads to the development of local power flow optimization and other upper layer design in the supervision system.

In the next chapter, the optimization of K_D is carried out and implemented in the upper layer for advanced energy management.

Chapter III. Supervision system design

The supervision of the power system is proposed as a multi-layer structure of local energy management based on: information about the end-user's request, estimated operating building appliances, weather forecasts, conditions concerning utility grid availability, possibilities of shedding building facilities... An operation layer is developed to control the balance of powers, taking into account multiple constraints. The aim of supervision control is to provide a continuous supply to the building with an energy cost optimized under constraints such as those provided by the utility grid (power limits, electricity prices, TOU) and the possibility of shedding some building equipment. It is matter of a constrained optimization related to risks like gap between forecasting and planning, on the one hand, and operational reality and utility grid requirements, on the other hand. Hence, taking into account forecasting data, storage capability, grid power limitations, grid TOU tariffs, the powers flow is optimized by mixed integer linear programming and solved by CPLEX solver. This is the energy management layer which is in charge of this optimization

The DC microgrid control is simulated for different cases of grid-connected mode and off-grid mode. The grid connected mode contains the cases that with and without optimized powers flow. Even with uncertainties of prediction, the simulation results validate the feasibility of microgrid and highlight how supervision improves the performance of the system with the requirements of the utility grid.

Based on the study of power system operation in grid-connected mode, this chapter further develops the supervision system in power balancing for both grid-connected and off-grid operation, power flow optimization, prediction data processing and HMI.

III.1. Supervision design overview

The supervision system is designed in four-layer structure, which consists of HMI, prediction layer that predicts load consumption and PVA production, energy management layer that optimizes the powers flow, and operation layer that balance instantaneous power in power system. The structure of the multi-layer supervision design and the adjacent layers coupled with some variables are suggested in Figure 32.

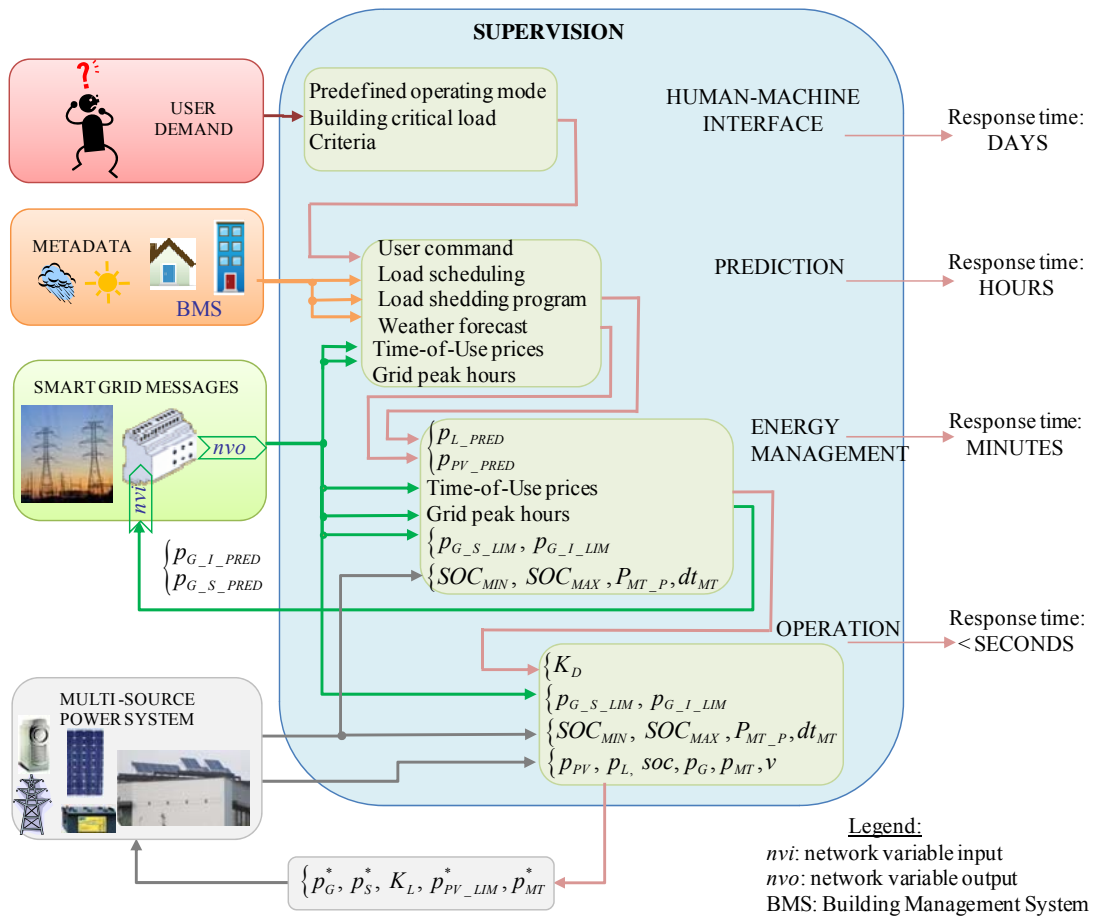


Figure 32. Supervision design overview.

By assigning values for the interface variables, the upper layer is able to control the lower layer operation. This supervision handles physical parameters of very different field: electric, building facilities, weather, smart grid communication... Also, it relates to different time scales: HMI relates to days, prediction layer relates to hours, energy management relates to minutes and operation layer has a response time less than a millisecond.

The bidirectional smart grid messages, acted by appropriate routers, are considered network variable input, nvi , and network variable output, nvo . The network variable output informs mainly the usage conditions of utility grid (prices, peak hours, power supply and power injection limits). The network variables input are the grid power injection prediction $P_{G_I_PRED}$ and the grid power supply prediction $P_{G_S_PRED}$, which could help in power balance of the utility grid.

Concerning the off-grid mode, MT is taken into account and the following parameters are defined: p_{MT} is the MT power, P_{MT_P} is the MT rated power, and dt_{MT} is the working duty cycle.

The detailed description, operating conditions and limits of each layer are given in the following sections.

III.2. Human-machine interface

HMI permits the end-users to adjust, define and customize the operation criteria such as minimizing energy cost or maximizing the comfort by including/excluding load shedding or limiting total load shedding amount in the operation. The HMI design is illustrated in Figure 33.

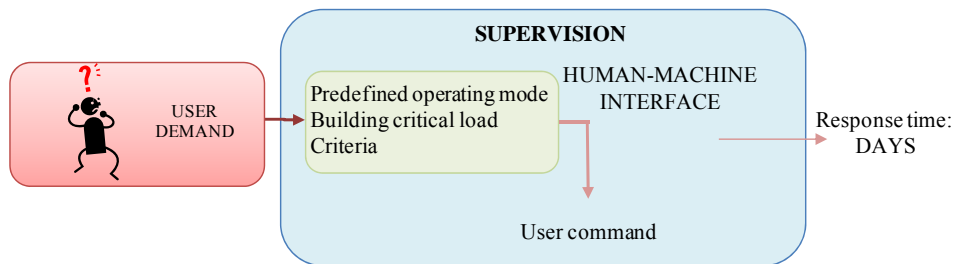


Figure 33. HMI design.

Parameters of system that are used in the supervision, including rated power of each element, constraints of each element, load shedding levels, etc... are also assigned in this layer.

According to the end-user demand, this layer could modify corresponding parameter value in the other layers. The end-user can also assign different priorities for each building appliance that would be involved in load shedding, as well as define critical load that requires an uninterruptible power supply.

Thus, different operating modes for different end-users type (office building or residential building) could be predefined. Some operating modes could follow a predefined lower limit of K_L . The end-users may also choose a criterion to take into account as to minimizing energy cost including or excluding load shedding if possible. Modify the optimization criteria or overwrite constraints is also possible in this layer.

This layer is assumed to be designed with graphical interface. At present, HMI is not developed, but this layer will be elaborated in further work.

III.3. Prediction layer

Prediction layer, whose design is presented in Figure 34, provides the necessary information for the energy management to perform energy optimization. Thus, this layer calculates possible PVA power and load power evolutions for the next hours, up to 24h.

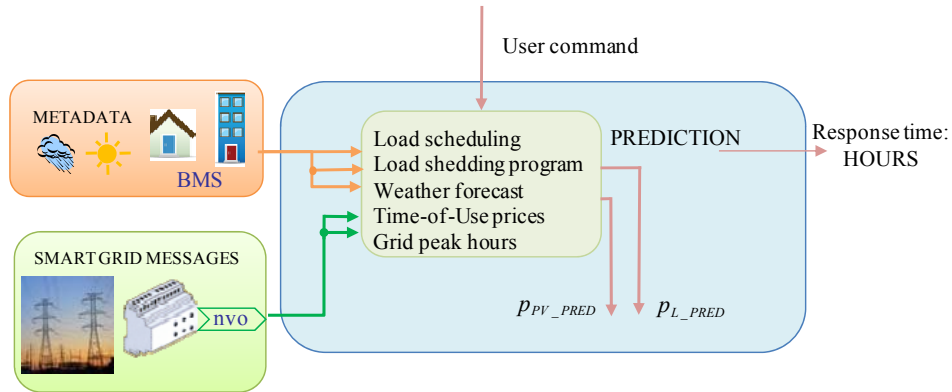


Figure 34. Prediction layer design.

PVA predicted power P_{PV_PRED} evolution could be calculated by forecast information of solar irradiance and temperature, sun position evolution and on PV model, built with parameters identification or PV solar irradiance mapping [97]. Furthermore, a three-dimension modeling of PVA also could provide precise prediction of PV energy yield production including shadow cases [98].

Load predicted power P_{L_PRED} evolution is calculated by statistical data and/or information from building management system (BMS), with respect to end-user demand [99]. The load scheduling, that represents the operating program of building facilities, building energy needs linked to weather, and the load shedding program are supposed known. They are implemented and updated continuously by the BMS to give the predicted load power. Depending on criteria chosen by the end-user, additional information from the smart grid could be needed as TOU and energy dynamic pricing.

Hence, metadata, smart grid messages, and the HMI output "user command", as discrete inputs, allow to the prediction layer to calculate the PVA predicted power P_{PV_PRED} and the load predicted power, P_{L_PRED} .

III.3.1. PVA power prediction

For advanced energy management in a DC microgrid, the PV power prediction is necessary and required by the future smart grid. The request of managing renewable production and integrating more renewable energy generation in utility grid, has stimulated the boost of weather forecast service related to renewable production. Nowadays, world-wide solar irradiance prediction service can be found. One

day-ahead solar irradiance forecasting can provide 36% root mean square error for regional forecasts [100], but 4-hours ahead solar irradiance and temperature forecasting gives the smallest error.

To carry on our study, weather prediction data is obtained from Meteo France, which provides hourly prediction data of solar irradiance for specific location. Based on solar irradiance and temperature forecasting, and on PV model, the calculation of PVA predictable power P_{PV_PRED} should be calculated with as less error as possible. Hence, weather forecast, mainly solar irradiance on PV panels, and PV model are the most significant factors to obtain the PVA power prediction.

III.3.1.1. Raw data processing considering sun position

According to available weather forecast services in this study, solar data is presented in the form of energy arriving on ground that is horizontal plane, and it is not compatible with the PV panel with inclination. An algorithm is developed to obtain solar irradiance on the PV panel from solar irradiance arriving on ground. The problem is illustrated in Figure 35. As the sun is far away from the earth, the light can be seen as parallel. So, the energy arrived on the panel equals to the energy arrived on the same area of the shadow.

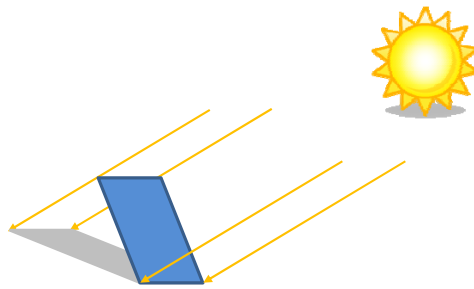


Figure 35. Principle of solar irradiance calculation on the panel from ground data.

Considering that solar irradiance is the energy during unity time on unity surface (W/m^2), it is considered that:

$$g_1 S_1 = g_2 S_2 \quad (3.1)$$

where g_1 is the solar irradiance on PV panel (W/m^2), S_1 is the panel area (m^2), g_2 is the solar irradiance on the ground (W/m^2), S_2 is the shadow area (m^2).

So, the desired solar irradiance can be obtained:

$$g_1 = \frac{g_2 S_2}{S_1} \quad (3.2)$$

In (3.2), S_1 and g_2 are known, S_2 changes according to solar position during a day. The sun position data is available on <http://www.sunearthtools.com>. The following figure shows the sun position evolution during a day in spherical coordinate on 31st of August, 2013.

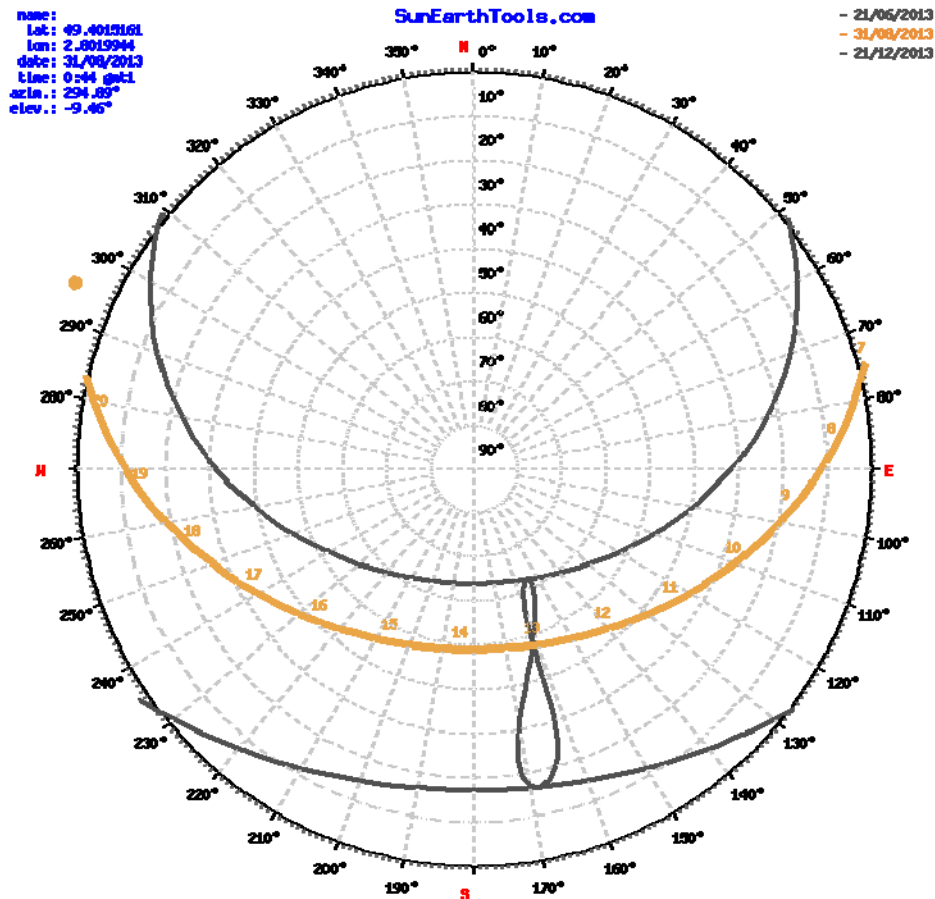


Figure 36. Solar position evolution during a day.(<http://www.sunearthtools.com>)

Establishing the problem in a Cartesian coordinates, the solar position can be represented by a unity direction vector $\langle x_0, y_0, z_0 \rangle$, and a vertex of the panel (x_1, y_1, z_1) has the projection (x'_1, y'_1, z'_1) on the ground, as shown in Figure 37.

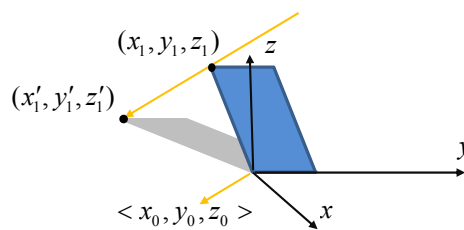


Figure 37. Calculation of shadow area.

The relationship can be described by the following equations:

$$\begin{cases} x'_1 = x_0k + x_1 \\ y'_1 = y_0k + y_1 \\ z'_1 = z_0k + z_1 \\ z'_1 = 0 \end{cases} \quad (3.3)$$

where k is only a parameter for calculation.

So, the vertex projection (x'_1, y'_1, z'_1) can be obtained. In the same way, other vertex and their shadow projection can be obtained, so that the area of the shadow S_2 can be calculated through Heron's formula.

Eventually, solar irradiance on the panel can be obtained by (3.2).

III.3.1.2. PVA model

Given solar irradiance prediction, an adequate PVA model should be chosen to give PV power production. As described earlier, the PV source has non-linear characteristics with a MPP. These characteristics vary depending on the operating conditions, *i.e.* solar irradiance \mathcal{G} and PV cell temperature θ . For a given PV cell temperature, the power varies proportionally with the solar irradiance, while for a given solar irradiance power decreases while increasing of the temperature of the PV cell. Hence, the PV model has to give enough precise prediction while simple to implement.

Thus, the model of the PV source must be able to estimate the MPP current $i_{PV_{MPP}}$ and MPP voltage $v_{PV_{MPP}}$, or directly the MPP power $P_{PV_{MPP}}$, within possible operating conditions, as shown schematically given in Figure 38. It requires a reliable model that could easily lead to the prediction of the PVA production.

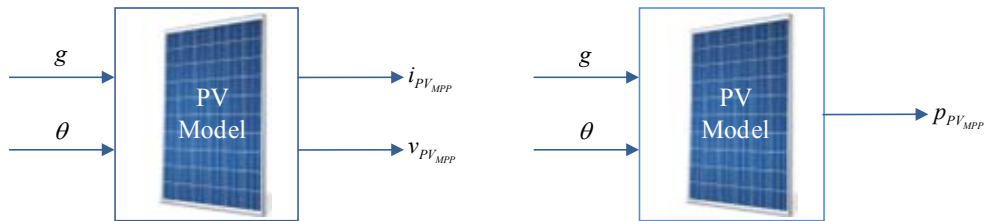


Figure 38. PV modeling generic schemes.

In this part, three PV models, linear model, single diode PV model and experimental model, are compared for PV power production calculation.

III.3.1.2.1. Linear model

The most simple PV source model is to consider PV source as linear power source according to the PV cell temperature and solar irradiance level [101]. PVA output power at MPP, $P_{PV_{MPP}}$, is obtained from (3.4):

$$P_{PV_{MPP}} = P_{MPP} \frac{\mathcal{G}}{1000} [1 + \gamma(\theta - 25)] N_{PV} \quad (3.4)$$

where P_{MPP} is PV panel maximum power at STC, which is available from the manufacturer data sheet, N_{PV} is the number of serial PV panels that compose the PVA, and γ is the power temperature coefficient at the MPP.

The estimation of $P_{PV_{MPP}}$ requires knowledge of γ parameter value. As the value of γ is highly dependent of solar irradiance and PV cell temperature, \mathcal{G} and θ , it should be estimated in experimental reference tests following real weather conditions day. Once this coefficient is estimated and validated, the power $P_{PV_{MPP}}$ could be calculated according to the weather data for any day.

The linear power model seems simple and easy to use for power prediction once the temperature coefficient γ was determined. In addition, it does not need special computation effort. However, the value of γ is varying according to the weather operating conditions, and the γ parameter calculation involves, at given weather conditions, current and voltage measurements corresponding at maximum power of PVA. Using a fixed value of γ corresponding to one day for any given day, involves errors that can range from acceptable to very large. Therefore, this model is simple enough to use, but it remains highly dependent on weather conditions. It does not take into account the various existing correlations with the PV cell temperature. The linear model of power could allow the PVA power prediction only with a set of γ values and assuming an error whose value must be compared with the errors of the weather forecast. So, it should be noted that a correct use of this model requires a mapping of values of γ for different irradiance and PV cell temperature values.

III.3.1.2.2. Single diode PV model

Single diode model provide enough precision with the less component. It is adopted to study the non-linear characteristics of the PVA for not only the MPP, but also the whole power range. As mentioned in the description of the experimental platform, the studied PVA, built on the roof of the university, consists of 16 PV panels Solar-Fabrik SF-130/2-125 connected in series. The characteristics of each PV panel are detailed in Table 4, which are given at STC.

Table 4. STC specifications of PV panel.

Solar-Fabrik SF-130/2-125		
N_S	Number of cells in series	36
I_{SC}	Short-circuit current	7.84A
V_{OC}	Open-circuit voltage	21.53V
I_{MPP}	Maximum power point current	7.14A
V_{MPP}	Maximum power point voltage	17.50V
P_{MPP}	Maximum power	124.95W
K_I	Temperature coefficient for current	0.00545A/K
θ^*	Cell temperature reference of STC	298K (25°C)
G^*	Solar irradiance reference of STC	1000W/m ²

Each panel consists of 36 cells. One of the PV cell model, shown in Figure 39, consists of a photo-current source (i_{ph}) for modeling the solar irradiance, in parallel to a diode for the polarization phenomena.

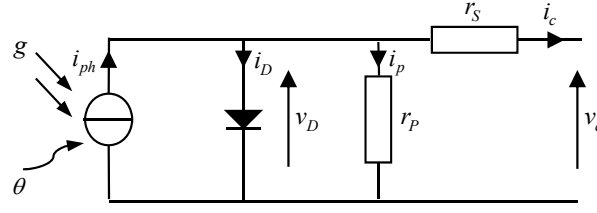


Figure 39. Single-diode PV cell model.

This model, includes series resistance (r_s) and a parallel resistance (r_p); it is called a single-diode model [97], with i_{ph} the current through the photo-current source (A), i_D the diode current (A), v_D the diode voltage (V), i_p is the current through r_p , i_c the PV cell output current (A) and v_c the PV cell output voltage (V). The resistances r_s and r_p represent the PV cell power losses. Regarding the PV power prediction, the single-diode model is enough simple yet accurate to be considered in this study.

The PV cell output current is:

$$i_c = i_{ph} - i_D - i_p \quad (3.5)$$

In this model, the photo current source i_{ph} changes according to the solar irradiance and temperature as:

$$i_{ph} = I_{SC} \left(\frac{g}{G^*} \right) \left(1 + K_I (\theta - \theta^*) \right) \quad (3.6)$$

where I_{SC} is the short-circuit current, G^* is the solar irradiance STC reference (W/m^2), K_I is the temperature coefficient for current temperature, and θ^* is the STC cell temperature reference taken in Kelvin ($\theta^* = 298\text{K}$).

The diode saturation current i_{sat} is a function of PV cell temperature:

$$i_{sat} = \frac{I_{SC} \left(\frac{\theta}{\theta^*} \right)^{\left(\frac{3}{n} \right)} \exp \left(\frac{-qE_G}{nK} \left(\frac{1}{\theta} - \frac{1}{\theta^*} \right) \right)}{\left(\exp \left(\frac{qV_{OC}}{nK\theta^*} \right) - 1 \right)} \quad (3.7)$$

where E_G is the band gap energy of semi-conductor (1.12eV for the silicon), n is the diode ideality factor which takes typically a value between 1 and 2, K and q are Boltzmann's constant and the electron charge, respectively.

Final current of the PV cell, i_c , is given in:

$$i_c = i_{ph} - i_{sat} \left(\exp \left(\frac{v_c + i_c r_s}{nV_T} \right) - 1 \right) - \frac{v_c + i_c r_s}{r_p} \quad (3.8)$$

where $V_T = K\theta/q$ is the thermal voltage. Equation (3.8) has five unknown parameters: i_{ph} , i_{sat} , n , r_s and r_p . According cases, the variations of the currents i_{ph} and i_{sat} could be taken into account, while

the other parameters n , r_s and r_p are kept constant or adjusted to fit better the current-voltage curve [97].

Taking into account N_s cells in series in one PV panel, and N_{pv} panels in series in the PVA, the PVA output current i_{pv} is given by :

$$i_{pv} = i_{ph} - i_{sat} \left(\exp \left(\frac{v_{pv} + i_{pv} N r_s}{n N V_T} \right) - 1 \right) - \frac{v_{pv} + i_{pv} N r_s}{N r_p} \quad (3.9)$$

where $N = N_s N_{pv}$.

So, the $i_{pv} - v_{pv}$ curve is an implicit and non linear equation with four variables, \mathcal{G} , θ , i_{pv} and v_{pv} , and three unknown parameters: n , r_s and r_p . This function can be expressed as $i_{pv} = f(\mathcal{G}, \theta, v_{pv}, i_{pv}, n, r_s, r_p)$

The classical single-diode model, with three unknown parameters whose values are depending to the weather operating conditions, involves an important computation effort. Thus, for each set of weather operating conditions, the model parameters must be computed using the measurement of weather conditions as well as the current and voltage measurement.

The parameter identification method uses experimental test results obtained at MPP of the PVA, for days having different solar irradiance profiles, and focuses on minimizing the error between the measured current and the calculated from the mathematical model [97, 102]. This minimization provides optimal values of the desired parameters. It is noted that the parameter values vary greatly depending on weather conditions. So, to obtain reliable and valid results for any operating condition, this model can lead to significant errors.

The use of parameter values shows that for every given pair of \mathcal{G} and θ , the modeling of PVA implies knowledge of current and voltage measurements of PVA to recalculate the parameters. So, knowing that the goal is to find a reliable model whatever the weather operation, this model cannot be adopted in our study.

The two models presented above show that their use requires measures of current and voltage, or power, in the parameter identification. Both models can be applied with a reasonable margin of error only for *a posteriori* applications.

To achieve our goal, *i.e.* forecasting PVA production, a purely experimental model based on measurements of current i_{pv} and voltage v_{pv} , measurements done for different couples (\mathcal{G}, θ) is proposed as follows.

III.3.1.2.3. Simple experimental prediction model

Depending on different PV technology and manufacturers, PV panel characteristics vary quite much. General PV models could be limited in reflecting these differences.

One experimental PV prediction model is proposed in [97]. Furthermore, it should be noted that this study has been part of a thesis focused on the PV modeling and developed in our laboratory research team [103]. The proposed simple experimental prediction model is based on PV panel indoor experimental tests. One exemplary PV panel is tested under different levels of constant irradiance and different cell temperature. The model is drawn from a series of MPP voltages and currents ($v_{PV_{MPP}}$ and $i_{PV_{MPP}}$) of a PV panel, measured for several levels of irradiance at given cell temperatures. The data are obtained from the measurement of maximum output voltage and current variation depending on PV cell temperature increasing under a constant irradiance. Then, as shown in Figure 40, they are combined to form two 2-dimension Look-Up Tables (LUT), whose inputs are \mathcal{G} and θ , and the outputs are $v_{PV_{MPP}}$ and $i_{PV_{MPP}}$. The LUT can then be used in prediction of PVA power.

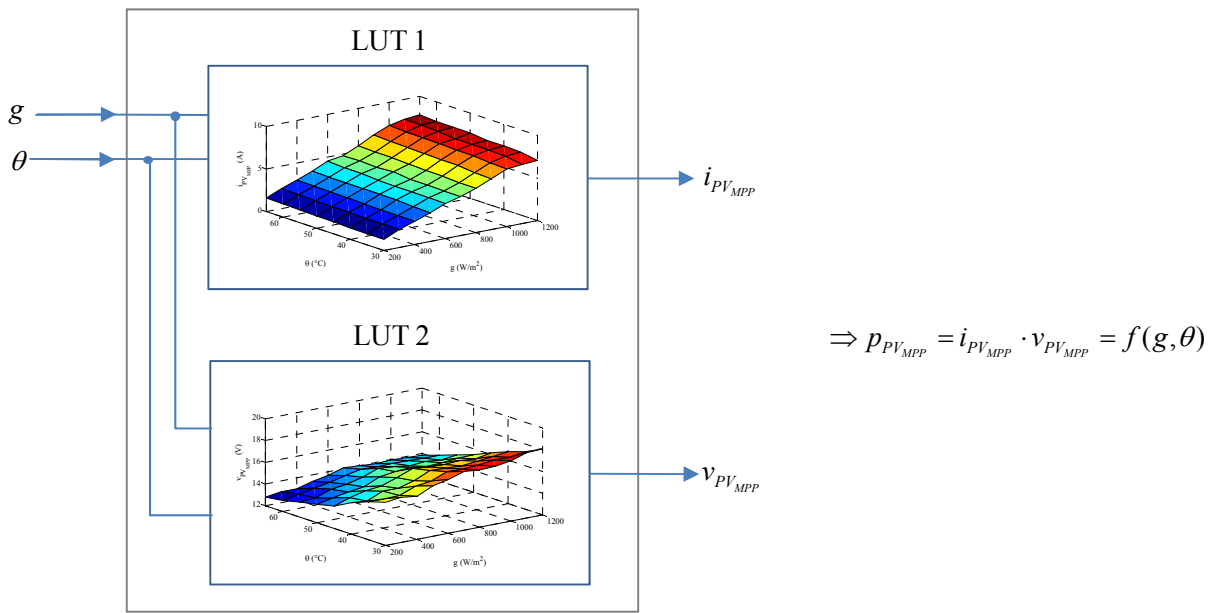


Figure 40. Experimental prediction model generic scheme.

Given the difficulty of making such measurements with desired solar irradiance (irradiance rapid change, or unwanted cell temperature), for this model, a bench test and measurement based on an artificial irradiance are proposed and realized.

Test bench description. The indoor experimental tests have been done on a PV panel identical to those installed on the roof, *i.e.* the PVA outdoor installation. The PV panel is shined with halogen lamps (18.6kW total power), as shown in Figure 41 (a). Depending on the projection distance, this device provides an irradiance range from 200W/m² to 1200W/m². The irradiance is measured with two pyranometers (spectral sensitivity is between 400nm and 1100nm), and two temperature sensors PT100 are used to measure the cell temperature, Figure 41 (b). If the PV panel is shined homogeneously, the readings of the pyranometers are the same; the same consideration is taken for temperature sensors. Tests were conducted only for those conditions that the two readings are homogeneous.

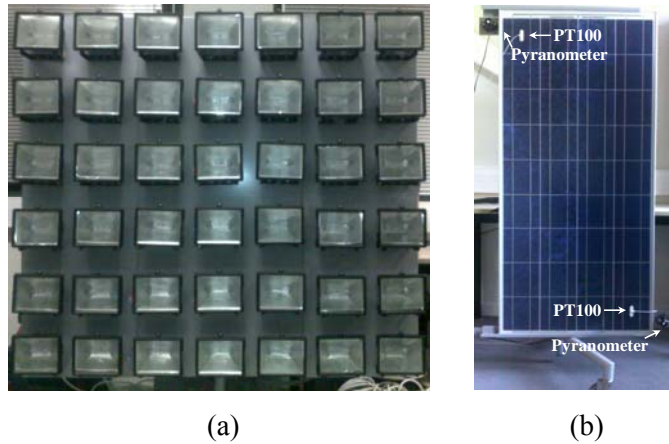


Figure 41. Images of the experimental devices.

Process measurements. For experimental test to extract the PV characteristics, the electrical scheme is shown in Figure 42: one PV panel, power converter leg B_1 , programmable DC electronic load used to absorb and dissipate the PV power, inductance $L_{PV} = 20\text{mH}$ whose internal resistance is neglected, and capacity $C = 1000\mu\text{F}$. All the measurements and the converter switching function f_{B1} are controlled in real time by dSPACE 1104. In order to obtain the current-voltage characteristic curve, a hysteresis control is used to impose a ramp current through the PV panel.

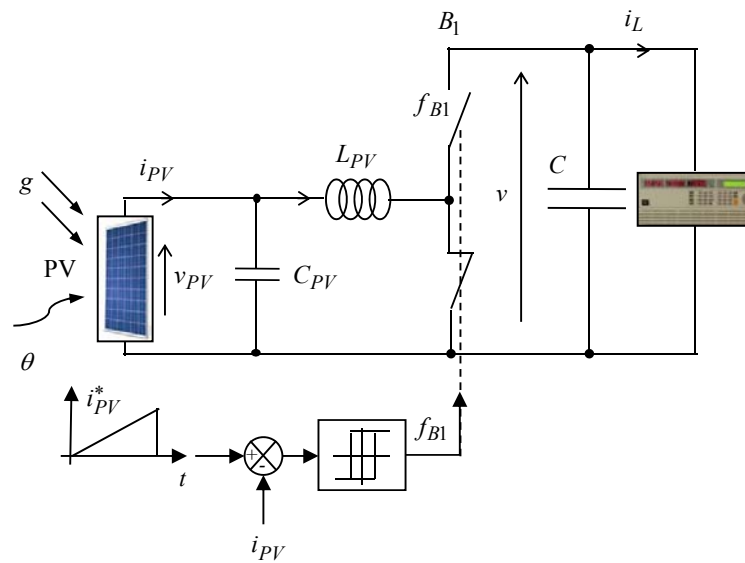


Figure 42. Process measurements electrical scheme.

Below it is given a typical example of current-voltage characteristics (Figure 43) and power-voltage (Figure 44) characteristics measured according to increasing temperature and under constant irradiance equal to $1000\text{W}/\text{m}^2$. The negative effect of PV cell temperature can be noted.

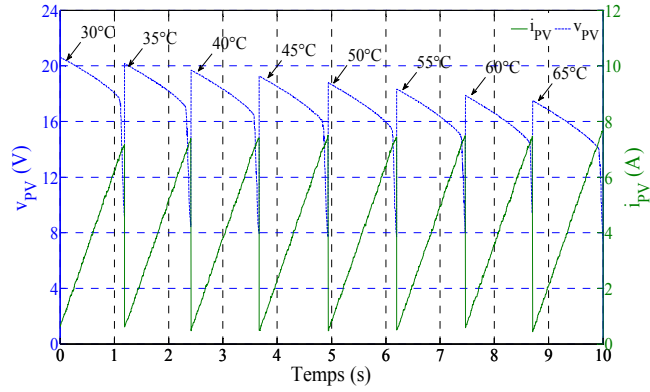


Figure 43. A typical example of current-voltage characteristics by proposed experimental test.

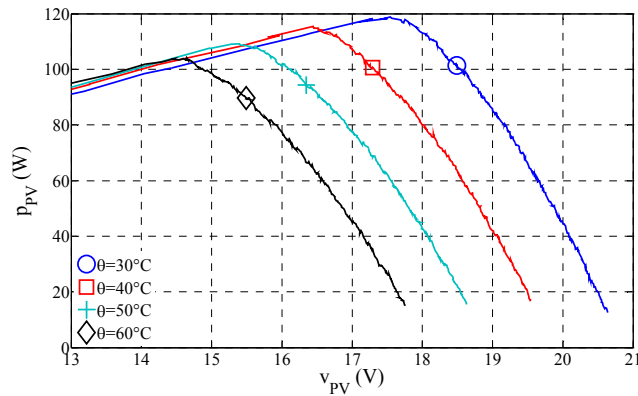


Figure 44. A typical example of power-voltage characteristics by proposed experimental test.

Experimental data acquisition. Once the characteristic is available for given irradiance and cell temperature, the voltage and the current, corresponding to MPP, are found. Concerning the maximum irradiance, 1200W/m^2 , and cell temperature, 65°C , for which the experimental tests were performed are normal limits according to findings on the actual weather conditions measured using the experimental platform during 2 years. However, the lower limits of irradiance and temperature that could be ensured during testing in our laboratory are 200W/m^2 and 30°C respectively. This is due to technical limitations of the experimental setup.

Figure 45 and Figure 46 show the obtained data that are stored in LUT. Hence, knowing the irradiance and cell temperature measurement, the values $v_{PV_{MPP}}$ and $i_{PV_{MPP}}$ could be found. For any irradiance or cell temperature value out of these data, the LUT uses a linear approximation of the values of $v_{PV_{MPP}}$ and $i_{PV_{MPP}}$ and then, the maximum power $P_{PV_{MPP}}$ can be estimated. Thus, $P_{PV_{MPP}}$ can be written as:

$$P_{PV_{MPP}} = f(g, \theta) \quad (3.10)$$

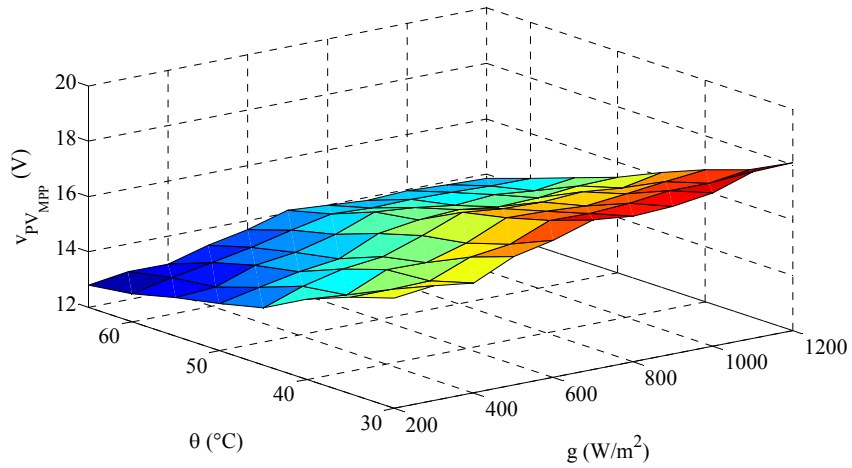


Figure 45. Experimental data of voltage model, measured function to g and θ .

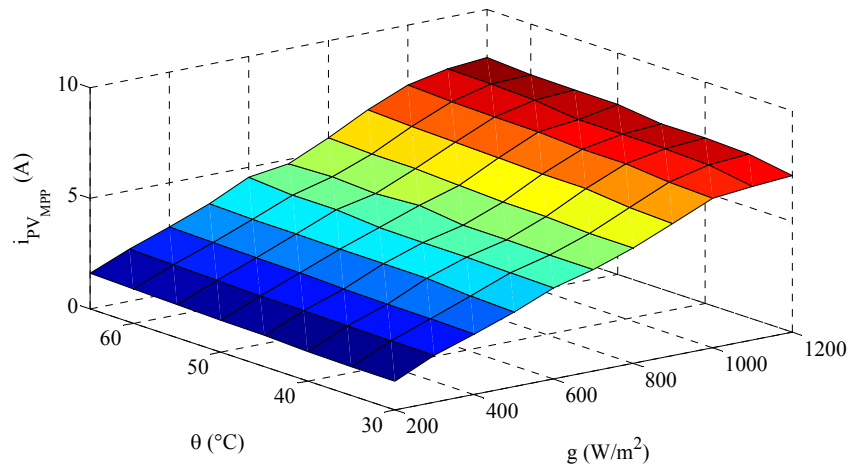


Figure 46. Experimental data of current model, measured function to g and θ .

This purely experimental model, designed from a PV panel, is extended to the PVA, which is used to calculate the PVA power for each measurement point.

III.3.1.2.4. Experimental validation of PV power prediction model

In order to give best PVA power prediction for advanced energy management in microgrid, the experiment goal is to validate prediction by the proposed experimental model. Three tests were carried out corresponding to three different irradiance profiles, on 1st, 5th and 26th of October 2011, in Compiègne, as illustrated in Figure 47.

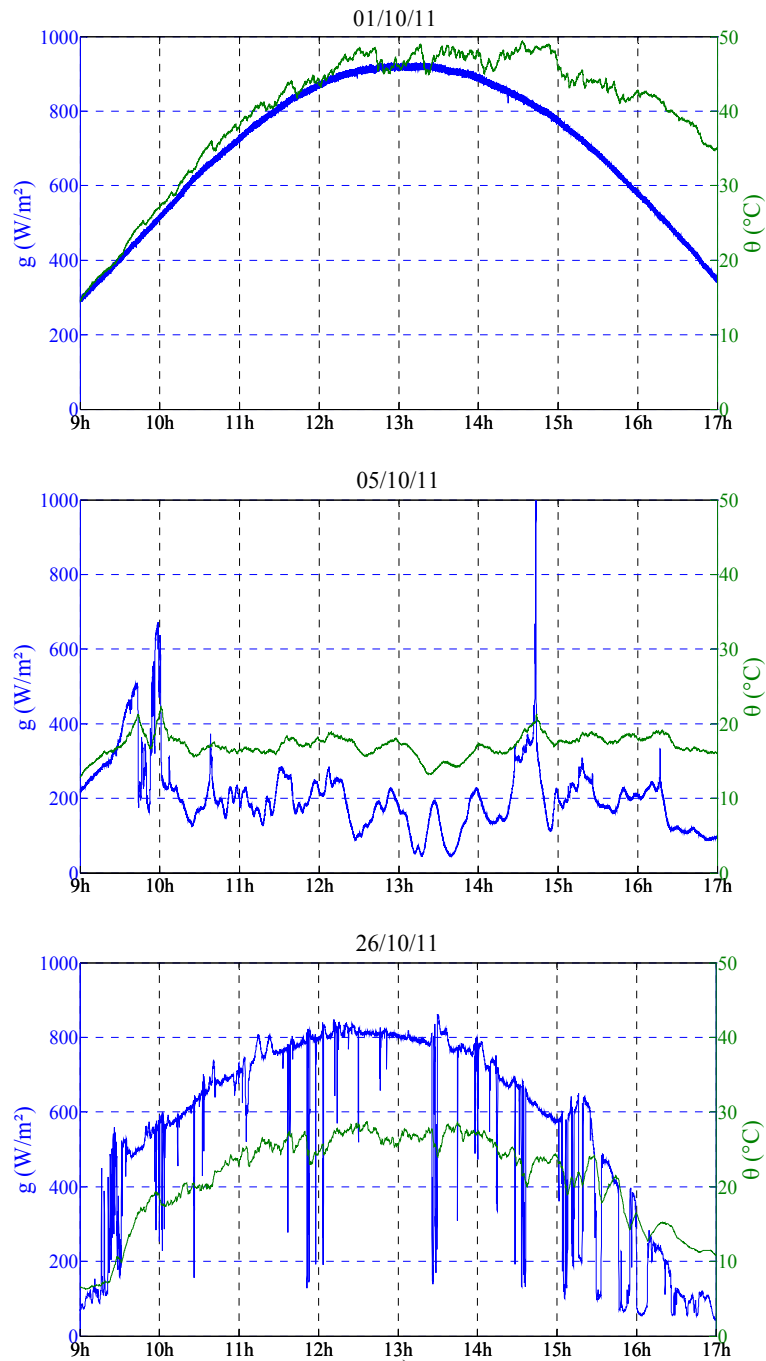


Figure 47. Operating conditions of the experimental tests.

The comparison of the power calculated by the experimental prediction model and the power measured during the test is presented in Figure 48, for the three solar irradiance cases. For the simple experimental prediction model, the power $P_{PV_{MPP}}$ is obtained following LUT for the same given weather conditions of each day of the test.

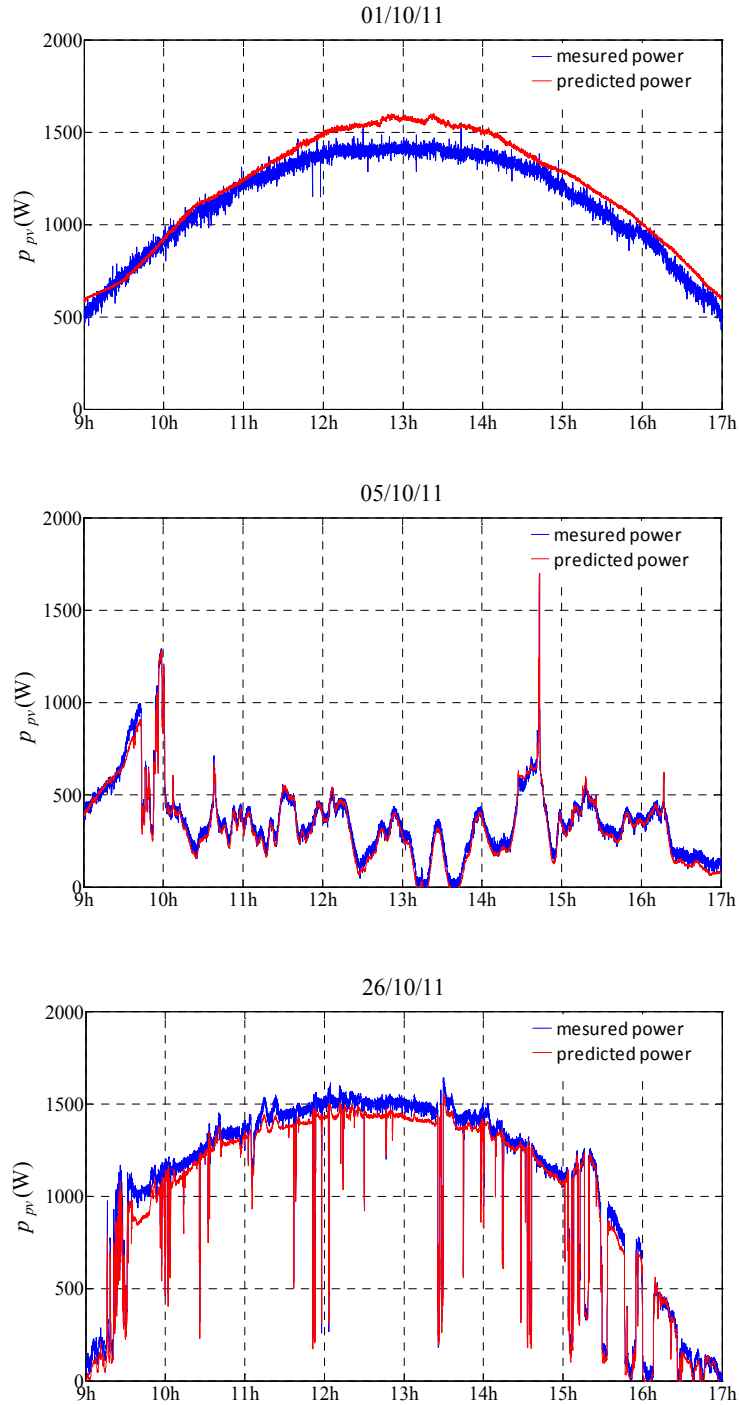


Figure 48. Comparison of PVA output power measured and predicted.

Accuracy is measured by the value of the mean absolute error of PVA output power of the proposed model, Δp_{PV} , which is calculated by (3.11) and presented in Table 5.

$$\Delta p_{PV} = \sum_{y=1}^z \frac{|p_{PVM}^y - p_{PV}^y|}{z} \quad (3.11)$$

where z is the total number of measurement points, $p_{PV_m}^y$ is the measured power for each measurement point y , and p_{PV}^y is the predicted power for each measurement point y calculated by the proposed prediction model.

Table 5 Mean absolute error given by the experimental prediction model.

Day test	Error of PVA output power
01/10/2011	84.9W
05/10/2011	30W
26/10/2011	58.7W

The proposed purely experimental model has a larger discrepancy in the measurement of October 1, with a mean absolute error of 84.9W. Despite this deficit, unlike the other two models, it can be useful in many applications, *a priori*, because there is no determination of necessary parameter depending on the operating conditions. However, the model accuracy depends on one hand on the number of data stored in the LUT, and on the linear approximation method, on the other hand, which is necessary for the calculation of the maximum power corresponding to the values that are not included in the two LUT by measurement data. Indeed, the laboratory conditions used for the construction of this model have led to record data for PV cell temperature taken between 30°C and 65°C and for irradiance between 200W/m² and 1200W/m². Thus, this model could be improved by at least adding more data, calculating PV cell temperature from ambient temperature and solar irradiance, and taking into account the PV ageing phenomena.

In conclusion, this kind of model, improved and adapted for each PV panel manufacturer, could be successfully used to predict the power.

III.3.2. Load power prediction

The second variable output prediction layer to calculate is the prediction power of the load, P_{L_PRED} . Every type of tertiary buildings, such as commerce, office, administration, two-shift manufacturing, has a unique pattern of energy consumption. Such profiles changes mainly according to occupants and weather conditions; whence the uncertainty of prediction is from.

However, from statistical data as average power readings available on the energy monitoring site of power providers for its customers subscribing to the service or information about building operation data given by automated BMS [99, 104] a predictive power can be obtained. This power curve must be correlated with the "user command" and information from the smart grid of the variable energy prices over time. The obtained result thus may also be confronted with the possible load shedding indicating the minimum level of power supply.

Concerning the management of a building appliances there are very few studies finished, but now, with the advent of smart meters, more work is being carried out in this direction [105-106]. At the present stage of the research, in this thesis a specific approach to correctly estimate the predicted load power P_{L_PRED} is not developed.

Since the experimental validation is based on a load emulator, this prediction is taken into account in the calculations of energy management layer as a random estimation with an error margin of $\pm 10\%$ with the chosen arbitrary load power curve demanded by the load during the test.

Regarding the load shedding possibilities, for simulation tests in this Chapter, arbitrary intervals and values are chosen and imposed. However, continuous load shedding is assigned to highlight the control respect to power limits in experimental results in Chapter IV. Moreover, the algorithms currently in place can be adapted easily and quickly to the development of automatic calculations of P_{L_PRED} and of load shedding limits.

III.4. Energy management layer

With the forecasted production and consumption, an optimization of microgrid power flow can be performed. The optimization goal is to obtain the best power distribution among the sources, so to reduce energy cost, reduce grid power peak consumption in grid-connected mode, minimize fuel consumption in off-grid mode and avoid load shedding and PVA shedding in both modes.

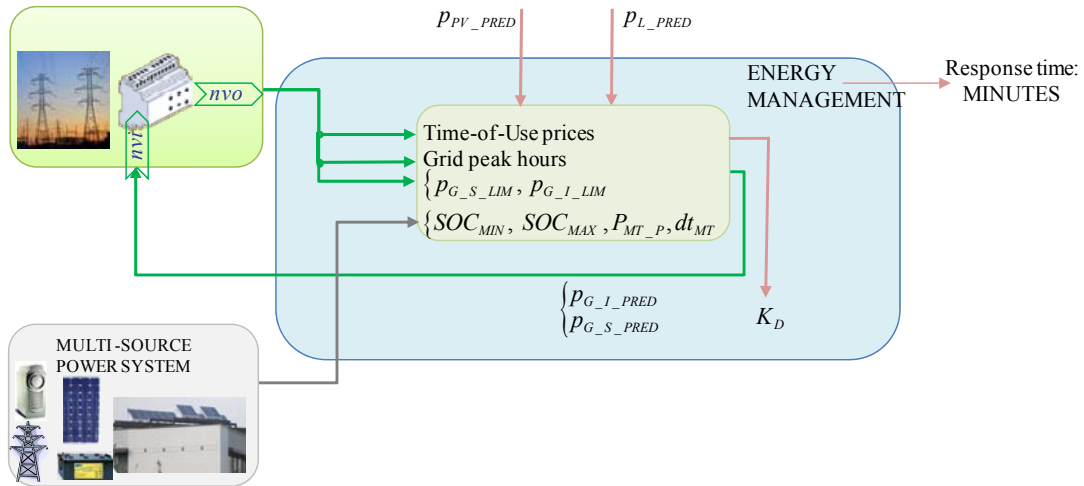


Figure 49. Energy management layer design.

Energy management and cost optimization is one of the most important layers of the supervision system and is illustrated in Figure 49.

The inputs of this layer are provided by the upper layer, P_{PV_PRED} and P_{L_PRED} , on the one hand, and the smart grid message, containing $P_{G_S_LIM}$ and $P_{G_I_LIM}$ as power limits, TOU energy tariff, on the other hand. Also, knowledge of the storage SOC limits should be provided.

The main output of this layer is the distribution coefficient K_D , signifying power sharing between the grid power p_G^* and the storage power p_S^* in grid-connected mode on the one hand, and triggering MT generation in off-grid mode on the other hand. Thus, this layer must calculate the required output to the proper functioning of the power system.

The objective of this layer is to compute off-line, but also able to calculate on-line with updated forecasting, the expected optimized operating power flow based on predicted powers previously calculated and taking into account the grid power limits and element constraints. The optimization focuses on minimizing energy costs, hence it needs to know in advance the TOU prices over time provided by the smart grid message. The main result is the calculation of K_D , which is time varying.

In addition, optimization results should allow the calculation of the expected power to be injected, $P_{G_I_PRED}$, into the utility grid, and of the power required in predictable absorption by the load from the utility grid, $P_{G_S_PRED}$. These two predictions can be transmitted to the smart grid, as network variable input messages. This is considered as helpful information for energy production planning at the central operator, for example.

III.4.1. Optimization problem formulation

Optimization should take into consideration the whole power flows in the power system, as well as satisfying the power balance with respect to conversion efficiency and all other imposed constraints.

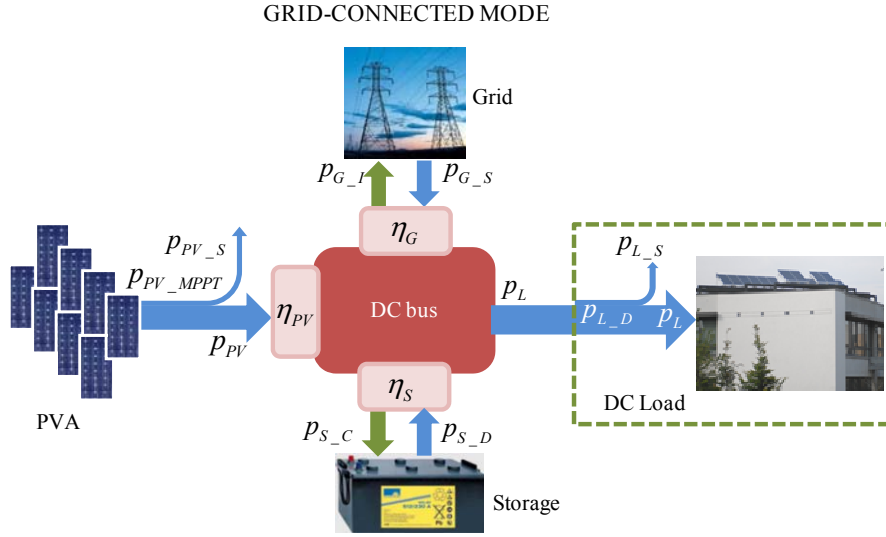
The controllability of the sources is different. PVA production changes according to weather condition and load is demanded by end-users; they cannot be fully controlled, but partially interfered by the supervision. Storage and grid can be fully controlled. MT is assigned to work in duty cycle and cannot be fully controlled neither.

Since constraints are different in grid-connected mode and off-grid mode, optimization problem is formulated separately.

III.4.1.1. Grid-connected mode

During the grid-connected mode, the main goals of the proposed DC microgrid are: decreasing grid peak consumption, avoiding undesired grid power injection, and reducing global energy cost.

An overview of power flow in grid-connected mode is shown in Figure 50. PVA, storage and grid are coupled on the DC bus through their dedicated converters, whose conversion efficiency are η_{PV} , η_S and η_G respectively. Load demands power directly from the DC bus.



Variables	Power (W)
p_{G_I}	Grid injection power
p_{G_S}	Grid supply power
p_L	Load power
p_{L_S}	Shed load power by load shedding
p_{L_D}	Load demand power
p_{PV}	PVA power
p_{PV_MPPT}	PVA power with MPPT algorithm
p_{PV_S}	Shed PV power
p_{S_C}	Storage charging power
p_{S_D}	Storage discharging power

Figure 50. Power flow in grid-connected mode.

In case of protecting storage from overcharging and respecting grid power injection limits from smart grid message, the PVA production can be partially shed by constrained PVA production algorithm. The PV shed power is noted as p_{PV_S} , and it is considered $p_{PV_S} = 0$ in the MPPT algorithm. For each time instant t , the PVA production p_{PV} is described by:

$$p_{PV}(t) = p_{PV_MPPT}(t) - p_{PV_S}(t) \quad (3.12)$$

The p_{PV_S} values are calculated by optimization, however, the PV shedding should not induce negative power, so it is constrained:

$$p_{PV}(t) \geq 0 \quad (3.13)$$

The load should be satisfied according to end-user demand. In case of insufficient storage and grid access limits given by smart grid message, the load power demand p_{L_D} cannot be fully met, and the load must be partially shed to maintain the operation of the critical load. The proportion in load power that must be shed is noted as p_{L_S} , and the load power p_L is following (3.14).

$$p_L(t) = p_{L_D}(t) - p_{L_S}(t) \quad (3.14)$$

The power p_{L_s} is determined by optimization; it should not induce negative power neither, so it is constrained:

$$p_L(t) \geq 0 \quad (3.15)$$

Temporary load partial shedding could be a solution to reduce utility grid mismatching, or to obtain less energy consumption, if agreed by end-user. These operations should be controlled by the supervision control (minimizing or avoiding load shedding...).

The storage is operated by current closed-loop control, and the storage power can be controlled by giving corresponding current reference. The storage state of charge soc must be respected to its upper and lower limits, SOC_{MAX} and SOC_{MIN} correspondingly, to protect the storage from overcharging and over discharging, as described by (3.16) with soc calculation given by (3.17).

$$SOC_{MIN} \leq soc(t) \leq SOC_{MAX} \quad (3.16)$$

$$soc(t) = SOC_0 + \frac{1}{3600 \cdot v_S \cdot C_{REF}} \int_{t_0}^t (p_{S_c}(t) - p_{S_d}(t)) dt \quad (3.17)$$

where storage power $p_s(t)$ is defined as $p_s(t) = p_{S_c}(t) - p_{S_d}(t)$, where $p_{S_c}(t)$ and $p_{S_d}(t)$ are storage charging and discharging power respectively.

When the soc limit is not reached, the PVA production should not be limited, as in (3.18).

$$p_{PV_s}(t) = 0 \text{ if } soc(t) < SOC_{MAX} \quad (3.18)$$

The grid connection is controlled by current closed-loop control. As already mentioned in this study, to integrate with the smart grid operation, limits for grid power supply $p_{G_s_LIM}$ and grid power injection $p_{G_I_LIM}$ are imposed by smart grid messages. By these two limits, grid problems, such as performing peak shaving, avoiding undesired injection or downscaling injection fluctuations caused by intermittent PV productions, can be improved. During microgrid operation, the grid power should be controlled to satisfy (3.19) and (3.20).

$$0 \leq p_{G_I}(t) \leq p_{G_I_LIM} \quad (3.19)$$

$$0 \leq p_{G_S}(t) \leq p_{G_S_LIM} \quad (3.20)$$

Considering that all powers are always positive, as sign convention, the physical law of power balancing is described by:

$$p_L(t) + \frac{1}{\eta_G} p_{G_I}(t) + \frac{1}{\eta_S} p_{S_c}(t) = \eta_G p_{G_S}(t) + \eta_S p_{S_d}(t) + \eta_{PV} p_{PV}(t) \quad (3.21)$$

Energy management layer objective is to minimize the total energy cost of system C_{total} , which consists of grid energy cost C_G , storage energy cost C_S , PVA shedding cost C_{PVS} , and load shedding cost C_{LS} , as in (3.22).

$$\text{Minimize } C_{total} = C_G + C_S + C_{PVS} + C_{LS} \quad (3.22)$$

Taking into consideration multi-criteria such as peak shaving, avoiding undesired injection, making full use of available storage capacity and avoiding possible load shedding and PVA shedding together, it is difficult to refer to real energy tariffs. In this study, tariff and cost function are rather a technique for optimizing multi-criteria at the same time, than only calculating energy invoices. On the other hand, concerning PVA shedding, load shedding and storage, their energy tariffs calculation is quite complex and depends on the chosen technology. This is why energy tariffs used in this study are somewhat arbitrary; however, numerical values of energy tariffs given here below are chosen to highlight the logic of management strategy which seems in energy trend for the next twenty years. Nevertheless, only relative energy tariff can change the optimization results, which means that the optimized power flow remains the same if the energy tariff absolute values are changed but the energy tariff for different sources remain in the same order.

By calculating the energy cost with each time increment Δt , C_G is defined by (3.23). According to this definition, the grid power could be bought or sold at the same price.

$$C_G = \frac{1}{3.6 \times 10^6} \sum_{t_i=t_0}^{t_F} [c_G(t_i) \cdot \Delta t \cdot (-p_{G_I}(t_i) + p_{G_S}(t_i))] \quad (3.23)$$

with $t_i = \{t_0, t_0 + \Delta t, t_0 + 2\Delta t, \dots, t_F\}$

Although today the PV energy grid injection benefits incentive tariffs, knowing that there is a heavily subsidized part, this study takes into account a single rate for energy purchased or sold, and the grid energy tariff is defined by (3.24) according to peak hour or normal hours:

$$c_G(t) = \begin{cases} c_{NH} = 0.1 \text{ €/kWh} & \text{for } t \in \text{normal hours (NH)} \\ c_{PH} = 0.7 \text{ €/kWh} & \text{for } t \in \text{peak hours (PH)} \end{cases} \quad (3.24)$$

with c_{NH} the normal hour tariff and c_{PH} the peak hour tariff. For normal hours, an average energy tariff, close to that offered by most providers, is considered. In contrast, for peak hours, a very penalizing purchase tariff is chosen which is not proposed today. The reason for this assumption lies in providing DR, for most critical hours, to perform power peak shaving.

Storage aging should be considered to give an energy tariff of storage using. However, for this study, the cost of storage C_S is defined in (3.25)

$$C_S = \frac{1}{3.6 \times 10^6} \sum_{t_i=t_0}^{t_F} [c_S(t_i) \cdot \Delta t \cdot (p_{S_C}(t_i) + p_{S_D}(t_i))] \quad (3.25)$$

with $c_s = 0.01$ €/kWh an arbitrary storage energy tariff.

After installation of PVA, only maintenance involves costs while the production does not need extra fees. However, shedding PV power represents that the asset is not fully used. So, the PVA power shedding is penalized in the optimization and the cost of PVA shedding is defined by (3.26):

$$C_{PVS} = \frac{1}{3.6 \times 10^6} \sum_{t_i=t_0}^{t_F} c_{PVS}(t_i) \cdot \Delta t \cdot p_{PV_S}(t_i) \quad (3.26)$$

with $c_{PVS} = 1$ €/kWh an arbitrary PVA power shedding tariff.

The load power is demanded by the end-user, load shedding introduces inconvenience for end-users and is penalized in optimization as well. The cost of load shedding is defined by (3.27):

$$C_{LS} = \frac{1}{3.6 \times 10^6} \sum_{t_i=t_0}^{t_F} c_{LS}(t_i) \cdot \Delta t \cdot p_{L_S}(t_i) \quad (3.27)$$

with $c_{LS} = 1$ €/kWh an arbitrary load power shedding tariff.

In order to limit the power grid fluctuations, grid power changing rate limits are introduced as:

$$\begin{cases} p_G(t_i) - p_G(t_{i-1}) \leq \text{Limit} \\ p_G(t_i) - p_G(t_{i-1}) \geq -\text{Limit} \end{cases} \quad (3.28)$$

As PVA energy grid injection benefits incentive tariffs, energy grid injection by power grid charged storage is forbidden. Thus, the following limits are imposed in order to ensure storage energy charge and grid injection only from PVA production.

$$\begin{aligned} p_G(t_i) \geq 0, p_S(t_i) \geq 0 & \quad \text{if} \quad \eta_{PV} p_{PV}(t_i) - p_{L_D}(t_i) \geq 0 \\ p_G(t_i) \leq 0, p_S(t_i) \leq 0 & \quad \text{if} \quad \eta_{PV} p_{PV}(t_i) - p_{L_D}(t_i) < 0 \end{aligned} \quad (3.29)$$

Finally, by considering the discrete time instant t_i , from t_0 to t_F , with the time interval Δt , the problem formulated by (3.22), can be completely mathematically expressed by :

Minimize $C_{total} = C_G + C_S + C_{PVS} + C_{LS}$

with respect to:

$$\begin{cases}
 p_L(t_i) + \frac{1}{\eta_G} p_{G_I}(t_i) + \frac{1}{\eta_S} p_{S_C}(t_i) = \eta_G p_{G_S}(t_i) + \eta_S p_{S_D}(t_i) + \eta_{PV} p_{PV}(t_i) \\
 SOC_{MIN} \leq soc(t_i) \leq SOC_{MAX} \\
 soc(t_i) = SOC_0 + \frac{1}{3600 \cdot v_S \cdot C_{REF}} \sum_{t_i=t_0}^{t_F} (p_{S_C}(t_i) - p_{S_D}(t_i)) \Delta t \\
 p_{PV}(t_i) \geq 0 \\
 p_L(t_i) \geq 0 \\
 0 \leq p_{G_I}(t_i) \leq p_{G_I_LIM} \\
 0 \leq p_{G_S}(t_i) \leq p_{G_S_LIM} \\
 p_G(t_i) - p_G(t_{i-1}) \leq \text{Limit} \\
 p_G(t_i) - p_G(t_{i-1}) \geq -\text{Limit} \\
 p_G(t_i) \geq 0, p_S(t_i) \geq 0 \quad \text{if} \quad \eta_{PV} p_{PV}(t_i) - p_{L_D}(t_i) \geq 0 \\
 p_G(t_i) < 0, p_S(t_i) < 0 \quad \text{if} \quad \eta_{PV} p_{PV}(t_i) - p_{L_D}(t_i) < 0 \\
 p_{PV_S}(t) = 0 \quad \text{if} \quad soc(t) < SOC_{MAX} \\
 t_i = \{t_0, t_0 + \Delta t, t_0 + 2\Delta t, \dots, t_F\}
 \end{cases} \quad (3.30)$$

III.4.1.2. Off-grid mode

In off-grid mode, the DC microgrid has to supply the DC load as indicated by the end-user while reducing global energy cost. The power flow in the off-grid mode is shown in Figure 51.

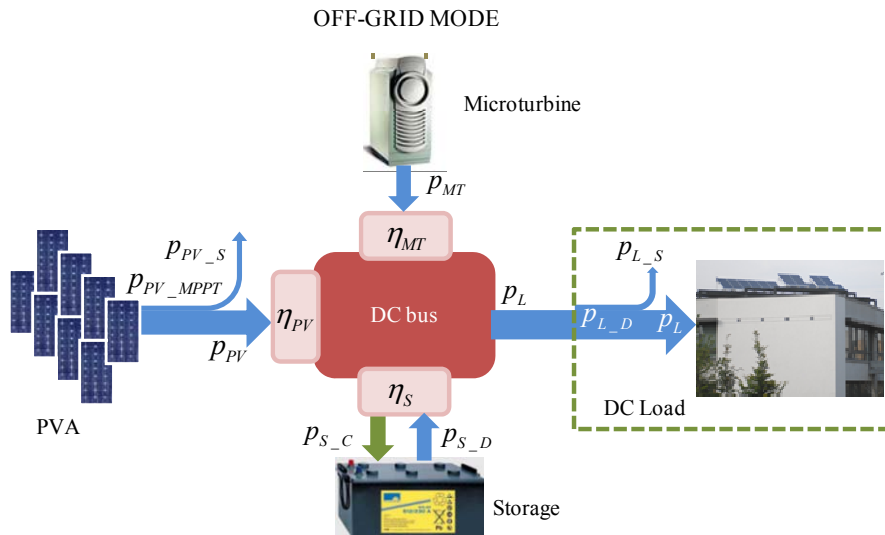


Figure 51. Power flow in off-grid mode.

The MT provides power only in off-grid mode; furthermore, MT cogeneration aspect is not considered in this work. During the off-grid mode, the main goals of the proposed DC microgrid are: minimizing MT fuel consumption, respecting soc limits, reducing load shedding and PVA shedding.

In off-grid mode, PVA, storage and load constraints remain the same, and the two controllable sources are storage and MT. The load supply safety is ensured by the MT whose converter efficiency is η_{MT} .

The power should be balanced on the DC bus considering conversion efficiency:

$$\eta_{PV} p_{PV}(t_i) + \eta_{MT} p_{MT}(t_i) + \eta_S p_{S_D} = \frac{1}{\eta_S} p_{S_C}(t_i) + p_L(t_i) \quad (3.31)$$

Due to low dynamic response, frequent start and stop or output low power reduces MT efficiency and introduces supplementary cost. In this study, the MT is assigned with two operating states: off and output rated power given by (3.32).

$$p_{MT}(t_i) = j P_{MT_P} \quad j \in \{0, 1\} \quad (3.32)$$

where P_{MT_P} is the rated power of the MT.

Working duty cycle is also assigned to the MT control as:

$$\begin{aligned} p_{MT}(t_i) &= p_{MT}(t_{i-1}) \quad \text{if } \text{rem}(t_i / dt_{MT}) \neq 0 \\ t_i &= \{t_0 + \Delta t, t_0 + 2\Delta t, \dots, t_F\} \end{aligned} \quad (3.33)$$

where dt_{MT} is the time duration of the MT working duty cycle, and rem is the function that returns the remainder of the division.

The MT consumes fuel and the cost is calculated as:

$$C_{MT} = \frac{1}{3.6 \times 10^6} \sum_{t_i=t_0}^{t_F} c_{MT}(t_i) \cdot p_{MT}(t_i) \cdot \Delta t \quad (3.34)$$

with $c_{MT} = 1.1$ €/kWh an arbitrary MT production tariff.

Since the MT works in duty cycle, it induces the case that storage is charged by rated PVA power plus rated MT power. The high charging rate can largely affect the storage life. Thus, in off-grid mode, the storage power is limited as:

$$-P_{S_MAX} \leq p_S(t_i) \leq P_{S_MAX} \quad (3.35)$$

Load shedding is not permitted when there is sufficient power supply, and PVA shedding is not permitted when the production can be totally consumed. These constraints are implied in the optimization objective, and are also given in explicit form:

$$\begin{aligned} &\text{if } \eta_{PV} p_{PV_MPPT}(t_i) > p_{L_D}(t_i) \quad \text{then } p_{L_S}(t_i) = 0 \\ &\text{if } \eta_{PV} p_{PV_MPPT}(t_i) = p_{L_D}(t_i) \quad \text{then } \begin{cases} p_{L_S}(t_i) = 0 \\ p_{PV_S}(t_i) = 0 \end{cases} \\ &\text{if } \eta_{PV} p_{PV_MPPT}(t_i) < p_{L_D}(t_i) \quad \text{then } p_{PV_S}(t_i) = 0 \end{aligned} \quad (3.36)$$

To ensure continuous operation, soc lower limit at the end of one operation can be assigned:

$$soc(t_F) \geq SOC_F \quad (3.37)$$

with SOC_F a constant for the soc value at final time.

Considering other elements constraints, the whole problem is formulated as:

$$\begin{aligned}
& \text{Minimize } C_{total} = C_{MT} + C_{PVS} + C_{LS} + C_S \\
& \text{with respect to:} \\
& \left\{ \begin{aligned}
& \eta_{PV} p_{PV}(t_i) + \eta_{MT} p_{MT}(t_i) + \eta_S p_{S_D} = \frac{1}{\eta_S} p_{S_C}(t_i) + p_L(t_i) \\
& p_S(t_i) = p_{S_C}(t_i) - p_{S_D}(t_i) \\
& p_{PV}(t_i) = p_{PV_MPPT}(t_i) - p_{PV_S}(t_i) \\
& p_L(t_i) = p_{L_D}(t_i) - p_{L_S}(t_i) \\
& \text{if } \eta_{PV} p_{PV_MPPT}(t_i) > p_{L_D}(t_i) \quad p_{L_S}(t_i) = 0 \\
& \text{if } \eta_{PV} p_{PV_MPPT}(t_i) = p_{L_D}(t_i) \quad \begin{cases} p_{L_S}(t_i) = 0 \\ p_{PV_S}(t_i) = 0 \end{cases} \\
& \text{if } \eta_{PV} p_{PV_MPPT}(t_i) < p_{L_D}(t_i) \quad p_{PV_S}(t_i) = 0 \\
& SOC_{MIN} \leq soc(t_i) \leq SOC_{MAX} \\
& soc(t_i) = SOC_0 + \frac{100\%}{3600 \cdot v_S \cdot C_{REF}} \sum_{t_i=t_0}^{t_F} p_S(t_i) \Delta t \\
& soc(t_F) \geq SOC_F \\
& p_{PV}(t_i) \geq 0 \\
& p_L(t_i) \geq 0 \\
& p_{PV_S}(t_i) \geq 0 \\
& p_{L_S}(t_i) \geq 0 \\
& 0 \leq p_{MT}(t_i) \leq P_{MT_P} \\
& -P_{S_MAX} \leq p_S(t_i) \leq P_{S_MAX} \\
& p_{MT}(t_i) = j P_{MT_P} \quad j \in \{0,1\} \\
& t_i = \{t_0, t_0 + \Delta t, t_0 + 2\Delta t, \dots, t_F\} \\
& \left\{ \begin{aligned}
& p_{MT}(t_i) = p_{MT}(t_{i-1}) \quad \text{if } rem(t_i / dt_{MT}) \neq 0 \\
& t_i = \{t_0 + \Delta t, t_0 + 2\Delta t, \dots, t_F\}
\end{aligned} \right.
\end{aligned} \right. \quad (3.38)
\end{aligned}$$

III.4.2. Solving the problem

Energy optimization are usually solved by linear programming [107] or dynamic programming [60, 108] technique. Dynamic programming can solve non-linear problem, while linear programming solves problems satisfying linear forms. Linear programming can be more efficiently solved with less time and memories [109].

Linear programming techniques are common approaches to solve optimization problems which can be expressed in the standard form:

difficult to solve than linear programs due the integer variables, our problem can be solved very efficiently by such a solver, even with a huge set of time points, as it can be seen in the result in section III.6. In fact, in order to express our problem in the syntax of the solver and to call the solving algorithm of the solver, a procedure written in C++ is used. This procedure output the optimal flow in a file for control parameter translation, which is then transmitted to the operation layer. The full C++ program that formulates the optimization problem in a CPLEX form and deals input/output files is given in Annex 3.

III.4.3. Interface for operation layer

The optimization calculates optimal power flow for both grid-connected mode and off-grid mode. Prediction layer provides the prediction of possible PVA power P_{PV_PRED} and load power evolutions P_{L_PRED} for the next day. According to the optimization formulation, energy management layer gives the optimized power flow of the sources. The optimized power flow is then translated to an interface parameter, which is the distribution coefficient K_D that is used for both grid-connected and off-grid mode, to control the microgrid in order to reproduce the optimization results in real operation.

With different operating mode, K_D is defined differently.

Firstly, in grid-connected mode, K_D represents the best power distribution between the grid and the storage. By the prediction metadata, the energy management layer estimates the optimum control power flow for the operation of next day, which is mainly the evolution of P_{S_D} , P_{S_C} , P_{G_S} , P_{G_I} .

The estimated optimum control power flow is then translated into control parameter K_D to run the operation layer. The optimum K_D is calculated by (3.42):

$$K_D = \frac{P_{S_C} + P_{S_D}}{P_{S_C} + P_{S_D} + P_{G_S} + P_{G_I}} \quad (3.42)$$

Thus, the optimum K_D sequence represents optimum power flow in one parameter. K_D is the interface parameter between the energy management layer and the operational layer. The advantage of using K_D lies in coupling easily power balancing and energy management, so that robust power balancing and optimization can be achieved at the same time. The power balancing strategy is designed to satisfy all constraints and is parameterized with K_D . Energy management layer gives only K_D through low speed communication to control the operation, instead of updating all power references in real time. Optimization can be re-perform on-line and update K_D sequence without interrupting power balancing, which takes full advantage of latest prevision and real-time system status. Moreover, since operation layer can keeps power balancing with any K_D value, the operation is robust to withstand prediction errors.

Secondly, in off-grid mode, the two controllable sources are storage and MT. Storage power can change continuously.

MT is assigned with two states: on or off. In this case, storage power is assigned in control strategy to balance power, and K_D is defined as switch signal for the MT as:

$$K_D = \text{boolean}(p_{MT} > 0) \quad (3.43)$$

When $K_D = 1$, the energy management layer orders the MT to start and output the rated power.

When $K_D = 0$, the MT has no specific order from the energy management layer.

It is the operation layer who determines to turn on or turn off the MT.

For the two operating modes, K_D is time variant sequence that contains sufficient information to represent optimized power flow.

III.5. Operation layer

Operation layer design is presented in Figure 52.

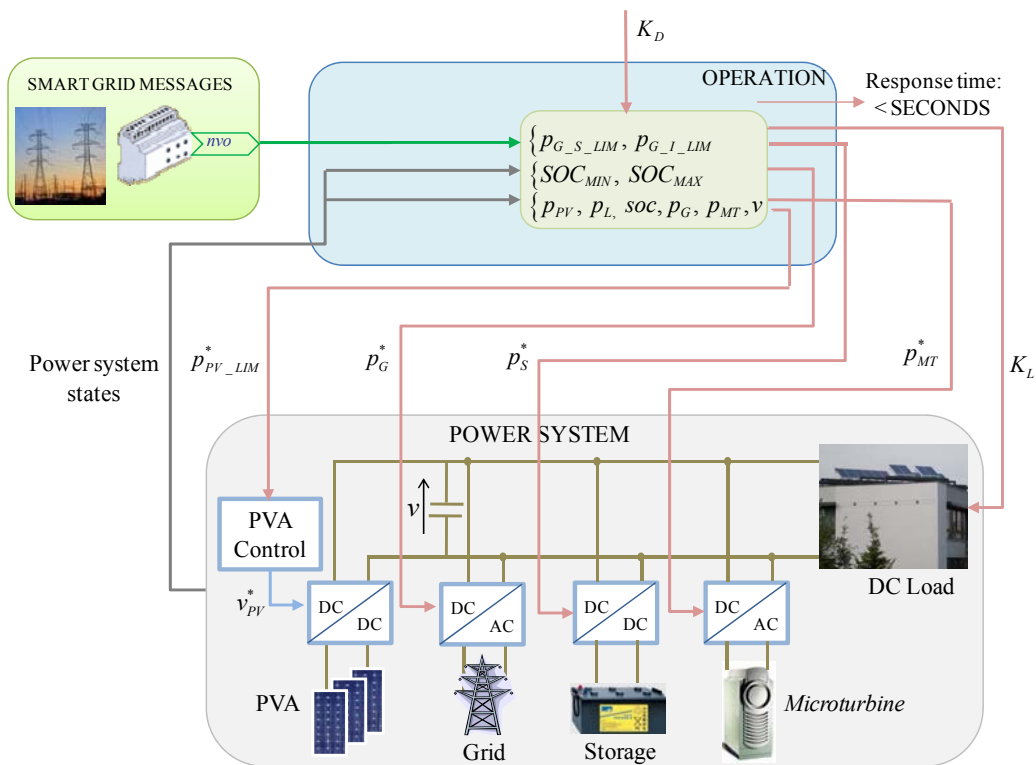


Figure 52. Operation layer design.

This layer aims at balancing power in the power system while respecting the energy management performed in upper layer.

Having defined K_D as interface between the energy management layer and the operation layer, adequate strategies in operation layer must be developed.

The control strategy should satisfy following requirements. On one hand, given the same predicted operating condition as in optimization, the control strategy is required to reproduce optimized power flow in real operating conditions. On the other hand, operation strategy must ensure robustness and withstand uncertainty introduced in predicted power (forecast data).

To ensure the correct operating of the power system, at least two algorithms are needed and have to be implemented, one for the PVA control, as described in section II.2, and the second to control the power balancing which description is given in this section. Theoretically, a third algorithm to control the load, by appliances shedding, should be required; however, as mentioned already, this is not developed in this thesis.

Based on the control strategy developed in power system study, this section gives operating algorithm for both grid-connected mode and off-grid mode with consideration of converter efficiency.

III.5.1. Grid-connected mode

Based on the power balancing strategy developed in Chapter II, an improved grid-connected power balancing control strategy for the supervision control is proposed, which takes into consideration the power electronic converter efficiency and permits continuous load shedding instead of three level load shedding.

In the developed algorithm for grid-connected operating mode, storage power control reference p_s^* is updated once more if grid power reaches its limit, signifying that the storage, if available, is used first in power balancing before performing load shedding or PVA constrained production.

Power balancing can be maintained with any K_D value. The power sharing proportion defined by K_D can be satisfied except for extreme cases. Concerning self-correcting ability in power balancing, the grid power represents the most important degree of flexibility, but PVA limited production and load shedding are also performed if necessary.

If there is not sufficient energy to supply the load (insufficient PVA production when the grid power is limited and the storage is empty), the load shedding is performed. In this case, the conversion efficiency is taken into consideration for load shedding.

As load shedding occurs only when storage reaches lower *soc* limit. The power flows from PVA and grid to the load. In such cases, the load power is expected not to exceed p_{L_LIM} , which is calculated as in (3.44).

$$p_{L_LIM}(t) = \eta_{PV} p_{PV}(t) + \eta_G p_{G_S_LIM}(t) \quad (3.44)$$

If the PVA production cannot be consumed, which means the storage reaches *soc* upper limit, the grid power reaches injection limit and the load does not consume enough. The PVA power should be limited. In this case, the power flows from PVA through the PVA converter to the DC bus. Load demands power directly from the DC bus. The grid demands power from DC bus through grid inverter.

The power to the DC bus should be equal to the power demanded from the DC bus. So, the powers balance should satisfy:

$$\eta_{PV} p_{PV_LIM}^* = p_L + \frac{1}{\eta_G} p_{G_I_LIM} \quad (3.45)$$

And the PVA production limit is:

$$p_{PV_LIM}^* = \frac{1}{\eta_{PV}} \left(p_L + \frac{1}{\eta_G} p_{G_I_LIM} \right) \quad (3.46)$$

The overall control strategy is given in Figure 53.

III.5.2. Off-grid mode

In off-grid mode, the MT works in bang-bang mode and only the storage can be controlled continuously, which results in more difficulty in power balancing since lack of one degree of freedom compared to grid-connected mode.

As aforementioned, in off-grid mode, it could happen that the PVA outputs rated power while the MT is turned on and load consumption is low. Charging storage with high power will shorten storage life, so, at least one source needs to be limited or cut-off. The priority is defined as shedding PVA first, and then cut-off MT if SOC_{MAX} is reached.

The overall control strategy is given in Figure 54.

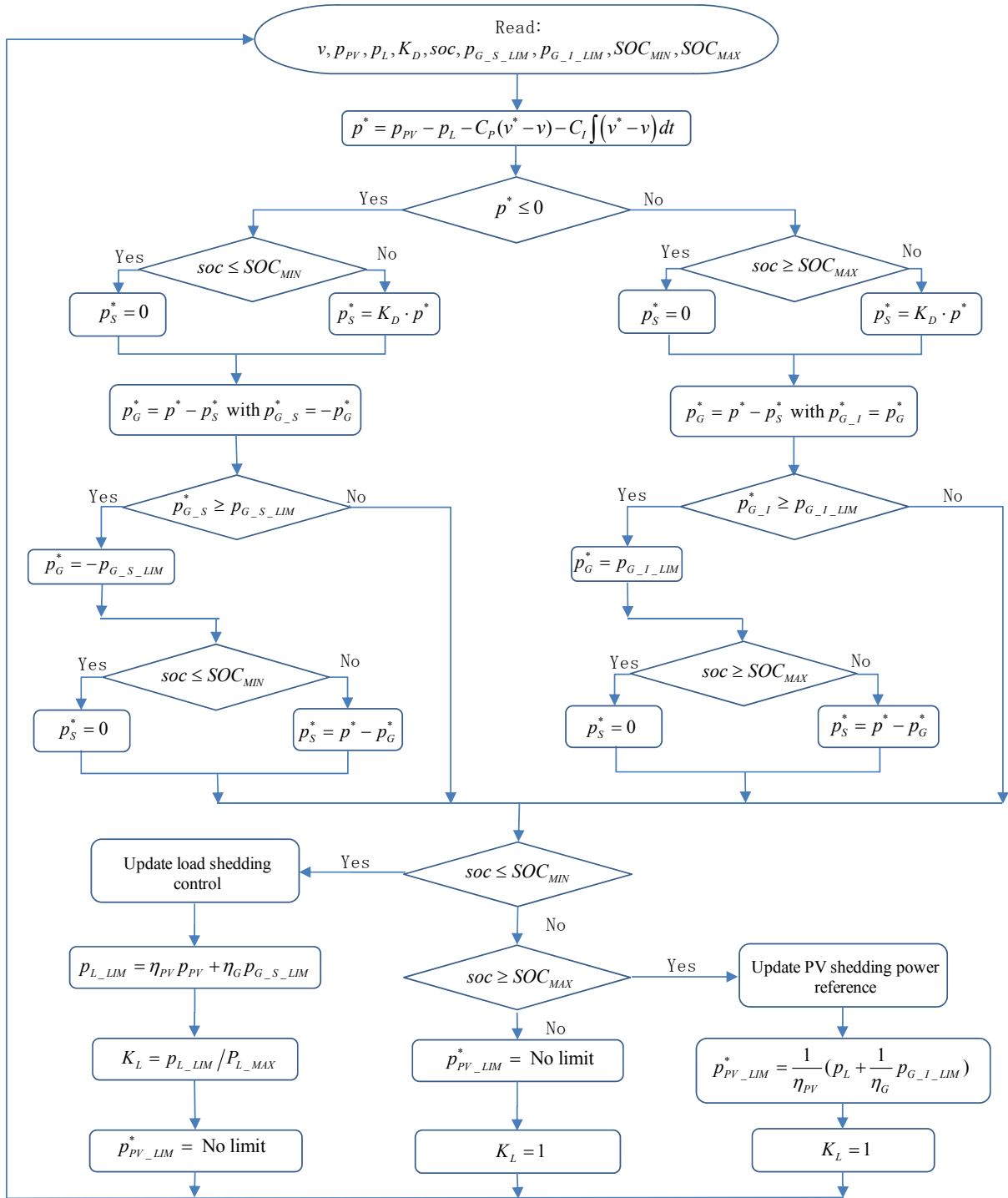


Figure 53. Operating algorithm for grid-connected operation.

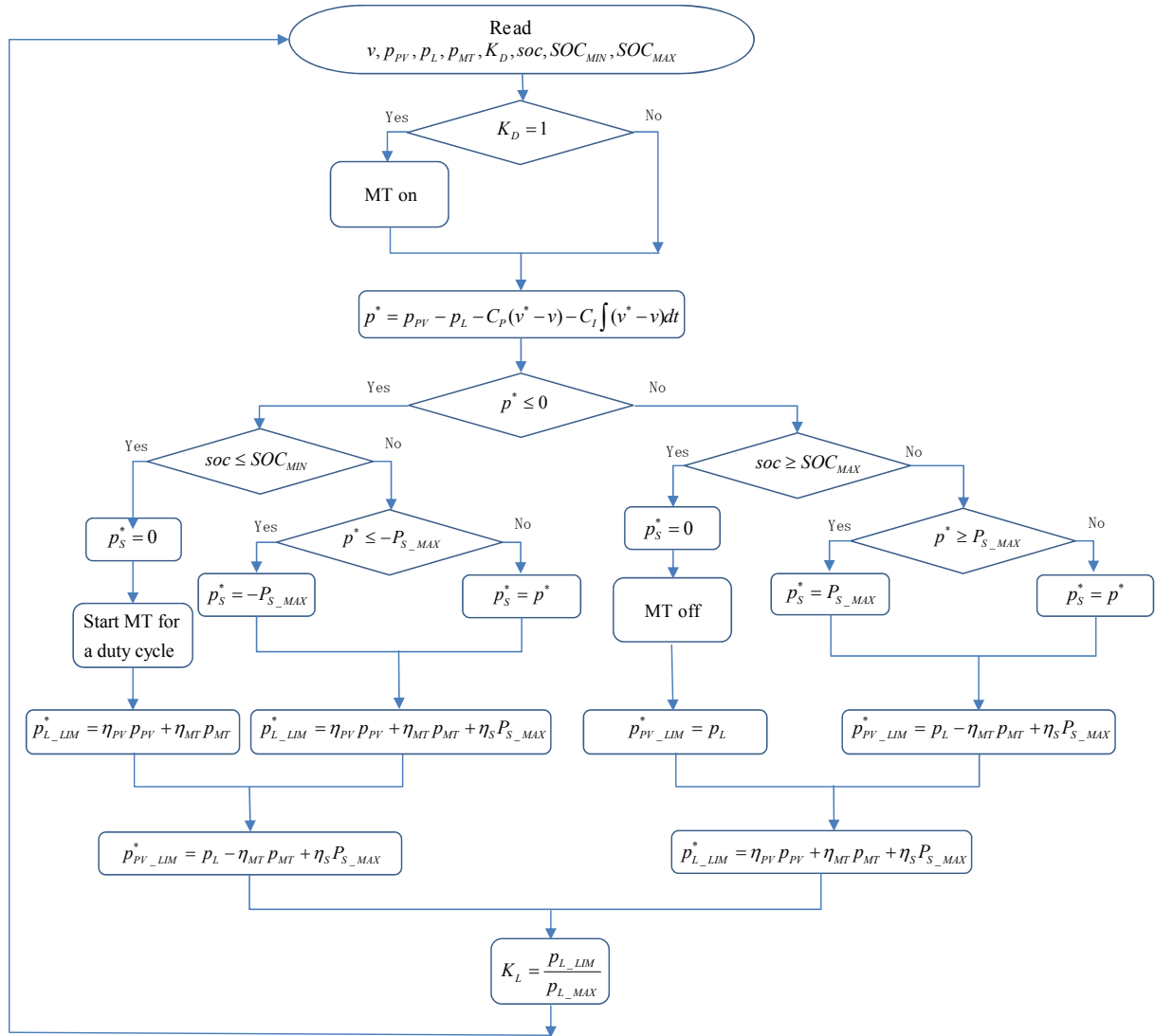


Figure 54. Operating algorithm for off-grid operation.

III.6. Simulation results of supervision control

The microgrid supervision control is simulated with numerical powers values based on the experimental DC microgrid platform. In the following sections, simulation results are given for both microgrid operating modes, *i.e.* grid-connected and off-grid mode.

III.6.1. Grid-connected mode

The supervision control for the grid-connected mode is simulated for operation based on the weather condition of on 23rd of April 2011 in Compiegne, France.

For simulation validation, the PVA prediction data are calculated from the real measurement data in order to assign the day-ahead prediction data uncertainty error as random.

The measured MPPT PVA power is shown in Figure 55: the green curve shows the real time PVA power evolution, while the gray bars are the hourly average PVA power. Figure 56 gives the considered PVA power prediction data, which are hourly data having $\pm 10\%$ random error with hourly average of the measurement data.

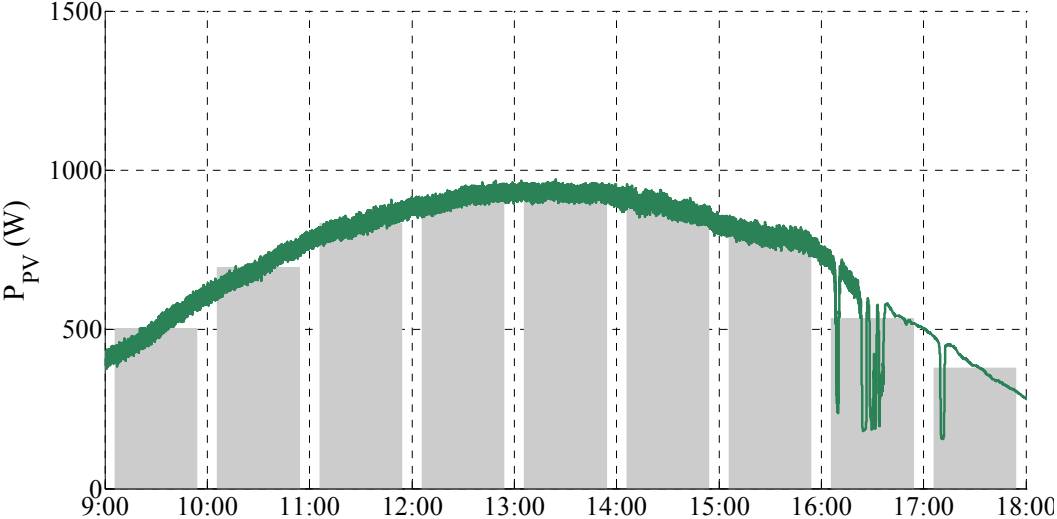


Figure 55. PVA MPPT power evolution for 23rd of April 2011.

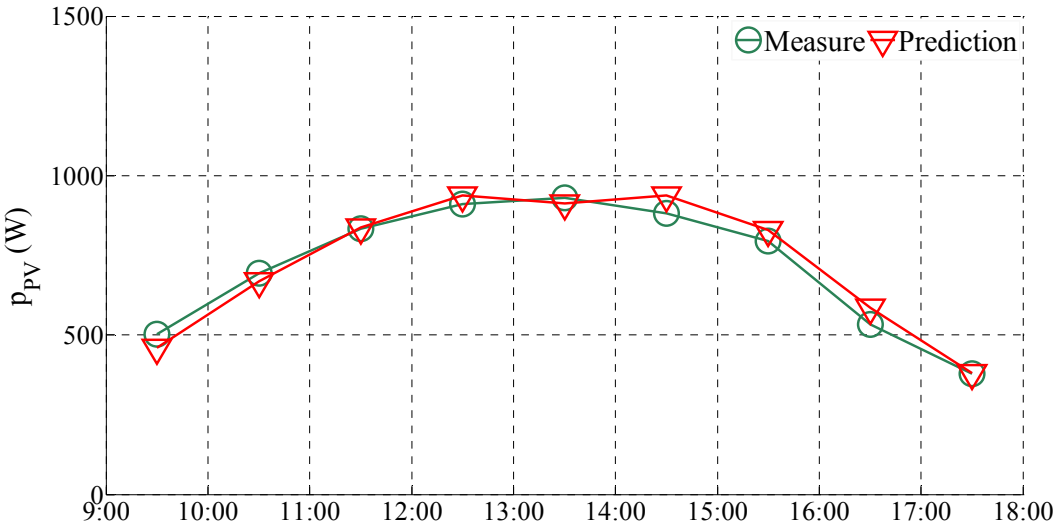


Figure 56. Hourly PVA power measurement and PVA power prediction.

Load prediction data are supposed to be given by building management system, which implies additional uncertainties. A simple arbitrary load power evolution is considered. The difference of load power and load power prediction is shown in Figure 57.

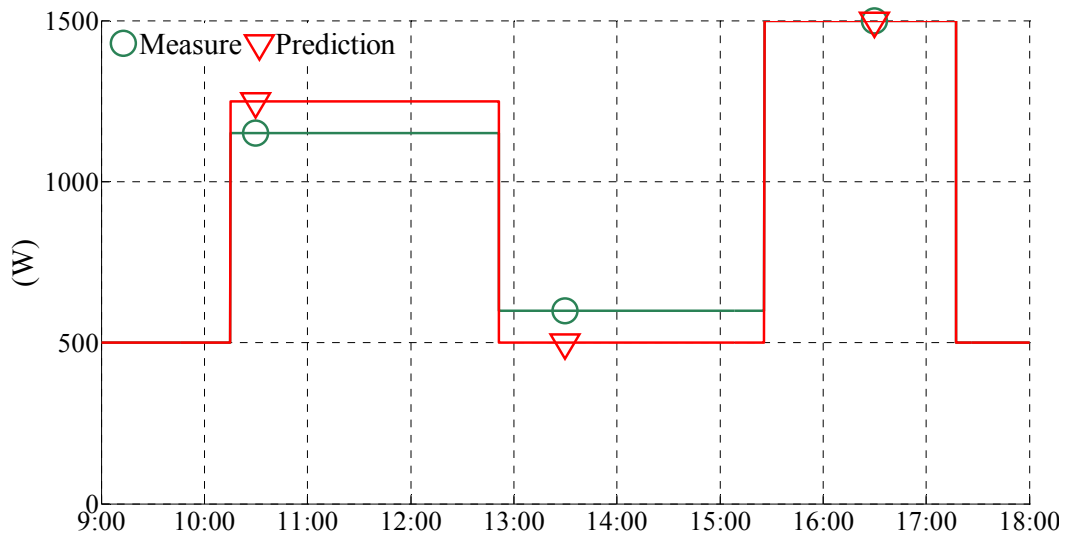


Figure 57. Load power measurement and day-ahead prediction.

Based on the prediction information, the energy management layer calculates the optimization problem by CPLEX and gives the optimum energy flow evolution, as presented in Figure 58. Corresponding K_D sequence is calculated by (3.42) from the optimum energy flow evolution as the controller parameter.

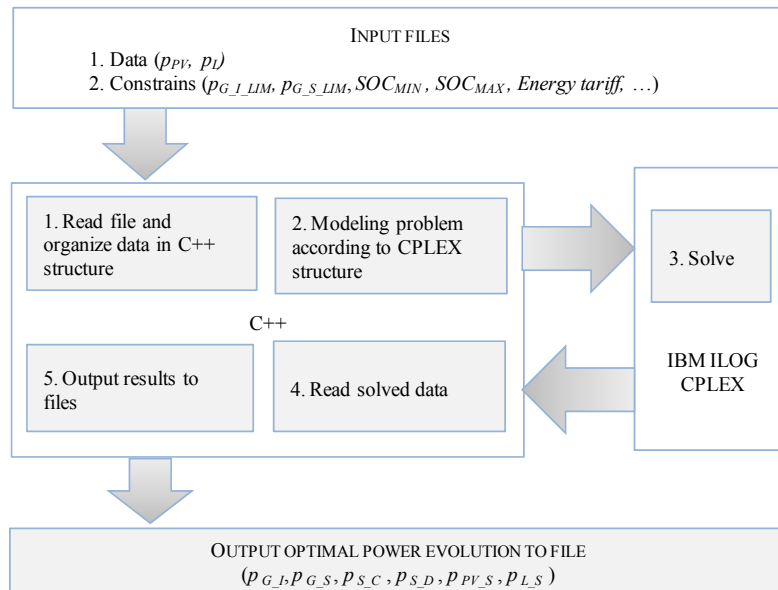


Figure 58. Flowchart of optimization solving

Taking into consideration the above power predictions, in our case study, the optimized power flow and K_D evolution, supposed to be calculated a few hours before the operation of 23rd of April, are shown in Figure 59 and in Figure 60 respectively.

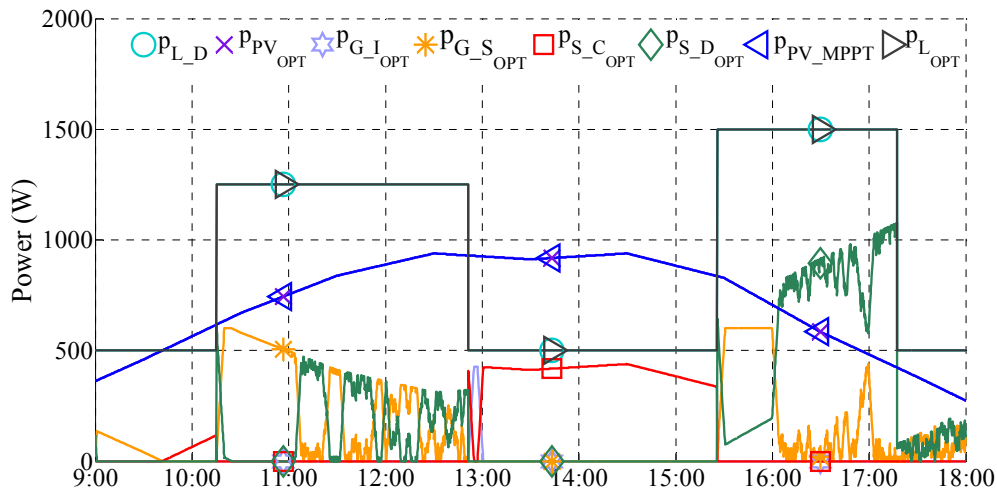


Figure 59. Optimized power flow by energy management layer for grid-connected mode.

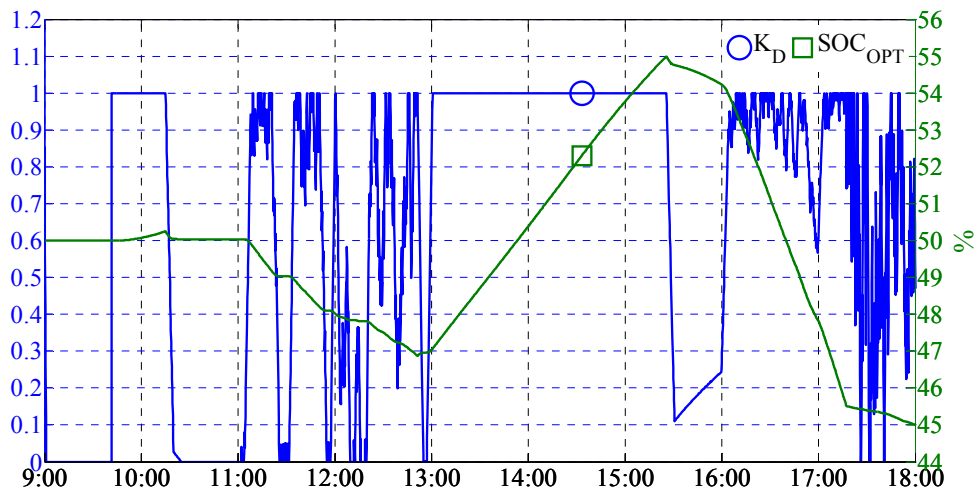


Figure 60. Optimized K_D and soc evolution by energy management layer for grid-connected mode.

Grid and storage constrains, as arbitrary values, are imposed for the system operation. Grid power injection limit is imposed as 700W, and supply limit as 600W.

Peak hour during the day is assumed 11:00-13:00 and 16:00-18:00. To mitigate grid power strong fluctuations, grid power changing limit is imposed as 2W/s. Arbitrary soc limits are considered as 45% and 55%, while the initial SOC is 50%. Considering the storage capacity of our experimental platform, which will be used in future experimental study, these soc limits are selected to show the system behavior with relevant storage events (full, empty) in a day run. For performing a day optimization during 9 hours, the data resolution is chosen at 1 point/10s, *i.e.* 3240 points each power curve. The optimization program execution time is within 10s for a computer with CORE i5 processor. The optimum cost estimated by CPLEX is 0.516 €.

The calculated K_D optimum evolution is given to the operation layer to run the power system following the conditions both meteorological and load given by 23rd of April 2011. The operation power flow, as real situation, simulated by MATLAB, is shown in Figure 61.

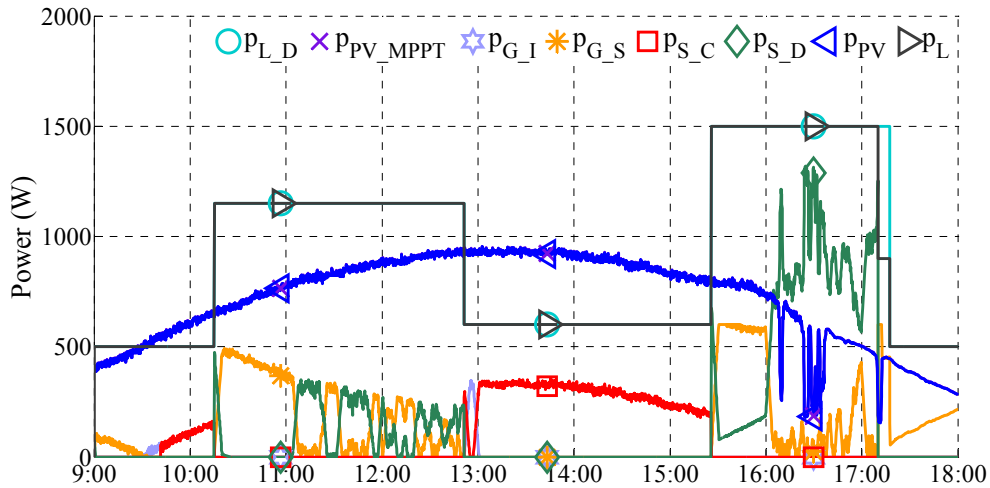


Figure 61. Simulated power flow with optimum K_D for grid-connected mode.

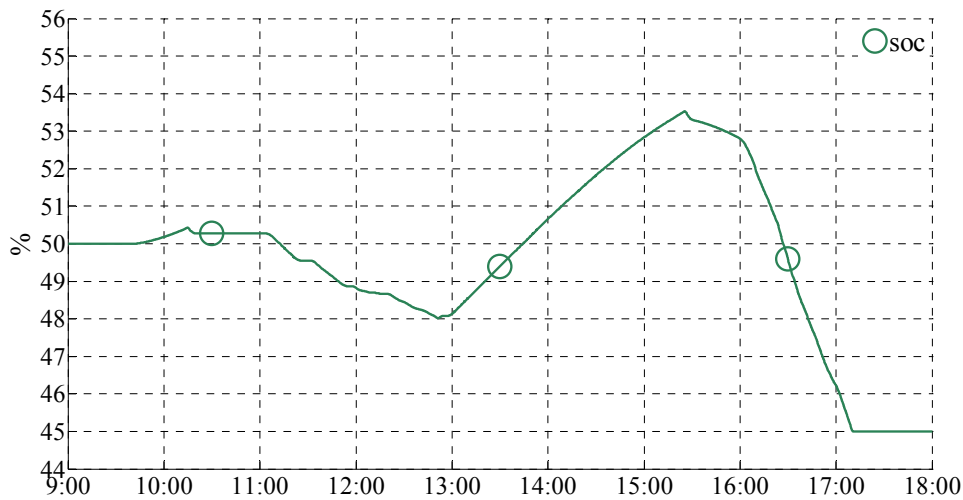


Figure 62. Simulated soc evolution with optimum K_D for grid-connected mode.

During this day operation, grid and storage share power for supplying energy or for receiving energy at the same time. During the first peak hours (11:00-13:00), the load is supplied by storage and grid, and surplus PVA production is injected into the grid in order to make the maximum profit. Aiming to reduce the energy cost by avoiding grid supply during peak hours, in the second peak hour period (16:00-18:00), the storage is mainly used for supplying the load. During 13:00-15:00 with the excess PVA production, the storage is charged for supplying in the second peak hour. Grid power injection limit and supply limit are respected. Short time load shedding can be seen in the operation after 17:00, when the battery is empty. The load shedding is performed based on instantaneous power information. To avoid load shedding fluctuations in PVA power fluctuating circumstances, it is also possible to impose duration for load shedding in CPLEX optimization.

Optimized load shedding information could also be given to operation layer to override the operation layer load shedding control if necessary. The energy cost is 0.512 €. The soc evolution with

the optimum K_D is illustrated in Figure 62 . This evolution is quite similar to the evolution presented in Figure 60, which is the optimization case calculated by the energy management layer.

By comparing with results presented in Figure 59 and Figure 61, it can be seen that the simulated power flow is different from the optimization due to the uncertainties of solar irradiance prediction and load power prediction. During the solar fluctuations between 16:00 and 17:00, the storage provided more powers. However, in this case, the storage is still able to be the main load supply during the second period of peak hours, but a slight load shedding occurs when the soc reaches its low limit.

In order to further analyze, a simulation case for a constant K_D is presented in Figure 63 and 64.

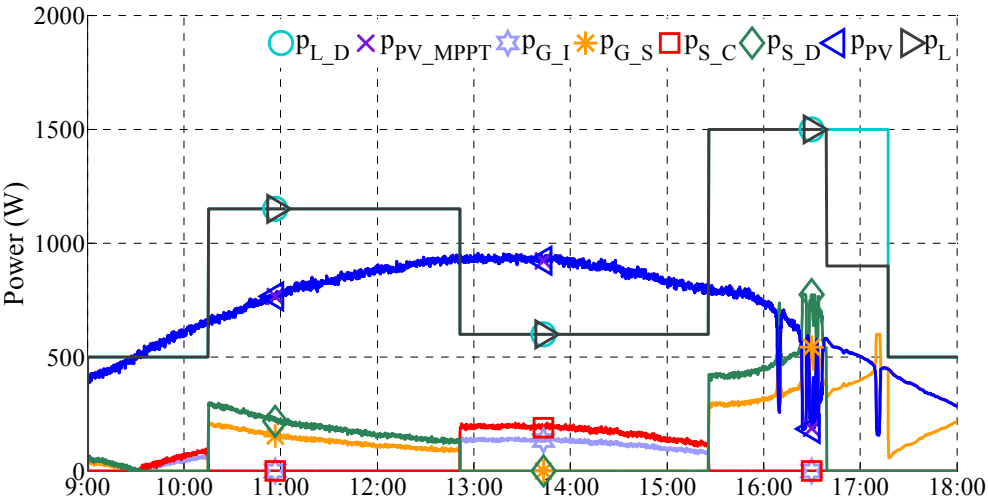


Figure 63. Simulated power flow with constant $K_D = 0.5885$ for grid-connected mode.

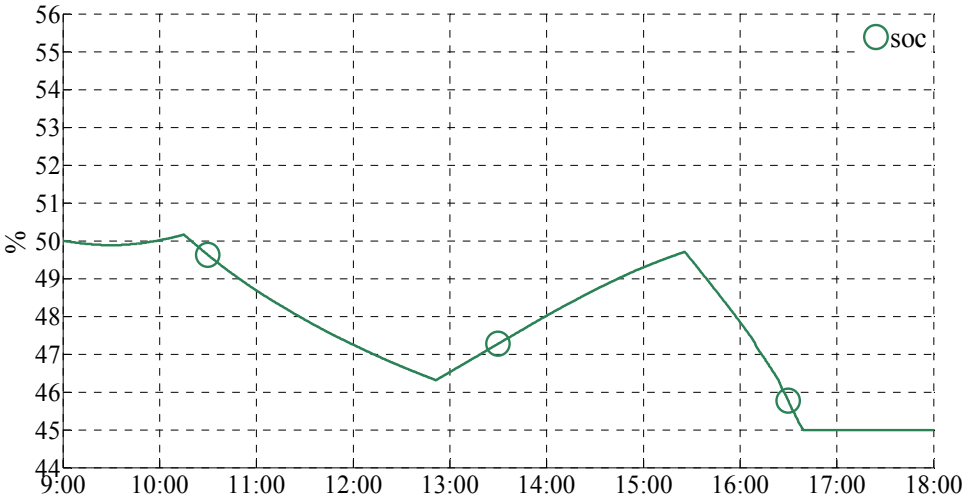


Figure 64. Simulated soc evolution with constant $K_D = 0.5885$ for grid-connected mode.

It is chosen as constant value $K_D = 0.5885$ which is the average value of optimum K_D evolution shown in Figure 60. In this case, the obtained energy cost, 0.651 €, is higher than the optimum cost, and longer load shedding can be seen during this operation. The soC evolution, illustrated in Figure 64, is very different from the optimum soC evolution.

Table 6 shows the energy cost results and occurrences of load shedding for these three cases: optimized operation by energy management layer with $\pm 10\%$ uncertainties prediction data, simulated operation in case of a real PVA production with the calculated optimum K_D sequence, and simulated operation with constant $K_D = 0.5885$.

Table 6. Comparison of different cases for grid-connected simulation test.

Case operation	K_D	Cost (€)	Load shedding duration
Optimization	Optimum K_D	0.516936	No shedding
Simulation	Optimum K_D	0.512591	Short time
Simulation	$K_D = 0.5885$	0.651807	Long time

It can be seen that simulated cost for the optimum K_D is close to the prediction cost, and the error is within 1%, which is due to the uncertainties of prediction. For the constant K_D case, the cost is 26% more than the prediction case; moreover, longer load shedding can be seen in this case. Even with some uncertainties, the optimized K_D operates the microgrid with respect of the utility grid requirements and storage capacity. This comparison validates the presented simulation case for the proposed supervision of a multi-source power system.

III.6.2. Off-grid mode

The supervision control for the off-grid mode is simulated for same operating condition on 23rd of April 2011 in Compiegne, France. The test condition is the same as in the grid-connected mode. The optimization power flows are given in Figure 65, while soC and K_D evolution are given in Figure 66. For better visibility of the power curves, p_{MT} is presented as negative value, although the value is positive in equations. This exception is used for figures of off-grid mode throughout the following part of this thesis.

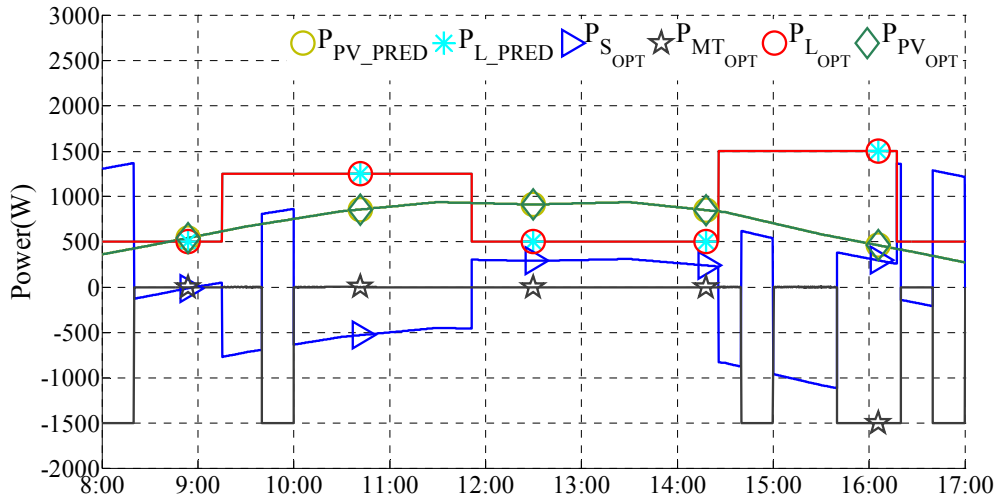


Figure 65. Optimized power flow by energy management layer for off-grid mode.

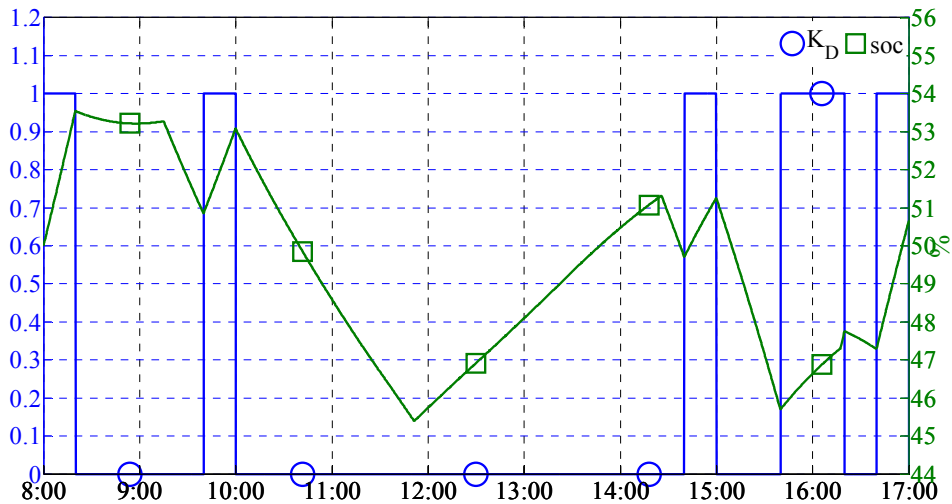


Figure 66. Optimized K_D and soc evolution by energy management layer for off-grid mode.

In off-grid case, the final soc SOC_F is imposed as 50% with the aim to maintain continuous operation for several days. It can be seen in power flow optimization, the MT is started for several duty cycles and the storage is operated within its power limits of 1500W and soc limits between 45% and 55%. Final soc value is above 50%. The optimized MT working cycle is translated as the control parameter K_D to control the on/off state of the MT in power balancing operation.

Based on the K_D value, the operation in off-grid mode is simulated with MATLAB-Simulink and Stateflow. The obtained power evolution and soc evolution are shown in Figure 67 and Figure 68 respectively. It can be seen even with uncertainty the simulated power flow is in accordance with the optimization power flow and MT is started with the optimization order. However, final soc value is less than the SOC_F .

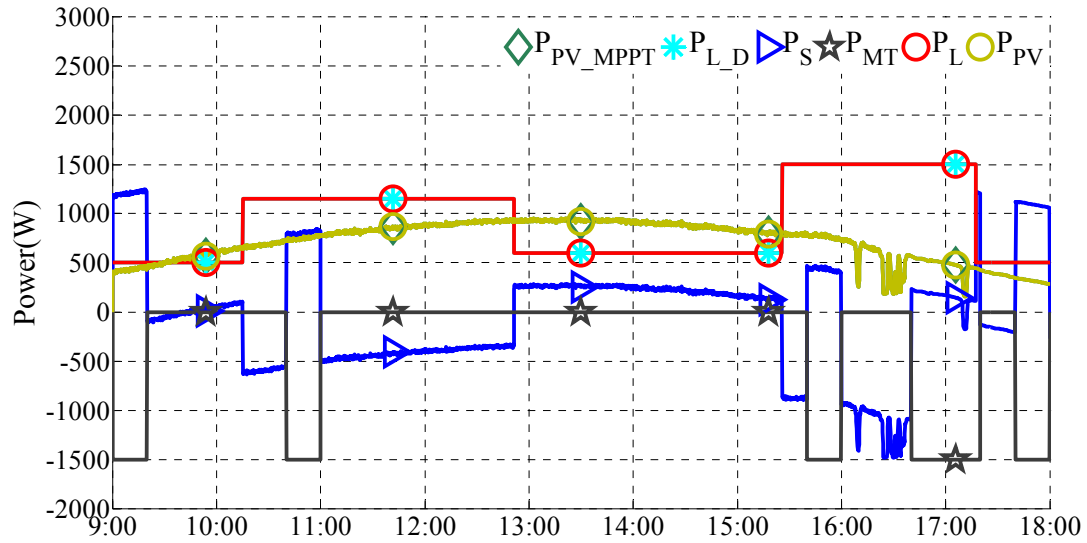


Figure 67. Simulated power evolution with optimum K_D for off-grid mode.

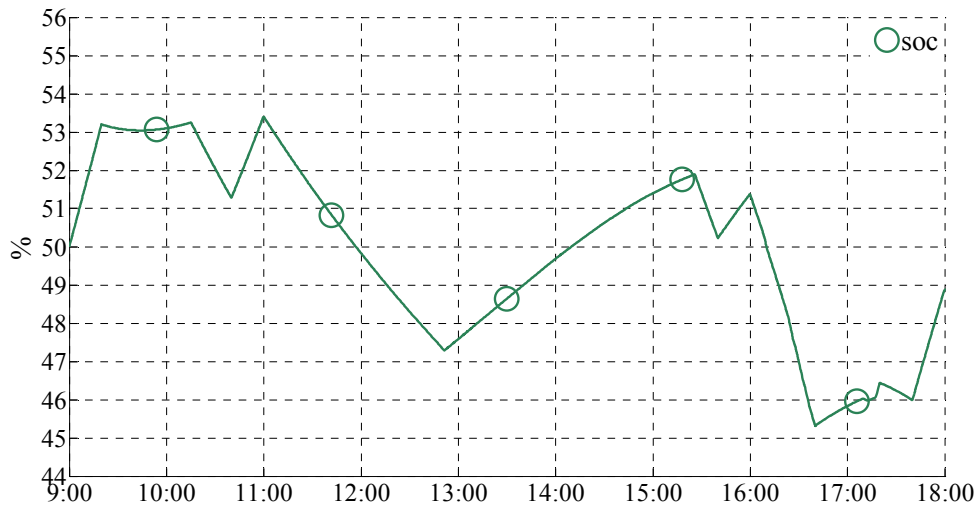


Figure 68. Simulated soc evolution with optimum K_D for off-grid mode.

Table 7 summarizes the test of off-grid mode. The optimization estimated that the overall cost of the operation is 3.29542€. The cost of simulated case is 3.27819€. The cost difference is about 0.5%. The simulation cost is less than the optimization cost, but the difference is not significant. This is due to prevision uncertainties between optimization and simulation on one hand, and on the other hand that the storage is used more than expected SOC_F , which is not penalized by the cost function.

Table 7. Comparison of different cases for off-grid mode simulation test.

Case operation	Cost (€)	Load shedding	PVA power limiting
Optimization	3.29542	No	No
Simulation	3.27819	No	No

It can be seen that simulated cost with the optimum K_D is close to the optimization cost and that the optimized power flow can be reproduced through simple interface in real operating conditions even with uncertainties. This comparison validates the presented simulation case for the proposed supervision of a multi-source power system.

III.7. Conclusion

In this chapter, the supervision control design is described. Simulation results have shown that the supervision control can maintain power balancing while performing optimized control, even with uncertainties of prediction and arbitrary energy tariffs. The optimized power balancing takes into account forecast of power production and load power demand. It handles also constraints such as storage capability, grid power limitations from smart grid, grid TOU pricing, grid peak hour in grid-connected mode and MT fuel consumption, working duty cycle and storage life time in off-grid mode. It can be concluded that the optimization gives better energy performance while minimizing load shedding and PVA shedding.

With $\pm 10\%$ random prediction errors between optimization and operation, it can be seen that the optimized power flow can be reproduced through simple interface in real operating conditions even with uncertainties. The cost is close with errors within 1%. It is proved that the proposed supervision control is feasible to apply optimized power flow in real operating conditions and withstand prevision uncertainties.

The designed operation layer can work with any K_D value, so the prediction errors and non-optimum K_D does not affect the power balance. The supervision control is robust and can perform optimization at the same time.

Moreover, in grid-connected mode, grid power limits from smart grid message are fully respected with the robust control. Thus the proposed DC microgrid control structure is feasible for advanced energy management and can respond to grid issues, such as reducing peak consumption or downscaling fluctuations, and to end-users, such as reducing energy cost.

Chapter IV. Experimental validation of supervision control

Through simulation tests in the last chapter, it validated that with $\pm 10\%$ random errors between prediction and simulated operating condition, the optimized power flow can be reproduced in operation through simple interface. In this chapter, the proposed supervision control is validated through experimental test in order to identify the merits and shortages in real operating conditions.

The experimental tests are carried out with our experimental platform, which is described in section II.1, where the scheme and elements are given for grid-connected mode. In off-grid mode, the scheme remains the same, and MT is considered as a single phase AC source and emulated by the same linear amplifier. However, the difference is that MT works only for supplying power and is assigned working duty cycle at rated power.

There are two reasons of assigning MT duty cycle. The first reason is that MT efficiency is highest to output rated power, it is fuel-wasting to make the MT always spinning and output low power or to frequently start and stop MT. The second reason is that storage can be used as a buffer for power balancing while MT works in duty cycle.

For these experimental tests, load profile is assigned arbitrary, although a real load profile prediction can be applied. The reason for choosing an arbitrary load profile is to show clearly as much

events involved in the supervision control as possible. The load profile is shown in Figure 69. The difference between predicted load demand and experimental load demand is assigned to be at the most 200W, which result in relative prediction errors ranging from 13.3% to 28.6%.

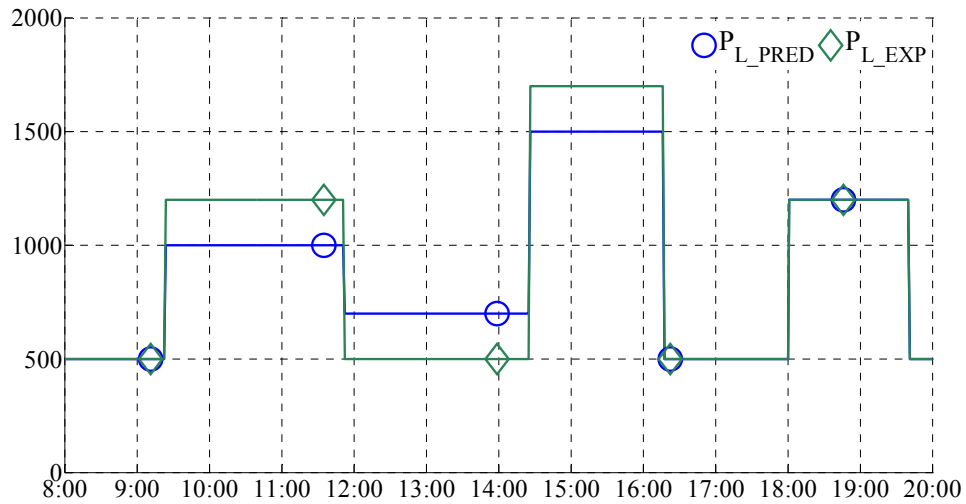


Figure 69. Load power prediction and load power demand for experiment.

Concerning PVA power prediction, it is calculated by the solar irradiance prediction data provided by the national weather forecast service Meteo France. The uncertainty of PVA power prediction is related to each forecast precision.

In optimizations, the power conversion efficiencies are involved. The power efficiency varies according to operating power and the ambient temperature; efficiency function should be taken into account for each converter. However, in this study, these efficiencies are considered as constant value and shown in Table 8. The chosen values take into account experimental experience.

Grid and MT are AC sources and their power conversion involves two power legs, so their conversion efficiency is less than PVA and storage converter for which only one power leg is used.

Table 8. Converter efficiencies for optimization.

Symbol	Description	Value
η_{PV}	PVA converter efficiency	90%
η_S	Storage converter efficiency	90%
η_G	Grid converter efficiency	85%
η_{MT}	MT converter efficiency	85%

IV.1. Validation for grid-connected mode

In this section, firstly an improvement of experimental platform is proposed concerning grid-connected filter. In the proposed microgrid, connecting AC grid with DC bus requires conversion stage with a filter. Inductor filter is not effective in smoothing current, while LCL filter is more attractive for less component value and high filtering ability. However, obvious grid power factor degradation can often be observed when using LCL filter in low power operation, which is often the case with PV generation according to weather conditions [113]. The degradation causes are studied and a phase error compensation structure is proposed. Experimental results conclude that the proposed compensation structure improves the grid power quality in case of low PV production, in both power factor and harmonics.

Then, a series of tests is given for validating the proposed supervision control in grid-connected operating mode.

IV.1.1. Improvement for experimental platform: simple phase compensation grid-connected inverter control with LCL filter

PV sources play an important role in distributed generation. Nevertheless, these renewable distributed powers undergo strong variation over time and can hardly be precisely predicted. Hence, a filter to satisfy high power quality over the full power operation range is required. The filter should enhance the important role of grid-connected inverter, in distributed generation, by two sides. Firstly, the grid-side current has to be controlled to follow given current reference to provide the active power and reactive power demand with as less distortion as possible. Secondly, with the power electronic devices working in PWM mode, the inverter outputs, voltage and current, include switching noise and harmonics. The filter should be able to reduce frequency noise, generated by the PWM inverter, and harmonics.

Traditionally, as L filter, a serial inductor is used, which is simple to control and can offer precisely current phase and amplitude control over the full operating range. However, as the attenuation ability is not satisfying for the full power range, a larger value inductance is required to get smooth current. Increasing inductance value is not cost-effective, especially for high current rating, and could also reduce the dynamic performance of the system.

LCL filter could be one of the solutions, which contains two inductors and one capacitor. Compared with the L filter, LCL filter could provide three times attenuation ability for high frequencies with less component values. Regarding PV generators, due to the strong variation of solar irradiance for a relatively short period of time, the grid injected power is usually strongly varying with large differences. In case of high solar irradiance, corresponding to high level power injection, the LCL performance is satisfactory. While in case of weak solar irradiance, the injected power could

have a very low level and, for low power operation, the LCL filter control usually results in obvious power factor degradation. Moreover, by different feedback methods of LCL filter control, the grid voltage could be a source which introduces more distortions in the grid current: phase error, amplitude error and harmonics. Thus, the low power operation of PV grid-connected inverter needs to be improved in order to inject power with high quality power injection.

According to recent researches [114-126], the LCL filter current control strategies are based on grid current feedback [115-116, 124-126] and inverter current feedback [115-123]. In [114], the currents are both used with corresponding weight to form a combined feedback. Grid current feedback control usually involves more control bandwidth and is tended to be unstable; the control loop gain is insufficient due to stability limit. Inverter current feedback requires less control bandwidth and offers sufficient control loop gain. It is more stable and robust and so is more often studied in the literature. However, the inverter current feedback cannot totally reject grid voltage disturbance in the grid current output.

In grid current feedback, extra feedback, or inner control loop which can increase the robustness of the control strategy, are often reported in literature [124-126]. Capacitor current inner loop feedback has the advantage of add damping to resonance; however, due to insufficient gain of current control, it is difficult to track low power command as mentioned by [124].

Regarding different controllers used, we note that they have different influence on grid current distortion. PI controller, relatively simple and robust, is the most widely used [115-117, 120, 122-124]. In frequency domain, it provides continuous gain. PI controller combined with state space control is studied by [118]. It makes state space control parameter tuning more simplified. Based on the fact that, in grid-connected inverter control, the current reference and grid voltage contain only some frequency elements, PR controller works on the principle of providing relatively significant controller gain at specified frequencies [114, 121]. Usually the major odd-order harmonics are considered. Compared with PI controller, PR controller provides more significant gain at desired frequency and less gain at natural resonance frequency introduced by LCL filter; so, the natural resonance can be eased. However, PR controller is prone to numerical problems.

Model predictive control, pole placement and state space control are used [118, 125-126]. These methods are usually depending on extra sensor or precise model parameter, or control parameter tuning procedures. Thus, the robustness could be an issue.

In order to deal with resonance problems, different damping strategies are used: passive damping [114, 120] that is simple, robust and does not need additional sensors, active damping with multi-loop control [117, 124], capacitor voltage lead-lag feedback [119, 123], filter based damping [115-116] and modern control strategy [118, 125-126]. Active damping either involves additional sensors or complex computation. Filter based active damping does not need additional sensors, but could decrease the system dynamic performances.

With inverter current feedback and PI or PR controller without compensation, the grid voltage cannot be rejected in grid current output and causes grid current phase error. The case is more obvious in low power operation and high grid voltage.

For grid current feedback combined with capacitor current inner loop, [127] propose a feed-forward compensation involving proportional, derivative and second derivative of grid voltage to deal with current distortion due to insufficient control loop gain. For inverter current feedback, the grid voltage introduces reactive power and harmonics in the grid current. Grid voltage feed-forward for compensating the grid voltage is used [127-129], but direct grid voltage feed-forward does not solve the problem.

Grid voltage related distortion is analyzed by [128], and compensation using capacitor current is proposed, while [130] proposed compensation structure using capacitor voltage. Capacitor current and capacitor voltage compensation are approximations of grid voltage compensation, and involve additional sensor for compensation. In this paper, by selecting inverter current feedback, the same compensation concept is employed, but the grid voltage is directly used for compensation with properly selecting sampling point, which do not need additional sensor.

IV.1.1.1. Grid connection control

The microgrid grid-connected inverter and LCL filter are shown in Figure 70, where C , L_I , L_G , C_{C_G} and R are DC bus capacitor, inverter-side inductor, grid-side inductor, filter capacitor and damping resistor; v , v_I , v_{C_G} and v_G are DC bus voltage, inverter output voltage, capacitor branch voltage and grid voltage.

The resistor R provides damping of resonance effects, otherwise, for $R=0$, the filter is without passive damping. A full-bridge (B_3 , B_4) controls power into the grid.

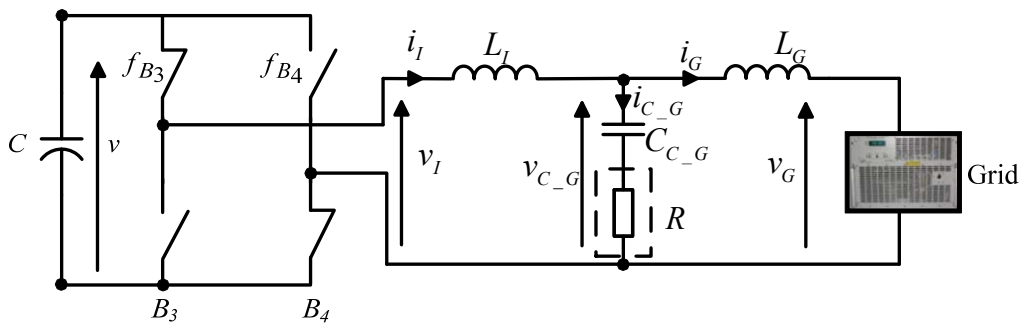


Figure 70. Microgrid grid-connected inverter by LCL filter.

Power system parameters are listed in Table 9.

Table 9. System parameters

Symbol	Description	Value
v	DC bus voltage	400V
v_G	Grid RMS voltage	230V
f_G	Grid voltage frequency	50Hz
L_I	Inverter-side inductance	20mH
C_{C_G}	Capacitor	10 μ F
R	Damping resistor	16 Ω
L_G	Grid-side inductance	5mH
f_C	Control frequency	10kHz

The inductors L_I and L_G have inherent internal resistance that is neglected in this study, considering that the internal resistance is relatively small compared to the impedance provided by the inductance. Hence, the block diagram of the system is shown in Figure 71.

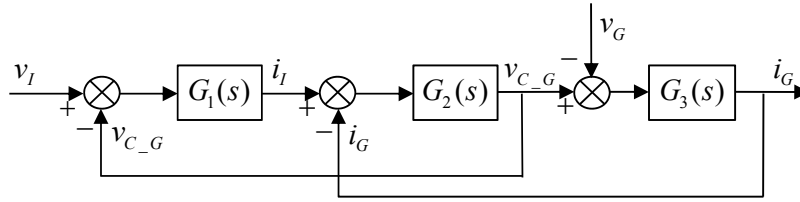


Figure 71. Block diagram of LCL filter.

In Figure 71, the concerned transfer functions in s domain are $G_1 = \frac{1}{L_I s}$, $G_2 = \frac{1}{C_{C_G} s} + R$, $G_3 = \frac{1}{L_G s}$,

where s is the Laplace operator. These three transfer functions have the same form: each of them offers infinite gain for DC and decreases of -20dB/Dec at high frequencies.

Grid current i_G is affected by two elements: the inverter voltage v_I and the grid voltage v_G . In a classical control problem, v_G is normally considered as disturbance for the control and is ignored in control design. It is supposed that a controller with enough gain at the same frequency of disturbance could reject this disturbance in the output, and only the transfer function concerning v_I and i_G are considered for the controller design.

However, according to the feedback structure, as analyzed later, v_G plays a role in i_G and cannot be always ignored. Taking into consideration both voltages, v_I and v_G , the closed loop relationship is given in (4.1) :

$$i_G(s) = \frac{G_1 G_2 G_3}{1 + G_1 G_2 + G_2 G_3} v_I(s) - \frac{(1 + G_1 G_2) G_3}{1 + G_1 G_2 + G_2 G_3} v_G(s) \quad (4.1)$$

The control plant is a third order system. According to different feedback and control structures, the closed loop relationship of i_G , v_I and v_G varies.

IV.1.1.2. Current feedback selection and grid voltage influence

In this section, aiming at analyzing the stability and phase error cause, two current control strategies are studied: feedback of the inverter-side current and the grid-side current. Stability and phase error principle are demonstrated using transfer function.

IV.1.1.2.1. Grid-side current feedback

The grid-side current feedback control block diagram is shown in Figure 72.

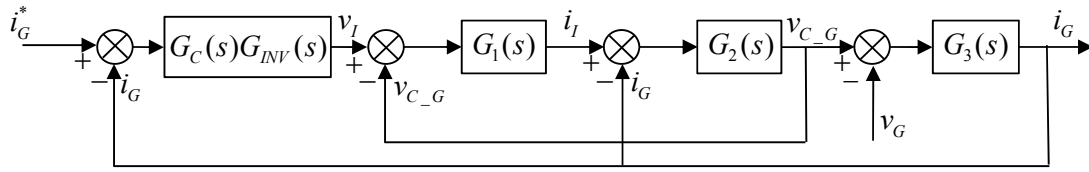


Figure 72. Current control by grid-side current feedback.

G_C is the controller transfer function and G_{INV} is the inverter transfer function. Neglecting switching transient in one PWM period, as the controller duty cycle output range $-1\sim 1$ represents the inverter output voltage range $-\nu\sim\nu$, $G_{INV}(s)$ can be considered as a gain ν . The open loop transfer function is given as:

$$\frac{i_G(s)}{i_G^*(s)} = \frac{G_C G_{INV} G_1 G_2 G_3}{1 + G_1 G_2 + G_2 G_3} \quad (4.2)$$

The closed loop relationship is:

$$i_G(s) = \frac{G_1 G_2 G_3 G_C G_{INV}}{1 + G_1 G_2 + G_2 G_3 + G_1 G_2 G_3 G_C G_{INV}} i_G^*(s) - \frac{G_3 + G_1 G_2 G_3}{1 + G_1 G_2 + G_2 G_3 + G_1 G_2 G_3 G_C G_{INV}} v_G(s) \quad (4.3)$$

with i_G^* the grid current reference.

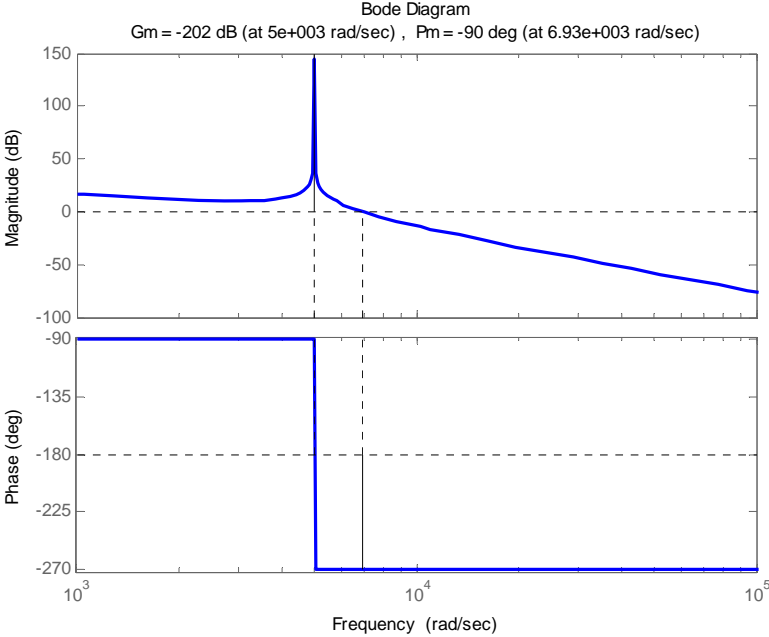
Supposing the controller could offer large enough gain at the frequency domain of grid current reference i_G^* and v_G , in (4.3) all the product elements, in both denominator and nominator, that are not containing G_C can be neglected. Thus, (4.3) can be simplified as:

$$i_G(s) = i_G^*(s) \quad (4.4)$$

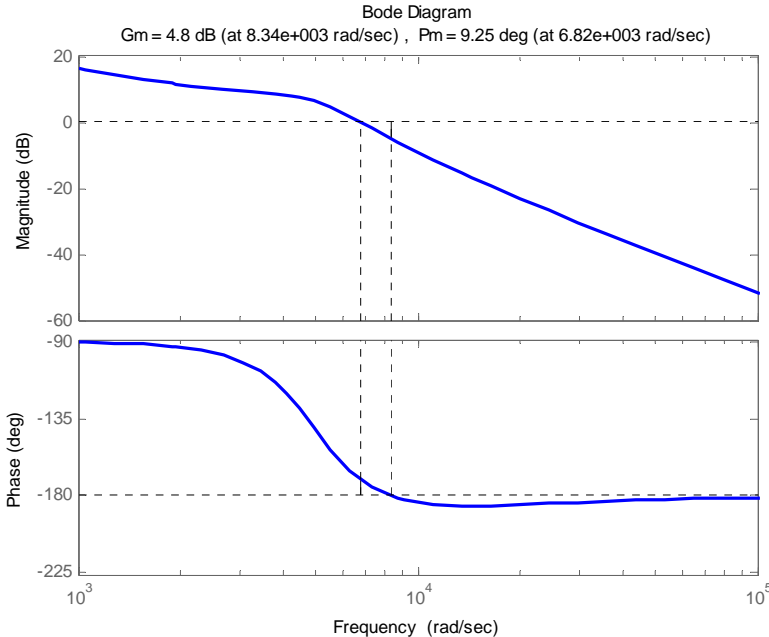
Following (4.4), with controller able providing sufficient gain, the grid current could follow the grid current reference, and v_G influence can be totally rejected, which is an ideal case. In real application, the stability problem could limit the controller gain, which could not be large enough for the necessary derivation from (4.3) to (4.4).

The open loop Bode diagram of (4.2) is shown in Figure 73 (a), which gives the stability margin of grid current feedback control without damping. It is indicated at the top of the figure that both phase margin (Pm in the figure) and gain margin (Gm in the figure) are negative, signifying that the control

structure is unstable. Based on stability analyze, the system is more stable if it has larger positive margin in the open loop Bode diagram.



(a)



(b)

Figure 73. Stability margin of grid-side current feedback: (a) without damping resistor, (b) with damping resistor.

In [116] the authors concluded that the grid current feedback control could be stable without passive damping, but only as long as the resonance frequency is between a quarter and half of the

control frequency. However, the current distortion is still an issue. So, stability and power quality should be improved.

By adding series damping resistor with the capacitor, the stability could be improved, and the open loop Bode diagram is shown in Figure 73 (b). It can be see the phase margin and gain margin are positive but relatively small, signifying the control loop gain could be limited for this control structure.

With gain increasing, the stability margin decreases. The system could be stable only with small gain values. In fact, with the stability limit, the stable control loop gain could hardly satisfy the current control objective in low power operation. So, for grid current feedback, inner loop control, additional sensors and control with large bandwidth are required to improve the problem.

However, in steady state of low power operation, the insufficient gain could give error to follow the current reference. Thus, other control structures are required.

IV.1.1.2.2. Inverter-side current feedback

If the inverter current control is selected, the control block diagram is as in Figure 74. It is expected that the grid current i_G could follow the inverter current reference i_i^* .

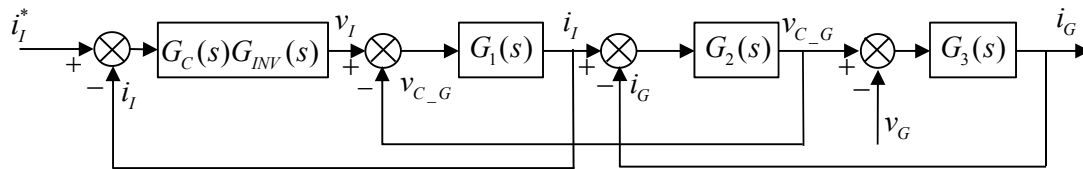


Figure 74. Current control by inverter-side current feedback.

The stability is analyzed by open loop transfer function, which is shown in (4.5).

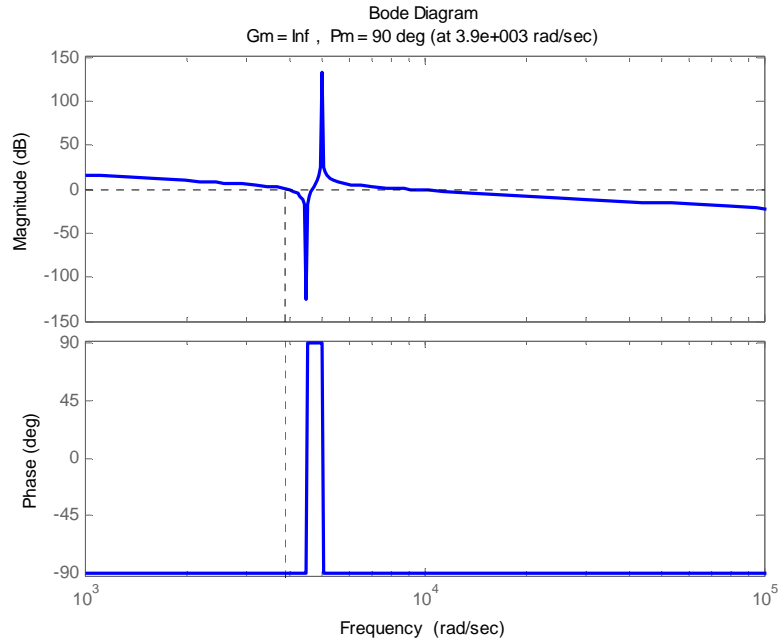
$$\frac{i_i}{i_i^*} = \frac{G_C G_{INV} G_1 (1 + G_2 G_3)}{1 + G_1 G_2 + G_2 G_3} \quad (4.5)$$

The stability margin of inverter current feedback control of (4.5) is shown in Figure 75. It can be seen for both cases of inverter current feedback, namely with or without passive damping, the system gain margin is infinite, meaning that the control is theoretically stable even with infinite control loop gain.

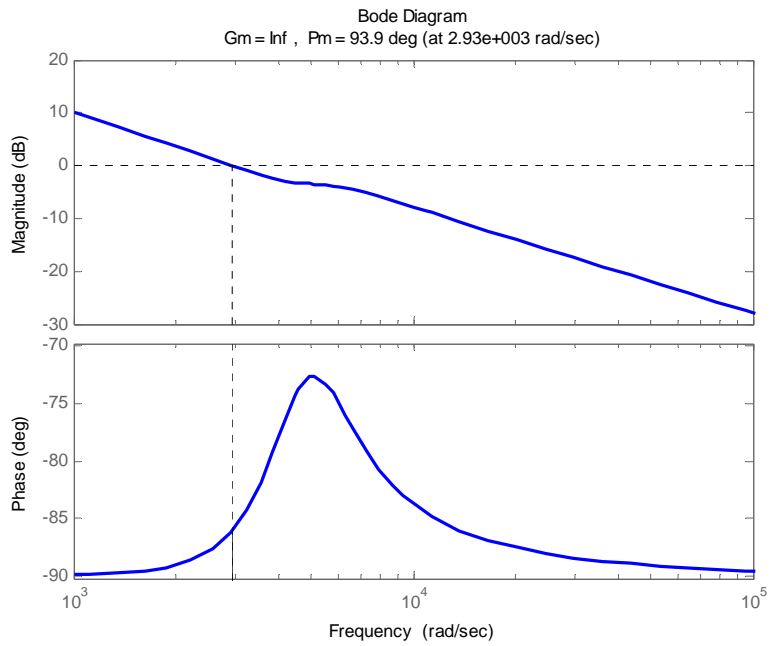
The infinite gain can avoid steady state error of the control.

The closed loop relationship of current feedback is shown in (4.6):

$$i_G(s) = \frac{G_C G_{INV} G_1 G_2 G_3}{1 + G_1 G_2 + G_2 G_3 + G_1 G_C G_{INV} + G_1 G_2 G_3 G_C G_{INV}} i_i^*(s) - \frac{G_3 (1 + G_1 G_2 + G_1 G_C G_{INV})}{1 + G_1 G_2 + G_2 G_3 + G_1 G_C G_{INV} + G_1 G_2 G_3 G_C G_{INV}} v_G(s) \quad (4.6)$$



(a)



(b)

Figure 75. Stability margin of inverter-side current feedback: (a) without damping resistor, (b) with damping resistor.

Supposing the controller could offer large enough gain (theoretically an infinite gain still maintains the stability of the control structure, while in practice the control loop gain cannot be infinite but still can be considered large enough) in the frequency domain of grid current reference i_G^* and v_G , all the product elements in (4.6), in both denominator and nominator, that not containing G_C can be neglected. Thus, (4.6) can be simplified as:

$$i_G(s) = \frac{G_2 G_3}{1 + G_2 G_3} i_l^*(s) - \frac{G_3}{1 + G_2 G_3} v_G(s) \quad (4.7)$$

From (4.7), it can be seen that only by controller parameter tuning design, even with ideal controller (which provides infinite gain), the grid voltage v_G influence on i_G could not be totally rejected. When i_l^* decreases, the current control becomes worse and v_G influence becomes more obvious. The grid voltage influence affects not only current control amplitude, but also current phase and power factor. In addition, if the grid voltage includes harmonic distortion, the grid current also suffers the same frequency harmonics distortion.

For inverter-side current feedback, the control structure is stable and can operate with sufficient gain to follow the current reference. The inconvenience is that grid voltage introduces an output in the grid current, which normally is reactive power and causes obvious phase error and low power factor in low power operation.

For a low power operation, the two objectives are to follow the current reference and to reject the disturbance caused by the grid voltage. Using grid-side current feedback, the drawback is that controller gain is insufficient, limited by stability. Because of insufficient controller gain, the current could not follow the reference in low power operation, which results in obvious phase error and distortion in low power operation. While the inverter-side current feedback control has no problem of following current reference, but the disturbance by grid voltage can result in obvious phase error and distortion in low power operation. Hence, making the choice of the inverter-side current control, the phase error elimination needs to be studied.

IV.1.1.3. Phase error compensation

The grid voltage related grid current distortion can be compensated by modifying the inverter-side current control reference as follow:

$$i_l^*(s) = i_G^*(s) + \frac{1 + G_1 G_2 + G_1 G_C G_{INV}}{G_C G_{INV} G_1 G_2} v_G(s) = i_G^*(s) + G_{COMP_FULL} v_G(s) \quad (4.8)$$

By introducing (4.8) into (4.6) and supposing that the controller offers sufficient gain, which can be theoretically infinite, every product element not containing G_C can be eliminated, and the grid voltage can be rejected from the grid current output as expressed by(4.9):

$$i_G(s) = \frac{G_C G_{INV} G_1 G_2 G_3}{1 + G_1 G_2 + G_2 G_3 + G_1 G_C G_{INV} + G_1 G_2 G_3 G_C G_{INV}} i_l^*(s) \approx i_G^*(s) \quad (4.9)$$

Thus, the full compensation transfer function is:

$$G_{COMP_FULL} = \frac{1 + G_1 G_2 + G_1 G_C G_{INV}}{G_C G_{INV} G_1 G_2} \quad (4.10)$$

Due to discrete effect and control delay, the controller gain cannot obtain infinite value, but can be still considered large enough. By ignoring the elements not containing $G_c G_{INV}$ the compensation transfer function can be simplified as (4.11).

$$G_{COMP_SIMP} = \frac{1}{G_2} = s C_{C_G} \quad (4.11)$$

Figure 76 shows Bode diagram of the compensation transfer function by full compensation and simplified compensation. It can be seen in the main grid voltage values and current harmonic frequency range (50Hz-1000Hz corresponding 314rad/sec-6280rad/sec), that the Bode diagram of the two compensations is nearly the same. At opposite, in high frequency range, the differences are obvious.

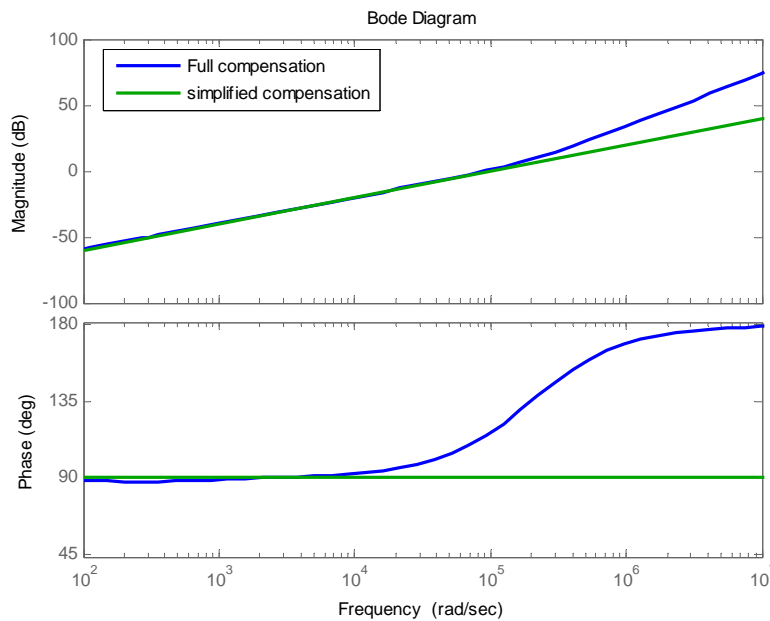


Figure 76. Differences of full compensation and simplified compensation in frequency domain.

The simplified compensation include the Laplace operator s , which means derivation in time domain. The derivation would amplify the noise of grid voltage measurement. By selecting sampling point during one PWM period, the noise can be reduced, especially the switching transient noise.

IV.1.1.4. Improvements for simplified phase error compensation

By choosing the inverter-side control strategy and phase error compensation based on (4.11), this section studies influences on the compensation strategies for different electromagnetic environments. As the simplified compensation is performed by differential operation on the grid voltage signal, in strong electromagnetic interference environment, the grid voltage signal noise could be over amplified and thus, worsen the operation. So the direct implementation of simplified phase error compensation should be improved. In such case, regeneration of smooth grid voltage is proposed using PLL. For

moderate electromagnetic environment, the simplified compensation could be directly performed, and the use of passive damping resistor could further improve power quality.

IV.1.1.4.1. Fundamental compensation using PLL

Firstly, for grid-connected system, grid voltage phase is obtained by a PLL [131], which also outputs the amplitude of fundamental voltage. Using PLL output amplitude and phase, a smooth fundamental voltage can be regenerated. Thus, it can be used for compensation without noise derivation problem. Compared with the real grid voltage signal, the generated signal contains only the fundamental information and the harmonic signals are not involved. So, in this study, using this generated signal is referred to as fundamental compensation.

IV.1.1.4.2. Passive damping

The capacitor branch includes a serial resistor R that provides passive damping of resonance effects. The capacitor branch transfer function can be:

$$G_2 = \frac{1}{C_{C_G} s} + R = \frac{RC_{C_G} s + 1}{C_{C_G} s} \quad (4.12)$$

Hence, the compensation transfer function is as in (4.13), and the compensation control structure is shown in Figure 77 (a).

$$G_{COMP_SIMP} = \frac{1}{G_2} = C_{C_G} s \cdot \frac{1}{RC_{C_G} s + 1} \quad (4.13)$$

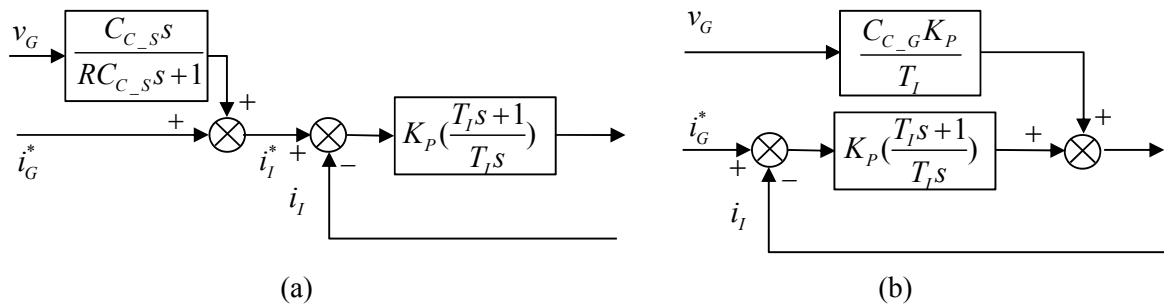


Figure 77. Compensation structure using passive damping by PI controller: (a) compensation control structure, (b) equivalent derived structure.

This compensation structure is based on PI controller that is easy for tuning. The PI controller equation is shown in (4.14).

$$G_{C(PI)} = K_P + \frac{K_I}{s} = K_P \left(\frac{T_I s + 1}{T_I s} \right) \quad \text{with } T_I = \frac{K_P}{K_I} \quad (4.14)$$

If the PI controller parameter is designed to obtain $T_I = RC_{C_G}$, the derivation and filter in compensation transfer function can also be replaced by proportional gain after several transfer function derivation. The final compensation transfer function structure is shown in Figure 77 (b).

Compared with active damping techniques, the major disadvantage of passive damping is power loss in the damping resistor. The power loss is calculated by (4.15).

$$P_R = Ri_{C_G}^2 = \frac{Rv_{C_G}^2\omega^2C_{C_G}^2}{1+R^2C_{C_G}^2\omega^2} \quad (4.15)$$

where $\omega = 2\pi f_G$.

By a well parameter selection, the power loss can be negligible compared with the injected power. Neglecting the inductor voltage drop and making the approximation $v_{C_G} \approx v_G$, the power loss relationship with capacitor *versus* resistor values can be drawn as shown in Figure 78. The power loss is less than 0.5% of rated injection power, which is 2000W in this study case.

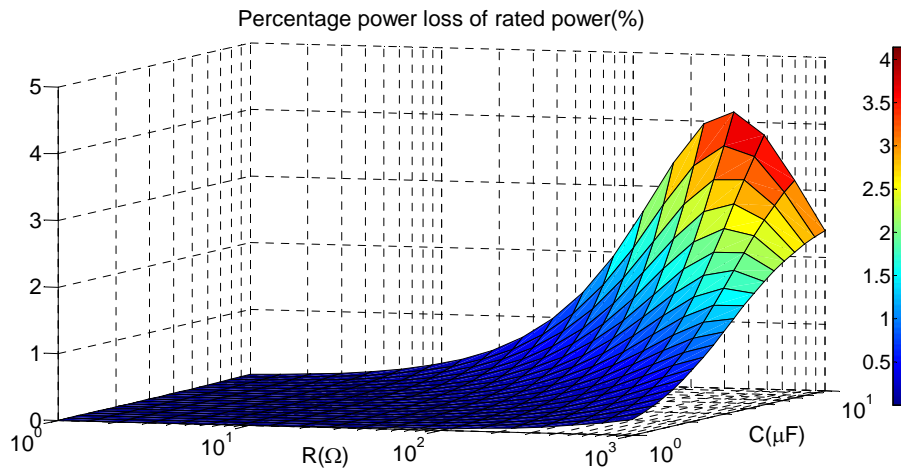


Figure 78. Passive damping power loss relationship with capacitor *versus* resistor values.

IV.1.1.5. Experimental results

In this section, experimental tests show results concerning phase error for LCL filter control strategy cases: without compensation, fundamental compensation, simplified compensation, as well as simplified compensation with passive damping. In order to compare different control strategies with strictly the same experimental condition, the solar irradiance based low power PV operation is emulated by constant DC supply with constant voltage at 400V.

The experiment platform, used to validate these results, is based on the Figure 70. It refers mainly to grid emulator (linear amplifier 3kVA), DC power supply, dSPACE 1103 controller board, and power electronic necessary devices (SEMIKRON SKM100GB063D, 600V-100A). The experimental data are recorded by Fluke 43B power quality analyzer.

The parameters values of LCL filter should be selected according to the following criteria: L_I should keep low inverter current ripple, C_{C_S} and R must be able to give a low damping loss, and L_G should maintain resonance frequency under control.

Power Factor (PF) and Displacement Power Factor (DPF) are used to describe the phase error and power quality with consideration of both fundamental frequencies and harmonics. For the single phase system, they are defined as in (4.16).

$$PF = \frac{P}{S} = \frac{P}{UI} \qquad DPF = \cos \varphi_1 \qquad (4.16)$$

where, P is the overall active power, S is the overall apparent power, U is the RMS value of phase voltage and I is the phase current RMS value, φ_1 is the phase error between fundamental voltage and fundamental current. A large difference between PF and DPF signifies obvious harmonic presence.

The current and voltage total harmonic distortion (THD) are defined as:

$$THD = \frac{\sqrt{\sum_{N=2}^{50} X_N^2}}{X} \qquad (4.17)$$

where X_N ($N=2, 3, \dots, 50$) are the corresponding harmonic RMS values of current or voltage, X is the RMS values of the measured signal.

In the experimental results, the current references are all given at 1A peak in phase with the grid voltage. Figure 79 shows the experimental result of phase error compensation by different control strategy under distorted grid voltage.

Due to grid access specific and restrictive conditions, for this experiment, the grid voltage is emulated by linear amplifier with measuring the real grid voltage in real time, which has an average THD of 3%.

Figure 79 gives the waveforms and power information of different compensation strategy. The active powers for all cases are around 155W, but large reactive power difference can be seen.

Without compensation, the reactive power is 216VAR and the current amplitude is not well controlled with peak value about 2A, as shown in Figure 79 (a).

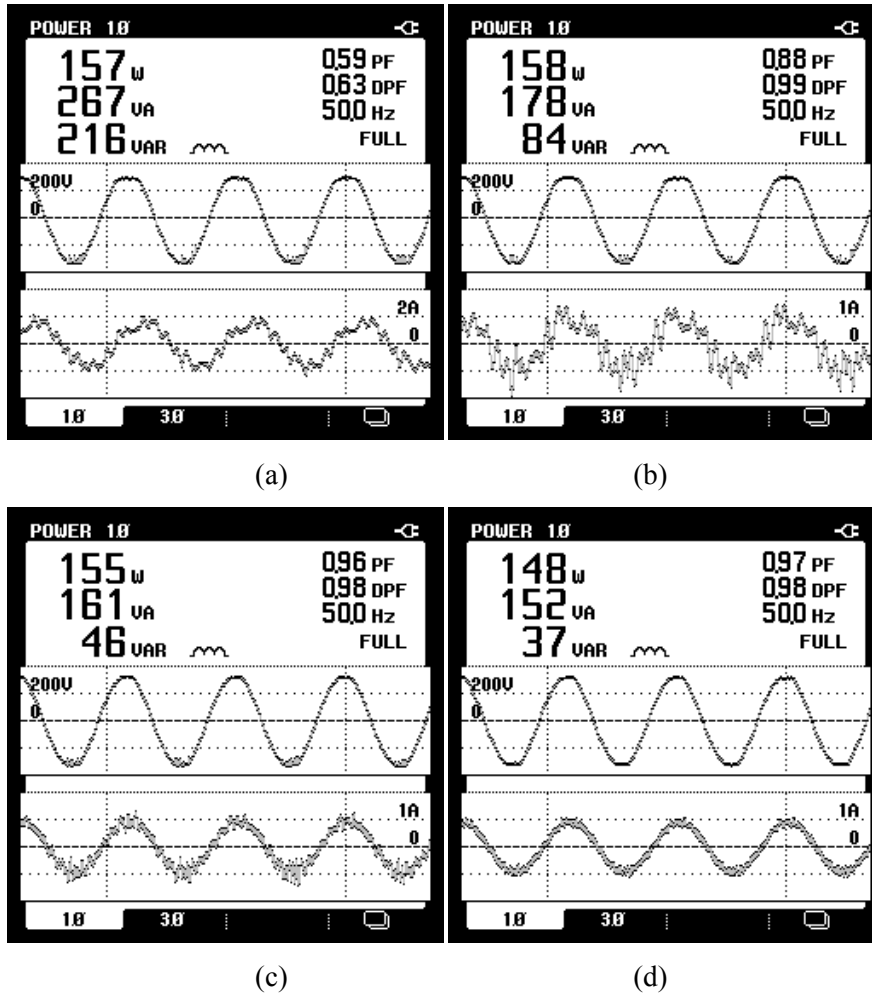


Figure 79. Experimental waveforms with peak current reference 1A following different compensation strategies: (a) no compensation, (b) fundamental compensation, (c) simplified compensation, (d) simplified compensation with passive damping.

Compared with no compensation, in cases of fundamental compensation, simplified compensation and simplified compensation with passive damping, the reactive power is reduced by 61.1%, 78.7%, 82.9% respectively, as shown in Figure 79 (b), (c), (d).

These results show that any of the compensations could significantly reduce the reactive power introduced by grid voltage. Thus, they can be used to improve the power factor.

Figure 80 gives the grid current distortion in frequency domain. In order to compare harmonics for different cases in the same scale, the percentage data are translated in the absolute total harmonic root square value by (4.18), which is derived from (4.17).

$$I_H = \sqrt{I_2^2 + I_3^2 + \dots + I_N^2} = THD \cdot I \quad (4.18)$$

Following (4.18), for four cases, which are no compensation, fundamental compensation, simplified compensation and simplified compensation with passive damping, the absolute total harmonic mean square value are 0.288A, 0.272A, 0.103A, 0.035A respectively.

Compared with no compensation, the total harmonics are reduced by 5.6%, 64.2% and 87.8% for fundamental compensation, simplified compensation and simplified compensation with passive damping respectively. Since the fundamental compensation signal does not contain harmonic information, the harmonic reduction is not obvious.

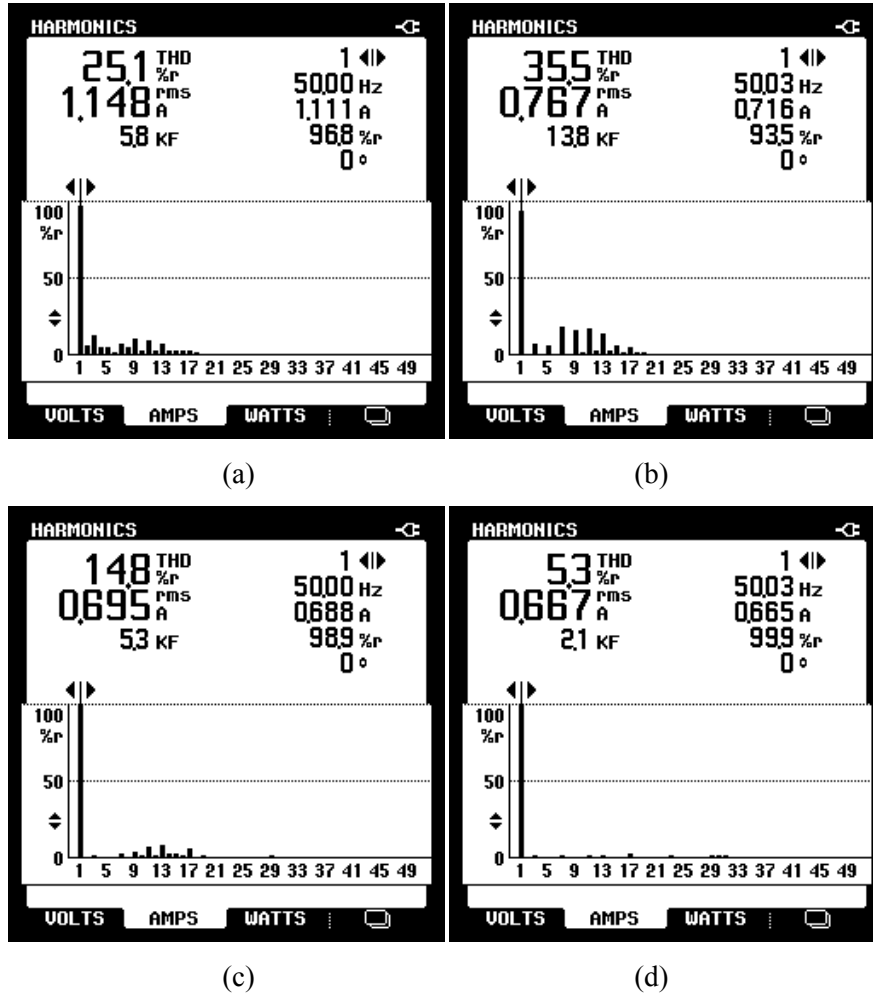


Figure 80. Current distortion in frequency domain with peak current reference 1A following different compensation strategies: (a) no compensation, (b) fundamental compensation, (c) simplified compensation, (d) simplified compensation with passive damping.

IV.1.1.6. Conclusion

For the proposed microgrid, LCL filter offers high power quality for grid current injection in case of rated power. But the grid voltage introduced reactive power and harmonics exists in the whole power operating range and results in obvious power factor degradations in low power operation, which is inevitable from solar irradiance variation, hence it must be improved. After studying the phase error cause of different control strategies by transfer function, a phase error compensation structure is proposed for inverter-side current feedback structure. Taking into account the no compensation case,

three different compensations (fundamental compensation, simplified compensation, and simplified compensation with passive damping) are comparatively studied for different grid-connected situations.

Fundamental compensation is suitable for no distorted grid voltage or in an environment with strong electromagnetic disturbances. Simplified compensation can be used in an environment with less electromagnetic disturbances. The passive damping can be added for further improve power quality at the cost of additional power loss.

The experimental results show that different compensation strategies can significantly reduce the unnecessary reactive power introduced by the grid voltage in low power operation by 61.1%-82.9%. Current harmonics can be reduced by 5.69%-87.8%.

The fundamental compensation gives good performance in reactive power rejection, but poor in harmonic reduction; it could be used for situations with strong noise interference where other two compensations don't work well.

Simplified compensation gives good performance, but the grid current distortion is the shortage; it is suitable for situations not demanding very high power quality. Simplified compensation with passive damping gives the best performance in power quality; damping power loss could be the shortage, however, by properly selecting the damping resistor and capacitor value, the power loss can be controlled quite reasonable. Simplified compensation with passive damping is suitable for situations where high power quality is given priority.

Concerning a better grid-connected operation for the proposed microgrid, the simplified compensation with passive damping is recommended, which is simple yet gives the least harmonic pollution into the grid in low power operations. The reduction of reactive power and harmonics is also suited for the whole operation range and high power quality can be obtained.

IV.1.2. Experimental tests of grid-connected supervision control

After the improvement of experimental platform, whose electric scheme is presented in Figure 5 in the section II.1, the grid-connected tests are carried out.

For grid-connected test, the parameters given in Table 10 are used for optimization and power balancing control strategy. These parameters are selected according to power system configuration with an aim to show as much system behavior as possible, such as storage events (full, empty), load shedding and PVA power limiting.

Table 10. Parameters for grid-connected operation.

Variable	Value
$P_{G_S_LIM}$	1000W
$P_{G_I_LIM}$	1000W
P_{L_MAX}	1700W
K_L	[0, 1]
P_{PV_P}	2000W
SOC_{MIN}	45%
SOC_{MAX}	55%
SOC_0	50%
v^*	400V
Grid peak hours	10:00-12:00, 17:00-19:00

Since the estimated conversion efficiency is not accurate, and that the measurement also contains errors due to power electronic device switching transient noise and temperature drift of components in the self-made current sensing board. It may occur that the load shedding and PVA power limiting calculation given by the operation layer algorithm can result in grid power reaching or even surpassing a little its limits. So, security margins are added to shed a little more load or PV power than calculation in order to keep grid power within its limit. That is also why in case of load shedding and PVA power limiting, the grid power is a little less than the give power limits in the following experimental results.

The experimental results are strongly influenced by the solar irradiance evolution and induced prediction errors. Hence, to analyze the proposed DC microgrid validation, many tests were operated. They have permitted to choose three typical cases. These case studies correspond to three types of solar irradiance evolution: high irradiance almost without fluctuations (test 1), high irradiance with strong fluctuations (test 2), and low irradiance with strong fluctuations (test 3).

IV.1.2.1. Test 1

Test 1 is performed for operation on the 21st of August 2013 in Compiègne, France. The load prediction uncertainty is shown in Figure 69. Concerning PVA prediction uncertainty, the PVA power raw data prediction, corrected prediction and measurement are shown in Figure 81.

It can be noted that compared with the raw data prediction, the corrected prediction is lower at the beginning and the end of the day, and higher in the middle of the day as the sun position changes. The prediction corresponds better the measurement during the first few hours, especially before 11:00. The measurement is lower than the corrected prediction after 11:00 due to two reasons: one is that a slight thin cloud that covers the sky is not predicted, the other is that the PVA cell temperature, which is hard to predict and not considered in PVA power prediction correction, increases significantly with the sunshine heating and results in power decrease.

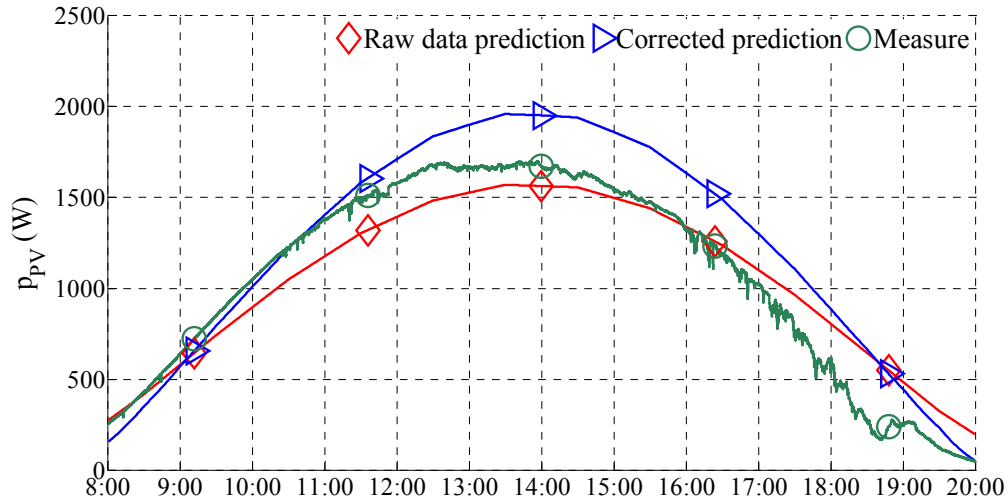


Figure 81. PVA power prediction and measure for grid-connected test 1.

According to the prediction information, the energy management layer solves the optimization problem by CPLEX and gives the optimum power flow evolution, as presented in Figure 82. The power flow optimization effect can be observed.

During peak hours, the excess power is optimized to be injected into the grid to increase benefits (10:10-12:00, 17:00-18:00). In case of supply during peak hours, the storage supplies the load for avoiding expensive grid peak supply (10:00-10:10, 18:00-19:00). In grid peak hours, the supervision control acts like a simple rule based control which simply inject excess power into grid and supply the load by storage. That is because this is the optimal way to reduce energy cost. Meanwhile, the optimization keeps storage available for the grid peak hours supply.

The difference between optimization and rule based control remains in off-peak grid hours. For example, storage charging is preferred to be done in off-peak grid hours for energy cost reduction. However, the storage charging is not necessary to be immediately started at the beginning of off-peak grid hours. Because with the storage fully charged too early, the latter excess PVA power may not be fully absorbed due to the grid power injection limit, which can result in PVA power limiting that waste energy and increase energy cost. Another issue is that if load power demand is low during peak hours, it is also possible for the storage to supply the load during off-peak hours. The storage charging or discharging proportion can hardly be determined by the rule based control, but the prediction based supervision control can easily determine these aspects from an overall viewpoint. That is why the storage is optimized to supply power during off-peak hours (for example 8:00-9:00, 9:20-10:00) and PV excess power is injected into the grid (for example 9:00-9:20). The optimization cannot be replaced by rule based control since the operation varies according to conditions for minimizing the energy cost.

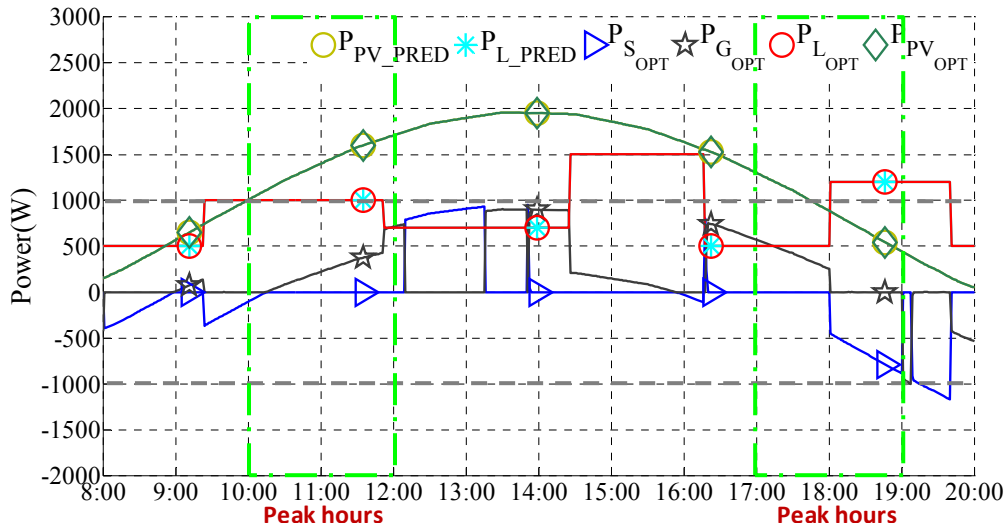


Figure 82. Power flow given by optimization for grid-connected test 1.

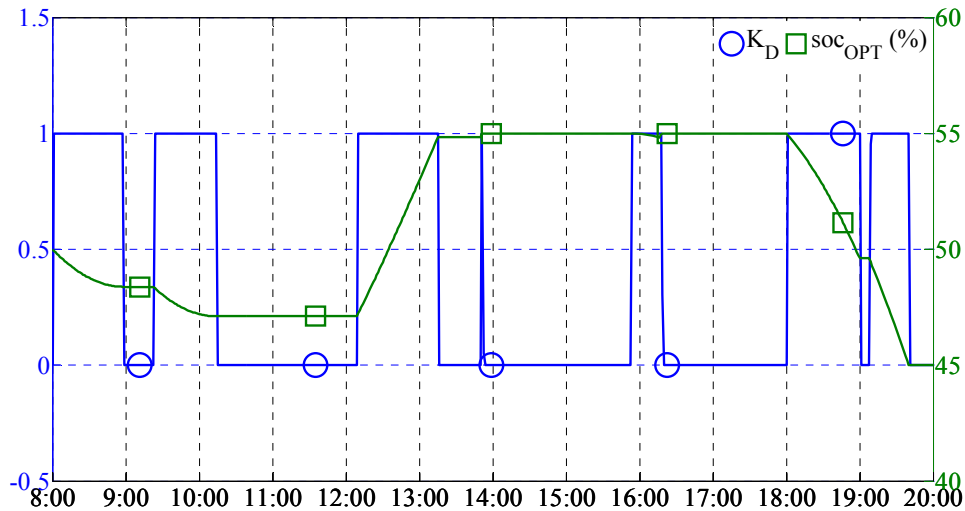


Figure 83. K_D and SOC evolution given by optimization for grid-connected test 1.

Based on optimum power flow evolution, optimum K_D sequence is calculated a few hours before the experimental operation of the 21st of August 2013, as shown in Figure 83.

The optimum cost estimated by CPLEX is -0.777€. The cost is negative because during this day, local renewable production is sold to grid and it can bring benefits that can compensate the energy consumption cost.

With the calculated K_D optimum sequence and the operation layer operating strategy, an experimental operation is performed. The operating conditions for PVA are shown in Figure 84.

The power evolution is recorded during this experimental operation and the power flow is shown in Figure 85. Experimental SOC and DC bus voltage evolution are shown in Figure 86. During this day operation, grid and storage supply or absorb power according to K_D except for the moment when SOC limits is reached in the period of 18:50-20:00. Due to uncertainties from both load prediction and PVA power prediction, the experimental power flow cannot evolve 100% as the optimization power flow.

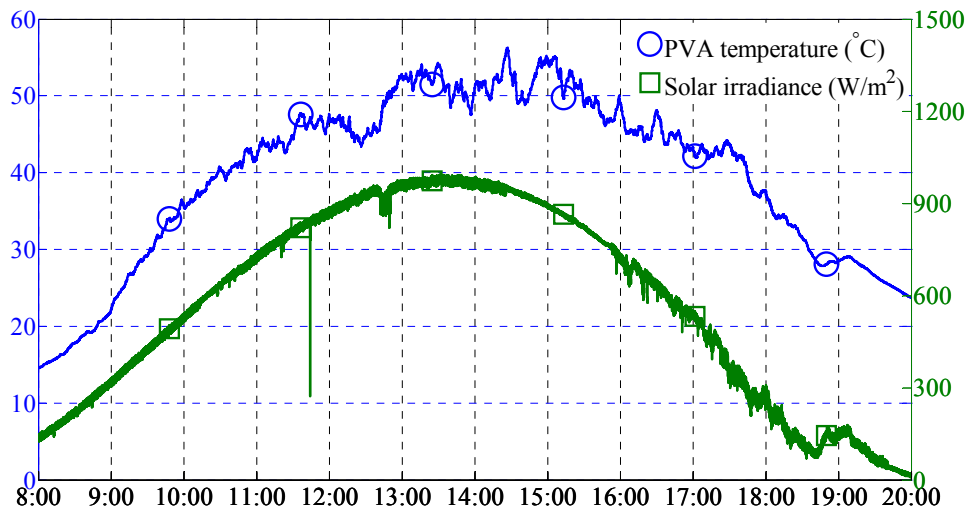


Figure 84. PVA cell temperature and solar irradiance on the 21st August 2013.

Since the PVA produces less power than predicted, the obvious result is that storage is not fully charged during the day and reaches its SOC_{MIN} earlier than expected, resulting in load shedding (18:50-19:40) according to power balancing control as grid supply is limited. When the grid is able to supply within its limits, the load is supplied by the grid without load shedding (19:40-20:00).

In detail, the experimental power flow corresponds well to the optimized power flow from 8:00-9:20. From 9:20 to 11:50, the PV power prediction error is not significant, while the load demands 200W more power than predicted. This results in more storage discharge than the prediction between 9:20 and 10:10.

In the period of 10:10-12:05, it is expected that the grid absorbs excess PVA power. Due to the error of load prediction, the grid supply during peak hour is involved at 10:10-11:00 and less power is injected in the grid from 11:00-12:05.

From 12:05-14:20, both PVA power and load demand are less than the prediction. As a result, the grid power and storage power corresponds to the optimization result.

From 14:20-16:15, the load demand is higher than prediction and the PVA power is less than the prediction, which is the period that introduced the largest error between optimization and actual power flow: the grid supplies power at 14:20-15:50 instead of power injection expected by optimization and the storage supplies more power than expected from 15:50-16:15.

From 16:20-18:00, the PVA power is less than prediction, so less power is injected into the grid. From 18:00-20:00, the storage capacity is less than optimization and it supplies more power than expected, so it is empty at 18:50 instead of 19:40. Then the grid supplies the load from 18:50-20:00 with load shedding as aforementioned.

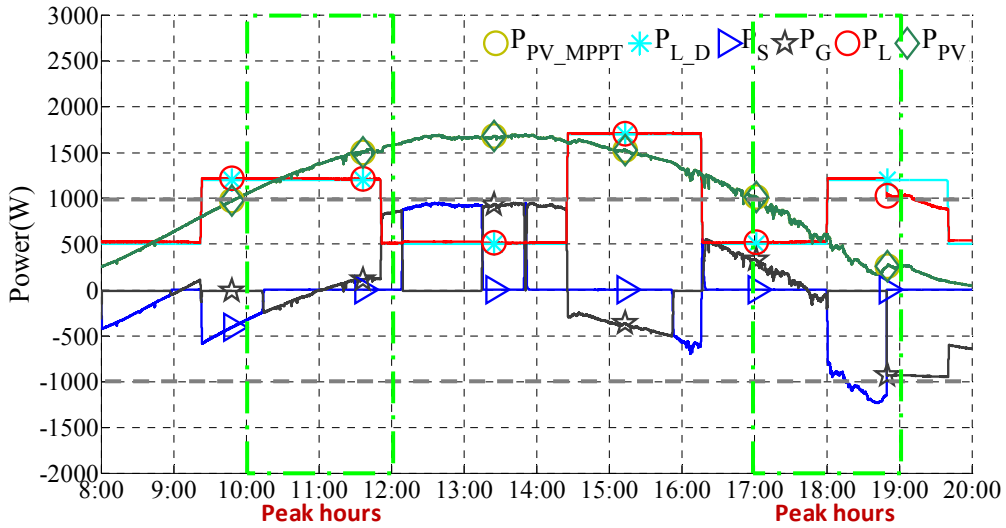


Figure 85. Experimental power flow for grid-connected test 1.

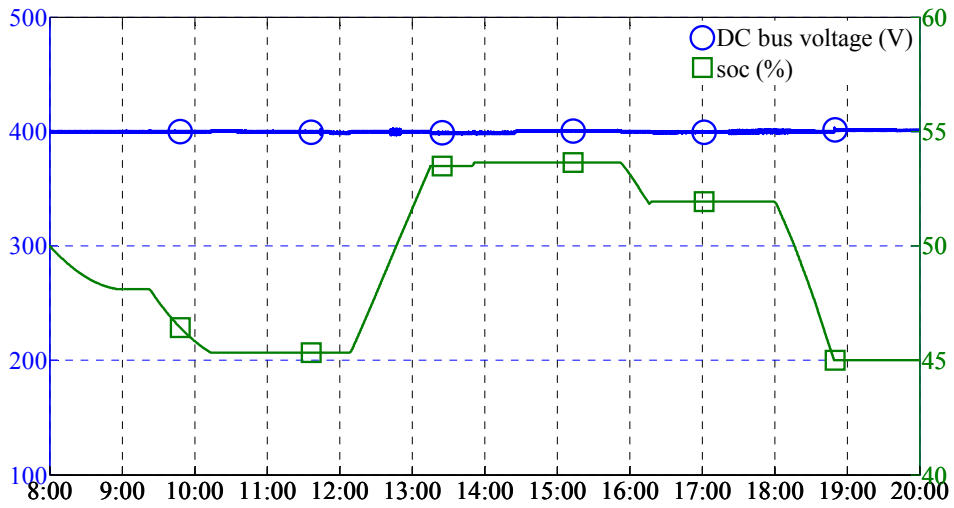


Figure 86. Experimental *SOC* evolution and DC bus voltage for grid-connected test 1.

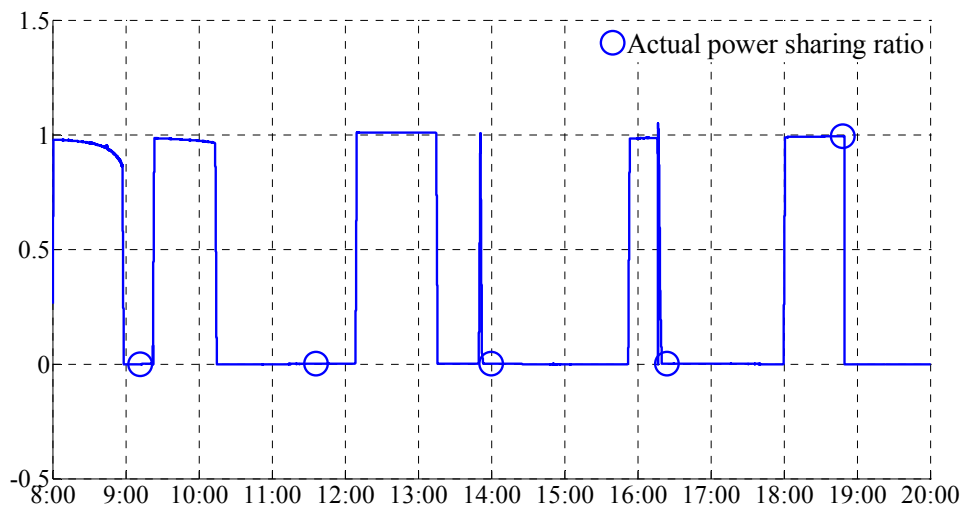


Figure 87. Actual power sharing ratio between storage and grid for grid-connected test 1.

It is noted that prediction error can affect the optimization performance. However, compared with prediction, if the actual production and consumption are with almost the same errors in the same

direction, *i.e.* the difference between the actual production and consumption corresponds to the difference given by prediction, the actual power flow of storage and grid can correspond to the optimization result, for example the period of 12:05-14:20.

Although that prediction error can affect the optimization performance, the prediction error does not affect power balancing. It is shown in Figure 86 that the DC bus voltage is steady, signifying the power is well balanced during the operation.

The actual power sharing ratio between storage and grid is shown in Figure 87. If compare the actual power sharing with K_D . We can see that the optimization command K_D is expected for most of the time, except for the short period in the end when the storage is empty. At that moment, operation layer performs load shedding to ensure power balancing. The slight difference is due to measurement errors.

Table 11 compares the energy cost between optimization and experiment. Due to uncertainties, the experimental cost is larger than optimization. The load shedding contributed to 24.4% of the cost error. The other error is introduced by excess grid and storage supply involved by uncertainties. After the experiment test, an optimization for real operating conditions is performed, which gives the ideal experiment cost. Even with uncertainties, it can be seen that experiment cost is not far from the ideal experiment cost.

Table 11. Comparison between optimization and experiment for grid-connected test 1.

Case operation	Cost (€)	Load shedding (€)	PVA power limiting (€)
Optimization	-0.777	0	0
Experimentation	0.225	0.244	0
Optimization for real conditions	-0.247	0	0

IV.1.2.2. Test 2

Test 2 is performed for operation on the 9th of August 2013. The PVA power prediction uncertainty is shown in Figure 88. As the prediction is given in the form of hourly data, the fluctuations presented in the real PVA power are not taken into account. In addition, the concave character of prediction around 14:30 is delayed around 15:45 in the actual condition.

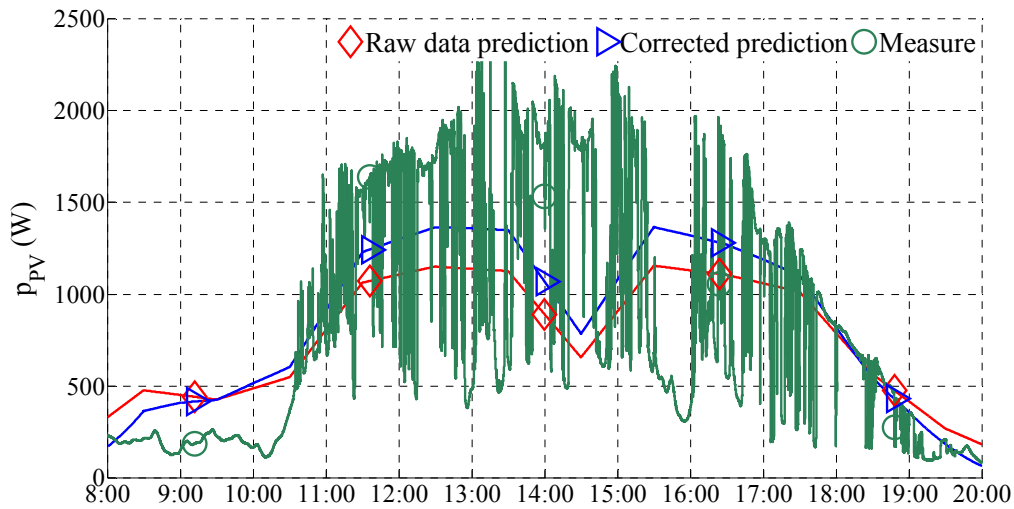


Figure 88. PVA power prediction and measure for grid-connected test 2.

The optimized power flow by CPLEX is shown in Figure 89. Based on optimum power flow evolution, optimum K_D sequence is calculated for the experiment as shown in Figure 90.

During peak hours, the microgrid injects the excess PVA power to grid and supplies the load by storage. In off-peak hours, optimization optimizes storage and grid power. With the optimization, neither load shedding nor PV power limiting is performed. The optimum cost estimated by CPLEX is -0.149€.

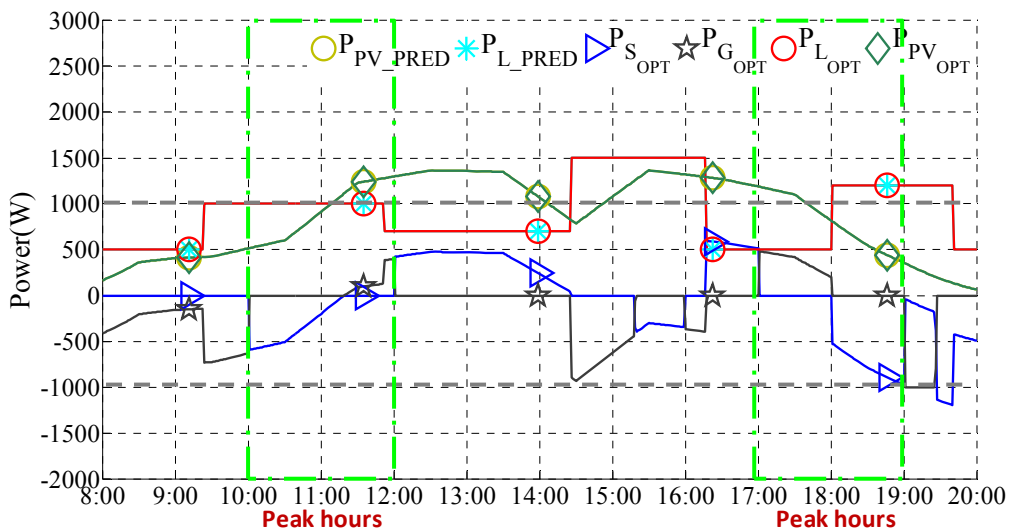


Figure 89. Power flow given by optimization for grid-connected test 2.

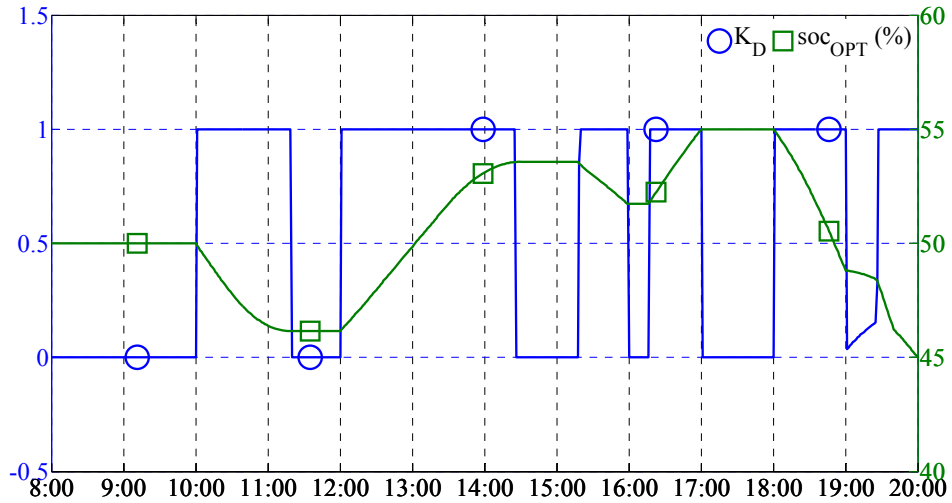


Figure 90. K_D and soc_{OPT} evolution given by optimization for grid-connected test 2.

The operating condition for PVA is shown in Figure 91.

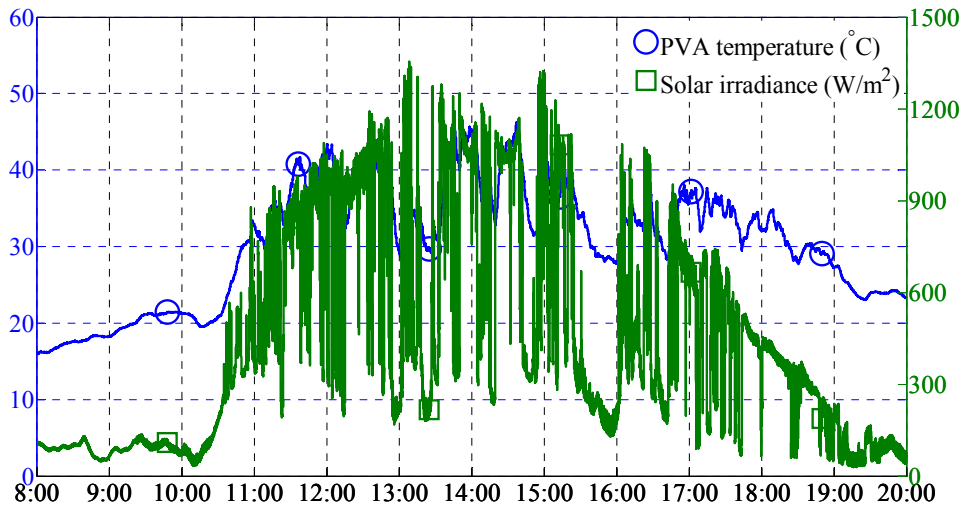


Figure 91. PVA cell temperature and solar irradiance on the 9th August 2013.

The experimental power evolution is obtained with K_D and operation layer control strategy for the operation. The power flow is shown in Figure 92. Experimental soc and DC bus voltage evolution are shown in Figure 93. During this day operation, grid and storage supply or absorb power according to K_D except for the period of when soc limits are reached or grid power limits are reached.

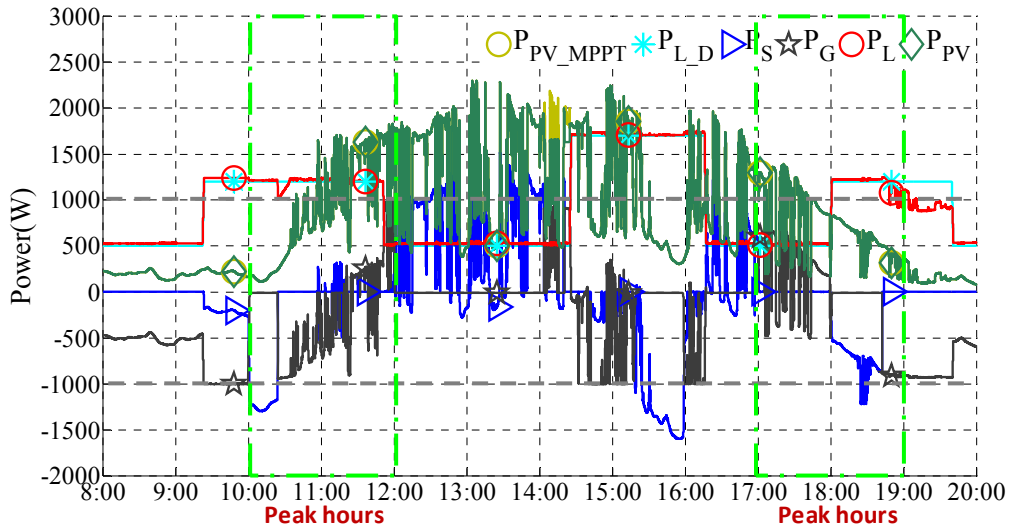


Figure 92. Experimental power flow for grid-connected test 2.

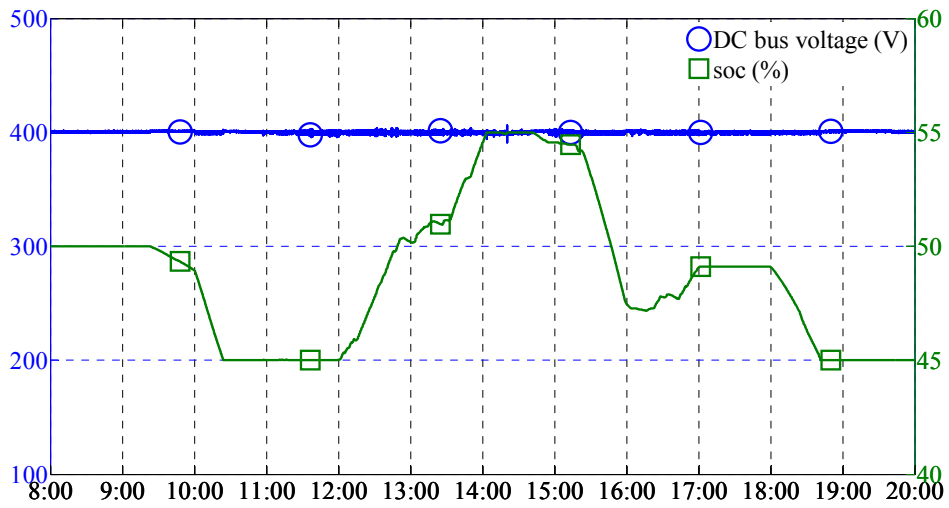


Figure 93. Experimental SOC evolution and DC bus voltage for grid-connected test 2.

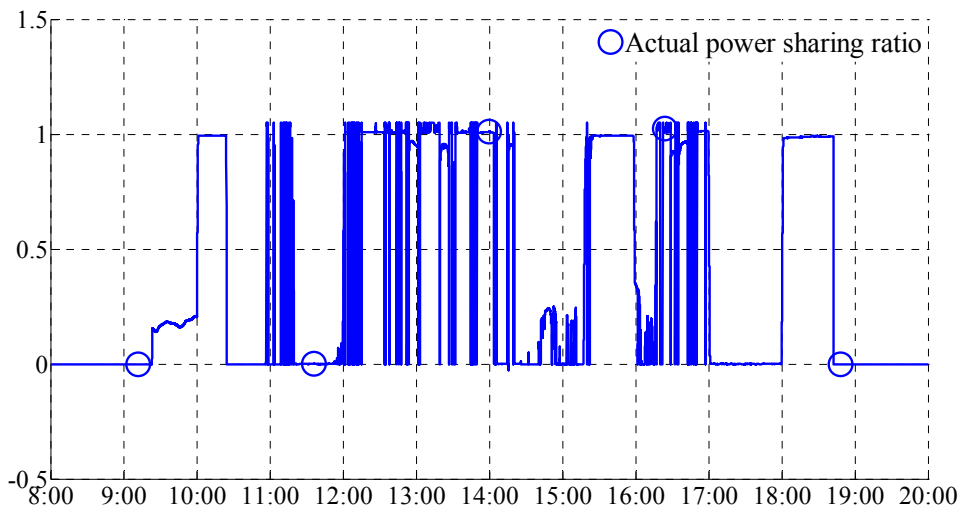


Figure 94. Actual power sharing ratio between storage and grid for grid-connected test 2.

From 8:00-9:20, grid supplies the load as commanded by K_D . From 9:20-10:00, the load demands more power than predicted that the grid alone is not able to supply. Since the storage is available for supply, *i.e.* $soc > SOC_{MIN}$, storage supplies power together with the grid, which is the self-correcting by operation layer control strategy.

During 10:00-10:20, the storage supplies the load according to K_D . The storage reaches SOC_{MIN} at 10:20 since it has supplied power before 10:00 and supplies more power to the load due to prediction uncertainties.

For 10:20-11:20, grid supplies the load for most of the time without regard of K_D by self correcting of operation strategy. Since grid supply power is limited, load shedding is performed around 10:25-10:35 to keep power balancing. During the PVA production fluctuations from 10:55 to 11:20, the storage is slightly charged and supplies again for a short while.

Grid is used for power balancing at 11:20-12:00, as commanded by K_D . Although grid supply is involved instead of pure injection grid, injection is more than supply during the fluctuations.

From 12:00 to 14:20, storage is charged following the commanded by K_D . As load consumes less than prediction, the storage is fully charged at 14:00. From 14:00 to 14:20, the excess PVA production is injected into the grid. Because the surplus PVA production exceed grid power injection limit, the surplus PVA production cannot be absorbed, so the PV power limiting is performed as self-correcting by operation layer control strategy. During this period, the actual PVA power (green curve) is less than estimated PVA MPPT production with the weather condition.

At 14:20-15:15, grid is commanded by K_D to supply the load. However, when the PVA production is too low and grid supply limit is reached, the storage supplies power as a result of self-correcting. The storage follows K_D command to supply power at 15:15-16:00.

From 16:00 to 16:15, the grid supplies the load and storage is involved when grid supply is limited. During 16:15-17:00, storage is charged following K_D command.

During 17:00-18:00, the power is mainly injected into grid, as commanded by K_D . From 18:00 to 20:00, storage supplies first but SOC_{MIN} is reached before expected and then grid supplies power. When grid power supply limit is reached, load shedding is performed to keep power balancing.

The steady DC bus voltage in Figure 93 signifies that the power is well balanced during the whole test.

In this test, although prediction involves uncertainty and the weather condition results in fluctuating PVA production, the power balancing is able to be maintained with respect of all rigid constraints such as grid power limits and SOC limits. The self-correcting effect of power balancing can be fully observed and load shedding and PVA power limiting appeared only for short durations.

The actual power sharing ratio between storage and grid is shown in Figure 94. Due to fluctuations and prediction uncertainties, K_D cannot be fully respected. However, the mean actual power sharing ratio value still represents the optimization information.

Table 12 compares the energy cost between optimization and experiment. Due to uncertainties, the experimental cost is larger than optimization. It can be seen that load shedding and PV power limiting formed 29.4% of the cost error, the other part is introduced by prediction uncertainties that result in both grid and storage extra power supplies during peak hours and off-peak hours. As for test 1, an optimization for real operating conditions is performed after experiment. Even with uncertainties, the experiment cost is not far from the ideal experiment cost.

Table 12. Comparison between optimization and experiment for grid-connected test 2.

Case operation	Cost (€)	Load shedding (€)	PVA power limiting (€)
Optimization	-0.149	0	0
Experimentation	0.929	0.266	0.052
Optimization for real conditions	0.357	0	0

IV.1.2.3. Test 3

Test 3 is performed for operation on the 30th of July 2013. The weather condition is cloudy with generally low solar irradiance. The PVA power prediction uncertainty is shown in Figure 95.

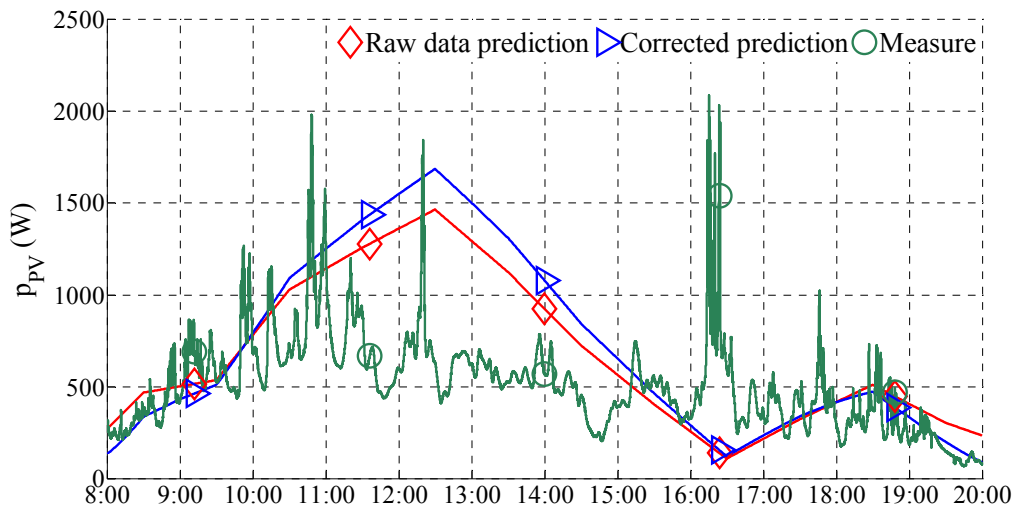


Figure 95. PVA power prediction and measure for grid-connected test 3.

The optimized power flow by CPLEX is shown Figure 96. The optimum K_D sequence, which is applied for the experimental operation of the 30th of July 2013, and the optimum SOC are shown in Figure 97.

During the first peak hours 10:00-12:00, it can be seen that the optimization injects the excess PVA power to grid and supply the load by storage.

During the second peak hours 17:00-19:00, since the storage is not able to be fully charged before the second peak hours. Grid supplies alone 17:40-18:10 and together with the storage 18:50-19:00.

In off-peak hours, optimization optimizes storage and grid power. It can be seen the optimization tries to maximally charge the storage.

The storage is also used to prevent load shedding when grid supplies at its power limit. With the optimization, neither load shedding nor PV power limiting is performed.

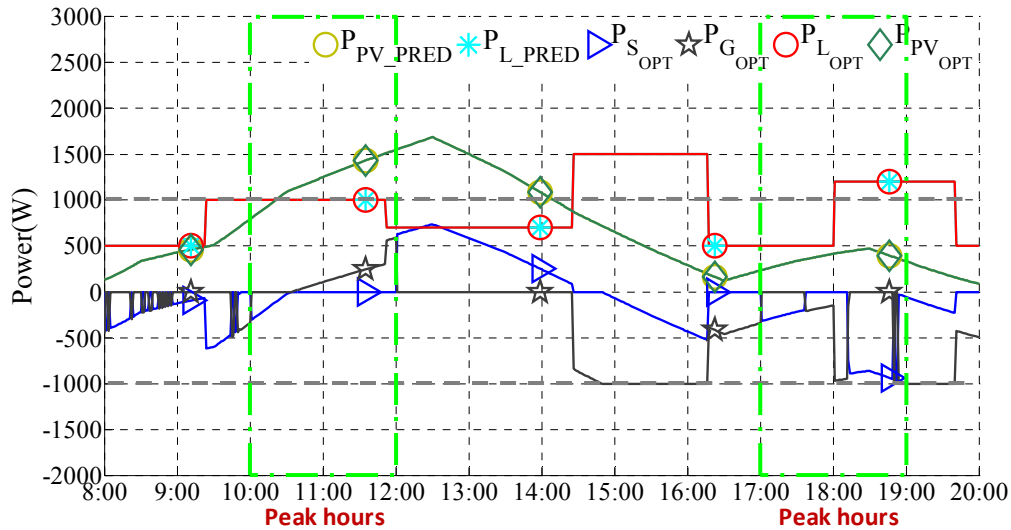


Figure 96. Power flow given by optimization for grid-connected test 3.

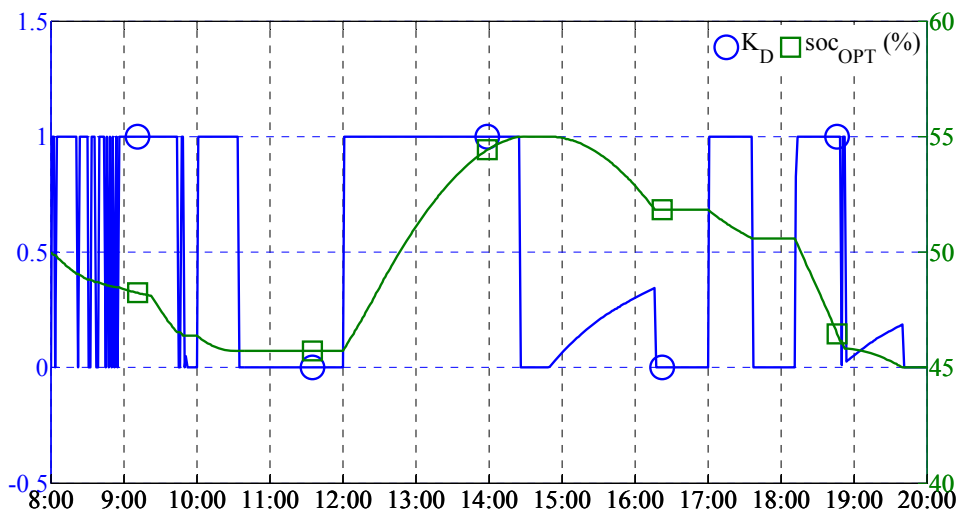


Figure 97. K_D and soc evolution given by optimization for grid-connected test 3.

The operating condition for PVA is shown in Figure 98.

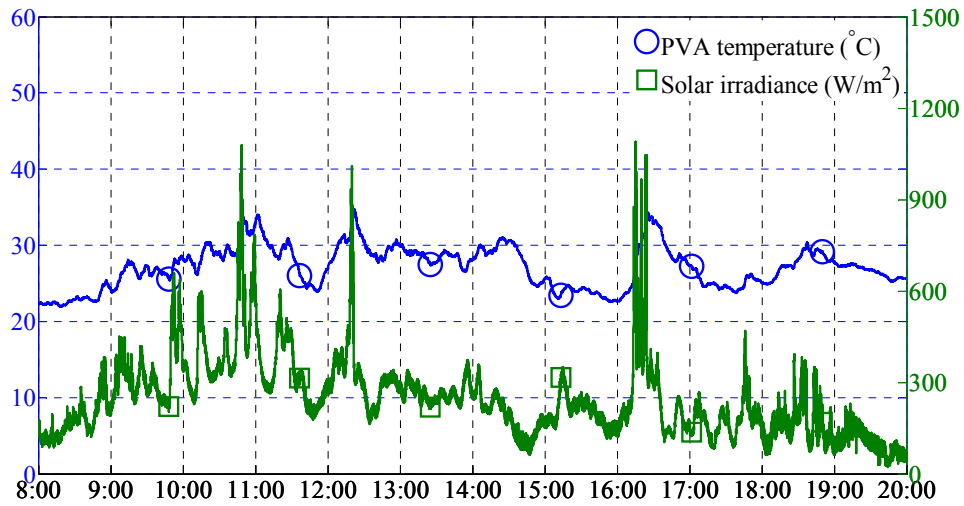


Figure 98. PVA cell temperature and solar irradiance on the 30th July 2013.

The experimental power evolution is shown in Figure 99. Experimental SOC and DC bus voltage evolution are shown in Figure 100.

Due to uncertainties, the storage reached SOC_{MIN} before 10:00 and does not participate in the supply during first peak hours. The storage is slightly charged around 12:10 and contributes too little in the subsequent power balancing. Due to the prediction uncertainties, the load power is supplied by the grid with respect to its power limits. When the grid power reaches the limit, load shedding is performed to keep power balancing 14:20-16:15, 17:55-19:40.

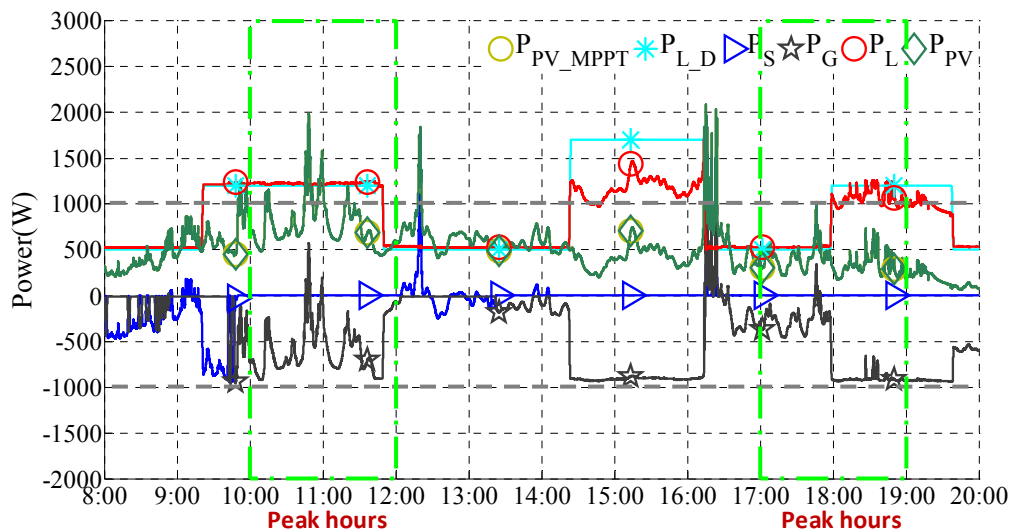


Figure 99. Experimental power flow for grid-connected test 3.

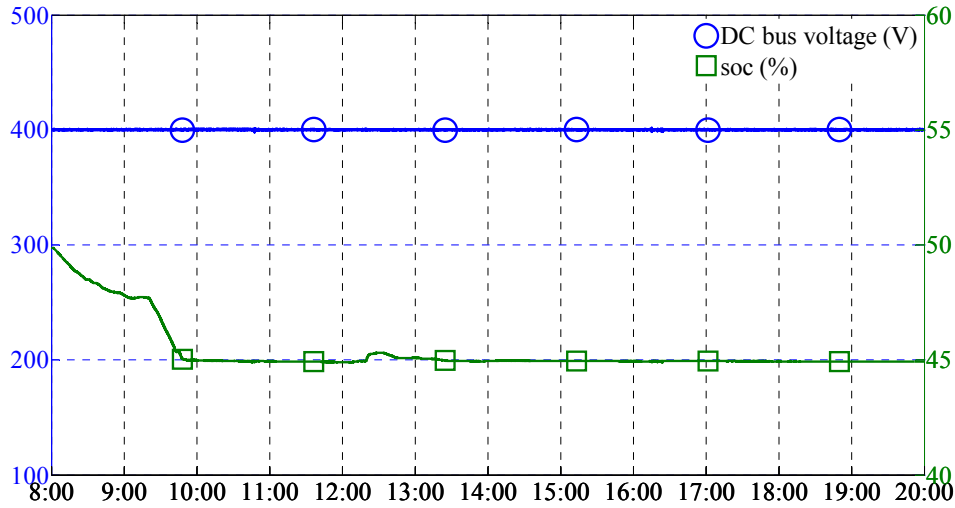


Figure 100. Experimental *SOC* evolution and DC bus voltage for grid-connected test 3.

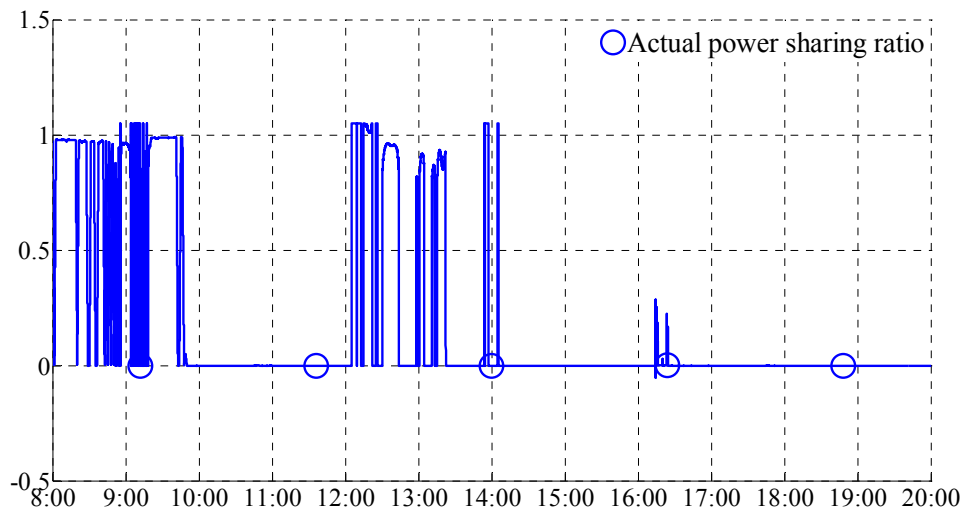


Figure 101. Actual power sharing ratio between storage and grid for grid-connected test 3.

In this test, the error between actual PVA production and prediction is significant. As a result, the storage is only used for a short period and does not participate in grid peak shaving. However, the power can be balanced successfully by the operation layer control strategy.

The actual power sharing ratio between storage and grid is shown in Figure 101. Due to prediction uncertainties, K_D can only be respected at the beginning and optimization does not suit the real conditions. However, the operation layer can keep robust power balancing.

Table 13 summarizes the energy cost between optimization and experiment.

Due to prediction uncertainties and low solar irradiance, the experimental cost is much greater than optimization. The load shedding formed 40.4% of the experimental cost. Grid peak hours supply cost is 1.626€, and formed 50.5% of the experimental cost. Due to uncertainties, the storage cannot be optimized to participate in the peak hour to supply. Whence the energy cost is largely increased by grid peak supply as well as load shedding. An optimization for real operating conditions is performed

after experiment. It can be seen that the difference between experiment and ideal experiment cost is the most significant in the three grid-connected tests, which is due to relatively large prediction uncertainties.

Table 13. Comparison between optimization and experiment for grid-connected test 3.

Case operation	Cost (€)	Load shedding (€)	PVA power limiting (€)
Optimization	0.386	0	0
Experimentation	3.219	1.300	0
Optimization for real conditions	2.165	0.257	0

IV.1.3. Conclusion

This section firstly proposed an improved control for enhancing grid power quality in case of low power operation, which is evitable with renewable energy production.

Then, three tests for grid-connected operating mode are provided and analyzed. As result, the proposed supervision control is experimentally validated and it is shown that it can work under different weather conditions while providing robust power balancing control strategy and interfacing with optimization. The difficulty of implementing optimization in real operation while respecting to rigid constraints is solved by the proposed supervision control which parameterizes power balancing strategy that provides interface for optimization.

Optimization effect can be seen in actual power flow with certain degree of uncertainties. For the first two tests it can be seen that even with uncertainties, the storage can participate in the peak hour power balancing for peak shaving, avoid undesired injection. For the third case, when the storage does not participate in peak hour power balancing, the energy cost can be increased largely by two aspects: grid peak supply and load shedding. The actual power flow is be better optimized when the prediction data provides more precision. Even with uncertainties, the experiment cost can be controlled near ideal experiment cost, which validated the effectiveness of the proposed supervision control.

From the point of view by the grid, no matter how the power evolves in the microgrid, the grid power can be maintained within its limits. For smart grid, it can simply regulate these limits to increase or decrease the supplied power and injected power, which facilitate DSM for grid operating.

It is also noted that if the prediction error for production and the error for consumption are similar and in the same direction; the power flow for the sources is less affected.

IV.2. Experimental validation of off-grid supervision control

For off-grid mode test, the parameters that are used for optimization and power balancing control strategy are given in Table 14. These parameters are selected according to system configuration with

an aim to involve as much system behavior as possible during the tests, such as storage events (full, empty), load shedding and PVA power limiting.

Table 14. Parameters for off-grid operation.

Variable	Value
P_{S_MAX}	1300W
P_{L_MAX}	1700W
P_{MT_P}	1500W
dt_{MT}	1200s
K_L	[0, 1]
SOC_{MIN}	45%
SOC_{MAX}	55%
SOC_0	50%
SOC_F	50%
v^*	400V

For the same reason as in grid-connected mode, security margins are added to shed a little more load or PV power than calculated in order to keep storage power within its limit. Besides these, once the PVA power limiting is triggered, it lasts for a period for avoiding storage charging discharging oscillations.

IV.2.1. Experimental tests of off-grid supervision control

As for grid-connected operating mode, three experimental tests are presented. The case studies retained for off-grid mode are: high irradiance almost without fluctuations (test 1), high irradiance with strong fluctuations (test 2), and mixed high irradiance with strong fluctuations and low irradiance without fluctuations (test 3).

IV.2.1.1. Test 1

Test 1 is performed for operation on the 4th September 2013. As in grid-connected mode, the load prediction uncertainty is the same as shown in Figure 69. PVA power prediction uncertainty is shown in Figure 102. It can be noted that during 10:30-18:50, the measure is lower than the corrected prediction by about 11% mainly due to the PV cell temperature as aforementioned. The optimized power flow by CPLEX is shown in Figure 103. It can be seen that the storage is used for power balancing and MT is started by duty cycles in order to keep continuous supply for the load and ensure that at the end of the operation, the storage capacity is above a preferred level SOC_F . Since MT cannot absorb power, when the storage reaches SOC_{MAX} the only way for keep power balancing is to limit PVA power production; this is why there is PVA power limiting in the period of 13:10-14:20.

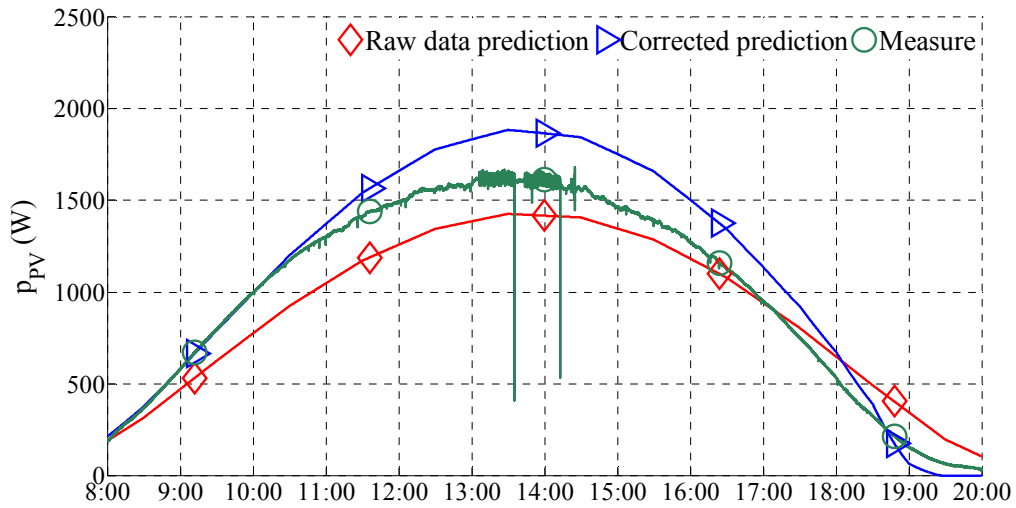


Figure 102. PVA power prediction and measure for off-grid test 1.

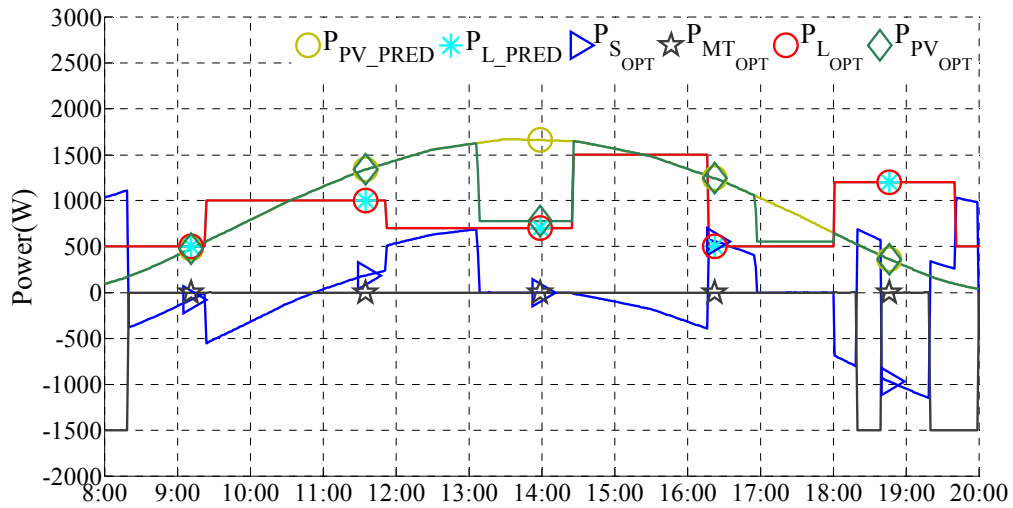


Figure 103. Power flow given by optimization for off-grid test 1.

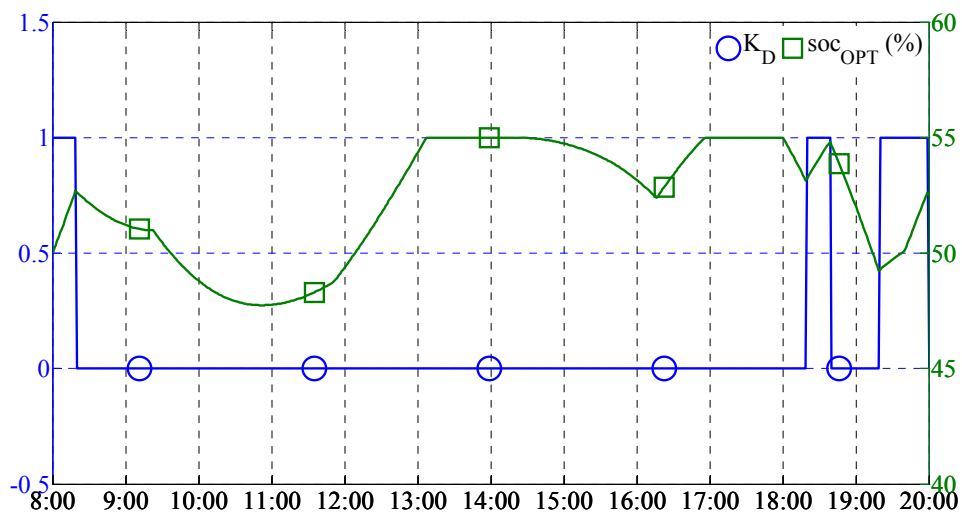


Figure 104. K_d and soc evolution given by optimization for off-grid test 1.

Based on optimum power flow evolution, optimum K_D sequence is calculated for the experimental operation, which is the on-off signal for the MT, as shown in Figure 104.

The control parameter K_D is used for the experimental operation whose PVA operating conditions are shown in Figure 105.

The operation is performed with K_D and operation layer off-grid control strategy. The obtained power flow is shown in Figure 106. Experimental SOC and DC bus voltage evolution are shown in Figure 107. In the power flow, MT is started by duty cycle as commanded by K_D for 8:00-8:20, 18:20-18:40, 19:20-20:00. No load shedding is performed. During 8:00-13:05, the power is balanced following K_D .

Despite uncertainties in both load and PVA power prediction, the storage is fully charged around 13:05, as expected by optimization.

During 13:05-14:20, there is no other source that can absorb PVA production, and it is hard to calculating the PVA power limiting reference for produce just the necessary power to supply the load for maintaining power. As a solution, the control strategy limits the PVA production a little more, inducing storage low power supply. After the SOC is reduced by certain amount, the PVA is recovered to produce MPPT power again until the SOC_{MAX} is reached again. That is why the PVA power oscillation between MPPT mode and power limiting mode can be observed.

During 14:20-20:00, except for that optimization order is followed that the storage is used for power balancing and MT is started following K_D , two difference with optimization can be noted: firstly, the PVA power limiting during 16:55-18:00 is not appeared in actual power flow due to actual higher load demand and lower PVA production which caused $soc < SOC_{MAX}$; secondly, MT is started for 19:00-19:20, which is controlled by the operation layer control strategy that starts MT when SOC approaches SOC_{MIN} .

The power is well balanced during the operation, as shown in Figure 107 by the steady DC bus voltage. The DC bus voltage fluctuates about 5% at the instants of PVA power limiting control and starting MT by control strategy, which is related to corresponding control dynamics and is acceptable. Due to uncertainties, the final SOC value is less than 50%.

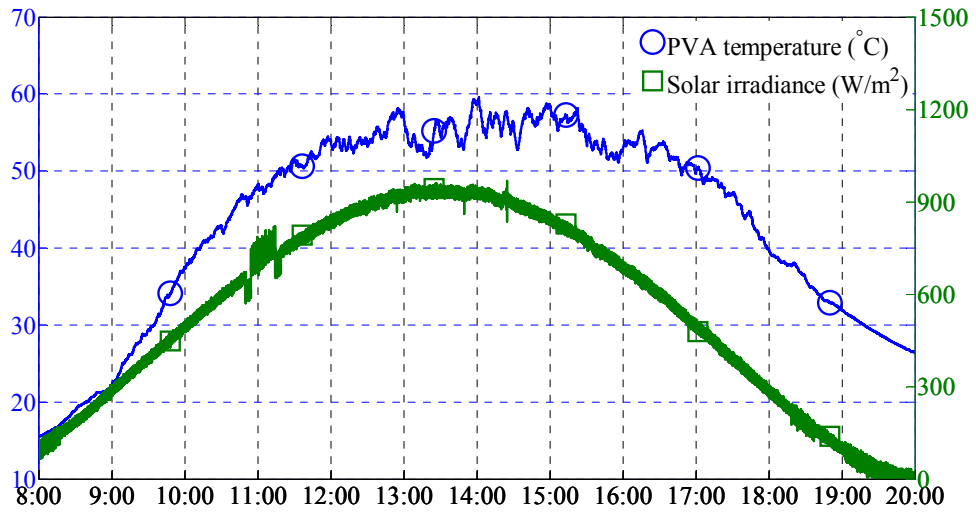


Figure 105. PVA cell temperature and solar irradiance on the 4th September 2013.

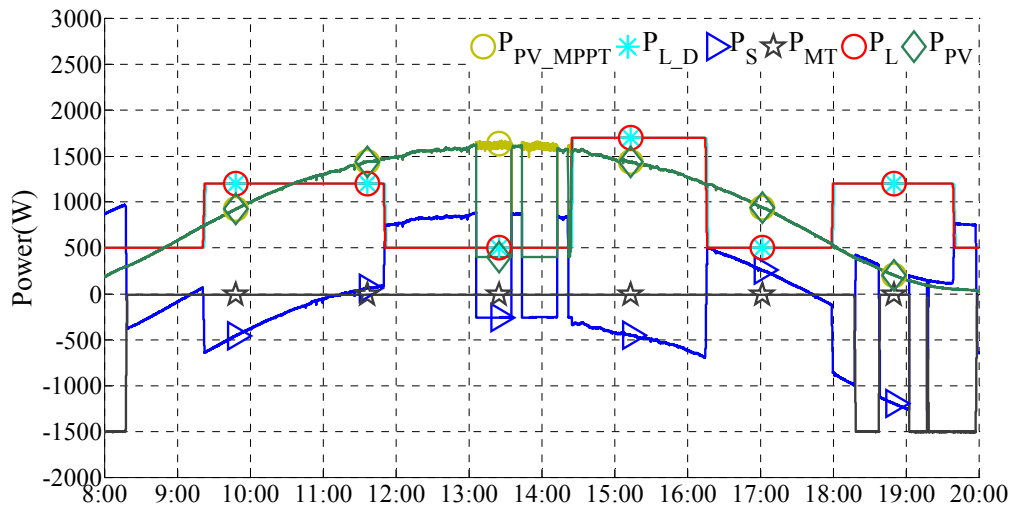


Figure 106. Experimental power flow for off-grid test 1.

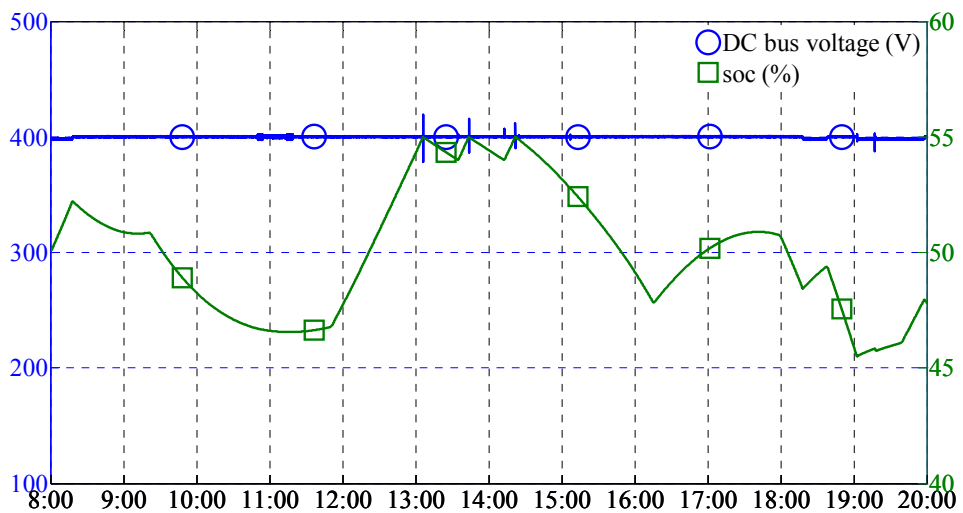


Figure 107. Experimental *soc* evolution and DC bus voltage for off-grid test 1.

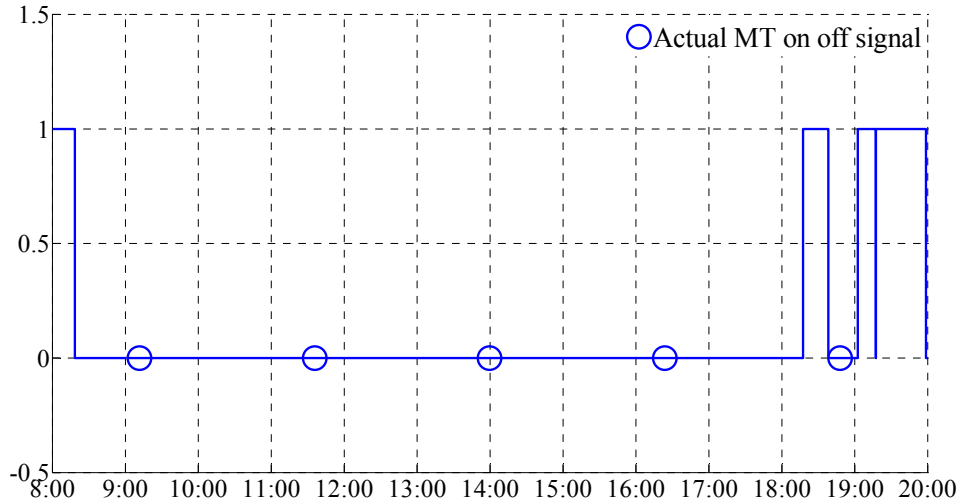


Figure 108. Actual MT on off signal for off-grid test 1.

The actual MT on-off signal is shown in Figure 108. If compare K_D with actual microturbine on-off operation. It can be seen that optimization command K_D is expected for most of the time, except for the additional duty cycle at last, which is the self correcting by operation layer.

Table 15 compares the energy cost between optimization and experiment. Due to uncertainties, the experimental cost is slightly more than optimization. During the experimental test, the PVA power limiting is less than the optimization by 23% and the MT generation is more than the optimization by 11.9%. An optimization for real condition is performed after the experiment. Even with prediction uncertainties, the experiment cost is close to ideal experiment cost.

Table 15. Comparison between optimization and experiment for off-grid test 1.

Case operation	Cost (€)	Load shedding (€)	PVA power limiting (€)	MT generation (€)
Optimization	3.629	0	1.463	2.166
Experimentation	3.658	0	1.121	2.423
Optimization for real conditions	3.380	0	1.180	2.2

IV.2.1.2. Test 2

Test 2 is performed for operation on 27th August 2013. PVA power prediction uncertainty is shown in Figure 109. It can be noted that the measure is less than the corrected prediction, for the periods of 8:00-10:00 and 15:30-20:00 the weather is heavily clouded which is not predicted.

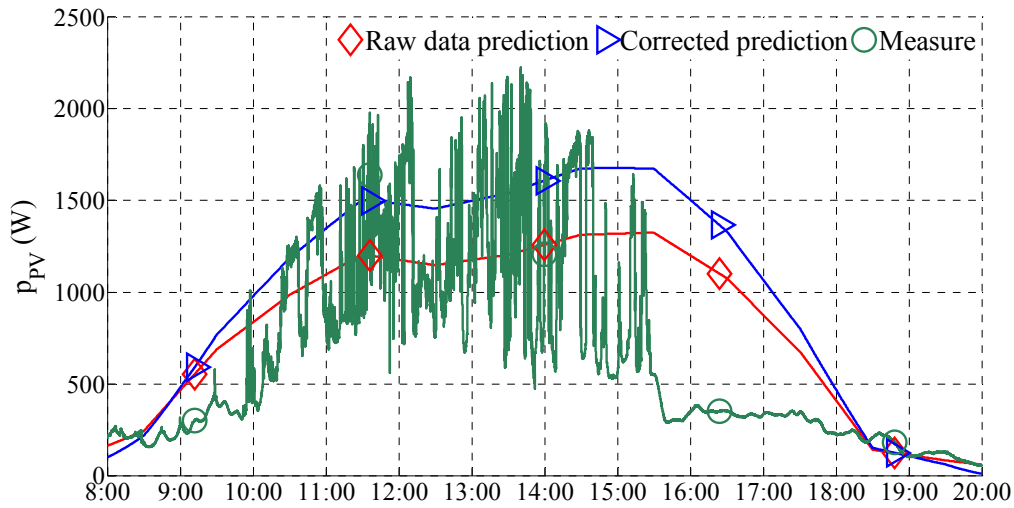


Figure 109. PVA power prediction and measure for off-grid test 2.

The optimized power flow by CPLEX is shown in Figure 110. As aforementioned when the storage reaches SOC_{MAX} the only way for keep power balancing is to limiting PVA power production, PVA power limiting must be performed. In this case, the PVA power limiting is distributed randomly during 10:45-17:20.

Based on optimum power flow evolution, optimum K_D sequence is calculated for the experimental operation, which is the on-off signal for the MT, as shown in Figure 111.

The control parameter K_D is used for the experimental operation whose operating conditions for PVA are shown in Figure 112.

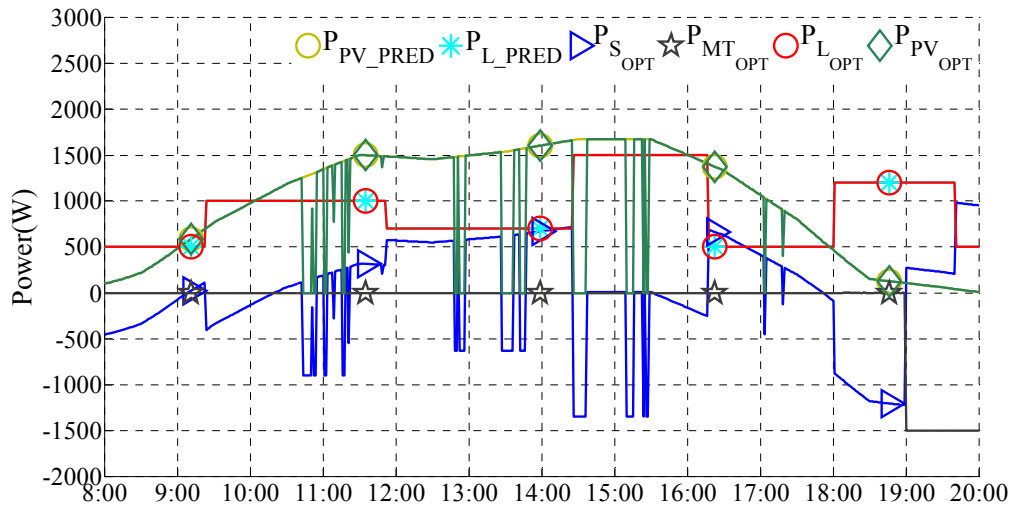


Figure 110. Power flow given by optimization for off-grid test 2.



Figure 111. K_D and SOC evolution given by optimization for off-grid test 2.

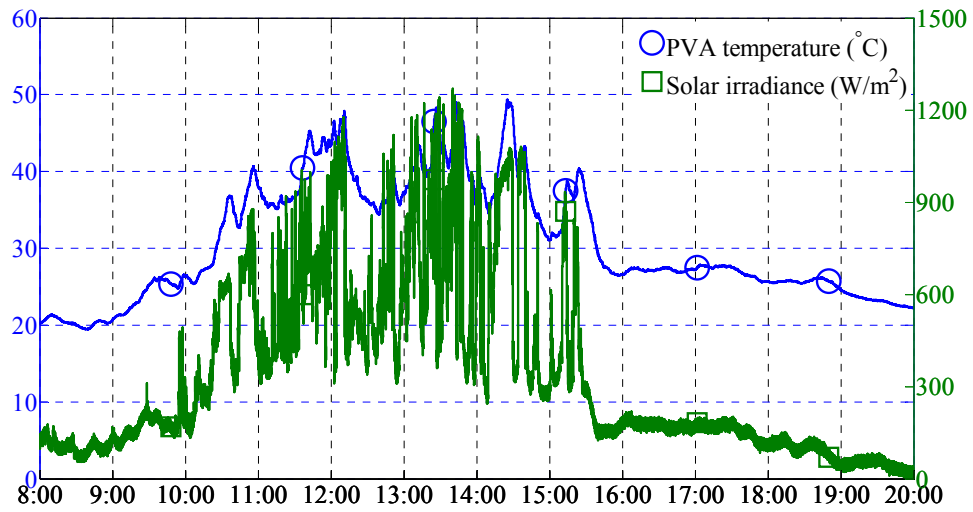


Figure 112. PVA cell temperature and solar irradiance on the 27th August 2013.

The operation is performed with K_D and operation layer off-grid control strategy. The obtained power flow is shown in Figure 113. Experimental SOC and DC bus voltage evolution are shown in Figure 114.

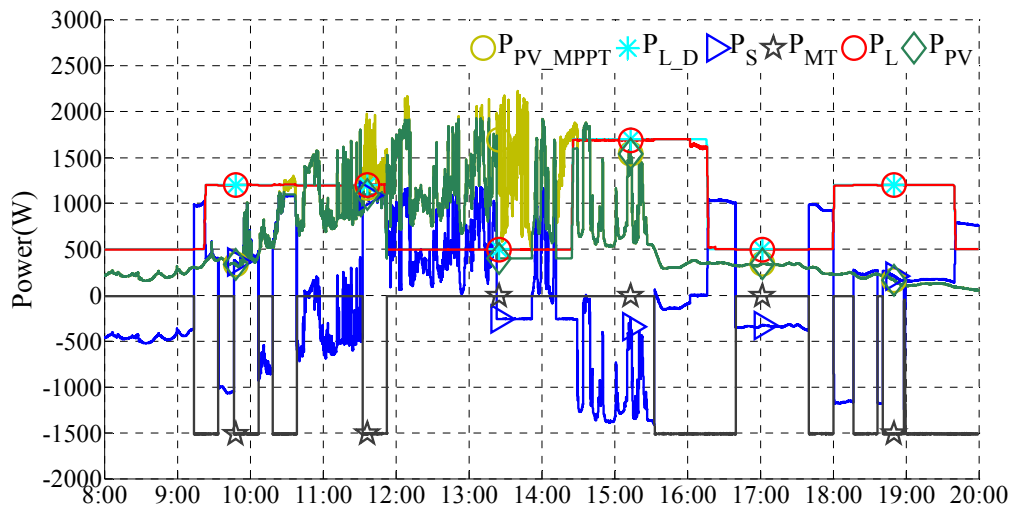


Figure 113. Experimental power flow for off-grid test 2.

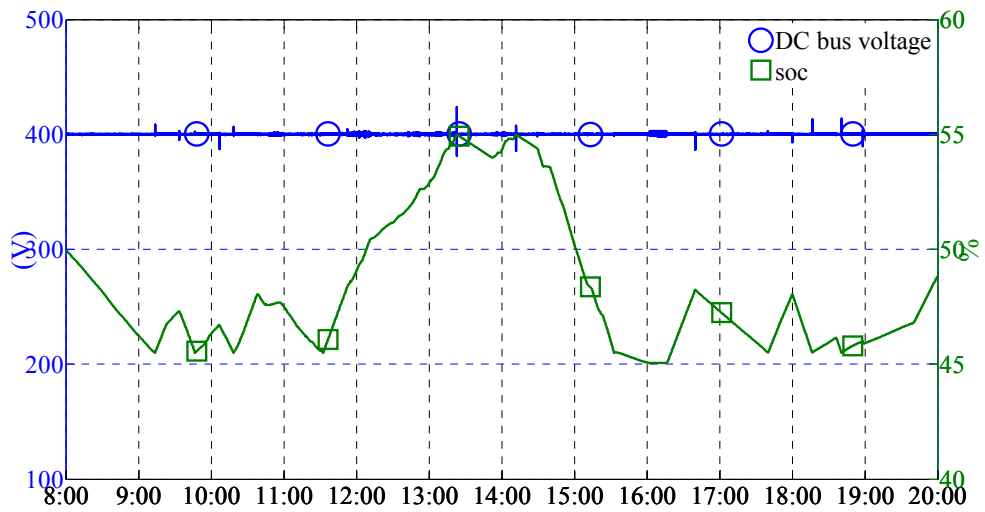


Figure 114. Experimental *SOC* evolution and DC bus voltage for off-grid test 2.

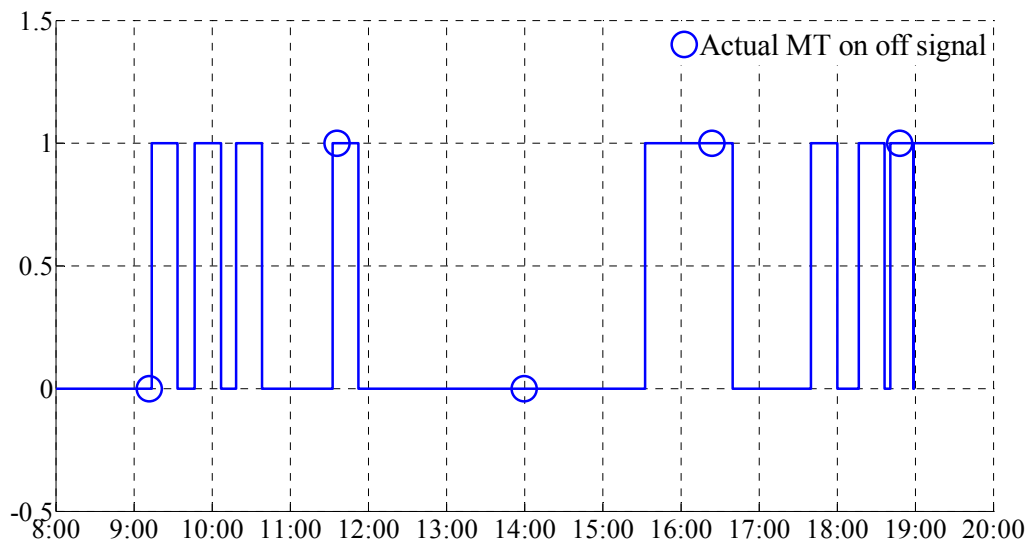


Figure 115. Actual MT on off signal for off-grid test 2.

During this day operation, storage is used for regulating the power balance. MT is started with interface value $K_D = 1$ for 19:00-20:00 or when the SOC approaches SOC_{MIN} , *i.e.* 9:10-9:30, 9:45-10:05, 10:15-10:35, 11:30-11:50, 15:40-16:40, 17:40-18:00, 18:15-18:35, 18:37-18:57.

Storage power is limited to avoid high power charging by high PVA power plus MT generation that can shorten the storage lifetime. So, in case of storage injection power exceeds storage power limit, the PVA production is limited to protect storage 11:30-11:50. When storage reaches SOC_{MAX} , PVA power limiting is performed 13:20-13:50.

To avoid oscillation, the PVA power limiting is recovered with hysteresis as aforementioned in test 1.

Load shedding is performed as another control degree of freedom in the case that when storage is empty and MT plus PVA power cannot supply the load demand 16:00-16:15. In this case, the prediction uncertainty is significant, so more MT generation is performed. Nevertheless, the power is able to be maintained. As indicated by steady DC bus voltage in Figure 114.

The actual MT on-off signal is shown in Figure 115. Due to prediction uncertainties, it can be seen that MT is started more than expected in order to keep continuous load supply.

Table 16 compares the energy cost between optimization and experiment.

Table 16. Comparison between optimization and experiment for off-grid test 2.

Case operation	Cost (€)	Load shedding (€)	PVA power limiting (€)	MT generation (€)
Optimization	3.259	0	1.575	1.684
Experimentation	7.807	0.211	0.835	6.761
Optimization for real conditions	7.596	0	1.030	6.566

Due to uncertainties, the experimental cost is much greater than optimization. However, the difference is obvious since more MT generation is involved to ensure power balance, when in real conditions the PVA production is much less than expected by prediction. An ideal experiment cost is calculated after the experiment. Given the prediction uncertainties and real operating conditions, the experiment cost is close to ideal experiment cost.

IV.2.1.3. Test 3

Test 3 is performed for operation on the 6th September 2013. The PVA power prediction uncertainty is shown in Figure 116. The prediction can correspond the two peak periods of production.

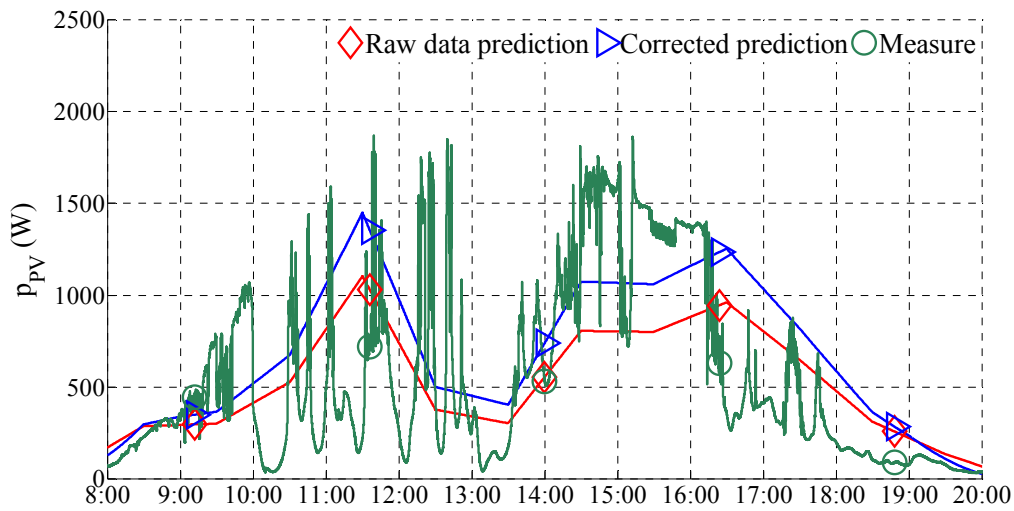


Figure 116. PVA power prediction and measure for off-grid test 3.

The optimized power flow by CPLEX is shown in Figure 117. As the irradiance is relatively low, no PVA power limiting is performed.

Based on optimum power flow evolution, optimum K_D sequence is given in Figure 118.

The control parameter K_D is used for the experimental operation whose PVA operating conditions are shown in Figure 119.

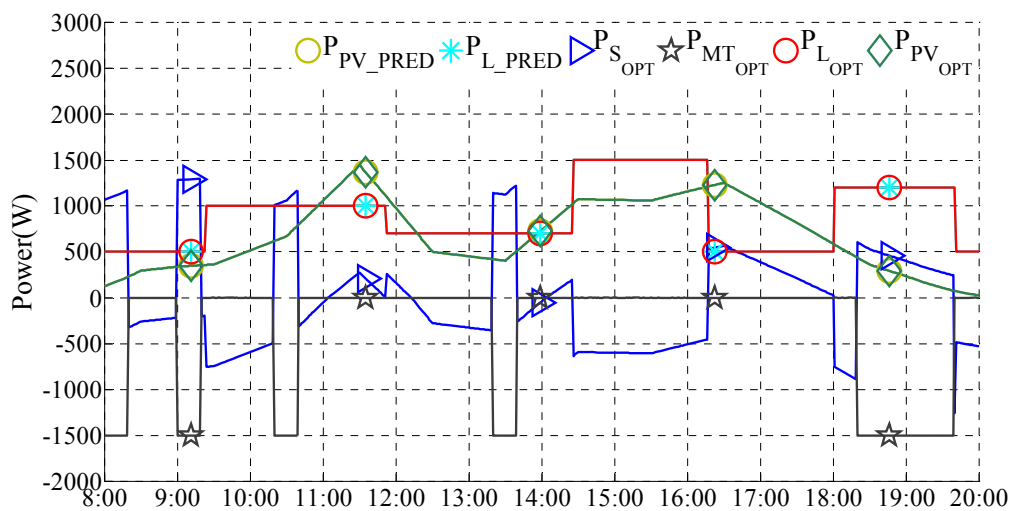


Figure 117. Power flow given by optimization for off-grid test 3.

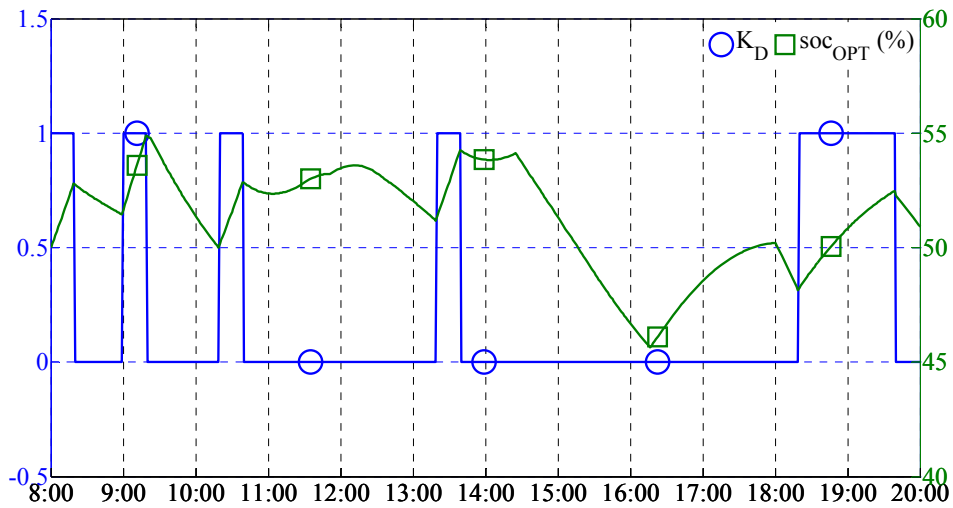


Figure 118. K_D and soc_{OPT} evolution given by optimization for off-grid test 3.

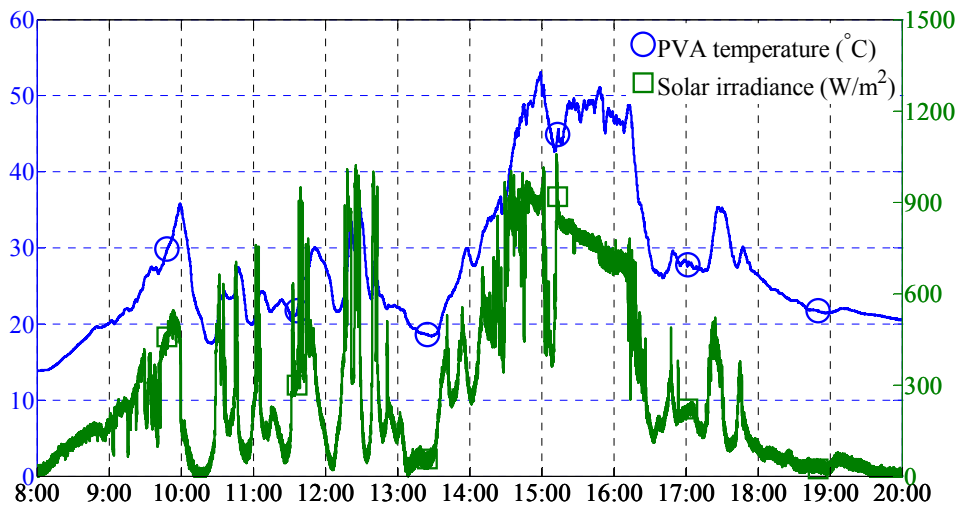


Figure 119. PVA cell temperature and solar irradiance on 6th September 2013.

The obtained experimental power flow is shown in Figure 120. Experimental soc and DC bus voltage evolution is shown in Figure 121.

As mentioned for test 2, storage power is limited to avoid high power charging by high PVA power plus MT generation that can shorten the storage lifetime. So in case of storage injection power exceeds storage power limit P_{S_MAX} , the PVA production is limited to protect storage (around 9:10, 10:30, 11:30, 12:30, 15:40 and 17:20). The uncertainties make the actual instantaneous power evolution different as predicated. Nevertheless, the power is able to be maintained and load can be supplied without load shedding. The power balancing is indicated by steady DC bus voltage in Figure 121.

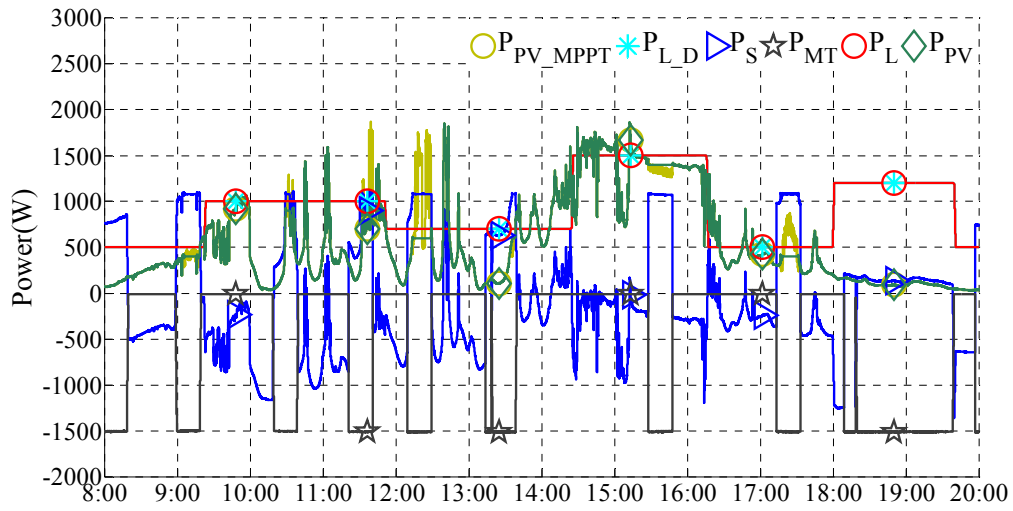


Figure 120. Experimental power flow for off-grid test 3.

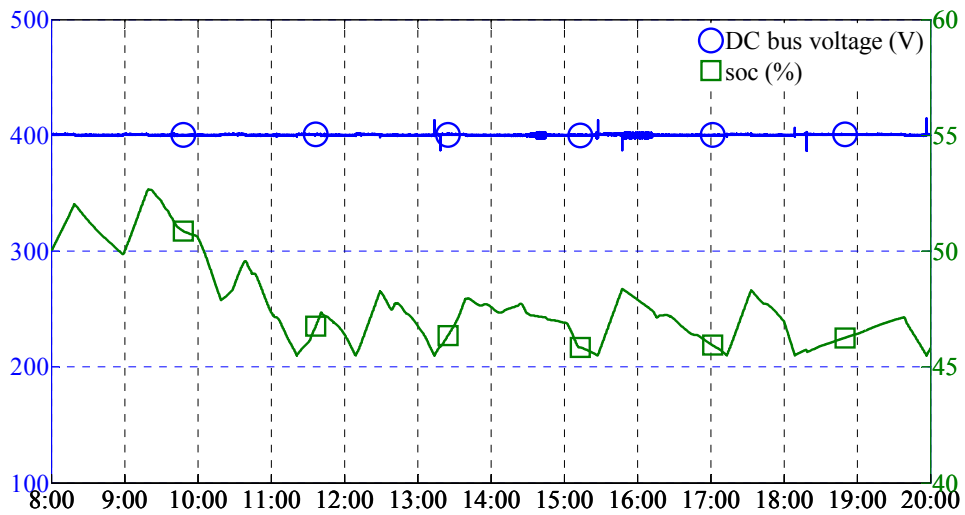


Figure 121. Experimental SOC evolution and DC bus voltage for off-grid test 3.

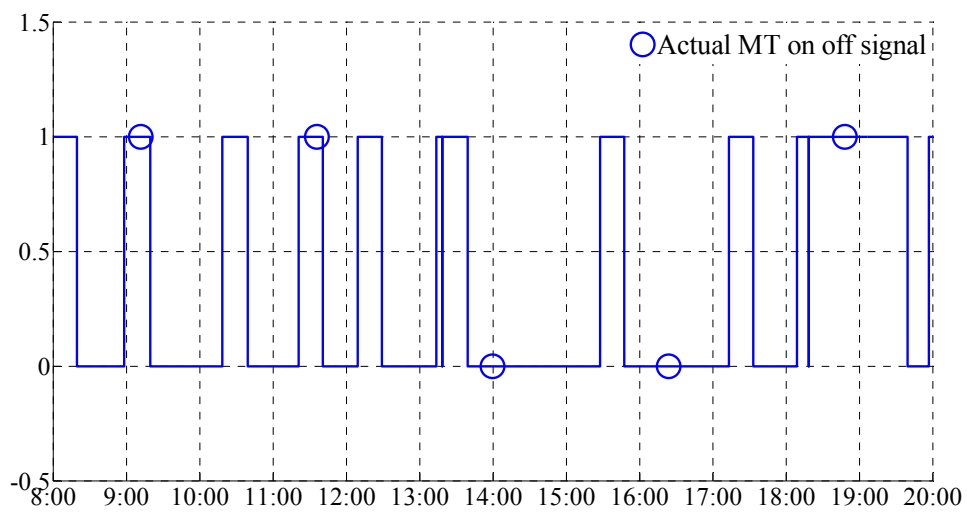


Figure 122. Actual MT on off signal for off-grid test 3.

The actual MT on-off signal is shown in Figure 122. Due to prediction uncertainties, it can be seen that MT is started more than expected in order to keep continuous load supply.

Table 17 compares the energy cost between optimization and experiment. Due to uncertainties, the experimental cost is larger than optimization by 53.2%. After the experiment, an ideal experiment cost is calculated. In real conditions, the experiment cost is close to ideal experiment cost.

Table 17. Comparison between optimization and experiment for off-grid test 3.

Case operation	Cost (€)	Load shedding (€)	PVA power limiting (€)	MT generation (€)
Optimization	4.366	0	0	4.366
Experimentation	6.689	0	0.175	6.514
Optimization for real conditions	6.017	0	0.001	6.016

IV.2.2. Conclusion

The experimental tests, for off-grid operating mode, provided in this section, validate the proposed supervision control which can work under different weather conditions for providing robust power balancing control strategy and interfacing with optimization. The optimization objective is to minimize MT fuel consumption and keep certain storage capacity at the end of the operation.

Optimization effectiveness depends on prediction precision. In the first test, except the MT duty cycles assigned by optimization, MT is started for one more duty cycle by operation layer control strategy, and the energy cost is closest to the optimization energy cost in the three tests. More MT duty cycle is started for the second test, but the final *SOC* is near to 50%. In third test, the final *SOC* is far from 50%. The power balancing can be maintained and rigid constraints such as storage power limit, storage capacity limit are fully respected.

Even with uncertainties, the experiment cost can be controlled close to ideal experiment cost, which validated the effectiveness of the proposed supervision control.

IV.3. Conclusion

In this chapter, an improved control for enhancing grid power quality in case of low power operation, which is inevitable with renewable energy production. Then, experimental tests are carried out to validate the proposed supervision control for both grid-connected and off-grid mode.

Therefore, given the obtained experimental results, the feasibility of implementing optimization in real operation, while respecting to rigid constraints, is validated. In addition, the proposed supervision control which parameterized power balancing strategy that provides interface for optimization is also technically verified. Even with uncertainties, the experiment cost can be controlled near ideal experiment cost, which validated the effectiveness of the proposed supervision control.

The supervision control handles various constraints at the same time, such as storage capability, grid power limitations, grid TOU pricing, grid peak hour, storage power limits, MT working duty cycle, etc. With the same constraints, a rule-based control strategy could be more complicated than optimization-based control.

Combined with robust power balance strategy, the optimization can optimize the power flow in order to make full use of produced energy and reduce reducing load shedding, PVA power limiting . It can also help reduce grid consumption, avoid undesired grid power injection in grid-connected mode, and minimize MT fuel consumption in off-grid mode.

As for grid-connected mode, from the point of view by the grid, no matter how the power evolves in the microgrid, the grid power can be maintained within its limits. For smart grid, it can simply regulate these limits to increase or decrease the supplied power and injected power, which facilitate DSM for grid operating.

The optimization effectiveness is mainly affected by the prediction precision. Other factors exist such as converter efficiency and security margin. As the general prediction data is provided for a large area about 20km², so for a single location, the prediction precision may not be satisfying, especially for cloudy weather conditions. Improvement can be done to add local forecasting techniques such as sky camera and local weather measurement and forecasting station. On the other hand, for these pilot tests, the storage is used for only 10% of its capacity that corresponds to the energy of 1.25kWh; however, this condition is imposed to show more control event during a day test. Certainly, a larger storage capacity could be more resistant to the prediction errors.

General conclusions and perspectives

Microgrid is believed to bring advantages in incorporating renewable energies, improving the overall energy efficiency and improving reliability by self-operating in isolated mode in case of grid fault. However, due to lack of grid interaction and local energy management together with power balancing control, a large scale deployment of microgrid may not make full of locally produced energy and improve overall grid performance. Even worse, the unmanaged fluctuating production by renewable sources may affect grid-wide functions such as frequency control and allocation of reserves.

In microgrid studies, power balancing control is mostly studied in single inverter or multi-inverter level and energy management/optimization is mostly carried out by simulation. However, power balancing control and energy management are separately studied and the difficulty of implementing optimization in real operation is seldom addressed, which may fail by violating rigid constraints due to uncertainties. This thesis attempted to cover the research gap by combining grid interaction and energy management with power balancing, which is tested by experiment.

This thesis proposes a multi-layer supervision control for a DC microgrid integrated in buildings, which represent a large sector of energy consumption. The proposed microgrid consists of a power system and a supervision system. The power system is composed of PVA, storage, grid connection, MT and controllable DC load. The supervision system is composed of four layers: operation layer, energy management layer, prediction layer and HMI. The four layers handle different functions of the

power balancing, energy management, data prediction, and interaction with the smart grid and the end-user.

The microgrid can work in both grid-connected mode and off-grid mode. As improving renewable energy penetration into grid is considered as an objective, the grid-connected mode, which requires the most consideration, is firstly considered and studied in detail through modeling. The off-grid mode can be considered as a simplified grid-connected case and is developed briefly based on grid-connected control.

The power balancing is firstly studied for grid-connected mode, in which various constraints should be considered. It is necessary to build a global energy model that adapted to the microgrid operation integrated with the smart grid communication, which concerns appropriate behavior with respect of constraints for each component. Interpreted PN modeling is used, which is easily translated into adequate MATLAB-Simulink Stateflow model for simulation. The modeling helps identify operating requirement and establish an overall power balancing control strategy. The control strategy is tested by both simulation and experiment. The control strategy provides an interface parameter K_D whose value can affect power flow. The control strategy can maintain power balancing with any K_D value, but the optimal sequence is expected to give best energy performance. The power flow can also be affected by power limits given by smart grid message to offer possibility for smart grid to manage grid usage. Algorithms for PVA power limiting and load shedding management are also developed to fulfill control strategy. For experimental tests, an improved control of grid-connected inverter is proposed for improving grid power quality in case of low power operation, which is inevitable with renewable energy production.

Energy management layer performs the optimization of the power flow based on prediction data. The optimization is formulated as a mixed integer linear programming problem with the objective to minimize the global energy cost, on the one hand, and to perform peak shaving, to avoid undesired injection in grid-connected mode, optimize MT fuel consumption in off-grid mode and to make full use of locally produced energy with respect to element constraints, on the other hand. The optimized power flow is then translated into the parameter K_D which is transmitted to the operation layer for real operation. With advantages provided by using K_D , optimized power flow can be taken into account in real operation while providing resistance to uncertainties.

Prediction layer gives the prediction data of PVA production and load consumption which are used for optimization. The PVA prediction raw data is provided by Meteo France. The raw data is processed with sun position and experimental PV model to provide more precision in PVA power. Compared with linear model and single-diode model, the experimental PV model provides higher precision. The limit for the experimental model is that the model works only for the same PV panel whose characteristics are extracted by experimental test, and for other types of panel, the experimental characteristics extraction must be re-performed. Concerning PVA power prediction to validate the

proposed supervision control, only solar irradiance is used, and the PVA cell temperature, which is hard to predict, is not involved for calculating PVA power prediction. Load consumption prediction is arbitrarily assigned.

HMI permits the end-users to adjust, define and customize the operation criteria and parameters through graphical interface which is not fully designed in this thesis.

Through experimental tests of the proposed supervision control for both grid-connected and off-grid mode, this study of microgrid concludes as given below.

It is experimentally validated that the feasibility of implementing optimization in real operation while respecting to rigid constraint by the proposed supervision control which parameterized power balancing strategy that provides interface for optimization. The supervision control handles various constraints at the same time, such as storage capability, grid power limitations, grid TOU pricing, grid peak hour, storage power limits, MT working duty cycle, etc. With the same constraints, a rule based control strategy could be very complicated.

Combined with robust power balance strategy, the optimization can optimize the power flow in order to make full use of produced energy and reduce load shedding, PVA power limiting. It can also help reduce grid peak consumption, avoid undesired grid power injection in grid-connected mode, and minimize MT fuel consumption in off-grid mode.

As for grid-connected mode, from the point of view by the grid, no matter how the power evolves in the microgrid, the grid power can be maintained within its limits. For smart grid, it can simply regulate these limits to increase or decrease the supplied power and injected power, which facilitate DSM for grid operating.

The originality of this thesis lies in the following aspects.

Firstly, the supervision control separates power balancing and energy management, yet links them through the interface parameter K_D . The power balancing control in operation layer is an independent function that can work with any K_D value. Energy management layer is able to optimize the microgrid operation through predictive data and thus obtain the optimized power flow. The optimized power flow is then translated into K_D sequence, which is a single value yet represents the power flow from different sources. The communication of K_D does not need high speed communication between layers. So, the supervision control provides the possibility of re-performing optimization and updating the K_D sequence during the operation without interrupting the power balancing.

Secondly, the proposed supervision control takes into consideration the prediction data and various constraints. Rigid constraints, such as grid power limits and storage capacity, can be fully respected for both optimization and real operation.

Thirdly, the supervision control is configured in a multi-layer structure, and each layer provides an independent function. The structure is flexible and can be implemented in several microcontrollers or computers so that real-time power balancing control and complicated optimization can be executed at

the same time without affecting each other. The multi-layer structure simplifies implementation of such complex control strategy.

Fourthly, the proposed microgrid is a DC microgrid with DC bus. DC microgrid is believed to be the trend of future development, which provides more advantages for energy efficiency. As microgrid research is initiated by AC microgrid, the DC microgrid has not been studied as much. This thesis contributes the DC microgrid study from an ensemble view combining power balancing, optimization and interaction with smart grid.

Last but not least, experimental validation of optimized microgrid control has not been reported in literature.

However, the limit of the supervision control is that optimizing effectiveness is affected on the prediction precision. Predictions uncertainties do not influence power balancing but the optimal energy cost is affected. Future research should focus on enhancing optimization performance, especially facing low prediction precision. The following solutions are suggested.

Firstly, it is noted that the prediction data is provided by weather forecast service for a large area. An improvement can be done with local weather forecast for a single location. The precision of forecast is expected to improve with the emerging of local weather forecasting techniques called "now casting", which aims at providing high precision forecast by directly "reading" from the sky by radar, sounder, or satellite images.

Secondly, optimization is performed once before the operation. Since the communication of K_D does not need high speed communication between layers, the optimization can be re-performed at any instant without interrupting the power balancing. Thus, hourly or more frequent optimization that update K_D sequence, with latest prediction and power system status, is expected to give better energy performance of the supervision control.

Besides, an optimization technique that able to optimize power flow with consideration on uncertainties of the prediction can be a perfect solution. A rule based algorithm in operation layer that corrects K_D in real time with respect of power system status can also be developed. A second storage can be installed as back-up for correcting the errors between optimized power and real operation.

Concerning other future works on DC microgrid than improving optimization, they can be linked with the HMI development and the implementing of communication between the supervision layers. Fully develop HMI with graphical interface, especially for the grid connected operation mode, more operating criteria or smart grid interaction mode can be designed, such as injecting or demanding constant power in grid during a specific period, authorizing battery injection into the grid. In addition, implementing the automatic communication between layers and realize a prototype of complete control in a unified device could lead to technological transfer. Smart grid interaction can be further developed and verified with several microgrids working together.

To sum up, the proposed DC microgrid supervision control structure combines grid interaction and energy management with power balancing. Although the microgrid only refers to a building scale and involves only a few sources, the idea of parameterize power balancing and interfacing with optimization, as well as smart grid interaction, can be generalized and thus can be used as solution for advanced energy management for other microgrids to optimize local power flow and improve future PV penetration.

References

- [1] T. Logenthiran, D. Srinivasan, and Shun Tan Zong, "Demand Side Management in Smart Grid Using Heuristic Optimization," *Smart Grid, IEEE Transactions on*, vol. 3, pp. 1244-1252, 2012.
- [2] A. Woyte, V. Van Thong, R. Belmans, and J. Nijs, "Voltage fluctuations on distribution level introduced by photovoltaic systems," *Energy Conversion, IEEE Transactions on*, vol. 21, pp. 202-209, 2006.
- [3] Hiroshi Yamaguchi, Junji Kondoh, Hirohisa Aki, Akinobu Murata, and Itaru Ishii, "Power fluctuation analysis of distribution network introduced a large number of photovoltaic generation system," in *Electricity Distribution, 2005. CIRED 2005. 18th International Conference and Exhibition on*, 2005, pp. 1-4.
- [4] Ioannis Hadjipaschalis, Andreas Poullikkas, and Venizelos Efthimiou, "Overview of current and future energy storage technologies for electric power applications," *Renewable and Sustainable Energy Reviews*, vol. 13, pp. 1513-1522, 2009.
- [5] S. V. Papaefthymiou, E. G. Karamanou, S. A. Papathanassiou, and M. P. Papadopoulos, "A Wind-Hydro-Pumped Storage Station Leading to High RES Penetration in the Autonomous Island System of Ikaria," *Sustainable Energy, IEEE Transactions on*, vol. 1, pp. 163-172, 2010.
- [6] B. V. Mathiesen and H. Lund, "Comparative analyses of seven technologies to facilitate the integration of fluctuating renewable energy sources," *Renewable Power Generation, IET*, vol. 3, pp. 190-204, 2009.
- [7] European Technology Smart Grid Platform. Smartgrids: Vision and strategy for European electricity networks of the future [Online]. Available: <http://www.smartgrids.eu/documents/vision.pdf>
- [8] U.S. Department of Energy. "Grid 2030" A National Vision for Electricity's second 100 years [Online]. Available: <http://energy.gov/oe/downloads/grid-2030-national-vision-electricity-s-second-100-years>
- [9] "IEEE Standard for Testing and Performance for All-Dielectric Self-Supporting (ADSS) Fiber Optic Cable for Use on Electric Utility Power Lines - Redline," *IEEE Std 1222-2011 (Revision of IEEE Std 1222-2004) - Redline*, pp. 1-55, 2011.
- [10] "IEEE Standard for Qualifying Hardware for Helically-Applied Fiber Optic Cable Systems (WRAP Cable)," *IEEE Std 1591.3-2011*, pp. 1-29, 2011.
- [11] "IEEE Standard for Testing and Performance of Hardware for Optical Ground Wire (OPGW)," *IEEE Std 1591.1-2012*, pp. 1-57, 2012.
- [12] M. Liserre, T. Sauter, and J. Y. Hung, "Future Energy Systems: Integrating Renewable Energy Sources into the Smart Power Grid Through Industrial Electronics," *Industrial Electronics Magazine, IEEE*, vol. 4, pp. 18-37, 2010.
- [13] Eefje Peeters, Regine Belhomme, Carlos Batlle, Francois Bouffard, Seppo Karkkainen, Daan Six, and Maarten Hommelberg, "ADDRESS: Scenarios and architecture for Active Demand development in the smart grids of the future," in *Electricity Distribution - Part 1, 2009. CIRED 2009. 20th International Conference and Exhibition on*, 2009, pp. 1-4.
- [14] R. H. Lasseter, J. H. Eto, B. Schenkman, J. Stevens, H. Vollkommer, D. Klapp, E. Linton, H. Hurtado, and J. Roy, "CERTS Microgrid Laboratory Test Bed," *Power Delivery, IEEE Transactions on*, vol. 26, pp. 325-332, 2011.
- [15] N. Hatziargyriou, H. Asano, R. Irvani, and C. Marnay, "Microgrids," *Power and Energy Magazine, IEEE*, vol. 5, pp. 78-94, 2007.
- [16] M. A. Hassan and M. A. Abido, "Optimal Design of Microgrids in Autonomous and Grid-Connected Modes Using Particle Swarm Optimization," *Power Electronics, IEEE Transactions on*, vol. 26, pp. 755-769, 2011.
- [17] H. S. V. S. Kumar Nunna and S. Doolla, "Multiagent-Based Distributed-Energy-Resource Management for Intelligent Microgrids," *Industrial Electronics, IEEE Transactions on*, vol. 60, pp. 1678-1687, 2013.

- [18] A. Chaouachi, R. M. Kamel, R. Andoulsi, and K. Nagasaka, "Multiobjective Intelligent Energy Management for a Microgrid," *Industrial Electronics, IEEE Transactions on*, vol. 60, pp. 1688-1699, 2013.
- [19] Wang Baochao, M. Sechilariu, and F. Locment, "Intelligent DC Microgrid With Smart Grid Communications: Control Strategy Consideration and Design," *Smart Grid, IEEE Transactions on*, vol. 3, pp. 2148-2156, 2012.
- [20] G. AlLee and W. Tschudi, "Edison Redux: 380 Vdc Brings Reliability and Efficiency to Sustainable Data Centers," *Power and Energy Magazine, IEEE*, vol. 10, pp. 50-59, 2012.
- [21] B. T. Patterson, "DC, Come Home: DC Microgrids and the Birth of the "Enernet"," *Power and Energy Magazine, IEEE*, vol. 10, pp. 60-69, 2012.
- [22] J. A. Jardini, J. L. P. Brittes, L. C. Magrini, M. A. Bini, and J. Yasuoka, "Power transformer temperature evaluation for overloading conditions," *Power Delivery, IEEE Transactions on*, vol. 20, pp. 179-184, 2005.
- [23] Zhang Qingchun, R. Callanan, M. K. Das, Ryu Sei-Hyung, A. K. Agarwal, and J. W. Palmour, "SiC Power Devices for Microgrids," *Power Electronics, IEEE Transactions on*, vol. 25, pp. 2889-2896, 2010.
- [24] C. G. C. Branco, R. P. Torrico-Bascope, C. M. T. Cruz, and F. K. de A. Lima, "Proposal of Three-Phase High-Frequency Transformer Isolation UPS Topologies for Distributed Generation Applications," *Industrial Electronics, IEEE Transactions on*, vol. 60, pp. 1520-1531, 2013.
- [25] Y. P. Hsieh, J. F. Chen, T. J. Liang, and L. S. Yang, "Novel High Step-Up DC-DC Converter for Distributed Generation System," *Industrial Electronics, IEEE Transactions on*, vol. 60, pp. 1473-1482, 2013.
- [26] T. J. Liang, J. H. Lee, S. M. Chen, J. F. Chen, and L. S. Yang, "Novel Isolated High-Step-Up DC-DC Converter With Voltage Lift," *Industrial Electronics, IEEE Transactions on*, vol. 60, pp. 1483-1491, 2013.
- [27] S. M. Chen, T. J. Liang, L. S. Yang, and J. C. Chen, "A Boost Converter With Capacitor Multiplier and Coupled Inductor for AC Module Applications," *Industrial Electronics, IEEE Transactions on*, vol. 60, pp. 1503-1511, 2013.
- [28] P. C. Loh, L. Zhang, and F. Gao, "Compact Integrated Energy Systems for Distributed Generation," *Industrial Electronics, IEEE Transactions on*, vol. 60, pp. 1492-1502, 2013.
- [29] Y. Li, S. Jiang, J. G. Cintron-Rivera, and F. Z. Peng, "Modeling and Control of Quasi-Z-Source Inverter for Distributed Generation Applications," *Industrial Electronics, IEEE Transactions on*, vol. 60, pp. 1532-1541, 2013.
- [30] M. Castilla, J. Miret, A. Camacho, J. Matas, and L. G. de Vicuna, "Reduction of Current Harmonic Distortion in Three-Phase Grid-Connected Photovoltaic Inverters via Resonant Current Control," *Industrial Electronics, IEEE Transactions on*, vol. 60, pp. 1464-1472, 2013.
- [31] A. Vidal, F. D. Freijedo, A. G. Yepes, P. Fernandez-Comesana, J. Malvar, O Lopez, and J. Doval-Gandoy, "Assessment and Optimization of the Transient Response of Proportional-Resonant Current Controllers for Distributed Power Generation Systems," *Industrial Electronics, IEEE Transactions on*, vol. 60, pp. 1367-1383, 2013.
- [32] R. J. Wai, C. Y. Lin, Y. C. Huang, and Y. R. Chang, "Design of High-Performance Stand-Alone and Grid-Connected Inverter for Distributed Generation Applications," *Industrial Electronics, IEEE Transactions on*, vol. 60, pp. 1542-1555, 2013.
- [33] Z. Yao and L. Xiao, "Control of Single-Phase Grid-Connected Inverters With Nonlinear Loads," *Industrial Electronics, IEEE Transactions on*, vol. 60, pp. 1384-1389, 2013.
- [34] M. Savaghebi, A. Jalilian, J. C. Vasquez, and J. M. Guerrero, "Autonomous Voltage Unbalance Compensation in an Islanded Droop-Controlled Microgrid," *Industrial Electronics, IEEE Transactions on*, vol. 60, pp. 1390-1402, 2013.
- [35] R. Majumder, "Reactive Power Compensation in Single-Phase Operation of Microgrid," *Industrial Electronics, IEEE Transactions on*, vol. 60, pp. 1403-1416, 2013.
- [36] P. Sharma and T. S. Bhatti, "Performance Investigation of Isolated Wind-Diesel Hybrid Power Systems With WECS Having PMIG," *Industrial Electronics, IEEE Transactions on*, vol. 60, pp. 1630-1637, 2013.

- [37] Q. C. Zhong and T. Hornik, "Cascaded Current-Voltage Control to Improve the Power Quality for a Grid-Connected Inverter With a Local Load," *Industrial Electronics, IEEE Transactions on*, vol. 60, pp. 1344-1355, 2013.
- [38] T. Hornik and Q. C. Zhong, "Parallel PI Voltage-H-infinity Current Controller for the Neutral Point of a Three-Phase Inverter," *Industrial Electronics, IEEE Transactions on*, vol. 60, pp. 1335-1343, 2013.
- [39] T. L. Lee, S. H. Hu, and Y. H. Chan, "D-STATCOM With Positive-Sequence Admittance and Negative-Sequence Conductance to Mitigate Voltage Fluctuations in High-Level Penetration of Distributed-Generation Systems," *Industrial Electronics, IEEE Transactions on*, vol. 60, pp. 1417-1428, 2013.
- [40] B. Bahrani, A. Karimi, B. Rey, and A. Rufer, "Decoupled dq-Current Control of Grid-Tied Voltage Source Converters Using Nonparametric Models," *Industrial Electronics, IEEE Transactions on*, vol. 60, pp. 1356-1366, 2013.
- [41] Lee Woo-Cheol, Lee Taeck-Ki, Lee Sang-Hoon, Kim Kyung-Hwan, Hyun Dong-Seok, and Suh In-Young, "A master and slave control strategy for parallel operation of three-phase UPS systems with different ratings," in *Applied Power Electronics Conference and Exposition, 2004. APEC '04. Nineteenth Annual IEEE, 2004*, pp. 456-462 Vol.1.
- [42] T. Vandoorn, B. Meersman, J. De Kooning, and L. Vandevelde, "Controllable Harmonic Current Sharing in Islanded Microgrids: DG Units With Programmable Resistive Behavior Toward Harmonics," *Power Delivery, IEEE Transactions on*, vol. 27, pp. 831-841, 2012.
- [43] Zhong Qing-Chang, "Harmonic Droop Controller to Reduce the Voltage Harmonics of Inverters," *Industrial Electronics, IEEE Transactions on*, vol. 60, pp. 936-945, 2013.
- [44] Q. C. Zhong, "Robust Droop Controller for Accurate Proportional Load Sharing Among Inverters Operated in Parallel," *Industrial Electronics, IEEE Transactions on*, vol. 60, pp. 1281-1290, 2013.
- [45] S. Xu, J. Wang, and J. Xu, "A Current Decoupling Parallel Control Strategy of Single-Phase Inverter With Voltage and Current Dual Closed-Loop Feedback," *Industrial Electronics, IEEE Transactions on*, vol. 60, pp. 1306-1313, 2013.
- [46] Y. F. Wang and Y. W. Li, "Three-Phase Cascaded Delayed Signal Cancellation PLL for Fast Selective Harmonic Detection," *Industrial Electronics, IEEE Transactions on*, vol. 60, pp. 1452-1463, 2013.
- [47] B. N. Alajmi, K. H. Ahmed, S. J. Finney, and B. W. Williams, "A Maximum Power Point Tracking Technique for Partially Shaded Photovoltaic Systems in Microgrids," *Industrial Electronics, IEEE Transactions on*, vol. 60, pp. 1596-1606, 2013.
- [48] R. Li and D. Xu, "Parallel Operation of Full Power Converters in Permanent-Magnet Direct-Drive Wind Power Generation System," *Industrial Electronics, IEEE Transactions on*, vol. 60, pp. 1619-1629, 2013.
- [49] T. L. Vandoorn, J. D. M. De Kooning, B. Meersman, J. M. Guerrero, and L. Vandevelde, "Voltage-Based Control of a Smart Transformer in a Microgrid," *Industrial Electronics, IEEE Transactions on*, vol. 60, pp. 1291-1305, 2013.
- [50] R. M. Kamel, A. Chaouachi, and K. Nagasaka, "Three Control Strategies to Improve the Microgrid Transient Dynamic Response During Isolated Mode: A Comparative Study," *Industrial Electronics, IEEE Transactions on*, vol. 60, pp. 1314-1322, 2013.
- [51] T. S. Ustun, C. Ozansoy, and A. Zayegh, "Fault Current Coefficient and Time Delay Assignment for Microgrid Protection System With Central Protection Unit," *Power Systems, IEEE Transactions on*, vol. PP, pp. 1-1, 2012.
- [52] W. K. A. Najy, H. H. Zeineldin, and W. L. Woon, "Optimal Protection Coordination for Microgrids With Grid-Connected and Islanded Capability," *Industrial Electronics, IEEE Transactions on*, vol. 60, pp. 1668-1677, 2013.
- [53] M. A. Zamani, T. S. Sidhu, and A. Yazdani, "A Protection Strategy and Microprocessor-Based Relay for Low-Voltage Microgrids," *Power Delivery, IEEE Transactions on*, vol. 26, pp. 1873-1883, 2011.
- [54] E. Sortomme, S. S. Venkata, and J. Mitra, "Microgrid Protection Using Communication-Assisted Digital Relays," *Power Delivery, IEEE Transactions on*, vol. 25, pp. 2789-2796, 2010.

- [55] M. A. Zamani, A. Yazdani, and T. S. Sidhu, "A Communication-Assisted Protection Strategy for Inverter-Based Medium-Voltage Microgrids," *Smart Grid, IEEE Transactions on*, vol. 3, pp. 2088-2099, 2012.
- [56] C. I. Chen, "Design of Measurement System Based on Signal Reconstruction for Analysis and Protection of Distributed Generations," *Industrial Electronics, IEEE Transactions on*, vol. 60, pp. 1652-1658, 2013.
- [57] R. Razzaghi, M. Davarpanah, and M. Sanaye-Pasand, "A Novel Protective Scheme to Protect Small-Scale Synchronous Generators Against Transient Instability," *Industrial Electronics, IEEE Transactions on*, vol. 60, pp. 1659-1667, 2013.
- [58] A. Camacho, M. Castilla, J. Miret, J. C. Vasquez, and E. Alarcon-Gallo, "Flexible Voltage Support Control for Three-Phase Distributed Generation Inverters Under Grid Fault," *Industrial Electronics, IEEE Transactions on*, vol. 60, pp. 1429-1441, 2013.
- [59] Chakraborty Sudipta, D. Weiss Manoja, and M. Godoy Simoes, "Distributed Intelligent Energy Management System for a Single-Phase High-Frequency AC Microgrid," *Industrial Electronics, IEEE Transactions on*, vol. 54, pp. 97-109, 2007.
- [60] Y. Riffonneau, S. Bacha, F. Barruel, and S. Ploix, "Optimal Power Flow Management for Grid Connected PV Systems With Batteries," *Sustainable Energy, IEEE Transactions on*, vol. 2, pp. 309-320, 2011.
- [61] Geng Bo, J. K. Mills, and Sun Dong, "Energy Management Control of Microturbine-Powered Plug-In Hybrid Electric Vehicles Using the Telemetry Equivalent Consumption Minimization Strategy," *Vehicular Technology, IEEE Transactions on*, vol. 60, pp. 4238-4248, 2011.
- [62] C. Bustos, D. Watts, and H. Ren, "MicroGrid Operation and Design Optimization With Synthetic Wind and Solar Resources," *Latin America Transactions, IEEE (Revista IEEE America Latina)*, vol. 10, pp. 1550-1562, 2012.
- [63] H. J. Avelar, W. A. Parreira, J. B. Vieira, L. C. G. de Freitas, and E. A. A. Coelho, "A State Equation Model of a Single-Phase Grid-Connected Inverter Using a Droop Control Scheme With Extra Phase Shift Control Action," *Industrial Electronics, IEEE Transactions on*, vol. 59, pp. 1527-1537, 2012.
- [64] D. Velasco de la Fuente, Rodri, x, C. L. T. guez, Garcera, G., E. Figueres, and R. O. Gonzalez, "Photovoltaic Power System With Battery Backup With Grid-Connection and Islanded Operation Capabilities," *Industrial Electronics, IEEE Transactions on*, vol. 60, pp. 1571-1581, 2013.
- [65] C. Trujillo Rodriguez, D. Velasco de la Fuente, G. Garcera, E. Figueres, and J. A. Guacaneme Moreno, "Reconfigurable Control Scheme for a PV Microinverter Working in Both Grid-Connected and Island Modes," *Industrial Electronics, IEEE Transactions on*, vol. 60, pp. 1582-1595, 2013.
- [66] D. Velasco de la Fuente, C. L. Trujillo Rodriguez, G. Garcer, E. Figueres, and R. Ortega Gonzalez, "Photovoltaic Power System With Battery Backup With Grid-Connection and Islanded Operation Capabilities," *Industrial Electronics, IEEE Transactions on*, vol. 60, pp. 1571-1581, 2013.
- [67] N. Bottrell, M. Prodanovic, and T. Green, "Dynamic Stability of a Microgrid with an Active Load," *Power Electronics, IEEE Transactions on*, vol. PP, pp. 1-1, 2013.
- [68] Manuela Sechilariu, Baochao Wang, and Fabrice Locment, "Building-integrated microgrid: Advanced local energy management for forthcoming smart power grid communication," *Energy and Buildings*, vol. 59, pp. 236-243, 2013.
- [69] D. Salomonsson, "Modeling, control and protection of low-voltage DC microgrids " *Doctoral Thesis, Royal Institute of Technology, Stockholm, Sweden, 2008.*
- [70] M. Ciobotaru, V. G. Agelidis, R. Teodorescu, and F. Blaabjerg, "Accurate and Less-Disturbing Active Antiislanding Method Based on PLL for Grid-Connected Converters," *Power Electronics, IEEE Transactions on*, vol. 25, pp. 1576-1584, 2010.
- [71] MINISTER OF ENERGY, "DEMAND-SIDE MANAGEMENT AND DEMAND RESPONSE IN THE ONTARIO ELECTRICITY SECTOR," 2004.
- [72] P. Palensky and D. Dietrich, "Demand Side Management: Demand Response, Intelligent Energy Systems, and Smart Loads," *Industrial Informatics, IEEE Transactions on*, vol. 7, pp. 381-388, 2011.

- [73] S Braithwait and Kelly Eakin, "The role of demand response in electric power market design," Edison Electric Institute, 2002.
- [74] M. H. Albadi and E. F. El-Saadany, "Demand Response in Electricity Markets: An Overview," in Power Engineering Society General Meeting, 2007. IEEE, 2007, pp. 1-5.
- [75] B. Venkatesh, Rost Alex, and Chang Liuchen, "Dynamic Voltage Collapse Index- Wind Generator Application," Power Delivery, IEEE Transactions on, vol. 22, pp. 90-94, 2007.
- [76] S. Eftekharijad, V. Vittal, G. T. Heydt, B. Keel, and J. Loehr, "Impact of Increased Penetration of Photovoltaic Generation on Power Systems," Power Systems, IEEE Transactions on, vol. PP, pp. 1-1, 2012.
- [77] Y. C. Chen and A. D. Dominguez-Garcia, "A Method to Study the Effect of Renewable Resource Variability on Power System Dynamics," Power Systems, IEEE Transactions on, vol. 27, pp. 1978-1989, 2012.
- [78] M. Yilmaz and P. Krein, "Review of the Impact of Vehicle-to-Grid Technologies on Distribution Systems and Utility Interfaces," Power Electronics, IEEE Transactions on, vol. PP, pp. 1-1, 2012.
- [79] Chompoo-inwai Chai, Lee Wei-Jen, P. Fuangfoo, M. Williams, and J. R. Liao, "System impact study for the interconnection of wind generation and utility system," Industry Applications, IEEE Transactions on, vol. 41, pp. 163-168, 2005.
- [80] B. C. Wang, M. Sechilariu, and F. Locment, "Power flow Petri Net modelling for building integrated multi-source power system with smart grid interaction," Mathematics and Computers in Simulation, vol. 91, pp. 119-133, 2013.
- [81] M. Sechilariu, Wang Baochao, and F. Locment, "Building Integrated Photovoltaic System With Energy Storage and Smart Grid Communication," Industrial Electronics, IEEE Transactions on, vol. 60, pp. 1607-1618, 2013.
- [82] David Harel, "Statecharts: A visual formalism for complex systems," Science of computer programming, vol. 8, pp. 231-274, 1987.
- [83] R. Zurawski and Zhou Mengchu, "Petri nets and industrial applications: A tutorial," Industrial Electronics, IEEE Transactions on, vol. 41, pp. 567-583, 1994.
- [84] T. Murata, "Petri nets: Properties, analysis and applications," Proceedings of the IEEE, vol. 77, pp. 541-580, 1989.
- [85] Xiong Rui, He Hongwen, Sun Fengchun, and Zhao Kai, "Evaluation on State of Charge Estimation of Batteries With Adaptive Extended Kalman Filter by Experiment Approach," Vehicular Technology, IEEE Transactions on, vol. 62, pp. 108-117, 2013.
- [86] He Hongwen, Xiong Rui, Zhang Xiaowei, Sun Fengchun, and Fan JinXin, "State-of-Charge Estimation of the Lithium-Ion Battery Using an Adaptive Extended Kalman Filter Based on an Improved Thevenin Model," Vehicular Technology, IEEE Transactions on, vol. 60, pp. 1461-1469, 2011.
- [87] Zhang Fei, Liu Guangjun, Fang Lijin, and Wang Hongguang, "Estimation of Battery State of Charge With H-infinity Observer: Applied to a Robot for Inspecting Power Transmission Lines," Industrial Electronics, IEEE Transactions on, vol. 59, pp. 1086-1095, 2012.
- [88] M. Charkhgard and M. Farrokhi, "State-of-Charge Estimation for Lithium-Ion Batteries Using Neural Networks and EKF," Industrial Electronics, IEEE Transactions on, vol. 57, pp. 4178-4187, 2010.
- [89] L. Liu, L. Y. Wang, Z. Chen, C. Wang, F. Lin, and H. Wang, "Integrated System Identification and State-of-Charge Estimation of Battery Systems," Energy Conversion, IEEE Transactions on, vol. 28, pp. 12-23, 2013.
- [90] V Salas, E Olias, A Barrado, and A Lazaro, "Review of the maximum power point tracking algorithms for stand-alone photovoltaic systems," Solar energy materials and solar cells, vol. 90, pp. 1555-1578, 2006.
- [91] Trishan Eram and Patrick L Chapman, "Comparison of photovoltaic array maximum power point tracking techniques," Energy Conversion, IEEE Transactions on, vol. 22, pp. 439-449, 2007.
- [92] Jonathan W Kimball and Philip T Krein, "Discrete-time ripple correlation control for maximum power point tracking," Power Electronics, IEEE Transactions on, vol. 23, pp. 2353-2362, 2008.

- [93] Nicola Femia, Giovanni Petrone, Giovanni Spagnuolo, and Massimo Vitelli, "Optimization of perturb and observe maximum power point tracking method," *Power Electronics, IEEE Transactions on*, vol. 20, pp. 963-973, 2005.
- [94] Issam Houssamo, Fabrice Locment, and Manuela Sechilariu, "Maximum power tracking for photovoltaic power system: Development and experimental comparison of two algorithms," *Renewable Energy*, vol. 35, pp. 2381-2387, 2010.
- [95] Baochao Wang, Issam Houssamo, Manuela Sechilariu, and Fabrice Locment, "A simple PV constrained production control strategy," in *Industrial Electronics (ISIE), 2012 IEEE International Symposium on*, 2012, pp. 969-974.
- [96] A. Sannino, G. Postiglione, and M. H. J. Bollen, "Feasibility of a DC network for commercial facilities," *Industry Applications, IEEE Transactions on*, vol. 39, pp. 1499-1507, 2003.
- [97] I. Houssamo, B. Wang, M. Sechilariu, F. Locment, and G. Friedrich, "A simple experimental prediction model of photovoltaic power for DC microgrid," in *Industrial Electronics (ISIE), 2012 IEEE International Symposium on*, 2012, pp. 963-968.
- [98] S. Poshtkouhi, V. Palaniappan, M. Fard, and O. Trescases, "A General Approach for Quantifying the Benefit of Distributed Power Electronics for Fine Grained MPPT in Photovoltaic Applications Using 3-D Modeling," *Power Electronics, IEEE Transactions on*, vol. 27, pp. 4656-4666, 2012.
- [99] N. Amjady, F. Keynia, and H. Zareipour, "Short-Term Load Forecast of Microgrids by a New Bilevel Prediction Strategy," *Smart Grid, IEEE Transactions on*, vol. 1, pp. 286-294, 2010.
- [100] E. Lorenz, J. Hurka, D. Heinemann, and H. G. Beyer, "Irradiance Forecasting for the Power Prediction of Grid-Connected Photovoltaic Systems," *Selected Topics in Applied Earth Observations and Remote Sensing, IEEE Journal of*, vol. 2, pp. 2-10, 2009.
- [101] M. Fuentes, G. Nofuentes, J. Aguilera, D. L. Talavera, and M. Castro, "Application and validation of algebraic methods to predict the behaviour of crystalline silicon PV modules in Mediterranean climates," *Solar Energy*, vol. 81, pp. 1396-1408, 2007.
- [102] I Houssamo, M Sechilariu, F Locment, and G Friedrich, "Identification of Photovoltaic Array Model Parameters. Modelling and Experimental Verification," in *Proc. of 10th International Conference on Renewable Energies and Power Quality ICREPQ'10*, 2010, pp. 23-25.
- [103] Issam Houssamo, "Contribution à l'étude théorique, à la modélisation et à la mise en oeuvre d'un système multisource appartenant à un micro-réseau électrique," *Doctoral Thesis, Université de Technologie de Compiègne, Compiègne, France*, 2012.
- [104] Rafal Weron, *Modeling and forecasting electricity loads and prices: A statistical approach* vol. 403: Wiley. com, 2007.
- [105] A Mohsenian-Rad, Vincent WS Wong, Juri Jatskevich, Robert Schober, and Alberto Leon-Garcia, "Autonomous demand-side management based on game-theoretic energy consumption scheduling for the future smart grid," *Smart Grid, IEEE Transactions on*, vol. 1, pp. 320-331, 2010.
- [106] Hassan Farhangi, "The path of the smart grid," *Power and Energy Magazine, IEEE*, vol. 8, pp. 18-28, 2010.
- [107] Sudipta Chakraborty, Manoja D Weiss, and M Godoy Simões, "Distributed intelligent energy management system for a single-phase high-frequency AC microgrid," *Industrial Electronics, IEEE Transactions on*, vol. 54, pp. 97-109, 2007.
- [108] Bo Geng, James K Mills, and Dong Sun, "Energy management control of microturbine-powered plug-in hybrid electric vehicles using the telemetry equivalent consumption minimization strategy," *Vehicular Technology, IEEE Transactions on*, vol. 60, pp. 4238-4248, 2011.
- [109] George B Dantzig, *Linear programming and extensions: Princeton university press*, 1998.
- [110] George B Dantzig, "Maximization of a linear function of variables subject to linear inequalities," *New York*, 1951.
- [111] George L Nemhauser and Laurence A Wolsey, *Integer and combinatorial optimization* vol. 18: Wiley New York, 1988.
- [112] IBM.com. IBM ILOG CPLEX Optimizer. Available: <http://www.ibm.com>.

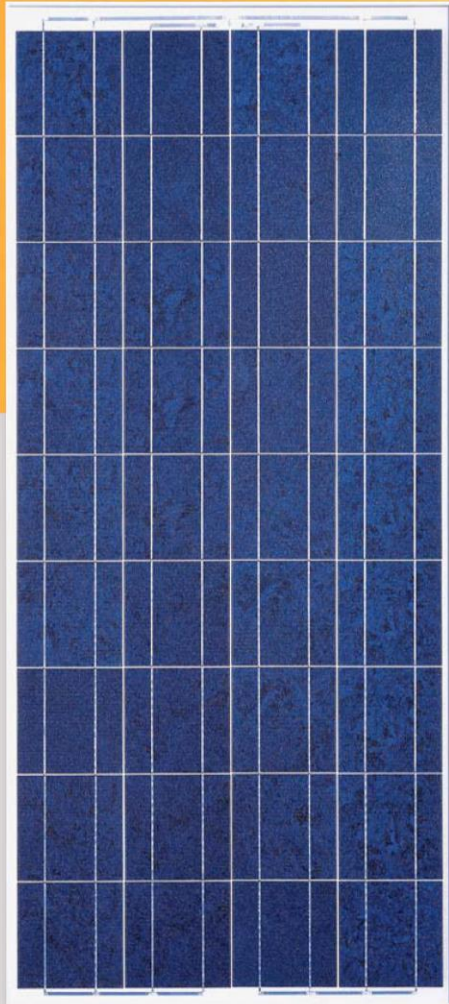
- [113] Baochao Wang, Manuela Sechilariu, and Fabrice Locment, "Simple Improved Control of Phase Error Compensation for Low Power Operation of PV Grid-Connected Inverter with LCL Filter," *European Journal of Electrical Engineering*, 2013.
- [114] Shen Guoqiao, Zhu Xuancai, Zhang Jun, and Xu Dehong, "A New Feedback Method for PR Current Control of LCL-Filter-Based Grid-Connected Inverter," *Industrial Electronics, IEEE Transactions on*, vol. 57, pp. 2033-2041, 2010.
- [115] J. Dannehl, M. Liserre, and F. W. Fuchs, "Filter-Based Active Damping of Voltage Source Converters With LCL Filter," *Industrial Electronics, IEEE Transactions on*, vol. 58, pp. 3623-3633, 2011.
- [116] J. Dannehl, C. Wessels, and F. W. Fuchs, "Limitations of Voltage-Oriented PI Current Control of Grid-Connected PWM Rectifiers With LCL Filters," *Industrial Electronics, IEEE Transactions on*, vol. 56, pp. 380-388, 2009.
- [117] J. L. Agorreta, M. Borrega, Lo, x, J. pez, and L. Marroyo, "Modeling and Control of N-Paralleled Grid-Connected Inverters With LCL Filter Coupled Due to Grid Impedance in PV Plants," *Power Electronics, IEEE Transactions on*, vol. 26, pp. 770-785, 2011.
- [118] J. Dannehl, F. W. Fuchs, and P. B. Thogersen, "PI State Space Current Control of Grid-Connected PWM Converters With LCL Filters," *Power Electronics, IEEE Transactions on*, vol. 25, pp. 2320-2330, 2010.
- [119] J. Dannehl, F. W. Fuchs, S. Hansen, and P. B. Thogersen, "Investigation of Active Damping Approaches for PI-Based Current Control of Grid-Connected Pulse Width Modulation Converters With LCL Filters," *Industry Applications, IEEE Transactions on*, vol. 46, pp. 1509-1517, 2010.
- [120] E. Figueres, G. Garcera, J. Sandia, F. Gonzalez-Espin, and J. C. Rubio, "Sensitivity Study of the Dynamics of Three-Phase Photovoltaic Inverters With an LCL Grid Filter," *Industrial Electronics, IEEE Transactions on*, vol. 56, pp. 706-717, 2009.
- [121] I. J. Gabe, V. F. Montagner, and H. Pinheiro, "Design and Implementation of a Robust Current Controller for VSI Connected to the Grid Through an LCL Filter," *Power Electronics, IEEE Transactions on*, vol. 24, pp. 1444-1452, 2009.
- [122] Jeong Hea-Gwang, Lee Kyo-Beum, Choi Sewan, and Choi Woojin, "Performance Improvement of LCL-Filter-Based Grid-Connected Inverters Using PQR Power Transformation," *Power Electronics, IEEE Transactions on*, vol. 25, pp. 1320-1330, 2010.
- [123] K. Jalili and S. Bernet, "Design of LCL Filters of Active-Front-End Two-Level Voltage-Source Converters," *Industrial Electronics, IEEE Transactions on*, vol. 56, pp. 1674-1689, 2009.
- [124] Liu Fei, Zhou Yan, Duan Shanxu, Yin Jinjun, Liu Bangyin, and Liu Fangrui, "Parameter Design of a Two-Current-Loop Controller Used in a Grid-Connected Inverter System With LCL Filter," *Industrial Electronics, IEEE Transactions on*, vol. 56, pp. 4483-4491, 2009.
- [125] S. Mariethoz and M. Morari, "Explicit Model-Predictive Control of a PWM Inverter With an LCL Filter," *Industrial Electronics, IEEE Transactions on*, vol. 56, pp. 389-399, 2009.
- [126] Y. A. R. I. Mohamed, "Mitigation of Dynamic, Unbalanced, and Harmonic Voltage Disturbances Using Grid-Connected Inverters With LCL Filter," *Industrial Electronics, IEEE Transactions on*, vol. 58, pp. 3914-3924, 2011.
- [127] Wang Xuehua, Ruan Xinbo, Liu Shangwei, and C. K. Tse, "Full Feedforward of Grid Voltage for Grid-Connected Inverter With LCL Filter to Suppress Current Distortion Due to Grid Voltage Harmonics," *Power Electronics, IEEE Transactions on*, vol. 25, pp. 3119-3127, 2010.
- [128] T. Abeyasekera, C. M. Johnson, D. J. Atkinson, and M. Armstrong, "Suppression of line voltage related distortion in current controlled grid connected inverters," *Power Electronics, IEEE Transactions on*, vol. 20, pp. 1393-1401, 2005.
- [129] L. Harnefors, L. Zhang, and M. Bongiorno, "Frequency-domain passivity-based current controller design," *Power Electronics, IET*, vol. 1, pp. 455-465, 2008.
- [130] Park Sung Yeul, Chen Chien Liang, Lai Jih Sheng, and Moon Seung Ryul, "Admittance Compensation in Current Loop Control for a Grid-Tie LCL Fuel Cell Inverter," *Power Electronics, IEEE Transactions on*, vol. 23, pp. 1716-1723, 2008.

- [131] R. M. Santos Filho, P. F. Seixas, P. C. Cortizo, L. A. B. Torres, and A. F. Souza, "Comparison of Three Single-Phase PLL Algorithms for UPS Applications," *Industrial Electronics, IEEE Transactions on*, vol. 55, pp. 2923-2932, 2008.

Annex 1: PV panel technical notice

Solar Module

Solar-Fabrik Series SF 130/2



Top quality across the entire range:

- Long term stability by use of highly transparent, specially doped solar glass with UV blocker.
- 100% preselection of cells
- Highest energy output achieved by careful processing and exact tuning of components (cp. „Power Check“ Report, Fraunhofer ISE)
- State of the art manufacturing technology and certified quality management (ISO 9001) guarantee best quality of products „made in Germany“.
- Optionally available with specially developed aluminium frame; rapid and versatile fitting with patented Profilink mounting system; recessed retaining elements for attractive appearance
- Increased load capacity: 5400 Pa according to IEC 61215 for framed modules
- Very narrow selection limits of only +/- 2.5 W (Δ 1.9%) remove the need to preselect panels.
- Calibration modules for output measurement regularly tested at Fraunhofer Institute for Solar Energy Systems

Dimensions

Series SF 130/2	frameless	Alu frame
L x W (mm)	1485 x 663	1491 x 669
Thickness (mm)	5	35
Weight (kg)	10,5	12,5

Qualifications/Certificate

EN IEC 61215 ed. 2
 Class II protection
 Guideline 89/336/EWG (CE)
 Guideline 73/23/EWG (CE)



Module data Solar-Fabrik Series SF 130/2

Type of module	SF 130/2-125	SF 130/2-130	SF 130/2-135
Solar cells per module (polycrystalline)	36	36	36
Max. system voltage	1000 V	1000 V	1000 V

Electrical data under STC (Standard Test Conditions: 1000 W/m², 25°C, AM 1.5)

Nominal Power*	P _{max}	125 W	130 W	135 W
Sorting limits		+/- 2.5 W	+/- 2.5 W	+/- 2.5 W
Voltage approx.	V _{MFP}	17.50 V	1.72 V	17.94 V
Open circuit voltage approx.	V _{OC}	21.53 V	21.69 V	21.86 V
Current approx.	I _{MFP}	7.14 A	7.34 A	7.52 A
Short circuit current approx.	I _{SC}	7.84 A	7.96 A	8.08 A

Electrical data at 800 W/m², NOCT, AM 1.5

Performance at MPP approx.	P _{max}	89 W	100 W	104 W
Voltage approx.	V _{MFP}	16.03 V	16.24 V	16.45 V
Open circuit voltage approx.	V _{OC}	19.69 V	19,85 V	20.00 V
Current approx.	I _{MFP}	5.54 A	5.69 A	5.84 A
Short circuit current approx.	I _{SC}	5.99 A	6.09 A	6.18 A

At an incident solar irradiance level of 200 W/m² and 25°C, efficiency is decreased by approx. 7% compared with the efficiency measured at STC.

Temperature data

Temperature coefficient voltage	T _K (U _{OC})	-72 mV/K
Temperature coefficient current	T _K (I _{SC})	5.45 mA/K
NOCT		48°C +/- 2K

Further information

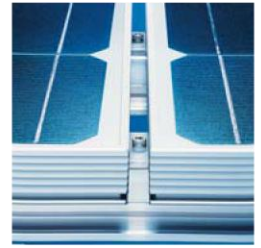
Connection technology	Lumberg system: 1.2 m connecting cable 4 mm ² with overmolded plug and chassis socket (for frameless modules 2 m cable length)
High voltage test	test voltage 3200 V _{DC} /max. 60µA
Hail resistance**	up to 25 mm diameter at 23 m/s
Storm resistance**	Wind speed up to 130 km/h = 800 Pa and safety factor 3
Show load**	without frame: 2400 Pa Δ 245 kg/m ²
Load capacity according to IEC 61215	with frame: 5400 Pa Δ 550 kg/m ²

* (+/- 5% tolerance of measurement)

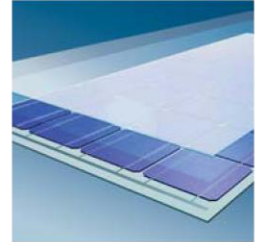
** in combination with our patented Profilink mounting system and the indicated attachment points (AP)

Warranty on electrical performance, 25 years according to our additional terms of warranty, which we will be glad to send you.

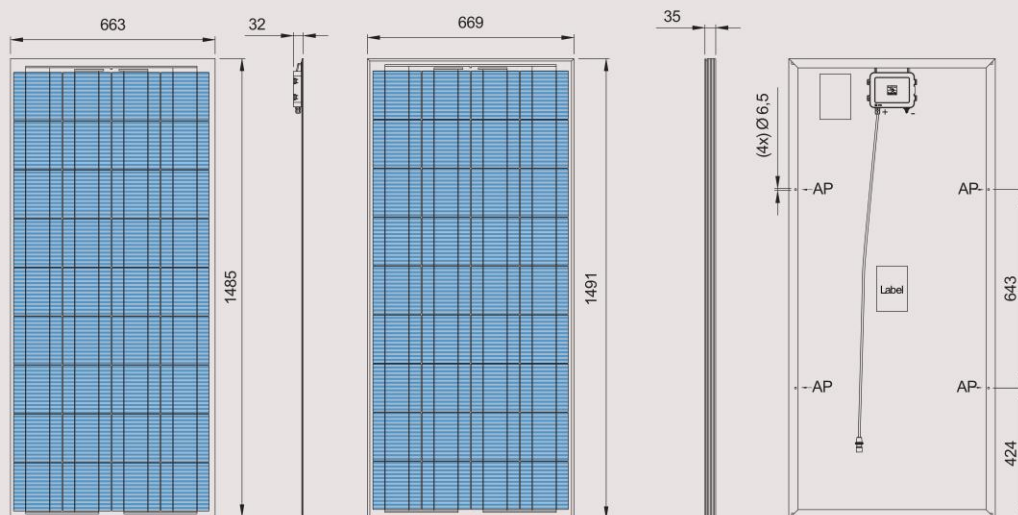
Certified by VDE according to DIN EN ISO 9001; Reg.Nr. 5002983/QM/11.2003 / DIN EN ISO 14001; Reg.Nr. 5002983/UM/11.2003



Efficient mounting system Profilink



Module assembly:
Panel construction:
Specially hardened low-iron glass, light-permeable ethyl-vinyl acetate (EVA) film, solar cells, EVA, Tedlar backing film.



SF 130/2 without frame

SF 130/2A framed



Solar-Fabrik AG
Munzinger Straße 10
79111 Freiburg / Germany
Tel. +49-(0)761-4000-0
Fax +49-(0)761-4000-199
www.solar-fabrik.de

Annex 2: Storage unit technical notice

The compact alternative for smaller solar applications.

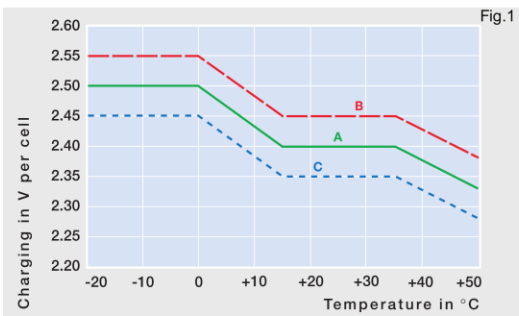
Sonnenschein Solar batteries are specially designed for small to medium performance requirements in leisure and consumer applications. The advantages of the maintenance free VRLA-batteries are enhanced by the worldwide high reputation and technical image of the dryfit technology. Typical applications are weekend and holiday houses without mains supply, street solar stations, information signs, parking meters, wireless emergency phone boxes and also other safety equipment power supplies.

	
Valve regulated	Grid plate
	
Nominal capacity 6.6-230 Ah	Block battery
	
800 cycles * acc. to IEC 896-2	Maintenance-free (no topping up)
	
Proof against deep discharge acc. to DIN 43 539 T5	Recyclable



Technical characteristics and data

Type	Part number	Nominal voltage V	Nominal capacity C_{100} 1.8 V/C Ah	Discharge current I_{100} A	Length (l) max. mm	Width (b/w) max. mm	Height up to top of cover (h1) max. mm	Height incl. connectors (h2) max. mm	Weight approx. kg	Terminal	Terminal position
S12/6.6 S	NGSO1206D6HS0SA	12	6.6	0.066	151.7	65.5	94.5	98.4	2.6	S-4.8	3
S12/17 G5	NGSO120017HS0BA	12	17.0	0.170	181.0	76.0	–	167.0	6.1	G-M5	1
S12/27 G5	NGSO120027HS0BA	12	27.0	0.270	167.0	176.0	–	126.0	9.7	G-M5	1
S12/32 G6	NGSO120032HS0BA	12	32.0	0.320	197.0	132.0	160.0	184.0	11.2	G-M6	2
S12/41 A	NGSO120041HS0CA	12	41.0	0.410	210.0	175.0	–	175.0	14.8	A-Terminal	1
S12/60 A	NGSO120060HS0CA	12	60.0	0.600	261.0	136.0	208.0	230.0	19.0	A-Terminal	1
S12/85 A*	NGSO120085HS0CA	12	85.0	0.850	353.0	175.0	–	190.0	27.3	A-Terminal	1
S12/90 A	NGSO120090HS0CA	12	90.0	0.900	330.0	171.0	213.0	236.0	31.3	A-Terminal	2
S12/130 A	NGSO120130HS0CA	12	130.0	1.300	286.0	269.0	208.0	230.0	39.8	A-Terminal	4
S12/230 A	NGSO120230HS0CA	12	230.0	2.300	518.0	274.0	216.0	238.0	70.0	A-Terminal	3

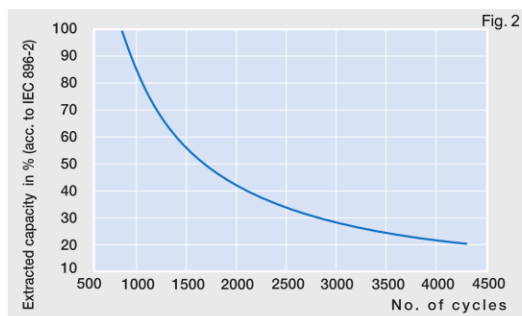
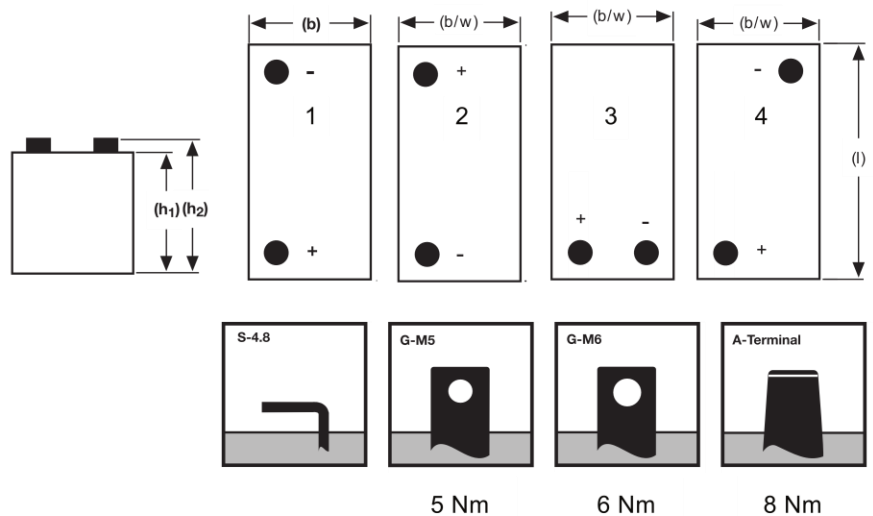


Charge mode (to Fig.1):

- 1.) with switch regulator (two-step controller)
 - charge on curve B (max. charge voltage) for max.2 hrs/day then switch over to continuous charge - curve C
- 2.) Standard charge (without switching) - curve A
- 3.) Boost charge (Equalizing charge with external generator)
 - charge on curve B for max. 5 hrs/month, then switch over to curve C

Type	Capacities $C_1 - C_{100}$ (20°C)				
	C_1 1.70 V/C	C_5 1.70 V/C	C_{10} 1.70 V/C	C_{20} 1.75 V/C	C_{100} 1.80 V/C
S12/6.6 S	2.9	4.6	5.1	5.7	6.6
S12/17 G5	9.3	12.6	14.3	15.0	17.0
S12/27 G5	15.0	22.1	23.5	24.0	27.0
S12/32 G6	16.9	24.4	27.0	28.0	32.0
S12/41 A	21.0	30.6	34.0	38.0	41.0
S12/60 A	30.0	42.5	47.5	50.0	60.0
S12/85 A	55.0	68.5	74.0	76.0	85.0
S12/90 A	50.5	72.0	78.0	84.0	90.0
S12/130 A	66.0	93.5	104.5	110.0	130.0
S12/230 A	120.0	170.0	190.0	200.0	230.0

Drawings with terminal position, terminal and torque



(to Fig. 2)

Endurance in cycles according to IEC 896-2

* S12/85 A = 400 cycles

Not to scale!

Annex 3: C++ program that formulates the optimization problem in CPLEX form and interfaces with CPLEX

```

#if !defined(_SMART_GRID_LP_solver_H)
#define _SMART_GRID_LP_solver_H

#define ILOUSESTL

#include <set>
#include <vector>
#include <string>
#include <iostream>
#include <fstream>
#include <algorithm>
#include <ilcplex/ilocplex.h>
#include <list>

using namespace std;

class SMART_GRID_exception : public std::exception{
    std::string info;
public:
    SMART_GRID_exception(const std::string& f):info(f) {}
    const char* what() const;
};

struct PERIODE {
public:
    IloInt lb;
    IloInt ub;
    IloNum C_GI;
    IloNum C_GS;
    IloNum C_SI;
    IloNum C_SS;
};

std::istream& operator>>(std::istream& f, PERIODE& p);
std::ostream& operator<<(std::ostream& f, const PERIODE& p);

class SMART_GRID_LP_solver {
protected:
    std::string instance_name;
    std::string parameters_name;
    IloEnv env;
    IloModel model;
    IloCplex cplex;
    unsigned int time_limit;
    unsigned int max_number_of_nodes;
    bool problem_computed; // true if the solver has been launched at least one time
    bool problem_proved; // true if the problem has been proved decision or optimisation

    unsigned int nb_time_pts;

    std::list<PERIODE> periodes;

    IloNum SOC_init;
    IloNum SOC_coeff;
    IloNum SOC_min;
    IloNum SOC_max;
    IloNum SOC_end_lb;
    IloNum P_DG_lim;
    IloNum P_WD_max;
    IloNum P_GS_lim;
    IloNum P_GI_lim;
    IloNum P_SS_lim;
    IloNum P_SI_lim;
    IloNum P_LOAD_max;
    IloNum P_PV_max;
    IloNum CPL_S;
    IloNum CPV_S;
    IloNum CWD_S;
    IloNum CDG;

```

```

IloNum PLS_total;
IloInt PLS_LEVEL;
IloInt PLS_inc;

IloExpr test;
IloExpr obj;
IloExpr obj_RES;
IloExpr obj_PLS;
IloExpr obj_DG;

IloIntArray t;
IloFloatArray PPV;
IloFloatArray PL;
IloFloatArray PWD;

IloIntVarArray PLS_Level;

IloFloatVarArray PWD_S;
IloFloatVarArray PDG;
IloFloatVarArray PG;
IloFloatVarArray PS;
IloFloatVarArray PS_S;
IloFloatVarArray PS_I;
IloFloatVarArray PPV_S;
IloFloatVarArray PL_S;
IloFloatVarArray PGINT;
IloFloatVarArray PLSINT;
IloBoolVarArray NOT_FULL_SOC;
IloBoolVarArray NOT_EMPTY_SOC;
IloBoolVarArray DG_ON;
bool use_PGINT;
bool use_PLSINT;
bool use_no_garabage_if_not_SOC_max;
bool use_no_DG_if_not_SOC_min;
bool use_PLS_total;
bool use_PLS_LEVEL;
unsigned int PGINT_dt;
unsigned int PLSINT_dt;
IloFloatVarArray SOC;

void build_model();
void add_CG_constant_by_interval_constraint(unsigned int dt);
void add_PLS_constant_by_interval_constraint(unsigned int dt);
void add_no_garabage_if_not_SOC_max_constraint();
void add_no_DG_if_not_SOC_min_constraint();
void add_PLS_total_constraint();
void add_PLS_level_constrain();
void read_parameters();

void record_results(const std::string& filename_of_results);
bool is_problem_computed() { return problem_computed; }
bool is_problem_proved() { return problem_proved; }
public:
SMART_GRID_LP_solver(const std::string& instance_filename, const std::string& parameters_filename);
~SMART_GRID_LP_solver();
void set_SOC_init(IloNum v) { SOC_init=v; }
void set_SOC_coeff(IloNum v) { SOC_coeff=v; }
void set_SOC_min(IloNum v) { SOC_min=v; }
void set_SOC_max(IloNum v) { SOC_max=v; }
void set_P_DG_lim(IloNum v) { P_DG_lim=v; }

void set_P_WD_max(IloNum v) { P_WD_max=v; }
void set_P_GS_lim(IloNum v) { P_GS_lim=v; }
void set_P_GI_lim(IloNum v) { P_GI_lim=v; }
void set_P_SS_lim(IloNum v) { P_SS_lim=v; }
void set_P_SI_lim(IloNum v) { P_SI_lim=v; }
void set_P_LOAD_max(IloNum v) { P_LOAD_max=v; }
void set_P_PV_max(IloNum v) { P_PV_max=v; }
void set_SOC_end_lb(IloNum v) { SOC_end_lb=v; }

```

```
void set_CPL_S(IloNum v) { CPL_S=v; }
void set_CPV_S(IloNum v) { CPV_S=v; }
void set_CWD_S(IloNum v) { CWD_S=v; }
void set_CDG(IloNum v) { CDG=v; }
void set_PLS_total(IloNum v) { PLS_total=v; }

IloNum get_SOC_init() const { return SOC_init; }
IloNum get_SOC_coeff() const { return SOC_coeff; }
IloNum get_SOC_min() const { return SOC_min; }
IloNum get_SOC_max() const { return SOC_max; }
IloNum get_P_DG_lim() const { return P_DG_lim; }

IloNum get_P_WD_max() const { return P_WD_max; }
IloNum get_P_GS_lim() const { return P_GS_lim; }
IloNum get_P_GI_lim() const { return P_GI_lim; }
IloNum get_P_SS_lim() const { return P_SS_lim; }
IloNum get_P_SI_lim() const { return P_SI_lim; }
IloNum get_P_LOAD_max() const { return P_LOAD_max; }
IloNum get_P_PV_max() const { return P_PV_max; }
IloNum get_SOC_end_lb() const { return SOC_end_lb; }
IloNum get_CPL_S() const { return CPL_S; }
IloNum get_CPV_S() const { return CPV_S; }
IloNum get_CWD_S() const { return CWD_S; }
IloNum get_CDG() const { return CDG; }
IloNum get_PLS_total() const { return PLS_total; }
const std::string& get_instance_name() const { return instance_name; }
const std::string& get_parameters_name() const { return instance_name; }
virtual void solve(const std::string& filename_of_results="results.txt");

void set_time_limit(unsigned int nbs) { time_limit=nbs; }

};

#endif
```

Main Program

D:\快盘\2012\论文V1\latest by chapter\Annex\main_annex.cpp

1

```
#include <iostream>
#include <string>
#include <sstream>
#include <vector>
#include <stdio.h>
#include "SMART_GRID_LP_solver.h"

void solve_instance(const std::string& name, const std::string& parameters, const std::string& results){
    try{
        std::cout<<"try solving "<<std::setw(20)<<name<<"...";
        SMART_GRID_LP_solver s(name, parameters);
        s.set_time_limit(144000);
        s.solve(results);
    }
    catch(SMART_GRID_exception& e){
        std::cout<<"error:"<<e.what()<<std::endl;
    }
    catch(IloException e){
        std::cout<<e.getMessage()<<std::endl;
    }
    catch(std::exception e){
        std::cout<<e.what()<<std::endl;
    }
}

int main( int argc, const char* argv[] ){

    switch(argc) {
    case 1:

        remove("./instances/pg2_8_20/results_pg2.txt");
        solve_instance("D:/PROJECTS/MG_standalone/instances/pg2_8_20/test1009.txt", "./instances/pg2_8_20/
pg2_offgrid.prm", "./instances/pg2_8_20/results_pg2.txt");

        break;
    case 4:
        solve_instance(argv[1], argv[2], argv[3]);
        break;
    default:
        std::cout<<"Erreur: Parametres incorrect"<<std::endl;
    }

    return 0;
}
```

```

#define OFFGRID
#ifdef ONGRID
#include "SMART_GRID_LP_solver.h"

ILOSTLBEGIN

const char* SMART_GRID_exception::what() const { return info.c_str(); }

std::istream& operator>>(std::istream& f, PERIODE& p) {
    f>>p.lb>>p.ub>>p.C_GI>>p.C_GS>>p.C_SI>>p.C_SS;
    return f;
}
std::ostream& operator<<(std::ostream& f, const PERIODE& p) {
    f<<"["<<p.lb<<" "<<p.ub<<" "<<" CGI="<<p.C_GI<<" CGS="<<p.C_GS<<" CSI="<<p.C_SI<<" CSS="<<p.C_SS;
    return f;
}

SMART_GRID_LP_solver::SMART_GRID_LP_solver(const std::string& instance_filename, const std::string&
    parameters_filename):
    instance_name(instance_filename),
    parameters_name(parameters_filename),
    nb_time_pts(0),
    SOC_init(0),
    SOC_coeff(0),
    SOC_min(0),
    SOC_max(0),
    P_GS_lim(0),
    P_GI_lim(0),
    time_limit(600),
    max_number_of_nodes(std::numeric_limits<unsigned int>::max()),
    problem_computed(false),
    problem_proved(false),
    use_PGINT(false),
    use_PLSINT(false),
    use_PLS_total(false),
    use_PLS_LEVEL(false),
    PGINT_dt(1),
    PLSINT_dt(1),
    use_no_garabage_if_not_SOC_max(false) {
    model=IloModel(env);
    read_parameters();
}

SMART_GRID_LP_solver::~SMART_GRID_LP_solver() {
    env.end();
}

void SMART_GRID_LP_solver::read_parameters() {
    using namespace std;
    ifstream fin(parameters_name.c_str());
    if (!fin) { throw SMART_GRID_exception("problem opening parameters file"); }
    std::string parameter;

    std::cout<<"Parameters :\n";
    while(!fin.eof()) {
        fin>>parameter;
        if (fin.eof()) break;
        cout<<parameter;
        if (!fin) { throw SMART_GRID_exception("problem reading parameter name"); }
        IloNum val=0;
        if (parameter=="SOC_init") {
            fin>>val;
            if (!fin) { throw SMART_GRID_exception("problem reading SOC_init value"); }
            set_SOC_init(val);
        }
        if (parameter=="SOC_min") {
            fin>>val;

```

```
        if (!fin) { throw SMART_GRID_exception("problem reading SOC_min value"); }
        set_SOC_min(val);
    }
    if (parameter=="SOC_max") {
        fin>>val;
        if (!fin) { throw SMART_GRID_exception("problem reading SOC_max value"); }
        set_SOC_max(val);
    }
    if (parameter=="SOC_coeff") {
        fin>>val;
        if (!fin) { throw SMART_GRID_exception("problem reading SOC_coeff value"); }
        set_SOC_coeff(val);
    }
    if (parameter=="P_GS_lim") {
        fin>>val;
        if (!fin) { throw SMART_GRID_exception("problem reading P_GS_lim value"); }
        set_P_GS_lim(val);
    }
    if (parameter=="P_GI_lim") {
        fin>>val;
        if (!fin) { throw SMART_GRID_exception("problem reading P_GI_lim value"); }
        set_P_GI_lim(val);
    }
    if (parameter=="P_SS_lim") {
        fin>>val;
        if (!fin) { throw SMART_GRID_exception("problem reading P_SS_lim value"); }
        set_P_SS_lim(val);
    }
    if (parameter=="P_SI_lim") {
        fin>>val;
        if (!fin) { throw SMART_GRID_exception("problem reading P_SI_lim value"); }
        set_P_SI_lim(val);
    }
    if (parameter=="P_LOAD_max") {
        fin>>val;
        if (!fin) { throw SMART_GRID_exception("problem reading P_LOAD_max value"); }
        set_P_LOAD_max(val);
    }
    if (parameter=="P_PV_max") {
        fin>>val;
        if (!fin) { throw SMART_GRID_exception("problem reading P_PV_max value"); }
        set_P_PV_max(val);
    }
    if (parameter=="SOC_end_lb") {
        fin>>val;
        if (!fin) { throw SMART_GRID_exception("problem reading P_PV_max value"); }
        set_SOC_end_lb(val);
    }
    if (parameter=="PGINT") {
        fin>>val;
        if (!fin) { throw SMART_GRID_exception("problem reading PGINT value"); }
        PGINT_dt=val;
        use_PGINT=true;
    }
    if (parameter=="PLSINT") {
        fin>>val;
        if (!fin) { throw SMART_GRID_exception("problem reading PLSINT value"); }
        PLSINT_dt=val;
        use_PLSINT=true;
    }
    if (parameter=="NO_GARBAGE_IF_NOT_SOC_max") {
        use_no_garabage_if_not_SOC_max=true;
    }
    if (parameter=="CPL_S") {
        fin>>val;
        if (!fin) { throw SMART_GRID_exception("problem reading CPL_S value"); }
        set_CPL_S(val);
    }
    if (parameter=="CPV_S") {
```

```

        fin>>val;
        if (!fin) { throw SMART_GRID_exception("problem reading CPV_S value"); }
        set_CPV_S(val);
    }
    if (parameter=="PLS_total"){
        fin>>val;
        if (!fin) { throw SMART_GRID_exception("problem reading PLS_total value"); }
        set_PLS_total(val);
        use_PLS_total=true;
    }
    if (parameter=="PLS_LEVEL"){
        fin>>val;
        if (!fin) { throw SMART_GRID_exception("problem reading PLS_LEVEL value"); }
        PLS_LEVEL=val;
        use_PLS_LEVEL=true;
    }
    if (parameter=="PLS_inc"){
        fin>>val;
        if (!fin) { throw SMART_GRID_exception("problem reading PLS_LEVEL value"); }
        PLS_inc=val;
    }
    if (parameter=="PERIODE"){
        PERIODE p;
        fin>>p;
        if (!fin) { throw SMART_GRID_exception("problem period value"); }
        if (!periodes.empty() && p.lb!= periodes.back().ub +1) {
            throw SMART_GRID_exception("list of periods should be adjacent (period.ub+1==next_period.
lb)");
        }
        periodes.push_back(p);
        cout<<p<<"\n";
    }else{
        cout<<"="<<val<<"\n";
    }
}
if (periodes.empty()) throw SMART_GRID_exception("coeff for the different periods should be provided")
;
}

void SMART_GRID_LP_solver::add_CG_constant_by_interval_constraint(unsigned int dt)
{
    for(unsigned int i=2; i<=nb_time_pts; i++)
    {
        if (t[i]%dt!=0)
            model.add(PPV_S[i]==PPV_S[i-1]);
    }
}

void SMART_GRID_LP_solver::add_PLS_constant_by_interval_constraint(unsigned int dt)
{
    for(unsigned int i=2; i<=nb_time_pts; i++)
    {
        if (t[i]%dt!=0)
            model.add(PL_S[i]==PL_S[i-1]);
    }
}

void SMART_GRID_LP_solver::add_PLS_total_constraint()
{
    test=IloExpr(env);
    for(unsigned int i=1; i<=nb_time_pts; i++)
    {
        test+=PL_S[i];
    }
    model.add(test*(t[2]-t[1])/3.6e6<=PLS_total);
}

void SMART_GRID_LP_solver::add_PLS_level_constrain()
{

```

```

    for(unsigned int i=1; i<=nb_time_pts; i++)
    {
        model.add(PL_S[i]==PLS_Level[i]*PLS_inc);
    }
}

void SMART_GRID_LP_solver::add_no_garabage_if_not_SOC_max_constraint() {
    NOT_FULL_SOC=IloBoolVarArray(env, nb_time_pts+1);
    for(unsigned int i=1; i<=nb_time_pts; i++) {
        if (PPV[i]>PL[i]) {
            IloNum epsilon=0.005;
            model.add(NOT_FULL_SOC[i]>=1-epsilon-(SOC[i]+epsilon)/get_SOC_max());
            model.add(PPV_S[i]<=PPV[i]*(1-NOT_FULL_SOC[i]));
        }
    }
}

void SMART_GRID_LP_solver::build_model() {
    using namespace std;
    ifstream fin(instance_name.c_str());
    if (!fin) { throw SMART_GRID_exception("problem opening instance file"); }

    fin >> nb_time_pts;
    if (!fin) { throw SMART_GRID_exception("problem reading number of time pts"); }

    t=IloIntArray(env, nb_time_pts+1);
    PPV=IloFloatArray(env, nb_time_pts+1);
    PL=IloFloatArray(env, nb_time_pts+1);

    PLS_Level=IloIntVarArray(env, nb_time_pts+1, 0, PLS_LEVEL);
    PG=IloFloatVarArray(env, nb_time_pts+1, P_GS_lim, P_GI_lim);
    PS=IloFloatVarArray(env, nb_time_pts+1, P_SS_lim, P_SI_lim);
    PL_S=IloFloatVarArray(env, nb_time_pts+1, 0, get_P_LOAD_max());
    PPV_S=IloFloatVarArray(env, nb_time_pts+1, 0, get_P_PV_max());
    SOC=IloFloatVarArray(env, nb_time_pts+1, SOC_min, SOC_max);

    t[0]=2*t[1]-t[2]; PPV[0]=0; PL[0]=0;
    SOC[0].setBounds(get_SOC_init(), get_SOC_init());
    PG[0].setBounds(0, 0);
    PS[0].setBounds(0, 0);
    PL_S[0].setBounds(0, 0);
    PPV_S[0].setBounds(0, 0);

    for(unsigned int i=1; i<=nb_time_pts; i++)
    {
        fin >> t[i];
        if (!fin) { throw SMART_GRID_exception("problem reading time pt"); }
        fin >> PPV[i];
        if (!fin) { throw SMART_GRID_exception("problem reading Alternative Resource"); }
        {
            fin >> PL[i];
        }
        if (!fin) { throw SMART_GRID_exception("problem reading PL"); }

        if (0.9*PPV[i]>PL[i])
        {
            PG[i].setLB(0);
            PS[i].setLB(0);
            PL_S[i].setUB(0);

            model.add(0.9*PPV[i]-0.9*PPV_S[i]==1/0.85*PG[i]+1/0.9*PS[i]+PL[i]-PL_S[i]);
        }
        if (0.9*PPV[i]==PL[i])

```

```

    {
        PG[i]. setBounds(0, 0);
        PS[i]. setBounds(0, 0);
        PPV_S[i]. setBounds(0, 0);
        PL_S[i]. setBounds(0, 0);

        model.add(0.9*PPV[i]-0.9*PPV_S[i]==0.85*PG[i]+0.9*PS[i]+PL[i]-PL_S[i]);
    }
    if (0.9*PPV[i]<PL[i])
    {

        PG[i]. setUB(0);
        PS[i]. setUB(0);
        PPV_S[i]. setUB(0);
        model.add(0.9*PPV[i]-0.9*PPV_S[i]==0.85*PG[i]+0.9*PS[i]+PL[i]-PL_S[i]);
    }

    model.add(SOC[i]==SOC[i-1]+100./get_SOC_coeff()*PS[i]*(t[i]-t[i-1]));

    model.add(PPV[i]-PPV_S[i]>=0);
    model.add(PL[i]-PL_S[i]>=0);
}

SOC[nb_time_pts]. setLB(get_SOC_end_lb());

obj=IloExpr(env);
obj_RES=IloExpr(env);
obj_PLS=IloExpr(env);

unsigned int i=1;
for(std::list<PERIODE>::iterator it=perioes.begin(); it!=perioes.end(); it++)
{
    ;
    while(i<=nb_time_pts && t[i]<=it->ub)
    {
        IloNum coeff_CG;
        IloNum coeff_CS;
        if (0.9*PPV[i]>=PL[i]) {
            coeff_CG=it->C_GI;
            coeff_CS=it->C_SI;
            obj+=1/3.6e6*(t[i]-t[i-1])*(-coeff_CG*PG[i]+coeff_CS*PS[i]);
        }
        else {
            coeff_CG=it->C_GS;
            coeff_CS=it->C_SS;
            obj+=1/3.6e6*(t[i]-t[i-1])*(-coeff_CG*PG[i]-coeff_CS*PS[i]);
        }
        obj_PLS+=1/3.6e6*(t[i]-t[i-1])*CPL_S*PL_S[i];
        obj_RES+=1/3.6e6*((t[i]-t[i-1])*CPV_S*PPV_S[i];
        i++;
    }
}

cout<<"CPL_S="<<get_CPL_S()<<"\n";

model.add(IloMinimize(env, (obj+obj_PLS+obj_RES)));
}

void SMART_GRID_LP_solver::record_results(const std::string& filename_of_results) {

```

```

using namespace std;
ofstream fRes(filename_of_results.c_str(), ios::app);
if (!fRes) throw std::exception("problem with file for results");
fRes<<setw(20)<<"instance=" <<setw(20)<<instance_name<<"\n";
fRes<<setw(20)<<"cpu=" <<setw(20)<<cplex.getTime()<<"\n";
fRes<<setw(20)<<"Grid+Storage=" <<setw(20)<<cplex.getValue(obj)<<"\n";
fRes<<setw(20)<<"Renewable shedding=" <<setw(20)<<cplex.getValue(obj_RES)<<"\n";
fRes<<setw(20)<<"Load shedding=" <<setw(20)<<cplex.getValue(obj_PLS)<<"\n";
fRes<<setw(20)<<"total=" <<setw(20)<<(cplex.getValue(obj)+cplex.getValue(obj_RES)+cplex.getValue
(obj_PLS))<<"\n";
fRes<<"\n\n";
fRes<<setw(20)<<"t[i]";
fRes<<setw(20)<<"PL[i]";
fRes<<setw(20)<<"PPV[i]";
fRes<<setw(20)<<"C->GRID";
fRes<<setw(20)<<"GRID->C";
fRes<<setw(20)<<"C->S";
fRes<<setw(20)<<"S->C";
fRes<<setw(20)<<"SOC(t)";
fRes<<setw(20)<<"PPV_S";
fRes<<setw(20)<<"PL_S";
fRes<<"\n";
for(unsigned int i=1; i<=nb_time_pts; i++){
    fRes <<setw(20)<<t[i];
    fRes <<setw(20)<<PL[i];
    fRes <<setw(20)<<PPV[i];
    cplex.getValue(PG[i])>=0? fRes<<setw(20)<<cplex.getValue(PG[i])<<setw(20)<<0: fRes<<setw(20)<<0<
<setw(20)<<-cplex.getValue(PG[i]);
    cplex.getValue(PS[i])>=0? fRes<<setw(20)<<cplex.getValue(PS[i])<<setw(20)<<0: fRes<<setw(20)<<0<
<setw(20)<<-cplex.getValue(PS[i]);
    fRes<<setw(20)<<cplex.getValue(SOC[i]);
    fRes<<setw(20)<<cplex.getValue(PPV_S[i]);
    fRes<<setw(20)<<cplex.getValue(PL_S[i]);
    fRes<<"\n";
}
fRes.close();
}

void SMART_GRID_LP_solver::solve(const std::string& filename_of_results)
{
    try {
        build_model();
        if (use_PGINT) add_CG_constant_by_interval_constraint(PGINT_dt);
        if (use_PLSINT) add_PLS_constant_by_interval_constraint(PLSINT_dt);
        if (use_no_garabage_if_not_SOC_max) add_no_garabage_if_not_SOC_max_constraint();
        if (use_PLS_total) add_PLS_total_constraint();
        if (use_PLS_LEVEL) add_PLS_level_constrain();

        std::cout<<get_instance_name()<<"\n";
        cplex=IloCplex(model);
        cplex.setOut(env.getNullStream());
        cplex.setParam(IloCplex::ClockType, 1);
        cplex.setParam(IloCplex::TiLim, time_limit);

        cplex.solve();

        problem_computed=true;
        problem_proved=(cplex.getCplexStatus()==1);
        std::cout<<setw(10)<<cplex.getStatus();
        std::cout<<" cpu="<<setw(10)<<cplex.getTime();
        std::cout<<"\n";
        if(problem_proved)
        {

```

```
        remove(filename_of_results.c_str());
        record_results(filename_of_results);

        std::cout<<" solve successeful, save file...";
    }
}
catch (IloAlgorithm::Exception& ex) {
    cerr << "Error: " << ex << endl;
}
catch (IloException& ex) {
    cerr << "Error: " << ex << endl;
}
catch (...) {
    cerr << "Other Exception" << endl;
}
}
```

```
#endif
```

```

#define OFFGRID
#ifdef OFFGRID
#include "SMART_GRID_LP_solver.h"

ILOSTLBEGIN

const char* SMART_GRID_exception::what() const { return info.c_str(); }

std::istream& operator>>(std::istream& f, PERIODE& p) {
    f>>p.lb>>p.ub>>p.C_GI>>p.C_GS>>p.C_SI>>p.C_SS;
    return f;
}
std::ostream& operator<<(std::ostream& f, const PERIODE& p) {
    f<<"["<<p.lb<<" "<<p.ub<<" "<<" CGI="<<p.C_GI<<" CGS="<<p.C_GS<<" CSI="<<p.C_SI<<" CSS="<<p.C_SS;
    return f;
}

SMART_GRID_LP_solver::SMART_GRID_LP_solver(const std::string& instance_filename, const std::string&
    parameters_filename):
    instance_name(instance_filename),
    parameters_name(parameters_filename),
    nb_time_pts(0),
    SOC_init(0),
    SOC_coeff(0),
    SOC_min(0),
    SOC_max(0),
    P_DG_lim(0),
    time_limit(600),
    max_number_of_nodes(std::numeric_limits<unsigned int>::max()),
    problem_computed(false),
    problem_proved(false),
    use_PGINT(false),
    use_PLSINT(false),
    use_PLS_total(false),
    use_PLS_LEVEL(false),
    PGINT_dt(1),
    PLSINT_dt(1),
    use_no_DG_if_not_SOC_min(false),
    use_no_garabage_if_not_SOC_max(false) {
    model=IloModel(env);
    read_parameters();
}

SMART_GRID_LP_solver::~SMART_GRID_LP_solver() {
    env.end();
}

void SMART_GRID_LP_solver::read_parameters() {
    using namespace std;
    ifstream fin(parameters_name.c_str());
    if (!fin) { throw SMART_GRID_exception("problem opening parameters file"); }
    std::string parameter;

    std::cout<<"Parameters :\n";
    while(!fin.eof()) {
        fin>>parameter;
        if (fin.eof()) break;
        cout<<parameter;
        if (!fin) { throw SMART_GRID_exception("problem reading parameter name"); }
        IloNum val=0;
        if (parameter=="SOC_init") {
            fin>>val;
            if (!fin) { throw SMART_GRID_exception("problem reading SOC_init value"); }
            set_SOC_init(val);
        }
        if (parameter=="SOC_min") {
            fin>>val;

```

```
        if (!fin) { throw SMART_GRID_exception("problem reading SOC_min value"); }
        set_SOC_min(val);
    }
    if (parameter=="SOC_max") {
        fin>>val;
        if (!fin) { throw SMART_GRID_exception("problem reading SOC_max value"); }
        set_SOC_max(val);
    }
    if (parameter=="SOC_coeff") {
        fin>>val;
        if (!fin) { throw SMART_GRID_exception("problem reading SOC_coeff value"); }
        set_SOC_coeff(val);
    }
    if (parameter=="P_DG_lim") {
        fin>>val;
        if (!fin) { throw SMART_GRID_exception("problem reading P_DG_lim value"); }
        set_P_DG_lim(val);
    }
    if (parameter=="P_SS_lim") {
        fin>>val;
        if (!fin) { throw SMART_GRID_exception("problem reading P_SS_lim value"); }
        set_P_SS_lim(val);
    }
    if (parameter=="P_SI_lim") {
        fin>>val;
        if (!fin) { throw SMART_GRID_exception("problem reading P_SI_lim value"); }
        set_P_SI_lim(val);
    }
    if (parameter=="P_LOAD_max") {
        fin>>val;
        if (!fin) { throw SMART_GRID_exception("problem reading P_LOAD_max value"); }
        set_P_LOAD_max(val);
    }
    if (parameter=="P_PV_max") {
        fin>>val;
        if (!fin) { throw SMART_GRID_exception("problem reading P_PV_max value"); }
        set_P_PV_max(val);
    }
    if (parameter=="SOC_end_lb") {
        fin>>val;
        if (!fin) { throw SMART_GRID_exception("problem reading P_PV_max value"); }
        set_SOC_end_lb(val);
    }
    if (parameter=="PLSINT") {
        fin>>val;
        if (!fin) { throw SMART_GRID_exception("problem reading PLSINT value"); }
        PLSINT_dt=val;
        use_PLSINT=true;
    }
    if (parameter=="NO_GARBAGE_IF_NOT_SOC_max") {
        use_no_garabage_if_not_SOC_max=true;
    }
    if (parameter=="NO_DG_IF_NOT_SOC_min") {
        use_no_DG_if_not_SOC_min=true;
    }
    if (parameter=="CPL_S") {
        fin>>val;
        if (!fin) { throw SMART_GRID_exception("problem reading CPL_S value"); }
        set_CPL_S(val);
    }
    if (parameter=="CPV_S") {
        fin>>val;
        if (!fin) { throw SMART_GRID_exception("problem reading CPV_S value"); }
        set_CPV_S(val);
    }
    if (parameter=="CDG") {
        fin>>val;
        if (!fin) { throw SMART_GRID_exception("problem reading CDG value"); }
        set_CDG(val);
    }
```

```

    }
    if (parameter=="PLS_total"){
        fin>>val;
        if (!fin) { throw SMART_GRID_exception("problem reading PLS_total value"); }
        set_PLS_total(val);
        use_PLS_total=true;
    }
    if (parameter=="PLS_LEVEL"){
        fin>>val;
        if (!fin) { throw SMART_GRID_exception("problem reading PLS_LEVEL value"); }
        PLS_LEVEL=val;
        use_PLS_LEVEL=true;
    }
    if (parameter=="PLS_inc"){
        fin>>val;
        if (!fin) { throw SMART_GRID_exception("problem reading PLS_LEVEL value"); }
        PLS_inc=val;
    }
}

void SMART_GRID_LP_solver::add_CG_constant_by_interval_constraint(unsigned int dt)
{
    for(unsigned int i=2; i<=nb_time_pts; i++)
    {
        if (t[i]%dt!=0)
            model.add(PPV_S[i]==PPV_S[i-1]);
    }
}

void SMART_GRID_LP_solver::add_PLS_constant_by_interval_constraint(unsigned int dt)
{
    for(unsigned int i=2; i<=nb_time_pts; i++)
    {
        if (t[i]%dt!=0)
            model.add(PL_S[i]==PL_S[i-1]);
    }
}

void SMART_GRID_LP_solver::add_PLS_total_constraint()
{
    test=IloExpr(env);
    for(unsigned int i=1; i<=nb_time_pts; i++)
    {
        test+=PL_S[i];
    }
    model.add(test*(t[2]-t[1])/3.6e6<=PLS_total);
}

void SMART_GRID_LP_solver::add_PLS_level_constrain()
{
    for(unsigned int i=1; i<=nb_time_pts; i++)
    {
        model.add(PL_S[i]==PLS_Level[i]*PLS_inc);
    }
}

void SMART_GRID_LP_solver::add_no_garabage_if_not_SOC_max_constraint() {
    NOT_FULL_SOC=IloBoolVarArray(env, nb_time_pts+1);
    for(unsigned int i=1; i<=nb_time_pts; i++){
        if (0.9*PPV[i]>PL[i]) {
            IloNum epsilon=0.005;
            model.add(NOT_FULL_SOC[i]>=1-epsilon-(SOC[i]+epsilon)/get_SOC_max());
            model.add(PPV_S[i]<=PPV[i]*(1-NOT_FULL_SOC[i]));
        }
    }
}

```

```

void SMART_GRID_LP_solver::add_no_DG_if_not_SOC_min_constraint()
{
    NOT_EMPTY_SOC=IloBoolVarArray(env,nb_time_pts+1);
    for(unsigned int i=1; i<=nb_time_pts; i++)
    {
        {
            IloNum epsilon=0.005;
            model.add(NOT_EMPTY_SOC[i]>=1-epsilon-(100-SOC[i])/(100-get_SOC_min()));
            model.add(PDG[i]<=P_DG_lim*(1-NOT_EMPTY_SOC[i]));
        }
    }
}

void SMART_GRID_LP_solver::build_model() {
    using namespace std;
    ifstream fin(instance_name.c_str());
    if (!fin) { throw SMART_GRID_exception("problem opening instance file"); }

    fin >> nb_time_pts;
    if (!fin) { throw SMART_GRID_exception("problem reading number of time pts"); }

    t=IloIntArray(env,nb_time_pts+1);
    PPV=IloFloatArray(env,nb_time_pts+1);
    PL=IloFloatArray(env,nb_time_pts+1);

    PLS_Level=IloIntVarArray(env,nb_time_pts+1,0,PLS_LEVEL);
    PDG=IloFloatVarArray(env,nb_time_pts+1,0,P_DG_lim);
    PS_I=IloFloatVarArray(env,nb_time_pts+1,0,P_SI_lim);
    PS_S=IloFloatVarArray(env,nb_time_pts+1,0,P_SS_lim);
    PL_S=IloFloatVarArray(env,nb_time_pts+1,0,get_P_LOAD_max());
    PPV_S=IloFloatVarArray(env,nb_time_pts+1,0,get_P_PV_max());
    SOC=IloFloatVarArray(env,nb_time_pts+1,SOC_min,SOC_max);

    t[0]=2*t[1]-t[2]; PPV[0]=0; PL[0]=0;
    SOC[0].setBounds(get_SOC_init(),get_SOC_init());
    PS_S[0].setBounds(0,0);
    PS_I[0].setBounds(0,0);
    PL_S[0].setBounds(0,0);
    PPV_S[0].setBounds(0,0);

    for(unsigned int i=1; i<=nb_time_pts; i++)
    {
        fin >> t[i];
        if (!fin) { throw SMART_GRID_exception("problem reading time pt"); }
        fin >> PPV[i];
        if (!fin) { throw SMART_GRID_exception("problem reading Alternative Resource"); }
        {
            fin >> PL[i];
        }

        if (0.9*PPV[i]>PL[i])
        {
            PL_S[i].setUB(0);
        }
        if (0.9*PPV[i]==PL[i])
        {
            PPV_S[i].setBounds(0,0);
            PL_S[i].setBounds(0,0);
        }
        if (0.9*PPV[i]<PL[i])
        {
            PPV_S[i].setUB(0);
        }

        model.add(0.9*PPV[i]-0.9*PPV_S[i]+0.85*PDG[i]+0.9*PS_S[i]==1/0.9*PS_I[i]+PL[i]-PL_S[i]);
        model.add(SOC[i]==SOC[i-1]+100./get_SOC_coeff()*(PS_I[i]-PS_S[i])*(t[i]-t[i-1]));
    }
}

```

```

        model.add(PPV[i]-PPV_S[i]>=0);
        model.add(PL[i]-PL_S[i]>=0);
    }

    SOC[nb_time_pts].setLB(get_SOC_end_lb());

    obj=IloExpr(env);
    obj_RES=IloExpr(env);
    obj_PLS=IloExpr(env);
    obj_DG=IloExpr(env);

    DG_ON=IloBoolVarArray(env,nb_time_pts+1);
    DG_ON[0].setBounds(0,0);
    PDG[0].setBounds(0,0);
    model.add(PDG[1]==1500*(DG_ON[1]));
    for(unsigned int i=2; i<=nb_time_pts; i++)
    {
        if (t[i]%1200!=0)
            model.add(DG_ON[i]==DG_ON[i-1]);
            model.add(PDG[i]==1500*(DG_ON[i]));
    }

    unsigned int i=1;
    for(std::list<PERIODE>::iterator it=perioes.begin(); it!=perioes.end(); it++)
    {
        IloNum coeff_CS=it->C_SS;
        while(i<=nb_time_pts && t[i]<=it->ub)
        {
            obj+=1/3.6e6*(t[i]-t[i-1])*coeff_CS*(PS_I[i]-PS_S[i]);
            obj_PLS+=1/3.6e6*(t[i]-t[i-1])*CPL_S*PL_S[i];
            obj_RES+=1/3.6e6*((t[i]-t[i-1])*CPV_S*PPV_S[i]);
            obj_DG+=1/3.6e6*(t[i]-t[i-1])*CDG*PDG[i];
            i++;
        }
    }
    cout<<"CPL_S"<<get_CPL_S()<<"\n";
    model.add(IloMinimize(env,(obj+obj_PLS+obj_RES+obj_DG)));
}

void SMART_GRID_LP_solver::record_results(const std::string& filename_of_results){

    using namespace std;
    ofstream fRes(filename_of_results.c_str(),ios::app);
    if (!fRes) throw std::exception("problem with file for results");

    fRes<<setw(20)<<"instance= " <<setw(20)<<instance_name<<"\n";
    fRes<<setw(20)<<"cpu= " <<setw(20)<<cplex.getTime()<<"\n";
    fRes<<setw(20)<<"Grid+Storage= " <<setw(20)<<cplex.getValue(obj)<<"\n";
    fRes<<setw(20)<<"Renewable shedding= " <<setw(20)<<cplex.getValue(obj_RES)<<"\n";
    fRes<<setw(20)<<"Load shedding= " <<setw(20)<<cplex.getValue(obj_PLS)<<"\n";
    fRes<<setw(20)<<"Distributed geneartion= " <<setw(20)<<cplex.getValue(obj_DG)<<"\n";
    fRes<<setw(20)<<"total= " <<setw(20)<<(cplex.getValue(obj)+cplex.getValue(obj_RES)+cplex.getValue
        (obj_PLS)+cplex.getValue(obj_DG))<<"\n";
    fRes<<"\n\n";
    fRes<<setw(20)<<"t[i]";
    fRes<<setw(20)<<"PL[i]";
    fRes<<setw(20)<<"PPV[i]";
    fRes<<setw(20)<<"C->S";
    fRes<<setw(20)<<"S->C";
    fRes<<setw(20)<<"SOC(t)";
    fRes<<setw(20)<<"PPV_S";
    fRes<<setw(20)<<"PL_S";
    fRes<<setw(20)<<"PDG[i]";

    fRes<<"\n";
    for(unsigned int i=1; i<=nb_time_pts; i++){
        fRes <<setw(20)<<t[i];

```

```

        fRes <<setw(20)<<PL[i];
        fRes <<setw(20)<<PPV[i];
        fRes <<setw(20)<<cplex.getValue(PS_I[i]);
        fRes <<setw(20)<<cplex.getValue(PS_S[i]);
        fRes<<setw(20)<<cplex.getValue(SOC[i]);
        fRes<<setw(20)<<cplex.getValue(PPV_S[i]);
        fRes<<setw(20)<<cplex.getValue(PL_S[i]);
        fRes<<setw(20)<<cplex.getValue(PDG[i]);
        fRes<<"\n";
    }
    fRes.close();
}

void SMART_GRID_LP_solver::solve(const std::string& filename_of_results)
{
    try {
        build_model();
        if (use_PGINT) add_CG_constant_by_interval_constraint(PGINT_dt);
        if (use_PLSINT) add_PLS_constant_by_interval_constraint(PLSINT_dt);
        if (use_no_garabage_if_not_SOC_max) add_no_garabage_if_not_SOC_max_constraint();
        if (use_PLS_total) add_PLS_total_constraint();
        if (use_PLS_LEVEL) add_PLS_level_constrain();
        if (use_no_DG_if_not_SOC_min) add_no_DG_if_not_SOC_min_constraint();

        std::cout<<get_instance_name()<<"\n";
        cplex=IloCplex(model);
        cplex.setOut(env.getNullStream());
        cplex.setParam(IloCplex::ClockType,1);
        cplex.setParam(IloCplex::TiLim,time_limit);
        cplex.solve();

        problem_computed=true;

        problem_proved=(cplex.getCplexStatus()==1);

        std::cout<<setw(10)<<cplex.getStatus();
        std::cout<<" cpu="<<setw(10)<<cplex.getTime();
        std::cout<<"\n";
        if(problem_proved)
        {
            remove(filename_of_results.c_str());
            record_results(filename_of_results);

            std::cout<<" solve successeful, save file...";
        }
    }
    catch (IloAlgorithm::Exception& ex) {
        cerr << "Error: " << ex << endl;
    }
    catch (IloException& ex) {
        cerr << "Error: " << ex << endl;
    }
    catch (...) {
        cerr << "Other Exception" << endl;
    }
}

#endif

```

Brief descriptions of the program files:

Head file: the data structure is defined and functions are declared in this file.

Main program: calls main function to solve the specific instance by specifying input and output file.

Grid-connected mode optimization functions: include functions that read input data and parameter, formulate the problem with respect to constraints, call CPLEX solver and record optimization results to file. The functions are specified for the grid-connected mode.

Off-grid mode optimization functions: include functions that read input data and parameter, formulate the problem with respect to constraints, call CPLEX solver and record optimization results to file. The functions are specified for the off-grid mode.